

Dissertation zur Erlangung des Doktorgrades
der Fakultät für Chemie und Pharmazie
der Ludwig-Maximilians-Universität München

Optical Single-Molecule Biosensors Assembled by DNA Origami

Sarah Elisabeth Ochmann

aus

Bielefeld, Deutschland

2022

Erklärung

Diese Dissertation wurde im Sinne von § 7 der Promotionsordnung vom 28. November 2011 von Prof. Dr. Philip Tinnefeld betreut.

Eidesstattliche Versicherung

Diese Dissertation wurde eigenständig und ohne unerlaubte Hilfe erarbeitet.

München, 25.03.2022

Sarah Elisabeth Ochmann

Dissertation eingereicht am 06.12.2021

1. Gutachter: Prof. Dr. Philip Tinnefeld

2. Gutachter: Prof. Don C. Lamb, PhD

Mündliche Prüfung am 20.01.2022

Veröffentlichungen der Dissertation

Teilergebnisse aus dieser Arbeit wurden in folgenden Beiträgen vorab veröffentlicht:

Publikationen

Sarah E. Ochmann, Carolin Vietz, Kateryna Trofymchuk, Guillermo P. Acuna, Birka Lalkens, Philip Tinnefeld: Optical Nanoantenna for Single Molecule-Based Detection of Zika Virus Nucleic Acids without Molecular Multiplication. *Analytical Chemistry*, 89, 13000–13007, 2017

Sarah E. Ochmann, Himanshu Joshi, Ece Büber, Henri G. Franquelim, Pierre Stegemann, Barbara Sacca, Ulrich F. Keyser, Aleksei Aksimentiev, Philip Tinnefeld: DNA Origami Voltage Sensors for Transmembrane Potentials with Single-Molecule Sensitivity. *Nano Letters*, 21, 8634-8641, 2021

Sarah E. Ochmann, Tim Schröder, Clara M. Schulz, Philip Tinnefeld: Quantitative Single-Molecule Measurements of Membrane Charges with DNA Origami Sensors. *Analytical Chemistry*, 94, 2633–2640, 2022

Tagungsbeiträge

Sarah E. Ochmann, Carolin Vietz, Birka Lalkens, Guillermo P. Acuna, Philip Tinnefeld: Detection of Zika by Fluorescence Enhancement of Single Molecules with Optical Antennas. *Future Trends in DNA-based Nanotechnology*, Dresden, 2017 (Poster)

Sarah E. Ochmann, Carolin Vietz, Birka Lalkens, Guillermo P. Acuna, Philip Tinnefeld: Detection of Zika by Fluorescence Enhancement of Single Molecules with Optical Antennas. *Braunschweiger JungChemikerTagung*, Braunschweig, 2017 (Poster)

Sarah E. Ochmann, Carolin Vietz, Kateryna Trofymchuk, Guillermo P. Acuna, Birka Lalkens, Philip Tinnefeld: Single Molecule-Based Detection of Zika Virus Nucleic Acids. *Fluorescence markers for advanced microscopy*, Les Houches, 2018 (Poster)

Sarah E. Ochmann, Carolin Vietz, Kateryna Trofymchuk, Guillermo P. Acuna, Birka Lalkens, Philip Tinnefeld: Single Molecule-Based Detection of Zika Virus Nucleic Acids. *CeNS Retreat*, Kleinwalsertal, 2018 (Poster)

Sarah E. Ochmann, Henri G. Franquelim, Ulrich F. Keyser, Philip Tinnefeld: Optical Voltage-Sensing Nano Devices based on DNA Origami. *CeNS Workshop*, Venedig, 2018 (Poster)

Sarah E. Ochmann, Ece Büber, Henri G. Franquelim, Ulrich F. Keyser, Philip Tinnefeld: Optical Voltage Sensing with DNA Origami Nanostructures. *SFB1032 Jahresworkshop*, Benediktbeuern, 2019 (Poster)

Sarah E. Ochmann, Ece Büber, Henri G. Franquelim, Ulrich F. Keyser, Philip Tinnefeld: Towards Single-Molecule Voltage Imaging with DNA Origami. *Nucleic Acid Nanotechnology*, Aalto, 2019 (Poster)

Sarah E. Ochmann, Ece Büber, Henri G. Franquelim, Ulrich F. Keyser, Philip Tinnefeld: DNA Nanotechnology for Optical Voltage Sensing. *Diagnostics4Future Conference*, Konstanz, 2019 (Poster)

Sarah E. Ochmann, Himanshu Joshi, Ece Büber, Henri G. Franquelim, Ulrich F. Keyser, Aleksei Aksimentiev, Philip Tinnefeld: Sensors for Membrane Voltage by DNA Nanotech. SFB1032 Jahresworkshop, online, 2020 (Vortrag)

Sarah E. Ochmann, Himanshu Joshi, Ece Büber, Henri G. Franquelim, Ulrich F. Keyser, Aleksei Aksimentiev, Philip Tinnefeld: Optical Single-Molecule Voltage Sensing with DNA Origami. DNA Node – Frontiers in DNA Nanotechnology, online, 2020 (Vortrag)

Sarah E. Ochmann, Himanshu Joshi, Ece Büber, Henri G. Franquelim, Ulrich F. Keyser, Aleksei Aksimentiev, Philip Tinnefeld: Optical Voltage Sensing on Biological Membranes. Single-Molecule Sensors and NanoSystems International Conference, online, 2020 (Vortrag)

Sarah E. Ochmann, Himanshu Joshi, Ece Büber, Henri G. Franquelim, Ulrich F. Keyser, Aleksei Aksimentiev, Philip Tinnefeld: Single-Molecule Voltage Imaging on Lipid Membranes. LMU/Cambridge Symposium, online, 2021 (Vortrag)

Sarah E. Ochmann, Himanshu Joshi, Ece Büber, Henri G. Franquelim, Ulrich F. Keyser, Aleksei Aksimentiev, Philip Tinnefeld: Sensors for Membrane Voltage by DNA Nanotech. SFB1032 Jahresworkshop, Herrsching, 2021 (Vortrag)

Abstract

Optical biosensing with single-molecule sensitivity requires high performant fluorescent probes. Many different functionalities have to be combined into small chemical entities. In this thesis, the DNA origami technique was used to tailor single-molecule biosensors according to their diverse needs as it offers a modular probe development with straightforward iteration possibilities. The focus was on a nucleic acid detection assay for future *in vitro* diagnostic applications and on voltage sensors to be applied to cell membranes.

Particularly, for the nucleic acid detection assay, a silver nanoparticle was bound to a DNA origami pillar yielding a so-called nanoantenna which enhances the fluorescence of a dye in close proximity through plasmonic field interaction. This phenomenon was used to increase the optical signal released from a single DNA hairpin equipped with a dye-quencher pair. In the presence of a specific target nucleic acid, the hairpin's secondary structure was broken and a fluorescence signal was observed. Using a hairpin sensing Zika specific sequences, the assay was characterized in terms of hairpin opening yield and fluorescence enhancement as well as single-nucleotide variation sensitivity and multiplexing ability. Further, diagnostic conditions were imitated by enriching heat-inactivated human serum with target DNA and using RNA targets. The presented detection assay yielded promising results for further development and future application in *in vitro* diagnostic assays at the point-of-care.

In addition, two single-molecule biosensors for electrical membrane potentials were developed; one sensor for transmembrane potentials and a second one for membrane surface charges of lipid head groups. Both sensors translated the voltage into Förster Resonance Energy Transfer (FRET) signals. A rectangular DNA origami was used as an assembly platform with different optional modifications, *i.e.* for membrane targeting, surface immobilization and voltage sensing. In both sensors, the sensing unit protruding from the origami plate, consisted of DNA and carried a FRET-compatible dye pair. The red dye anchored the sensing unit to the membrane and provided a stable FRET acceptor. A green dye was placed on DNA between the membrane and the DNA origami plate and flexibly changed its conformation in response to the voltages which resulted in the desired FRET change. For both, the transmembrane and the surface charge sensor, the sensing unit's chemical structure was adapted to meet the different requirements.

The functionality of the transmembrane potential sensor was tested using liposomes with defined electrical potentials. It was shown that changes in the transmembrane potential were translated into different single-molecule FRET signals. Further, by introducing small chemical variations in the molecular structure of the sensing unit, the biosensor's sensitivity was changed to respond either to de- or hyperpolarized membranes. Also, the membrane charge sensor yielded promising results; changes in the amounts of anionic lipids in liposomes resulted in different FRET signals. These findings suggested a quantitative translation of membrane surface charges into optical signals and were read out on the level of single sensors. Both sensing mechanisms were further characterized with molecular dynamic (MD) simulations for the transmembrane potential sensor and with fluorescence correlation spectroscopy (FCS) for the membrane surface charge sensor.

Overall, three different biosensors with optical single-molecule read-out were introduced in this thesis using DNA origami as an assembly platform. The sensors were examined for potential diagnostic applications and future *in vivo* voltage imaging. The presented results underline the potential of DNA origami for further single-molecule biosensors beyond the ones investigated within this thesis.

Content

1	Introduction.....	3
1.1	DNA Nanotechnology for Biosensing with Fluorescent Read-Out.....	4
1.2	Optical Single-Molecule <i>in vitro</i> Diagnostics	6
1.2.1	State of the Art.....	6
1.2.2	Optical Nanoantennas for Single-Molecule Sensing	7
1.3	Membrane Biosensing with Single-Molecule Sensitivity	8
1.3.1	Electrical Transmembrane Potential Measurements.....	9
1.3.2	Optical Biosensing of Membrane Surface Charges.....	10
2	Theoretical Background.....	12
2.1	Fluorescence.....	12
2.1.1	Non-Radiative Energy Transfer	13
2.1.2	Photobleaching and Photostabilization	15
2.2	Single-Molecule Fluorescence Studies	15
2.3	DNA Nanotechnology.....	17
2.4	Nanophotonics.....	18
2.5	Electrostatic Properties of Lipid Membranes	20
3	Methods.....	22
3.1	Confocal Microscope	22
3.2	TIRF Microscope.....	22
3.3	DNA Origami Production.....	23
3.4	Nanoparticle Functionalization.....	23
3.5	Liposome Preparation	24
3.6	Preparation of Microscopy Slides.....	24
4	DNA Origami for Single-Molecule <i>in vitro</i> Diagnostics	25
5	Single-Molecule Membrane Sensors with DNA Origami	28
5.1	Transmembrane Potential Sensing.....	28
5.2	Membrane Surface Charge Sensing.....	31
6	Conclusion and Outlook.....	34
7	Appendix.....	38
7.1	Associated publication P1.....	38
7.2	Associated publication P2	60

7.3	Associated publication P3	108
8	List of Figures.....	134
9	Abbreviations.....	135
10	References	136
11	Acknowledgements	147

1 Introduction

An organism is a masterpiece of evolution. What seems almost magical from the outside, is the most complex biochemical interplay existing. The way cells interact, form agglomerates and how the whole biosynthesis is controlled is remarkable. Ever since, mankind has been keen to understand these processes where a visual inspection of biological phenomena has always been a standard tool. With the invention of the first microscope in the late 16th century, a revolutionary step was made to overcome the resolution limit of the eye.¹ Although microscopes were further improved, with the first fluorescence microscopes in the early 20th century, a new era began. Unlike simple light microscopy, fluorescence allowed for a more specific visualization of objects.² What was first limited to staining, *e.g.* specific cell compartments, was soon extended to labeling specific molecules of interest with organic fluorophores or fluorescent proteins. Finally, in 1989 scientists were able for the very first-time to observe the absorption,³ and in 1990, the fluorescence of a single molecule;⁴ the field of optical single-molecule spectroscopy was born. Soon, it was also applied in biological contexts^{5,6} and has meanwhile become an established method. Furthermore, based on the detection of single-molecules, super-resolution methods have evolved to overcome Abbe's diffraction limit⁷ which until then prevented scientist to resolve structures below the size of about half the wavelength used.⁸⁻¹⁰

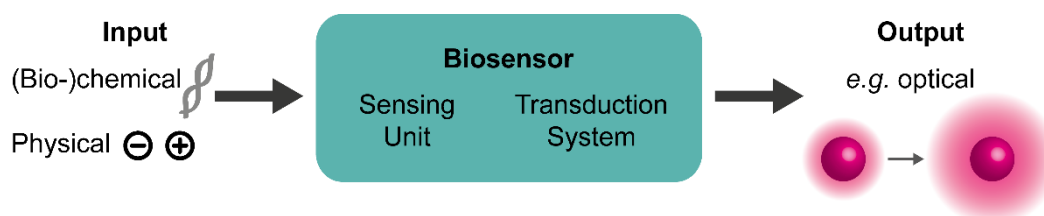


Figure 1. Principle of a biosensor. A biological parameter can be (bio-)chemical or physical and serves as an input for the biosensor. The biosensor consists of a sensing unit and a transduction system. It generates a measurable output which can be for example an optical signal.

The broader application of single-molecule techniques also calls for compatible fluorescent probes. While some attempts focus on the development of brighter and more photostable dyes^{11,12} or on the manipulation of the blinking behavior,¹³ other approaches try to optimize the labeling strategy for increasing the specificity and decreasing the label size.¹⁴ However, conventional fluorophores simply emit light after excitation while they are typically lacking any specific response to changes in the system. This is achieved by extending them with smart functionalities yielding so-called biosensors. In principle, a biosensor is a machine that feels a biological parameter and translates it into a measurable chemico-physical output (Figure 1). For optical single-molecule applications, these machines are nanometer-sized and transduce the parameter of interest into, *e.g.* a change in fluorescence signal. This can involve a change in intensity, fluorescence lifetime, the absorption or emission spectra, *etc.*. The biological parameter which is to be sensed can either be (bio-)chemical such as a nucleic acid, a small molecule, a protein and beyond, or it can have a physical nature such as a mechanical or electrical force. Besides the parameter and the signal read-out, biosensors can be roughly classified by their application; while some biosensors act *in vitro*, others are used to study processes *in vivo*. This suggests different requirements on the sensor and hence, yields different sensing approaches. Within this thesis, different single-molecule biosensors were developed that are based on DNA origami nanostructures – one for *in vitro* diagnostic applications and two for sensing different electrical membrane properties.

1.1 DNA Nanotechnology for Biosensing with Fluorescent Read-Out

The demands on an optical biosensor are versatile and many different functionalities have to be combined into small chemical entities. The sensor has to “feel” the parameter of interest, it has to transduce it into an optical signal and in the context of single-molecule biosensing, the signal has to be stable and bright enough for detection. Additionally, depending on the application, biocompatibility and specific targeting of a cell compartment are mandatory. A promising tool to combine all these requirements is DNA nanotechnology.¹⁵ DNA nanotechnology is based on the hybridization of DNA strands programmed *via* their base sequence;¹⁶ only complementary bases can form hydrogen bonds¹⁷ and if longer parts of the DNA strands are complementary, a DNA duplex results. The potential of DNA’s programming ability to build nanometer-sized objects was first suggested by Nadrian C. Seeman^{18,19} – the founder of the DNA nanotechnology field. Nowadays, there are many different kinds of DNA nanostructures available, *e.g.* tile-based,^{20,21} wireframe²² or DNA origami structures.^{23,24} To build the latter, long single-stranded DNA (ssDNA) – the scaffold – is folded into a desired shape by hybridization with short, so-called staple strands. They are complementary to distinct parts of the scaffold, thereby introduce crossovers to different regions and finally yield billions of identical nanostructures produced in a one-pot self-assembly reaction. The great advantage of DNA origami and other DNA nanotechnology approaches is the straight forward positioning of chemical moieties with sub-nanometer spatial and stoichiometric precision. By tagging an oligonucleotide used for building the structure, the modification is easily incorporated. Various kinds of modifications are commercially available on oligonucleotides^{25,26} such as dyes or quenchers, lipophilic molecules, polar or non-polar spacers and linkers, but also functional groups, *e.g.* for click chemistry, are available. Thereby, post-folding custom-designed DNA-protein conjugates can be yielded. This broad selection of possible modifications makes DNA nanotechnology a versatile tool to design hybrid structures for any desired need as the modifications can be placed on the nanostructure serving as a molecular breadboard.

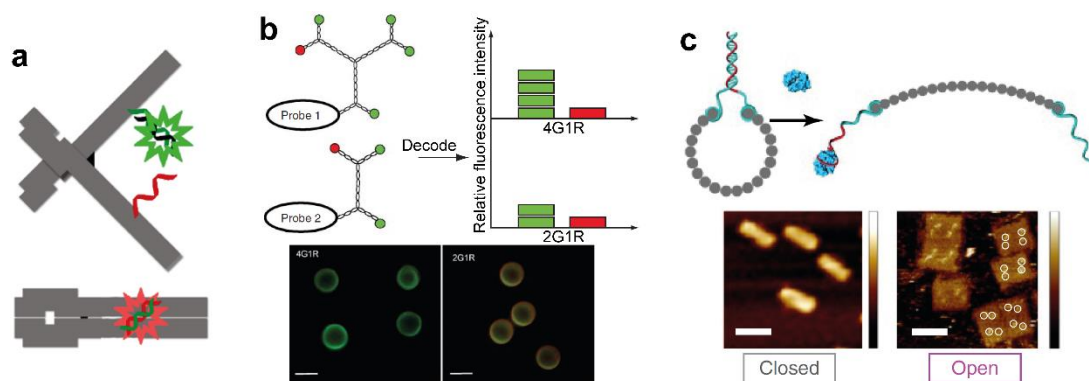


Figure 2. DNA nanotechnology-based biosensors. (a) Split, dye-labelled aptamer for ATP placed on two DNA origami levers connected by a hinge. In the presence of ATP, the structure is in a closed conformation and FRET takes place between the two dyes. Reprinted with permission from ²⁷. (b) Nanobarcodes with fluorescent labels for multiplexed dendritic signal amplification. Reprinted with permission from ²⁸. (c) Top: Tubular DNA origami nanorobot opened by binding of aptamer (red) to nucleolin (blue). Bottom: Atomic force microscopy images of closed and opened structure. On opened structure, eight thrombin molecules are visible on each structure. Reprinted with permission from ²⁹.

Using DNA nanotechnological ideas, various biosensors have been realized. The DNA mostly functions as an assembly scaffold for the sensing unit and the read-out system, but can also fulfill the sensing itself, *e.g.* in the form of aptamers.^{30,31} Aptamers are oligonucleotides that show a strong affinity to a species of interest such as small molecules, ions or proteins, and bind it – similar to an antibody. Walter *et al.*²⁷ combined the specificity of aptamers with a DNA origami structure that consists of two levers connected by a hinge (Figure 2a).^{32,33} On each of the two levers, they positioned parts of a split aptamer for ATP.²⁷ In the absence of ATP, the construct

was opened due to electrostatic repulsion of the two levers, but in the presence of ATP, the structure underwent a conformational change and the two lever parts were in close proximity. The researchers positioned FRET-capable fluorophores on both parts and by monitoring the energy transfer efficiency, the presence of ATP was detected.

Another interesting application of DNA nanotechnology in the biosensing context is for signal enhancement. If a target has to be detected at an extremely low concentration, the signal contrast released by the optical element is often not high enough to be distinguishable from the background. A possible solution is the enhancement of the fluorescence signal. Exploiting DNA's programming ability, DNA-based dendrimers can be built and very strong fluorescence signals can be gained by introducing dye-labelled oligonucleotides.^{34,35} This approach was used for barcoding by combining dye labels with different colors and it was finally applied for diagnostic purposes (Figure 2b).²⁸ Particularly, with dendritic signal amplification, single cancer cells were visualized with high specificity.³⁶ A different strategy for signal amplification can be achieved with DNA walkers where a trigger DNA strand induces a cascade of DNA strand displacements.³⁷ Either the release of fluorescent labels to the solution or the accumulation of fluorophores on the surface of a nanoparticle can occur.^{38,39} Different biosensors based on DNA walkers were introduced⁴⁰ and for example applied for HIV biosensing as suggested by Zheng *et al.*⁴¹ A gold nanoparticle served as a platform to bind the assay including dye-labelled oligonucleotides whose fluorescence was quenched. In the presence of HIV DNA, a cascade was initiated and more and more dye-labelled strands were released increasing the fluorescence intensity of the solution. Also, DNA origami has been used to build fluorescence amplifiers that exploit a physical mechanism which is discussed in detail in the chapter "Optical Nanoantennas for Single-Molecule Sensing".⁴²

Furthermore, DNA nanotechnology has proven to be a suitable method for *in vivo* applications. It is highly biocompatible and reasonably stable in cellular environments. Additionally, there are several strategies to increase the DNA nanostructure lifetime⁴³ and prevent it from nuclease degradation including shielding of the structure,⁴⁴⁻⁴⁷ covalent helix crosslinking^{48,49} or specific structure designs where degradation is less likely.⁵⁰ Accordingly, different *in vivo* DNA nanotechnology applications have been realized. For example, a high cellular uptake was achieved by coating structures with virus capsid proteins.⁴⁷ Addressing specific cells was first demonstrated in 2012 by Douglas *et al.*,⁵¹ and inspired by that, Li *et al.* introduced a nanorobot targeting and acting in cancer tissue (Figure 2c).²⁹ For their biosensor, an aptamer on a DNA origami structure was used for targeting tumor cells as well as a molecular trigger to open the tubular nanostructure. Once opened, a protein was exposed that activated blood coagulation at the tumor site. Besides, intracellular sensing was demonstrated for example of miRNA by Liu *et al.*⁵² Their DNA nanocube was delivered to cells and exhibited metastable dye-labelled hairpins complementary to tumor-related miRNA. Upon binding of the miRNA, a chain reaction was triggered and the hairpins showed an altered configuration. The different proximity between the dyes was read out as a change in the Förster Resonance Energy Transfer (FRET) efficiency.

Overall, DNA nanotechnology holds great potential for the development of biosensors applied *in vivo*, for diagnostic purposes and beyond. By modularly designing and developing different functionalities, complex biosensors can be built where, *e.g.* specific targeting, effective sensing, signal amplification, *etc.*, is combined yielding smart sensors. These advantages hold potential to create sensors with a read-out down to the level of individual probes and thereby push the field of single-molecule technology as realized in this thesis for an *in vitro* diagnostic assay and for membrane biosensors.

1.2 Optical Single-Molecule *in vitro* Diagnostics

In vitro biosensing is often related to the field of diagnostics. In particular, this involves the detection of disease markers which can either originate from patients such as markers for cancer, Alzheimer or cardiovascular diseases, or it can originate from pathogens, *i.e.* viruses or bacteria. In some cases, a qualitative characterization is sufficient, whereas other cases require a quantitative determination of the biomarker concentration.

In diagnostics, the concentration of the target molecule is often in the pico- to attomolar range, especially at early stages of a disease. This sets high demands on diagnostic tests as an early disease detection is key for a successful treatment. For example, the detection of specific cancer markers at an early stage paves the way for personalized medicine, or if infectious diseases are diagnosed early, a fast treatment can increase the effectiveness of the therapy and reduce the risk of spreading. The low-concentration range of biomarkers suggests that the targets have to be concentrated or molecularly amplified (*e.g.* by polymerase chain reaction, PCR) to gain the required signal-to-noise ratio and to be detectable with conventional imaging solutions. However, for some samples a molecular amplification is either not possible or not sufficient. In this context, it is extremely beneficial, if each single biomarker gives rise to a signal that is easily detectable. Thereby, even a low number of target molecules in a sample delivers a detectable signal which pushes the limit-of-detection (LOD) to its minimum, enables an early disease detection and thus, enhances the chances for successful treatment. Ideally, the detection of single disease markers is performed at the point-of-care (POC), *e.g.* in the doctor's office, at home or in areas without sufficient medical care. Therefor easy sample handling and simple read-out are essential for making these techniques accessible to none-specialists and outside of a high-tech laboratory setting.

1.2.1 State of the Art

One direction of optical *in vitro* single-molecule biosensing is based on localized surface plasmon resonance (LSPR). Zijlstra *et al.* demonstrated how binding of a single target to the tip of a biotin-functionalized nanorod influenced its plasmon resonance (Figure 3a).⁵³ Based on this principle, the detection of single DNA molecules was shown.⁵⁴ A ssDNA strand was placed on the tip of the nanorod and upon hybridization with a DNA target in the solution, a plasmon resonance shift was observed. Also, DNA containing a three-basepair mismatch induced a different result and even the introduction of a small, 1 kDa-sized intercalating dye lead to a strong signal change.

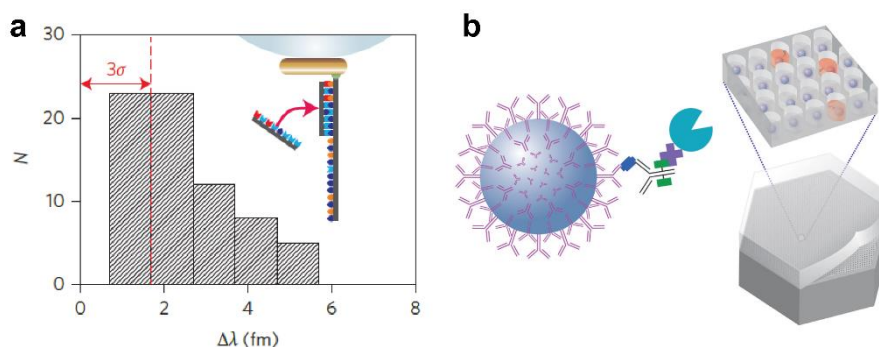


Figure 3. Single-molecule biosensing for *in vitro* diagnostic applications. (a) Plasmon resonance shift obtained due to hybridization of ssDNA to a DNA-functionalized nanorod. Reprinted with permission from ⁵⁴. (b) Single-molecule ELISA detection with beads containing antibody that binds to an antigen and forms a sandwich assay (left). Individual beads are bound in wells and a fluorescence signal is read out (right). Reprinted with permission from ⁵⁵.

Besides LSPR, fluorescence is another possibility for optical single-molecule diagnostics. In this context, a remarkable technique is based on the concept of the enzyme-linked immunosorbent assay (ELISA) yielding single-molecule sensitivity.⁵⁵ First, a low-abundant protein of interest in

blood was captured on microbeads *via* antibody-antigen interaction (Figure 3b). On each bead, there was either one or no target bound. Second, an enzymatic reporter was added and the beads were immobilized in 50 fL-sized reaction chambers in which exactly one individual bead could be isolated. Finally, an enzyme target was added that resulted in a fluorescence signal if degraded by the enzyme. This way, fluorescence imaging revealed which of the cavities were filled with a bead and single target molecules were detected.

These single-molecule biosensors are great examples for single-molecule biosensors. However, for LSPR-based assays, nowadays high-tech equipment is needed making a POC application challenging. On the contrary, POC-compatible read-out systems for the ELISA approach are rather easily developed, but the sample preparation and handling involve multiple steps. This requires well-trained technical staff and more complexity increases the probability for human error. Additionally, the more manual steps the diagnostic test involves, the longer it takes to gain the result. To overcome these limitations, in this thesis a new sensing strategy is presented based on plasmonic fluorescence enhancement holding potential for single-molecule POC diagnostics.

1.2.2. Optical Nanoantennas for Single-Molecule Sensing

One of the challenges in any diagnostic test is the visibility of the specific signal against the background. For fluorescence signals, usually multiple dyes are needed to overcome this barrier. Classically, the fluorescence intensity measured can either originate from multiple targets with one dye each, or from a single target molecule with multiple dyes. However, both ways either compromise the LOD or the simplicity of the test. A possibility to circumvent this problem is a physical enhancement of the fluorescence signal which can be achieved, *e.g.* by plasmonic effects.⁵⁶ With plasmonic fluorescence enhancement, the fluorescence intensity of each single dye is strong enough to yield a high signal-to-noise ratio needed for the detection with low-tech devices in complex media.

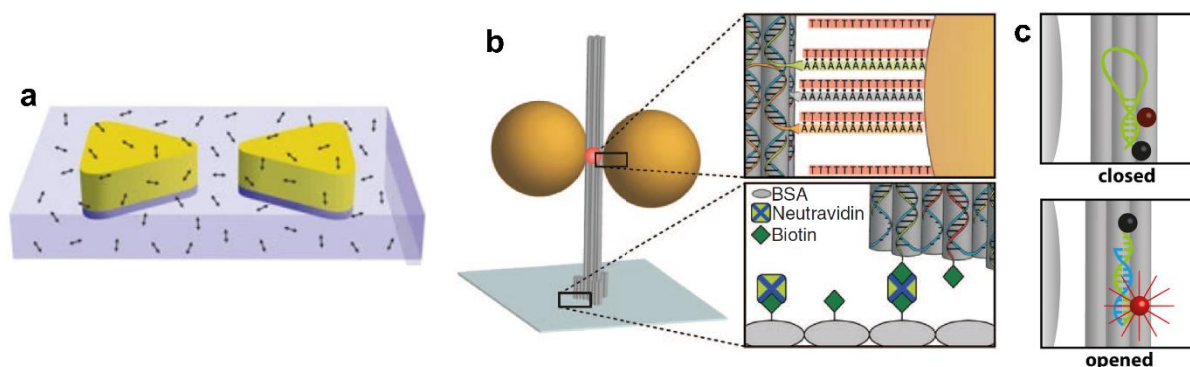


Figure 4. Optical nanoantennas. (a) Bowtie antenna consisting of two gold triangles and dyes (arrows). Reprinted with permission from ⁵⁷. (b) DNA origami nanoantenna with two gold nanoparticles (yellow) attached *via* DNA hybridization (top inset) and a dye (red) attached to a passivated glass surface (bottom inset). Reprinted with permission from ⁴². (c) Concept of fluorescence-quenched hairpin in its closed form (top) and upon hybridization with a target strand, in its opened form (bottom). Reprinted with permission from ⁵⁸.

Plasmonic fluorescence enhancement relies on the resonant illumination of metallic nanoparticles which leads to an electric field enhancement in close proximity to the particles.^{59,60} This way, so-called plasmonic hotspots form. If fluorophores are placed in these hotspots, their fluorescence signal is enhanced due to higher excitation and emission rates. Based on this concept, several groups introduced optical antennas for fluorescence enhancement,⁵⁶ *e.g.* the bowtie antenna by Kinkhabwala *et al.* (Figure 4a).⁵⁷ Using electron-beam lithography, they fabricated two triangles at a distance of 10 nm and measured a fluorescence enhancement of up to 1340-fold of single dyes diffusing through the hotspot. However, a major drawback of these lithography-based antennas is the lacking possibility to precisely position the dye with respect

to the metallic particles. Relying on diffusion, important parameters influencing the fluorescence enhancement, such as gap size, distance of the dye to the particles, *etc.*, cannot be addressed sufficiently.

Using DNA origami, Acuna *et al.* developed an optical nanoantenna overcoming these drawbacks and allowing a precise positioning and stoichiometric control of single dye molecules in plasmonic hotspots (Figure 4b).⁴² A DNA origami pillar functioned as a scaffold to arrange two spherical gold particles forming a 23 nm-sized gap. In this gap, a dye was placed and a fluorescence enhancement of up to ~120-fold was detected. As the signal of a single dye molecule was extremely bright, even measurements in 25 μM dye solutions were realized and for low-quantum yield dyes, a fluorescence enhancement of 5000-fold measured.⁶¹ Testing the applicability for a potential biosensing assay where dyes of different colors could be detected, Vietz *et al.* showed that the fluorescence enhancement of a broad spectral range is possible by using silver instead of gold nanoparticles.⁶² Further, Vietz *et al.* proved that a dye's fluorescence can be successfully quenched in the plasmonic hotspot in a contact or dynamic mode.⁵⁸ In a DNA hairpin configuration, it was possible to spatially separate quencher and dye by hybridization with a specific DNA target (Figure 4c) and thereby, recover a strongly enhanced fluorescence signal originating from the dye in the plasmonic hotspot.

The great progress on DNA origami-based optical nanoantennas suggests that a specific detection of single nucleic acid target molecules and hence, an application for diagnostic assays should be possible. Therefore, in chapter "DNA Origami for Single-Molecule *in vitro* Diagnostics" of this thesis, a DNA nanotechnology-based *in vitro* diagnostic assay is introduced with an enhanced fluorescence and single-molecule read-out based on a DNA hairpin.

1.3 Membrane Biosensing with Single-Molecule Sensitivity

The single-molecule visualization of biological processes is a powerful tool enabling the collection of most detailed information. For example, if a heterogeneous sample consisting of different species is measured by fluorescence microscopy in an ensemble, the species cannot be distinguished. Instead, an averaged value is measured resulting from the contribution of all species. Also, if only a single species is observed, which undergoes fast dynamic changes, it might not be possible to resolve these fluctuations and again an average value is measured. To prevent such information losses, the molecular species of interest can be diluted until the molecules are spatially separable and individual molecules can be observed. Although being resolution limited, single structures and their dynamics can be detected on the nanoscale while not compromising a real time observation as in *e.g.* electron microscopy.

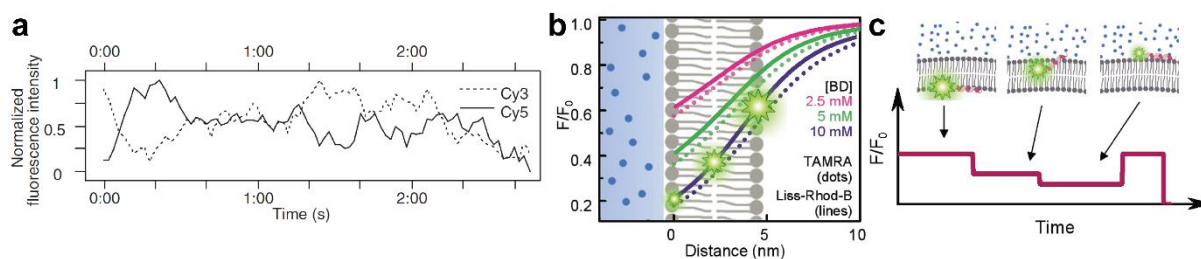


Figure 5. Single-molecule *in vivo* biosensing. (a) Single-molecule FRET transient measured on a cell membrane. Reprinted with permission from ⁶³. (b) Principle of queenFRET where a single fluorophore transfers energy to multiple quenchers in the surrounding solution. This way, the precise position within the cell membrane is determined as demonstrated in (c). Reprinted with permission from ⁶⁴.

For the measurement of biological parameters at lipid membranes, there have been a few fluorescence tools introduced enabling single-molecule resolution such as Förster Resonance Energy Transfer (FRET) where two components are labelled with a fluorescent tag.^{65,66} A

distance-dependent, non-radiative energy transfer can occur between them; the closer the donor is to the acceptor, the more energy is transferred and the higher is the signal collected from the acceptor. In this way, single-molecule FRET functions as a molecular ruler. In 2000, single-molecule FRET studies were performed on cell membranes of mammalian cells for the first time (Figure 5a).⁶³ Nowadays, this technique is frequently used for studies on intramolecular changes, *e.g.* in a protein, or on intermolecular processes and it is also applicable to cytosolic observations.⁶⁷

Applying single-molecule FRET for biosensing, Hou *et al.* visualized transmembrane motions of lipids flip-flopping between the two membrane leaflets as well as the transmembrane transition of different proteins such as the host defense peptide LL-37.⁶⁴ In their approach, the biomolecule of interest was fluorescently labelled and underwent FRET with multiple quenchers floating in the extracellular environment (Figure 5b and c). As a result, they obtained the sub-nanometer precise position of the molecule in the lipid membrane and unraveled different states of a molecule while transitioning the cell membrane.

Overall, the cell membrane holds many important features and observing molecules flip-flopping through the membrane is just one example for possible investigations. Other interesting parameters are for example of physical nature where forces induce or transmit certain cellular pathways or functions, including electrical forces. The latter is relevant in excitable cells where changes in the electrical transmembrane potential are used for signal transmission, or in non-excitable cells where the electrical surface potential is a parameter involved in various signaling pathways. Although there is a huge variety of voltage sensors, there is still the need for further progress and especially, for single-molecule compatibility as further discussed in chapter 1.3.1 for the transmembrane potential and in chapter 1.3.2 for membrane surface charges.

1.3.1 Electrical Transmembrane Potential Measurements

The electrical transmembrane potential $\Delta\Psi$ results from a charge imbalance between the intra- and the extracellular compartments and measures around $\Delta\Psi = -70\text{ mV}$ for cells in a resting state.⁶⁸ Excitable cells, including neurons or heart cells, use changes in the transmembrane potential to transmit signals along the length of the cell upon a stimulus. Particularly, it comes to a transient depolarization of the membrane to $\Delta\Psi \approx 40\text{ mV}$ – the so-called action potential. Tracking firing neurons on the cellular level is one of the pieces required to understand how the brain works and first observations of the transmembrane potential were fulfilled with pipette-based electrophysiological approaches.⁶⁹ These experiments are extremely time-consuming while being invasive. With the introduction of fluorescence probes for voltage imaging, a more straightforward and easy application was possible.⁷⁰ One class of probes are genetically-encoded voltage indicators (GEVIs).^{71,72} Based on membrane proteins, GEVIs intrinsically target cell membranes and hence, are concentrated at the point-of-interest. The read-out is fulfilled with fluorescent proteins bound to the membrane proteins – either by fluorogenicity or in a FRET configuration. As fluorescent proteins are relatively dim and tend to photobleach fast, the imaging duration is limited. Therefore, hybrid approaches have been developed where GEVIs are combined with organic fluorophores which greatly enhances the signal contrast and the possible imaging durations.^{73,74}

However, these assays can only be applied in transfected cell lines or transgenic animals limiting the field of application. In this regard, non-genetically encoded sensors are beneficial; the first generation of prior mentioned was based on the Stark effect.^{75,76} Although easily applied, the signal contrast was rather low. In this respect, González and Tsien made major contributions to the field with the introduction of FRET-based voltage indicators (Figure 6a).^{77,78} Their sensors consisted of two optical components from which one remained in a fixed position at the

membrane surface and the other one inserted into the lipid core. Depending on the transmembrane potential, the component in the lipid core changed the equilibrium position and as FRET could occur between both of them, the FRET efficiency differed and a high-contrast signal was detected. Nevertheless, a huge drawback of this approach is that the components are not chemically linked and thus, a high probe concentration has to be used leading to capacitive loading of the membrane and thereby, disturbance of cellular functions.⁷⁹

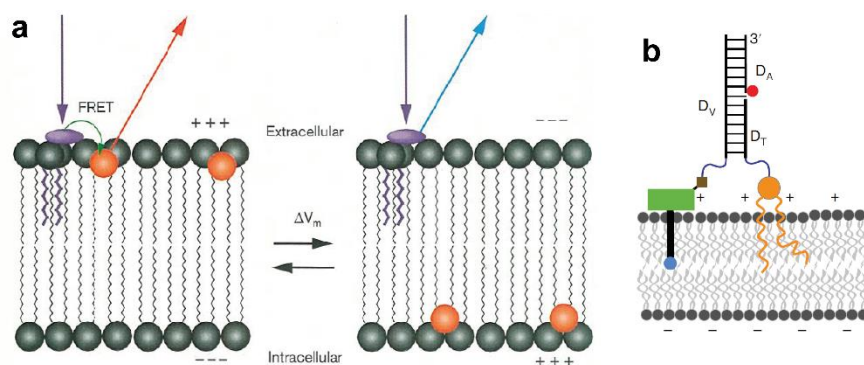


Figure 6. Probes for imaging of the transmembrane potential. (a) A dye (purple) is anchored to the lipid membrane and upon excitation, it can transfer its energy to a second dye (orange) in the lipid core which then fluoresces. Depending on the transmembrane potential, the dye in the lipid core can change its equilibrium position to the inner leaflet and no FRET takes place. Reprinted with permission from ⁷⁸. (b) DNA nanotechnology-based voltmeter with a voltage-sensing dye (left, green-blue), a hydrophobic anchor (right, orange) and an internal reference dye (red). Reprinted with permission from ⁸⁰.

Obviously, it is challenging to combine all the different functionalities required for an optical voltage sensor into small chemical accessible entities. This issue has been addressed recently with different nanotechnological approaches. One direction by Shimon Weiss and co-workers is based on semiconductor nanoparticles.^{81,82} By coating these particles with peptides, an insertion to lipid membranes was enabled and due to the great optical properties, single-particle resolution was achieved. However, the proper read-out depends on a perpendicular orientation of the sensor with respect to the membrane, which was difficult to achieve. Another nanotechnological direction was suggested by Saminathan *et al.* who introduced an *in vivo* membrane voltage sensor that combined a voltage-sensing dye with a second fluorophore for ratiometric read-out and a targeting module for different organelles (Figure 6b).⁸⁰ This was realized using DNA as a scaffolding material.

These two examples suggest interesting directions. First of all, if each individual voltage sensor can be read-out as a long-lived fluorescence signal, the effective probe concentration to be applied to cells can be reduced substantially. This way, the capacitive loading of the membrane is limited as well and the cell vitality is less effected. Also, reading out single molecules enables the collection of information gained from the nanoscale beyond the diffraction limit which is yet impossible in live cell settings. Second of all, the DNA nanotechnology-based example demonstrates that with a modular combination of the different functionalities, a sensor tailored exactly for the desired requirements can be developed.

Following these directions, in chapter 5.1 of this thesis a DNA-origami based transmembrane potential sensor is presented showing single-molecule sensitivity. The different components were chosen individually and assembled on the DNA origami platform including membrane targeting, voltage sensing and signal read-out.

1.3.2 Optical Biosensing of Membrane Surface Charges

The cell membrane consists of different phospholipids from which between 10-30% have negatively charged head groups.⁸³ Most of them belong to the class of phosphatidylserine (PS).

These negatively charged lipids are not distributed equally between the two membrane leaflets and in eukaryotes, an asymmetric distribution is highly conserved resulting in an accumulation at the cytoplasmic side.⁸⁴ Due to the anionic charges, the so-called electrical membrane surface potential arises locally around the lipid head groups. Therefore, the inner leaflet of the cell membrane has an electrical potential of ~ -30 mV.⁸⁵ This enables the binding of cationic protein motifs and supports the negative curvature of the membrane.^{86,87} An interplay of different enzymes maintains the asymmetry which is only disturbed under certain conditions. On the one hand, non-directional re-ordering of the lipids is relevant in apoptosis, but also a mediator for blood clotting.⁸⁸ On the other hand, a directional and transient exposure of PS at the cell exterior is involved in *e.g.* T-cell activation where additional local heterogeneities of PS are observed.^{89,90}

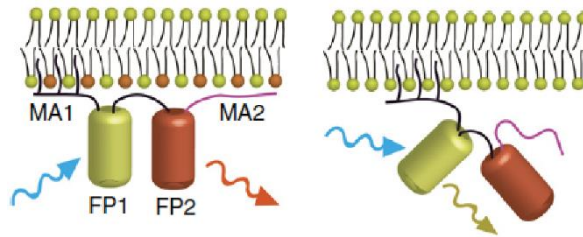


Figure 7. Ratiometric sensor for membrane surface charges. The sensor consists of the peptide MA1 permanently attached to the membrane, two fluorescent proteins (FP1 in yellow and FP2 in red) and the peptide MA2. The cationic MA2 is bound to the negatively charged membrane (left) and unbound if uncharged (right). Thereby, the FRET efficiency varies. Reprinted with permission from ⁹¹.

Visualizing membrane surface charges can report on changes that are involved in signaling processes – especially in the context of live cell imaging.⁹² To do so, dye-labelled PS can be used and clustering of charged lipids can be observed, but fluorescent PS cannot report on whether the lipid is at the inner or the outer membrane leaflet. Also, these kinds of probes tend to distort cellular functions. A great progress was made with the introduction of protein-based sensors.⁹³⁻⁹⁵ For example, the genetically-encoded sensor of Yeung *et al.* consisted of the cationic protein R-pre which was linked to a fluorescent protein.⁹⁵ If the membrane surface potential was negative, R-pre accumulated at the membrane and an increase of the fluorescence intensity was measured. These kinds of sensors, however, lack an internal signal referencing and thus, are concentration-dependent. Addressing this issue, Ma *et al.* developed an R-pre-based sensor with FRET read-out (Figure 7).⁹¹ As FRET enables ratiometric measurements, with this sensor, a quantitative estimation of the membrane charge density was possible as well as cell-to-cell comparisons.

As discussed for the transmembrane potential sensors in the chapter above, genetically-encoded sensors limit the field of application although fairly easily developed. A non-genetically-encoded one would greatly complement the selection existing as well as a sensor for the outer membrane leaflet where to date no measurements can be performed. Moreover, the currently existing sensors do not allow observations on the nanoscale, although it is known that in certain cellular pathways small clusters of PS form. In order to visualize such local heterogeneities, a resolution beyond the diffraction limit has to be achieved in live cell experiments which could be done with single-molecule fluorescence approaches. For that purpose, as part of this thesis, a membrane surface charge sensor was developed allowing quantitative single-molecule measurements using the DNA-origami technique, and the results are presented in chapter 5.2.

2 Theoretical Background

2.1 Fluorescence

Light follows the wave-particle duality and is characterized by wave and particle properties. It is an electromagnetic wave that propagates in space and whose smallest possible units are photons. These photons possess a specific energy E which can be quantified with the Planck relation as

$$E = \frac{hc}{\lambda} \quad (1)$$

with h as the Planck constant, c as the speed of light and λ as the wavelength. Certain molecules such as fluorophores can absorb photons and undergo transitions from the electronic singlet ground state S_0 to an excited state such as S_1 , S_2 or S_n .⁹⁶ Only if the photon's energy corresponds to the energy difference between two states, the photon is absorbed. Elsewise, it is transmitted or scattered. Within each of the electronic states, there are different vibrational levels v characterized by vibrational quantum numbers where $v=0$ describes the vibrational ground state, $v=1$ the first excited vibrational state, *etc.*, quantified by wave functions. Hence, photons possessing different energies can be absorbed by the molecule where each transition leads to an absorption band. Therefore, absorption spectra have a broad wavelength range and describe the probability of a photon absorption at a specific wavelength. These probabilities are described by the Franck-Condon principle;⁹⁷⁻⁹⁹ the higher the overlap of the wavefunctions between the ground and the excited state, the higher the probability. During the transitions, the molecular geometry does not change as this process is faster than the vibration of the nucleus.¹⁰⁰

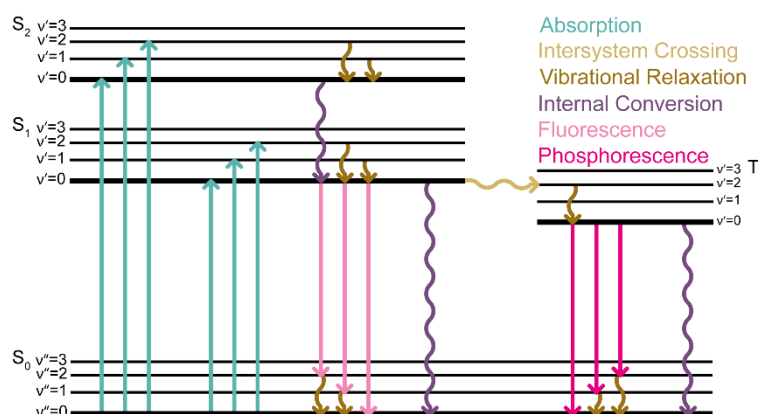


Figure 8. Jablonski diagram. S describes the singlet states, T the triplet state and v the vibrational levels. All radiative processes are illustrated with straight lines including absorption (turquoise), fluorescence (rose) and phosphorescence (pink) and all non-radiative with wavy lines including intersystem crossing (beige), vibrational relaxation (brown) and internal conversion (purple).

Once in an excited state S_n , the electron transitions to the lowest vibrational level within S_n *via* vibrational relaxation.¹⁰¹ For the depopulation back to the electronic ground state S_0 , different processes can take place as summarized in the Jablonski diagram in Figure 8.⁹⁶ Basically, radiative and non-radiative processes are distinguished. From higher excited states S_n , the relaxation takes place non-radiatively *via* internal conversion into the lowest excited state S_1 . Also, from S_1 to S_0 , the relaxation can occur by internal conversion. Another possibility is fluorescence upon which a photon is spontaneously emitted. The energy of the emitted photon is lower than the absorbed photon's one as different energy-consuming processes take place beforehand. Thus, the emitted photon has a higher wavelength. This phenomenon is called Stokes shift.¹⁰² Analogous to the photon absorption, the fluorescence can also result in different vibrational levels of S_0 leading to multiple emission bands and hence, a broad emission spectrum.

From an excited singlet state, under spin conversion a depopulation to the triplet state T_1 can happen referred to as intersystem crossing. The relaxation to S_0 can take place non-radiative *via* internal conversion or radiative *via* phosphorescence. According to the Pauli exclusion principle, two electrons with the same spin cannot occupy the same quantum state. Therefore, the relaxation from the triplet state involves a spin conversion which is why these processes are slower than the relaxation from the singlet states.

The quantification of each of the described processes as rates k is used to characterize the photophysical properties of fluorophores. In this context, the ratio of radiative relaxation over all relaxation processes is an important parameter described by the quantum yield Φ as

$$\Phi = \frac{k_r}{k_r + k_{nr}} \quad (2)$$

where k_r is the depopulation rate for all radiative processes and k_{nr} for all non-radiative processes. Accordingly, the fluorescence lifetime τ is defined as

$$\tau = \frac{1}{k_r + k_{nr}} \quad (3)$$

and quantifies the time that the molecule stays in the excited singlet state. Typically, the fluorescence lifetime is in the order of nanoseconds. Each molecule undergoes multiple excitation-emission cycles and within a defined period of time, the fluorescence intensity is proportional to the number of excitation cycles. The intensity change over time $\frac{dI_{Fl}(t)}{dt}$ can be described with

$$\frac{dI_{Fl}(t)}{dt} = -(k_r + k_{nr})I_{Fl}(t). \quad (4)$$

The integration of this term reveals an exponential fluorescence decay for multiple excitation-emission cycles as

$$I_{Fl}(t) = I_{Fl}^0 \cdot e^{-(k_r + k_{nr})t} = I_{Fl}^0 \cdot e^{-\frac{t}{\tau}} \quad (5)$$

with I_{Fl}^0 as the fluorescence intensity at $t = 0$ and reveals the fluorescence lifetime τ .

2.1.1 Non-Radiative Energy Transfer

Under certain conditions, energy can be transferred non-radiatively from a donor molecule to an acceptor molecule. At distances below 1 nm, this happens by the so-called Dexter energy transfer and involves the exchange of an electron.¹⁰³ Above 1 nm, other processes are predominant such as the FRET.¹⁰⁴ Often, this phenomenon refers to the transfer between two fluorophores, but it can also take place from a fluorophore to *e.g.* a quencher. Figure 9a explains the mechanism based on a simplified Jablonski diagram for a green and a red fluorophore. After the donor molecule absorbs photons in the green spectral range, it relaxes to the lowest vibrational level $\nu' = 0$ in the excited state S_1 , from which it can either depopulate into the ground state by emission or it can transfer the energy to an acceptor upon which the donor molecule is in the ground state and the acceptor in the excited state. By vibrational relaxation, the acceptor molecule occupies $\nu' = 0$, from which it can emit in the red spectral range and depopulate to the electric ground state S_0 .

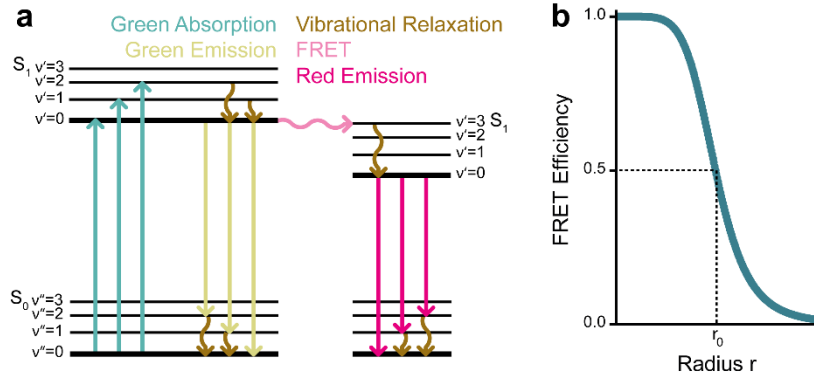


Figure 9. Concept of FRET. (a) Jablonski diagram illustrating FRET between a green (left) and a red fluorophore (right) with green absorption in turquoise, green emission in green, FRET in rose, red emission in pink and vibrational relaxation in brown. (b) Dependency of the FRET efficiency on the distance r between two fluorophores with r_0 as the distance where the FRET efficiency is 0.5.

Generally, the efficiency of this process is defined by different parameters. One important requirement is the spectral overlap J between the donor emission and the acceptor absorption, as the energy transfer is isoenergetic; the energy donated and the energy accepted are identical. Hence, the higher the spectral overlap J , the higher is the probability for a successful energy transfer. The spectral overlap integral J is described by

$$J = \int f_D(\lambda) \varepsilon_A(\lambda) \lambda^4 d\lambda \quad (6)$$

with the emission spectrum of the donor $f_D(\lambda)$, the absorption spectrum of the acceptor $\varepsilon_A(\lambda)$ and the wavelength λ . Besides the spectral overlap, the relative orientation between the donor and the acceptor is another important parameter. Basically, FRET is a dipole-dipole interaction between transition dipole moments. A parallel orientation of the dipole moments leads to a resonance and the probability for FRET is maximized. In this context, the orientation factor κ^2 describes the relative orientation of donor and acceptor to each other with

$$\kappa^2 = \cos\theta_{DA} - 3\cos\theta_D \cdot \cos\theta_A. \quad (7)$$

Here, θ_{DA} is the angle between the donor and acceptor dipole moments, θ_D is the angle of the donor's dipole moment and θ_A the angle of the acceptor's dipole moment. κ^2 can take values from 0 to 4, where 0 describes a perpendicular, 1 a parallel and 4 a collinear orientation of the donor and the acceptor. For freely rotating dyes, $\kappa^2 = \frac{2}{3}$ is approximated. The third parameter determining the FRET efficiency is the distance r between donor and acceptor as the magnitude of the dipole-dipole interaction decays with r^{-6} which is illustrated in Figure 9b. Typically, FRET occurs between ~ 1 -10 nm. The distance at which the probabilities for an energy transfer and for fluorescent emission of the donor are equal, is called the Förster radius r_0 and is described with the following equation:

$$r_0 = \sqrt[6]{\frac{9\Phi_D \ln(10) \kappa^2 J}{128\pi^5 n^4 N_A}} \quad (8)$$

Here, Φ_D is the donor's quantum efficiency, n the refractive index and N_A the Avogadro constant. The Förster radius r_0 includes all parameters discussed above and is used to quantify the FRET efficiency E as

$$E = \frac{r_0^6}{r_0^6 + r^6}. \quad (9)$$

FRET has established as a fluorescent technique and is *e.g.* applied in biology for investigations of different binding partners where two molecules are labelled with fluorophores, but also as FRET is highly distance dependent, it is used as a molecular ruler to for example observe conformational changes in proteins and beyond.^{105,106}

2.1.2 Photobleaching and Photostabilization

Typically, a fluorophore undergoes multiple excitation-emission cycles, before it photobleaches which results from an irreversible damage of the fluorophore's chemical structure. Photodamage can only occur when the molecule is in an excited state. As the time in the triplet state is substantially higher than in the singlet state, the photochemical reactivity in the triplet state is maximized. The most probable photobleaching events involve molecular oxygen.¹⁰⁷ On the one hand, oxygen depopulates the triplet state upon which singlet oxygen forms. This highly reactive species on the other hand chemically reacts with fluorophores resulting in a destroyed fluorophore.¹⁰⁸

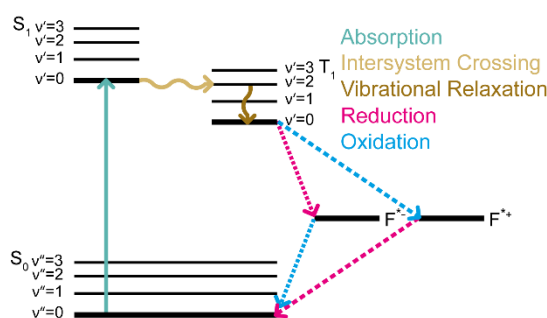


Figure 10. Simplified Jablonski diagram illustrating the ROXS mechanism. The absorption is shown in turquoise, intersystem crossing in beige and vibrational relaxation in brown by straight lines, and by dashed lines the reduction in pink and the oxidation in light blue. $F^{\bullet-}$ is the anionic radical state and $F^{\bullet+}$ the cationic radical state.

A possibility to limit photobleaching and thus, increase the number of excitation-emission cycles, is by decreasing the fluorophore's time in the triplet state. This can be achieved by the introduction of a reducing and oxidizing system (ROXS).¹³ Once the molecule is in the triplet state, a photoinduced electron transfer (PET) takes place with either a reducing or an oxidizing agent (Figure 10). This brings the molecule into a radical state from which it depopulates to the ground state by oxidation or reduction, respectively. These redox reactions are faster than the usual relaxation from the triplet state and therefore, the probability of a photochemical reaction with singlet oxygen is lower. To further increase the photostability, oxygen can be removed from the system, *e.g.* enzymatically.¹⁰⁹ Here, the combination with a ROXS system is essential to prevent long dark times; otherwise a depopulation from the triplet to the ground state cannot be ensured.¹¹⁰

2.2 Single-Molecule Fluorescence Studies

Studying processes on the level of single molecules holds the advantage that a high content of information is collected.¹¹¹⁻¹¹³ For example, in fluorescence microscopy, if a sample contains different species, often it is impossible to distinguish them with conventional methods due to ensemble averaging. Also, dynamics of stochastic processes need to be synchronized to study them on the ensemble level. On the single-molecule level, they can be visualized directly and are also accessible when synchronization is not possible. These limitations can be solved when single molecules are investigated for which different requirements have to be fulfilled.

First, the choice of the fluorescent label is essential. Depending on the experimental needs, mostly synthetic organic dyes are used, but also fluorescence proteins, quantum dots or fluorescent nanoparticles are possible. The photophysical properties of the label have to be

considered, where a high quantum yield and a high extinction coefficient result in a sufficient brightness.¹¹ Also, the photostability is important which can be further tuned with strategies discussed in chapter 2.1.2.

Second, the concentration range has to be taken into account. In conventional fluorescence microscopy, hundreds to thousands of molecules are investigated at the same time due to two reasons. On the one hand, the diffraction limit does not allow a differentiation of objects that are below ~ 300 nm apart for visible light.⁷ On the other hand, considering this limit, the sample density is essential.¹¹⁴ Under physiological conditions, interactions of biomolecules are in the concentration range between 1 nM and 1 M. This high density causes an observation of many molecules simultaneously, if all of them are fluorescently labelled. To successfully enable single-molecule fluorescence studies, the density of labelled molecules has to be decreased until the molecules are spatially separable. This is achieved by concentrations of around 1 pM to 1 nM.

Third, single-molecule fluorescence studies set high demands on the optical setup. In order to visualize the molecule, a high signal-to-background ratio has to be obtained^{112,113} which can be reached with *e.g.* widefield or confocal microscopes.

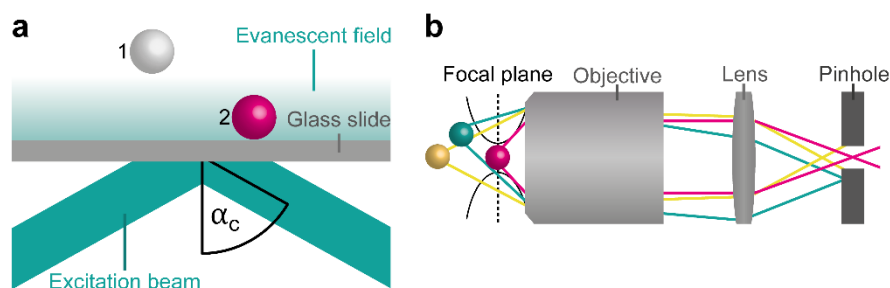


Figure 11. Single-molecule microscopy techniques. (a) Sketch illustrating the concept of TIRF. An excitation laser beam (cyan) hits a glass surface (grey) at the critical angle α_c and induces an evanescent field above the glass slide. Molecule 1 (white) positioned above the evanescent field is not excited and does not fluoresce whereas molecule 2 (pink) is exposed to the electric field and thus, fluoresces. (b) Sketch illustrating the concept of confocal microscopy. The emission light paths are shown for three molecules from which the pink one is in the focal plane and the cyan and yellow ones are out of focus. After passing the objective, their light is focused by a lens onto a pinhole and only the light originating from the pink molecule passes the pinhole whereas from the other two, the emitted light is blocked.

A widefield microscope offers the possibility to illuminate a large field of view so that multiple molecules can be investigated simultaneously and individually due to broadening of the laser beam.¹¹⁵ However, not only the focal plane is illuminated, but also the whole depth of the sample. This results in a low signal-to-background ratio. To reduce the excitation volume, widefield microscopes are often used in the Total Internal Reflection Fluorescence (TIRF) configuration. In this approach, only molecules at a distance roughly up to 200 nm from the glass surface are excited. This is achieved if the light hits a surface between two materials with different refractive indices n_1 and n_2 , respectively, below a critical angle α_c defined as

$$\alpha_c = \sin^{-1} \left(\frac{n_1}{n_2} \right) \quad (10)$$

where $n_1 < n_2$. For water and glass, this critical angle is approximately $\alpha_c = 60^\circ$. Although the light is totally reflected, an exponentially decaying evanescent electric field is induced at the surface (Figure 11a). Thus, only molecules close to the surface are excited and the signal-to-background ratio is significantly improved. TIRF microscopy is a great tool for high-throughput single-molecule studies, but has a limited time resolution which is mostly related to the temporal limits of the detectors used; the emission light is focused on the chip of a charge coupled device (CCD) or of a complementary metal-oxide-semiconductor (CMOS) camera whose typical frame rates are between 30 and 80 frames/s, respectively.^{116,117}

This temporal limitation can be overcome with confocal microscopy where single-photon detectors are used. Conceptually, in confocal microscopy the laser is focused on a single spot of the sample.¹¹⁵ In the detection path, the emitted light from different z positions is collected. With a lens, the light is focused on a pinhole which neglects all light originating from above or below the focal plane (Figure 11b). This leads to a very high signal-to-background ratio. A confocal microscope can be used for solution measurements where the sample diffuses through the focal volume and single bursts are obtained for each molecule.¹¹⁸ Also, surface-based measurements can be performed. Therefore the surface is scanned in a raster pattern so that each individual point is measured and the whole picture is assembled. This technique can be extended for time-correlated single photon counting (TCSPC).¹¹⁵ Here, a pulsed laser is used to excite the sample every *e.g.* 20 ns and the time delay is measured until the photon is detected on the single-photon detector. This is repeated multiple times and according to equation (5), an exponential decay of the fluorescence intensity is observed. Finally, mono-exponential fitting reveals the fluorescence lifetime of the single molecule investigated.

Overall, fluorescence microscopy is a great tool for single-molecule studies. Considering the concentration limitations and choosing an appropriate fluorescent label, the measurements can be easily performed for which there are different microscopic techniques available. While TIRF microscopy offers a high throughput by a simultaneous excitation and detection of a broad area, confocal scanning microscopy holds an extremely high temporal resolution enabling fluorescence lifetime measurements of single molecules.

2.3 DNA Nanotechnology

Deoxyribonucleic acid or DNA is the carrier of genetic information.¹⁶ This polymeric molecule is built up by nucleotides consisting of a sugar, a phosphate group and a nucleobase (Figure 12a) and has two ends; the 5' end terminating with the phosphate group and the 3' end terminating with the sugar. The sequence of the four nucleobases adenine, cytosine, guanine and thymine can be translated to a sequence of amino acids and thereby act as the genetic code. According to Watson and Crick, between adenine and thymine and between cytosine and guanine, hydrogen bonds can form.¹⁷ In the presence of a complementary DNA, the two strands hybridize and a DNA double helix results.

Nadrian C. Seeman was the first one who used the programming properties of DNA to build nanostructures and founded the field of DNA nanotechnology.¹⁸ In his approach, branched junctions were connected *via* sticky ends (Figure 12b) to form crystalline arrays although the yield of structures was relatively low.^{119,120} A revolutionary development in the field of DNA nanotechnology was made by Paul Rothemund in 2006 with the introduction of DNA origami.²³ In this approach, long ssDNA derived from the M13 phage functions as a scaffold for the nanostructure (Figure 12c). By hybridization with short so-called staple oligonucleotides, different parts of the scaffold are spatially cross-linked. In a self-assembly, DNA nanostructures result in a shape programmed prior to folding by the DNA sequences. In a one-pot reaction, billions of DNA origami nanostructures are yielded simultaneously and different designs such as triangles or stars are presented in his work and exemplary show in Figure 12d. Shortly after the conceptual demonstration of this approach, more complex 3D structures were introduced.²⁴ Besides the DNA origami technique, in recent years other methods have evolved yielding *e.g.* DNA wireframe²² or brick structures.²¹

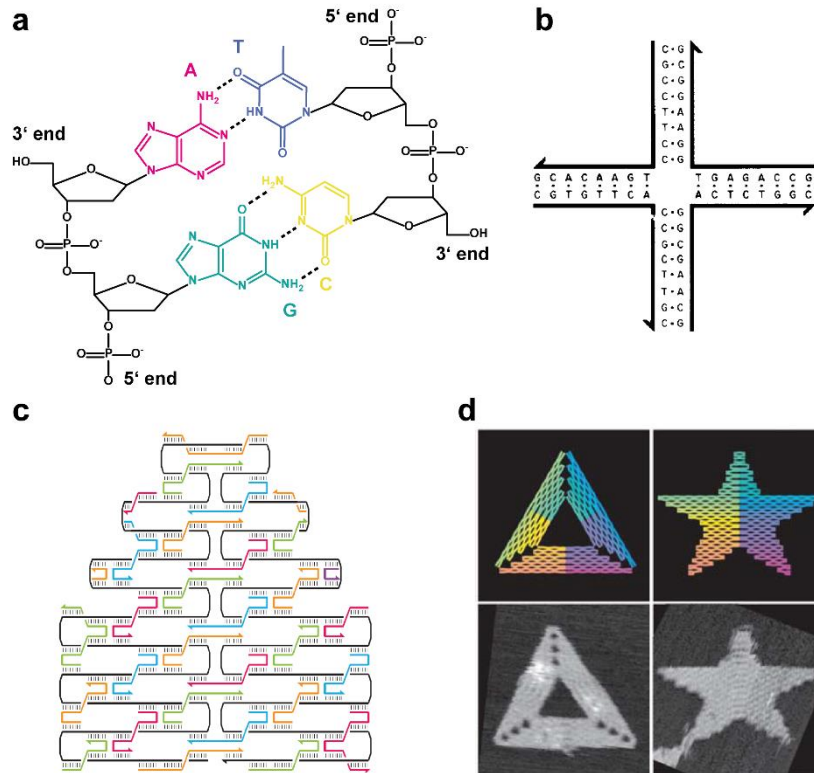


Figure 12. DNA and DNA nanotechnology. (a) Chemical structure of DNA with the nucleobases adenine (pink) and guanine (cyan) in one DNA strand and thymine (blue) and cytosine (yellow) in a second DNA strand hybridizing to a DNA duplex *via* hydrogen bonds (dashed lines). (b) DNA forming a 4-arm branched junction with the 5' end illustrated by a half-arrowhead. Reprinted with permission from ¹⁸. (c) Concept of DNA origami with long scaffold strand (black) hybridized to short staple strands (colored) forming crossovers to different helices. Reprinted with permission from ²³. (d) Top row: DNA origami designs for a triangle and a star including crossovers. The color code describes the base-pair index where red is the first base and purple the 7000th base. Bottom row: Atomic-force microscopy image of the folded DNA origami structures with scan dimensions of 165 nm x 165 nm. Reprinted with permission from ²³.

As DNA oligonucleotides are easily tagged with chemical moieties, various modifications can be positioned in DNA nanostructures with base-pair precision and stoichiometric control, for example proteins, fluorophores, nanoparticles, lipophile molecules and beyond. Therefore, DNA nanotechnology has been successfully used as an assembly platform for the development of drug delivery systems,^{121,122} nanorobots,^{51,123} biosensors¹⁵ and beyond.

2.4 Nanophotonics

In nanophotonics, light is manipulated on the nanoscale. This can for example occur by exposing a metallic nanoparticle to light of a certain wavelength where the excitation leads to a polarization of the conducting band electrons. In particular, it comes to a delocalization of the electrons in the particle as the electric field of the light induces a collective electron oscillation, if the frequency matches the eigenfrequency of the particle.⁵⁹ For nanoparticles that are much smaller than the wavelength of the incident light, a quasi-static dipole can be approximated⁶⁰ as illustrated in Figure 13a. This phenomenon is called the localized surface plasmon resonance (LSPR). The resonance frequency ω_{LSPR} is described by

$$\omega_{LSPR} = \sqrt{\frac{Ne^2}{m_e \epsilon_0 (\epsilon_\infty + \kappa \epsilon_m)}} \quad (11)$$

where N is the density of free electrons, e the electron's elementary charge, m_e the electron mass, ϵ_0 the permittivity in free space, ϵ_∞ the permittivity of the induced polarization, κ a shape factor and ϵ_m the permittivity of the surrounding medium.¹²⁴ Hence, the resonance frequency

depends on the material of the nanoparticle and different metals can interact with light at distinct wavelengths.

The polarizability $\alpha(\omega)$ at a certain frequency ω is estimated by the Clausius–Mossotti relation as

$$\alpha(\omega) = (1 + \kappa)V\varepsilon_0 \left| \frac{\varepsilon(\omega) - \varepsilon_m}{\varepsilon(\omega) + \kappa\varepsilon_m} \right|. \quad (12)$$

Here, V is the volume of the nanoparticle and $\varepsilon(\omega)$ the permittivity at a specific frequency. The volume in this equation implies a higher $\alpha(\omega)$ for larger sizes of nanoparticles. In addition, the equation contains the shape factor κ ; the shape of the particle predetermines how well the electric field can be concentrated. With decreased symmetry, the local fields are increased, *e.g.* in a nanorod there is a dipole moment oscillating perpendicular and one oscillating parallel to the rod's axis. The parallel dipole moment is concentrated at the tips¹²⁵ (Figure 13b) unlike in a sphere where all around the nanoparticle the same electric field enhancement is observed (Figure 13c). For a spherical particle, $\kappa = 2$, whereas for a rod-like structure or a triangle, it is larger.¹²⁴

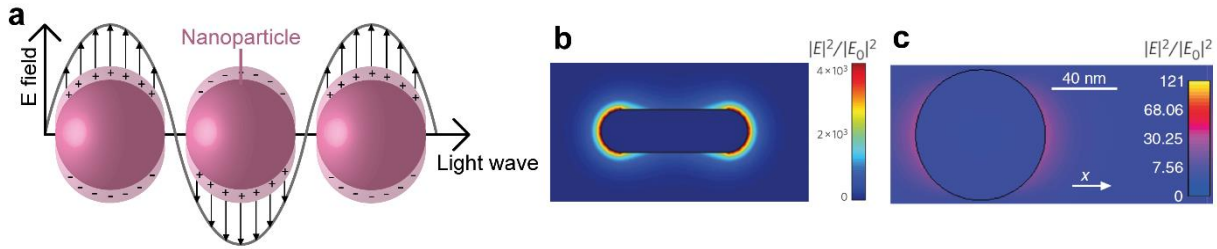


Figure 13. Plasmonic nanoparticles. (a) Nanoparticles exposed to light which induces a displacement of the conducting electrons and a quasi-static dipole. (b) Simulation of the electric field enhancement $|E|^2/|E_0|^2$ for a 31x9 nm-sized gold nanorod and (c) for a 80 nm gold sphere. Reprinted with permission from¹²⁶ for (b) and for (c) with permission from⁴².

If a quantum emitter such as a fluorophore is placed in close proximity to a nanoparticle which is excited by its resonance frequency, an interaction can occur. A requirement for this is the overlap between the absorption and emission spectra of the fluorophore and the near-field spectrum of the nanoparticle.¹²⁶ Under this circumstance, additional to the electric field of the photon, the fluorophore is exposed to the electric field induced by the nanoparticle.¹²⁷ This leads to an increased excitation rate k_{ex} of the fluorophore and thus, to an enhanced fluorescence intensity I_{Fl} as

$$I_{Fl} \propto k_{ex}\Phi. \quad (13)$$

Besides the fluorophore's excitation, the relaxation processes are also influenced by the nanoparticle. The fluorophore can transfer its energy non-radiatively to the nanoparticle which introduces an additional relaxation process decaying with the rate k_{NP} . Therefore, the rate summarizing all non-radiative processes k_{nr} as discussed in the chapter above is extended to k_{nr}^m . Also, the rate for all radiative processes k_r changes as the nanoparticle can release photons resulting in the extended rate for radiative processes k_r^m . The fluorophore's quantum yield Φ^m is defined as

$$\Phi^m = \frac{k_r^m}{k_r^m + k_{nr}^m} \quad (14)$$

and is increased, if it is not around 1 without the proximity to a nanoparticle. With a higher Φ^m , the fluorescence intensity is additionally increased with respect to equation (5). Accordingly, the fluorescence lifetime changes to

$$\tau^m = \frac{1}{k_r^m + k_{nr}^m} \quad (15)$$

which implies a reduced lifetime for higher fluorescence intensities.

The assembly of fluorophores and plasmonic nanoparticles yield so-called nanoantennas which can be used for the photophysical manipulation of fluorophores.^{56,128} One strategy for it is the use of nanolithography where the plasmonic structures are formed in a top-down approach resulting in very concise structures.⁵⁷ However, the precise positioning of the fluorescing component is challenging. Other strategies involve functionalized nanoparticles,¹²⁹ e.g. with DNA oligonucleotides where a better spatial control is achieved, but no stoichiometric control. Both a spatial and a stoichiometric control is reached by the combination with DNA nanotechnological approaches such as DNA origami.⁴² Here, the “molecular breadboard” advantage discussed in chapter 2.3 can be used to address the applications’ needs.

2.5 Electrostatic Properties of Lipid Membranes

The eukaryotic cell membrane features various electrostatic properties which result from diverse origins illustrated in Figure 14a. The transmembrane potential $\Delta\Psi$ is induced by different ion concentration on both sides of the membrane and is described with

$$\Delta\Psi = \Psi_{in} - \Psi_{out} \quad (16)$$

where Ψ_{in} is the potential inside and Ψ_{out} is the potential outside.¹³⁰ Each ion in the electrolyte solution around has an impact on the potential stated by Coulomb’s law as

$$\Psi(r) = \frac{q}{4\pi\epsilon_a\epsilon_0r}. \quad (17)$$

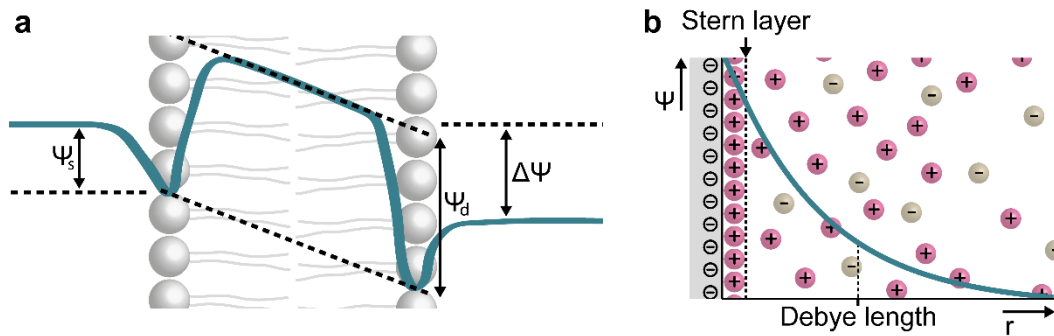


Figure 14. Electric potentials at lipid bilayers. (a) Sketch illustrating the potentials at a lipid membrane in cyan including the surface potential Ψ_s , the transmembrane potential $\Delta\Psi$ and the dipole potential Ψ_d . (b) Drop of the potential Ψ (cyan) at a charged surface (grey) with respect to the distance r in an electrolyte solution. At the charged surface, a layer of counter ions (Stern layer, pink) is adsorbed followed by a mixture of both cations and anions (beige) in which the Debye length is defined as $1/e$.

Here, r is the distance from the ion, q is the charge of an ion, ϵ_a is the dielectric constant of the medium and ϵ_0 the permittivity of free space. As a result, different concentrations of ion species between two sides of a lipid membrane induce an electrical potential and can be described with the Nernst equation⁶⁸ as

$$\Delta\Psi = \frac{RT}{ZF} \ln\left(\frac{c_{out}}{c_{in}}\right) \quad (18)$$

where R is the gas constant, T the temperature, Z the charge of the ion, F the Faraday constant and c_{out} and c_{in} the ion concentration outside and inside, respectively. By an interplay between different channels in the cell membrane of excitable cells, the ion gradient across the membrane

is changed which results in a transient depolarization of the membrane. This is used in *e.g.* neurons for signal transmission along the length of the cell.¹³¹

Considering a lipid bilayer thickness of ~ 4 nm, the transmembrane potential is long-range compared to the membrane surface potential as illustrated in Figure 14a. The surface potential Ψ_s is caused by charges in the head groups of the lipids forming the membrane and arises locally around the membrane-water interphase. According to Gouy and Chapman,^{132,133} the surface potential Ψ_s depends on the surface charge density σ and the Debye length κ^{-1} by

$$\Psi_s = \frac{\sigma}{\varepsilon_a \varepsilon_0 \kappa}. \quad (19)$$

The Debye length is a measure of how far an electrostatic effect persists in *e.g.* an electrolyte solution and highly depends on the ionic strength.¹³⁴ In a monovalent electrolyte solution, it is defined as

$$\kappa^{-1} = \sqrt{\frac{\varepsilon_a \varepsilon_0 k_b T}{2 N_A e^2 c}}. \quad (20)$$

k_b is the Boltzmann constant, N_A the Avogadro constant and c the ionic strength of the electrolyte. As illustrated in Figure 14b, the potential drops exponentially at the membrane with x as the distance from the membrane according to

$$\Psi(x) = \Psi_s e^{(-\kappa x)}. \quad (21)$$

A closer look at the surface potential reveals that at the surface a layer of counter ions is adsorbed – the so-called Stern layer (Figure 14b).¹³⁵ It is followed by the slipping plane in which counterions accumulate due to electrostatic attraction, but also some co-ions are present and both species diffuse around. Overall, the membrane surface potential is involved in various signaling pathways such as T-cell activation^{84,89} and blood clotting,⁸⁸ but also the charged surface offers binding sites for positively charged proteins.^{94,136,137}

The third potential at the lipid membrane is the dipole potential caused by the alignment of dipolar residues of the lipids and water molecules.¹³⁸ It is located inside of the membrane's lipid core and measures around $\Psi_d = 200$ -400 mV depending on the lipid (Figure 14a). This positive potential enhances the permeability of the membrane for anions compared to cations by five orders of magnitude.¹³⁹

3 Methods

In this chapter, the methods used for the different experiments are briefly explained. Details are found in the respective related publications. If not declared differently, chemicals were purchased from Merck KGaA.

3.1 Confocal Microscope

For this work, two different home-built confocal microscopes were used that were conceptually similar, but varied in a few components.

The data for the nanoantenna project was acquired on a setup based on an Olympus IX-71 microscope body and had a pulsed 640 nm laser (LDH-D-640, Picoquant) and a pulsed 532 nm laser (LDH-P-FA530B, Picoquant). Both were used with a repetition rate of 80 MHz. The green and the red excitation were altered through an AOTF filter (AOTFnc-VIS, AA optoelectronic). Circular light was achieved by combining a linear polarizer and a quarter-wave plate. An oil-immersion objective (UPlanSApo 60XO/1.35 NA, Olympus) was used to focus the light onto the sample and with a piezo stage (P-517.3CL, Physik Instrumente GmbH & Co. KG), the confocal beam was precisely positioned. A dual-band dichroic beam splitter (Dualband z532/633, AHF) separated excitation from emission light. The emission light was focused on a 50 μm pinhole (Linos), spectrally separated by a dichroic beam splitter (640DCXR, AHF) and cleaned with spectral filter (red, ET 700/75m, AHF and RazorEdge LP 647, Semrock; and green, HC582/75, AHF and RazorEdge LP 532, Semrock). For detection, single-photon avalanche diodes (τ -SPAD-100, Picoquant) were used and for TCSPC counting, a PC card (SPC-830, Becker & Hickl) connected the computer with the detector. The control was fulfilled with a home-written software based on LabView (National Instruments).

For the second home-built confocal microscope, only the components and parameters differing from the setup described before are mentioned. The green laser was used with a repetition rate of 50 MHz. As an objective, the UPLSAPO100XO, NA 1.40 (Olympus Deutschland GmbH) was used and the piezo stage P-517.3CD by Physik Instrumente (PI) GmbH & Co. KG controlled by a piezo controller (E-727.3CDA, Physik Instrumente (PI) GmbH & Co. KG). The dichroic mirror separating the excitation from the emission light was the zt532/640rpc (Chroma), the 50 μm pinhole was from Thorlabs and the dichroic mirror for separating green and red was the 640 LPXR (Chroma). The avalanche photo diodes were SPCM-AQRH-14-TR by Excelitas and the TCSPC unit the HydraHarp400 by PicoQuant. A commercial package was used for the microscope control (SymPhoTime64, Picoquant).

3.2 TIRF Microscope

The widefield FRET experiments were executed on a home-built TIRF setup based on the Olympus IX71 microscope body. With an acousto-optical tunable filter (AOTF, PCAOM-VIS, Crystal Technology) at a frequency of 10 Hz, the light of a green laser (Sapphire 532 nm, 100 mW, Coherent) and of a red laser (iBeam Smart 640 nm, 150 mW, Toptica Photonics) were altered. An oil-immersion objective (APO N 60XO/ 1.49 NA TIRF, Olympus) was used. To separate the excitation from the emission light, a dual line beamsplitter was used and the emission further spectrally separated in an Optosplit III (Cairn Research) equipped with a dichroic beam splitter (640 DCXR, Chroma Technology), a bandpass filter for green (BrightLine HC 582/75, Semrock) and a longpass filter for red (647 nm RazorEdge, Semrock). With the Optosplit, a dual-view configuration was achieved and the emission light focused on the chip of a back-illuminated sCMOS camera (KURO 1200B sCMOS, Princeton Instruments). For data acquisition, the commercial software LightField (Princeton Instruments) was used.

3.3 DNA Origami Production

Different DNA origami designs were used for the projects presented in this thesis. For the diagnostics-related topics, a DNA origami pillar^{61,62} was used whereas the membrane potential sensors were based on a flat rectangular plate.^{140,141} The exact designs can be found in the related publications.

The DNA origami were based on long ssDNA derived from the M13 bacteriophage functioning as a scaffold which was folded into shape with hundreds of short oligonucleotides (from Integrated DNA Technologies, biomers.net GmbH and Eurofins Scientific). Details on the sequences are listed in the SI for the respective publications. The oligonucleotides were mixed with the scaffold in a 10x excess. To introduce modifications, some of the oligonucleotides carried chemical moieties and were added at 30x excess. The mixture contained 10 mM Tris, 1 mM EDTA and 14 mM MgCl₂ for the pillar and 12.5 mM MgCl₂ for the plate. It was heated to 96°C and a temperature ramp to slowly cool down the mixture was driven to induce a stepwise hybridization of the oligonucleotides with the scaffold, until the structures were folded into the desired shape.

Afterwards, the folded DNA origami structures were purified from excess oligonucleotides either by size exclusion with Amicon filters (100 kDa) or by precipitation with PEG.

For the size exclusion centrifugation, the sample and the buffer for washing were added to the filter and the tube spun for 5 min at 20°C and 10 krcf. This step was repeated two times with buffer for washing. For the sample regeneration, the filter was flipped and placed in a fresh tube. By centrifugation at 1 krcf and 20°C for 5 min the purified sample was collected.

The PEG precipitation was achieved by mixing the sample in a 1:1 ratio with buffer containing 12% PEG-8000 (w/v), 10 mM Tris, 1 mM EDTA, 500 mM NaCl and 12 mM MgCl₂ at pH 7.5 and centrifugation for 30 min at 16 krcf and 4°C. The supernatant was discarded and the DNA origami pellet dissolved in the folding buffer containing 10 mM Tris, 1 mM EDTA and 12.5 mM MgCl₂. This washing step was repeated six times.

If required, the structures were post-folding labelled with further modifications by incubation with the oligonucleotides in a 10x excess over-night and another purification procedure followed. Finally, the DNA origami structures were ready for usage and stored at -20°C or 4°C for the samples with cholesterol modifications.

3.4 Nanoparticle Functionalization

For the nanoantenna experiments, silver particles were used with a size of 80 nm (BBI Solutions). In order to bind them to DNA origami structures, they were functionalized with ssDNA oligonucleotides with a 25T sequence (Ella Biotech GmbH). At the oligonucleotide's 5' end, a thiol moiety realized the binding to the silver nanoparticle *via* a sulfide bridge.

A volume of 2 mL of the nanoparticle dispersion (BBI Solutions) was heated to 40°C while stirring and 20 µL of a 20% Tween20 solution and 20 µL of a potassium phosphate buffer (4:5 mixture of 1 M monobasic and dibasic potassium phosphate, P8709 buffer and P8709 buffer, Sigma Aldrich) was added as well as 10 µL of a 50 nM solution of the thiolated DNA oligonucleotide. After an incubation for 1 h, 750 mM NaCl was added to the solution stepwise over the period of 45 min. For purification from excess oligonucleotides, the nanoparticles were mixed in a 1:1 ratio with 1xPBS, 10 mM NaCl, 2.11 mM P8709 buffer, 2.89 mM P8584 buffer, 0.01% Tween20 and 1 mM EDTA (PBS as tablets from Thermo Fisher Scientific). This mixture was centrifuged at 2.8 krcf and 20°C for 15 min. The supernatant was discarded, the pellet dissolved in the previously mentioned buffer and the mixture centrifuged again. This washing step was repeated

six times, before the pellet was dissolved in buffer. To dilute them to the appropriate concentration to be added to the DNA origami, the absorption at its maximum of ~450 nm was measured and the solution diluted until an absorption of ~0.1 was achieved (Nanodrop 2000, Thermo Scientific). Finally, the functionalized nanoparticles were ready for binding to the DNA origami structures and stored at 4°C.

3.5 Liposome Preparation

The phospholipids for the liposome/LUV formation were purchased as a chloroform solution (Avanti Polar Lipids, Inc.) and added to a glass vial at $n=1$ mmol. The chloroform was evaporated under a nitrogen stream and the resulting lipid film was further dried under vacuum in a desiccator for 4 h. Then the lipids were dissolved in buffer as specified in the publications and due to the low solubility of lipids in water, liposomes of various sizes formed spontaneously. To yield unilamellar vesicles, seven freeze-and-thaw cycles were performed and to obtain vesicles of a specific size, the solution was extruded (LiposoFast-Basic, Avestin, Inc.) through a 100 nm PC membrane (Whatman® Nuclepore™) for 21 times. The resulting large unilamellar vesicles were stored at 4°C until used.

3.6 Preparation of Microscopy Slides

For imaging, Nunc® Lab-Tek® II chambered slides (Thermo Fisher Scientific) were used. First, they were cleaned by incubation with 1 M KOH for 4 h and washed with 1xPBS. Afterwards, for the nanoparticle samples the slides were passivated with BSA-biotin (Thermo Fisher Scientific) and for the Large Unilamellar Vesicles (LUV) samples with biotinylated PLL-*g*-PEG (Susos AG) both at 0.5 mg/mL in 1xPBS over night at 4°C. The slides were washed with 1xPBS and by incubation with 0.25 mg/mL neutravidin (Thermo Fisher Scientific) in 1xPBS for 20 min and another washing procedure with 1xPBS, binding sites for the biotin-modified DNA origami were formed and the slides ready to use.

The DNA origami pillar for building nanoantennas were immobilized on the slides at a concentration of ~50 pM. Then the diluted nanoparticles were added and incubated for 48 h at 4°C. A washing step with 10 mM Tris, 1 mM EDTA, 12 mM MgCl₂ and 100 mM NaCl followed and the nanoantennas were ready for imaging.

The DNA origami structures for the LUV samples were for 2 h or overnight incubated with 100x excess of LUVs at 20°C and immobilized in the Lab-Tek chambers at a concentration of ~50 pM. To prevent LUV bursting in the following washing step, 500 µL of the LUV buffer as mentioned above was added, mixed and pipetted out. This dilution-washing step was repeated for 6x and the samples were ready for imaging.

For samples with a transmembrane potential, after the first round of imaging the outside buffer was exchanged by dilution and washing as described before and the ionophore valinomycin was added at a concentration of 37.5 nM. Valinomycin complexes potassium ions very specifically and builds up a transmembrane potential, if there is a potassium concentration gradient across the membrane.¹⁴² The sample was incubated for 10 min with the valinomycin, before imaging. To destroy the potential, gramicidin was added at a concentration of 10 nM and incubated for 10 min, before imaging.

4 DNA Origami for Single-Molecule *in vitro* Diagnostics

A rapid and reliable detection of pathogens is essential in the fight against infectious diseases. The Corona pandemic even more demonstrated its importance in order to get the crisis under control. A fast diagnosis at early stages reduces the risk of spreading, but also – if applicable – enables an early and effective treatment. In this thesis, a diagnostic assay was developed proposing an alternative sensing strategy potentially yielding a low LOD while avoiding molecular amplification. Instead, the signal originating from single target molecule recognition was enhanced physically by a plasmonic nanoantenna.⁴² Its working principle was demonstrated exemplarily by detecting Zika-specific nucleic acids.

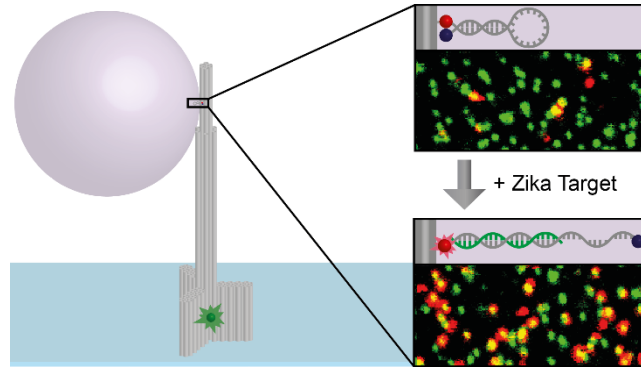


Figure 15. Plasmonic nanoantenna enhancing fluorescence for diagnostic purposes. A DNA origami pillar is equipped with a silver nanoparticle that enhances the fluorescence signal originating from a dye in close proximity. The dye is part of a dye-quencher hairpin which only fluoresces in presence of a specific target. After hybridization of the target with the hairpin, the dye exhibits an enhanced signal. To localize the DNA origami on confocal scans, they are equipped with a green fluorophore. Reprinted with permission from ¹⁴³.

To build this nanoantenna, a DNA origami pillar was used. It contained sites for binding functionalized 80 nm-sized silver nanoparticles. A target recognition unit was placed closely to the nanoparticle at sub-nanometer precision. In detail, a DNA hairpin contained a fluorophore and a quencher modification (ATTO647N and BBQ650) which were close together in the default hairpin form. As a result, fluorescence contact quenching was observed and no signal detected.⁵⁸ The hairpin loop as well as part of the stem had a complementary sequence to the gene for the Zika virus capsid protein. In the presence of a nucleic acid encoding for this protein, it hybridized with the hairpin DNA, opened it. Thus, no quenching took place and a fluorescence signal was measured. Due to the close proximity to the silver nanoparticle, plasmonic fluorescence enhancement occurred in this DNA origami nanoantenna.

First, it was proven by single-molecule confocal microscopy that a DNA target was able to open the hairpin structure and that the nanoparticle did not disturb it. Therefore confocal scans and single-molecule trajectories were analyzed. For both, with and without a nanoparticle bound, a hairpin opening of ~50% was observed. The nanoparticle binding apparently did not interfere with the hairpin assay. However, the DNA origami nanoantenna was equipped with two particle binding sites, but the enhancement factors of only up to 60-fold indicated that only one nanoparticle could bind. This was likely related to steric hindrance induced by the DNA hairpin. Next, the sensitivity of the assay was tested for mismatches in the target sequence to the hairpin. It was shown that the introduction of two mismatches already lead to a significant decrease in hairpin opening. Then, heat-inactivated blood serum was enriched with the target DNA to mimic realistic diagnostic conditions and the test was performed. The results for the serum and the serum-free samples were comparable in terms of target binding and fluorescence enhancement. Therefore, the functionality for physiologically relevant samples was further investigated and RNA targets were used. In the context of Zika, this is an interesting parameter as it is an RNA

virus similar to many other viruses. The target opening was slightly reduced compared to the DNA target which is likely related to more secondary structures in RNA. Lastly, the multiplexing capability for this assay was demonstrated. A second nanoantenna carrying a hairpin complementary to another target DNA was mixed with the Zika-specific nanoantenna. At the base of the DNA origami pillars, the two samples were labelled with fluorescent dyes emitting at different wavelengths. This enabled the distinction between the two samples within one confocal field of view by color barcoding. Although the signals originating from the hairpins were in the same spectral range, they could be differentiated easily by color barcodes in the pillars' bases. The introduction of more complex color barcoding would enable the detection of even more targets simultaneously.

All together, these results show the feasibility of physical signal enhancement as an alternative to molecular amplification such as PCR in diagnostic contexts. Single target molecules could be detected and visualized which holds potential for yielding an extremely low LOD, if single molecules are counted. Therefore the assay could be combined with spotting approaches on microfluidic chips. Furthermore, by using low-tech detection devices such as a modified smart phone camera, the assay could be applied at the point-of-care and hence, function as a rapid diagnostic test in the fight against infectious diseases.

Associated publication P1

Optical Nanoantenna for Single Molecule-Based Detection of Zika Virus Nucleic Acids without Molecular Multiplication

by

**Sarah E. Ochmann, Carolin Vietz, Kateryna Trofymchuk,
Guillermo P. Acuna, Birka Lalkens, Philip Tinnefeld**

published in

Analytical Chemistry, 89, 13000-13007 (2017)

For the full publication see the appendix 7.1.

5 Single-Molecule Membrane Sensors with DNA Origami

5.1 Transmembrane Potential Sensing

The intracellular signal transmission in excitable cells such as neurons goes along with a depolarization of the cell membrane.⁶⁸ Based on the DNA origami technique,^{23,24} an optical biosensor was developed that sensed transmembrane potentials in liposomes and transduced it into optical single-molecule signals.

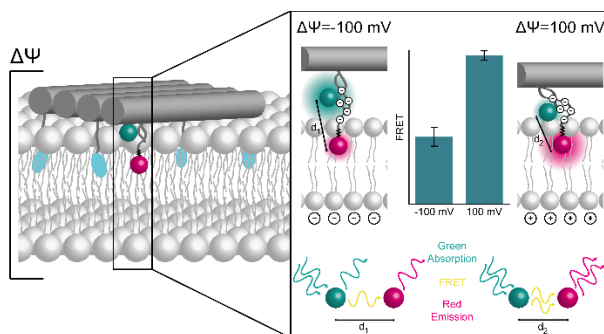


Figure 16. Single-molecule transmembrane potential sensor based on DNA origami. The DNA origami is anchored on a lipid membrane with cholesterol (left, blue) and carries the voltage-sensing unit centrally (left, cyan and pink). The inset shows the concept where a voltage-induced conformational change of the sensing unit results in different inter-dye distances d and thus, in different FRET efficiencies. Reprinted with permission from ¹⁴⁴.

In particular, a DNA origami plate was used for the assembly of different functionalities. Biotin modifications were introduced to immobilize the nanostructures on the surface of passivated and functionalized glass cover slips *via* biotin-neutravidin interactions to perform TIRF measurements. For specific membrane targeting, the nanostructure carried cholesterol moieties that anchor it to lipid bilayers. The key component of the DNA origami sensor was the sensing unit placed in the center of the nanostructure. On the one hand, it had to sense the potential, and on the other hand, it had to translate it into a fluorescence signal. Therefore double-stranded DNA (dsDNA) protruded from the plate carrying the green fluorophore ATTO532 on the dsDNA. Both, the ATTO532 and the DNA are negatively charged and would potentially react to changes in the membrane voltage. Additionally, one of the DNA strands was extended and labelled with the red fluorophore ATTO647N which anchored the sensing unit closely to the membrane surface. These two fluorophores are capable of FRET so that conformational changes resulting in a different distance between the two components lead to a change in energy transfer efficiency.

The performance of the transmembrane potential sensors was tested on liposomes. It was first ensured that the origami bound to the membrane and that the sensing unit was anchored to it. Single-molecule FRET measurements on a TIRF microscope were conducted and a reduction in the energy transfer efficiency in the presence of liposomes was observed. This was in good agreement with molecular dynamic (MD) simulations of the voltage-sensing unit with and without a lipid membrane which unraveled an increased distance between the two fluorophores in the presence of a membrane.

Next, voltage biases at the membrane were created using the ionophore valinomycin which shuffles potassium ions across the membrane with high specificity. If a potassium concentration gradient is introduced across the membrane, valinomycin equilibrates it and thereby induces an electrical transmembrane potential according to the Nernst equation. The sensor was tested for transmembrane potentials ranging from -125 mV to 125 mV and a FRET increase of ~5% for potentials above 50 mV was observed. This suggested a mechanism in which the anionic voltage-

sensing unit is attracted to the membrane, if the membrane's inner leaflet is positively charged. This hypothesis was further supported by a set of MD simulations.

To finally demonstrate the power of DNA nanotechnology for the development of voltage sensors, a small molecular change in the sensing unit was introduced and interestingly, the sensor's sensitivity was shifted from positive to negative transmembrane potentials.

Overall, a DNA origami-based sensor was engineered that translated changes in the electrical transmembrane potential into fluorescence signals. It additionally features single-molecule sensitivity which – once applied in cellular systems – enables the use of lower probe concentrations and thereby reduces invasiveness. Also, a single-molecule read-out holds potential for the collection of information on the nanoscale beyond the resolution limit. Further, the underlying working principle was characterized with the help of MD simulations. With this knowledge, the sensor requirements are better understood and specific changes can be applied to the sensor potentially optimizing the signal-contrast.

Associated publication P2

DNA Origami Voltage Sensors for Transmembrane
Potentials with Single-Molecule Sensitivity

by

Sarah E. Ochmann, Himanshu Joshi, Ece Büber, Henri G. Franquelim, Pierre Stegemann, Barbara Saccà, Ulrich F. Keyser, Aleksei Aksimentiev, Philip Tinnefeld

published in

Nano Letters, 21, 8634-8641 (2021)

For the full publication see the appendix 7.2.

5.2 Membrane Surface Charge Sensing

Changes in the membrane surface charge are involved in different signaling pathways⁸⁸⁻⁹⁰ and visualizing these changes can help to better understand the underlying biological principles. To do so, in this work a membrane surface charge sensor was presented that acts at the membrane's outer leaflet without the need for transfection complementing the existing sensors. Additionally, the read-out of single sensors was achieved.

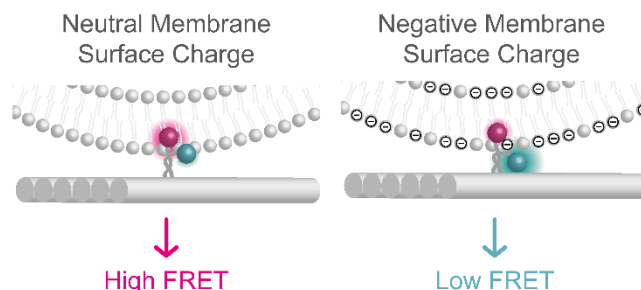


Figure 17. DNA origami-based surface charge sensor. The DNA origami translates an uncharged membrane into a high-FRET signal, whereas a negatively charged membrane results in a low-FRET signal. Reprinted with permission from ¹⁴⁵.

To build these sensors, DNA origami nanostructures were used for the assembly of the different sensor components. As in the previous chapter "Transmembrane Potential Sensing", a rectangular DNA origami was equipped with biotin molecules for surface immobilization on biotinylated surfaces *via* neutravidin-biotin interaction. This allowed for surface-based TIRF and confocal measurements. Multiple cholesterol modifications enabled the binding of the DNA origami to liposomes. A sensing unit protruded from the origami platform and consisted of dsDNA carrying the fluorophore ATTO647N as a membrane anchor and a ssDNA extension with an ATTO542 fluorophore modification. ATTO542 is highly anionic matching the intrinsic charge of DNA. The single-stranded nature of this construct facilitated this negatively charged construct to undergo conformational changes upon different membrane surface charges. Additionally, the two fluorophores could undergo FRET translating changes in the inter-dye distance into precise fluorescence signals.

The functionality of the DNA origami-based membrane surface charge sensors was tested with liposomes composed of a mixture of zwitterionic lipids (DOPC) and anionic lipids (DOPG). The ratio between the two lipids was varied resulting in different negative surface charge densities. The liposomes were mixed with the DNA origami sensors and immobilized on a surface to perform single-molecule FRET measurements on a TIRF microscope. First, the sensors showed a FRET reduction in the presence of uncharged liposomes compared to the liposome-free sample. This finding suggested an insertion of the ATTO647N anchor to the membrane as intended and previously observed. Second, a further FRET decrease was measured upon exposure to liposomes with DOPG contents up to 80%. A consistent FRET drop was observed upon a stepwise DOPG increase implying that the sensor was able to quantitatively translate the membrane surface charge into an optical signal.

Fluorescence correlation spectroscopy (FSC) analysis of confocal data revealed dynamics in the system. Apparently, the DNA-ATTO542 leash switches between two states in the presence of a lipid membrane. An extended shrinking-gate approach delivered the dwell times in both of the two states as well as the fluorescence lifetime of the ATTO542.¹⁴⁶ It could be shown that the leash switches between a membrane-bound, high-FRET state and a membrane-unbound, low-FRET state. Depending on the surface charge, the equilibrium constant is shifted towards the unbound state. Also, the equilibrium position of the low-FRET state is further away from the

membrane. As the integration time in the TIRF measurements was longer than the timescale of the dynamics, the mean value between the states was measured and appeared as a FRET reduction for negatively charged membranes.

Next, a small change in the molecular structure of the sensor was introduced removing one anionic charge and instead adding a hydrophobic carbon chain. Interestingly, the FRET reduction upon an increase of the DOPG content was consistent, but steeper for high DOPG contents compared to the previous sensor design. Hence, by including a small change, the sensor's sensitivity was shifted towards higher surface charges.

In summary, a sensor for membrane surface charges was developed, using DNA origami as a platform, that shows a strong and quantitative FRET change upon different contents of negatively charged lipids. This approach holds potential for *in vivo* applications as DNA origami structures are biocompatible and various strategies against DNase degradation have been demonstrated.^{51,147,148} Once applied to cellular systems, the sensor could give insights on the surface charge of the cell membrane's outer leaflet complementing the current picture of charge-induced cell signaling. Moreover, nanoclusters could be visualized under physiological conditions.

Associated publication P3

Quantitative Single-Molecule Measurements of
Membrane Charges with DNA Origami Sensors

by

Sarah E. Ochmann, Tim Schröder, Clara M. Schulz, Philip Tinnefeld

Analytical Chemistry, 94, 2633–2640 (2022)

For the full publication see the appendix 7.3.

6 Conclusion and Outlook

As part of this thesis, DNA origami was used to develop optical single-molecule biosensors. Different functionalities were combined into small chemical entities by assembling them on a nanostructure platform. Thereby, the different needs for specific biosensing applications were addressed which can be used for future *in vitro* and membrane biosensing applications.

In chapter 4, an assay was presented for the diagnostic *in vitro* detection of nucleic acids. It was demonstrated that using plasmonic fluorescence enhancement, a high signal-to-background ratio can be obtained. In this assay, the translation of single Zika-specific nucleic acid targets into fluorescence signals for each individual molecule was achieved. This holds potential for an extremely low LOD, if each individual target molecule in a patient's sample can be counted while a low sample volume is sufficient. Unlike in other optical nanoantennas, with DNA origami it was possible to precisely position fluorescence-quenched DNA hairpins closely to plasmonic nanoparticles. Relevant characteristics for diagnostic applications were further investigated and it was proven that the assay is working in a blood serum as a medically relevant sample and that the detection can be extended from DNA to RNA targets. However, although the target molecule was present in a huge excess, only ~50% of the hairpins showed a signal. Additionally, the low fluorescence enhancement suggested that only one metallic nanoparticle was bound to the nanoantenna despite the antenna being equipped with two binding sites. In previous investigations with this antenna design, this was not an issue^{40,61,62} except for a prior study with a hairpin assay.⁵⁸ Likely, it came to steric hindrance and only one nanoparticle was capable of binding.

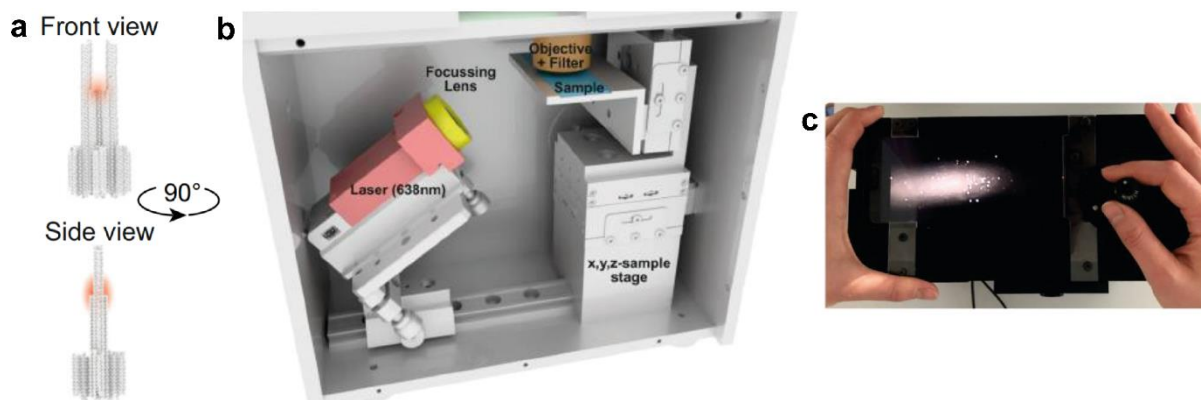


Figure 18. Improved DNA origami nanoantenna for single-molecule imaging on portable microscope. (a) Adopted DNA origami design with cleared hotspot for binding two nanoparticles and positioning a target binding site in the plasmonic hotspot. (b) Sketch illustrating the basic concept of the portable microscope. (c) Single-molecule signals derived from nanoantennas on the portable microscope. Reprinted with permission from ¹⁴⁹.

These limitations have been recently addressed by Trofymchuk *et al.* by changing the DNA origami design to yield a cleared hotspot (Figure 18a).¹⁴⁹ This way, even with a DNA-sensing assay, two nanoparticles were bound and thus, higher fluorescence enhancement was achieved. Furthermore, the sensing assay was adopted; using a so-called sandwich assay, up to 80% target binding was detected. It was moreover demonstrated that the signal obtained is high enough to be visualized on a portable microscope with a smartphone camera (Figure 18b and c). The compatibility with easy and low-cost detection devices is a big step towards POC diagnostics. Another demand for this is a reliably high fluorescence enhancement. So far, the enhancement is rather inhomogeneous and ranges from no to up to ~400-fold. Previously, it was shown that the fluorescence intensity of ten dye molecules is the lower detection limit the presented smartphone-based microscope.¹⁵⁰ This implies that the fluorescence enhancement from each

DNA origami nanoantenna has to be at least ten-fold in order to enable counting each single target molecule.

Another important parameter for a potential POC application is finding the target molecule in a reasonable time. To reduce the incubation time, the assay could be combined with micro- or nanofluidics where the binding kinetics would be increased. Further, spotting the DNA origami nanoantennas in certain areas on a coverslip would greatly increase the chances of finding the target molecules. As the sensing assay can be easily extended for the detection of various targets by changing the sequence of the capturing DNA strand, many different targets can be detected in one shot. On the one hand, nanoantennas for different targets can be spotted in certain areas and the sample solution can be exposed to all of them. On the other hand, using dyes fluorescing in different spectral regions, color barcoding enables the distinction even in the same field of view. Besides the assay-based improvements, the target range can be extended from nucleic acids to other disease markers such as small molecules or proteins by *e.g.* using aptamers. First attempts have been demonstrated by Pfeiffer *et al.*¹⁵¹ All of these future directions would make DNA origami nanoantennas applicable in POC diagnostic assays where single-molecule counting would enable the detection of low abundant disease markers in small sample volumes.

Besides this potential diagnostic test, single-molecule biosensors for electrical membrane properties were introduced in chapter 5. Specifically, one sensor was able to read out electrical transmembrane potentials and the other one membrane surface charges. The functionality of these sensors was tested on liposomes. Both sensors were based on a rectangular DNA origami to assemble the required functionalities. Unlike other design strategies, with DNA origami the different functionalities were modularly chosen and easily combined including membrane targeting *via* cholesterol and surface immobilization *via* biotin. The sensing unit was placed in the center of the platform and could iteratively be adjusted to the needs. It consisted of DNA protruding from the origami that carried a FRET dye pair. An ATTO647N dye served as an acceptor as well as a membrane anchor, while a green fluorophore – acting as a donor – remained in the aqueous solution. The experiments and a set of MD simulations suggested that the ATTO647N is not only embedded in the membrane as previously proposed,¹⁵² but it is even stuck in a certain position. In the context of developing a membrane sensor, this offers the opportunity to precisely introduce changes to the sensing unit in the aqueous solution while the ATTO647N anchor is unaffected. The molecular structure of the sensing units differed for the transmembrane potential and surface charge applications, but the read-out relied on conformational changes for both leading to different inter-dye distances and appearing as FRET changes. As the sensors are build up with DNA nanotechnology, the iterative adjustments of the sensor are easier and faster compared to genetically-encoded sensors while the specific targeting of the membrane is not compromised.

For the transmembrane potential sensor in chapter 5.1, different molecular structures of the sensing unit were screened showing either a FRET increase or decrease in response to voltage changes which were found to be reversible. Unlike with previous FRET-based voltage sensors *e.g.* by Tsien and co-workers,^{77,78} the sensing components were linked. Thus, for each sensor the number of fluorescing components is fully controlled enabling comparison of different sample batches. In future projects, the temporal response should be investigated. This is a relevant parameter for tracking neuronal activity because action potentials appear on the lower millisecond time scale.

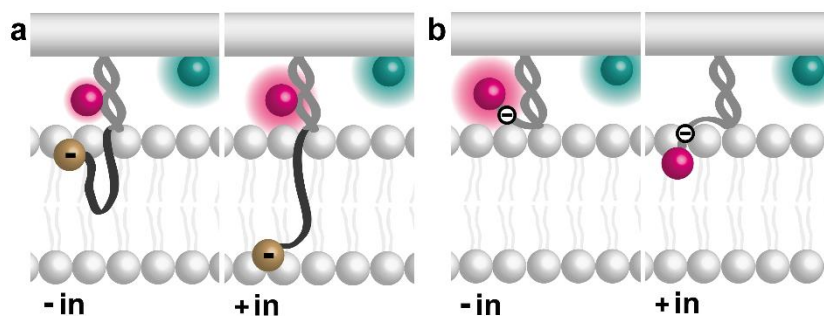


Figure 19. Transmembrane potential sensor designs for improved signal contrast. (a) Protruding from the DNA origami, a hydrophobic leash (dark grey) carrying a dark quencher (brown) switches from the outer to the inner leaflet of the membrane according to the transmembrane potential. Thereby, the fluorescence of the dye shown in pink is more or less quenched while the dye illustrated in green is for a ratiometric read-out. (b) On a similar DNA origami construct, an environmentally sensitive dye dips into the hydrophobic core in response to the transmembrane potential. Within the lipid core it is not fluorescing.

Furthermore, different design strategies could be tested to improve the signal contrast. For example, instead of sensing the transmembrane potential at the outer membrane leaflet, the sensing element could be placed into the hydrophobic core where it is more likely to find its energetically most favorable position close to the lipid head groups (Figure 19a). Upon reverse transmembrane potentials, the element is either at the inner or the outer leaflet which translates to a distance change of ~ 3 nm. If FRET can occur between the components in the membrane core and outside, a high FRET contrast results. Similar strategies have been introduced for FRET-based voltage probes.^{77,78} However, in the previous approaches, the two components were chemically not linked, so it was not presumed that each of the molecules in the lipid core had a FRET partner at the membrane surface. To compensate this, high probe concentrations were required while lacking single-molecule compatibility. Another sensing strategy could take advantage of environmentally sensitive dyes fluorescing in aqueous solution and being quenched in hydrophobic environments such as the lipid core (Figure 19b). A possible dye for this application could be silicon rhodamine (SiR)¹⁵³ or derivatives¹⁵⁴ placed on a ssDNA leash on the DNA origami. By referencing with a second fluorophore far beyond the FRET radius, an all-or-nothing signal could be read-out for different transmembrane potentials.

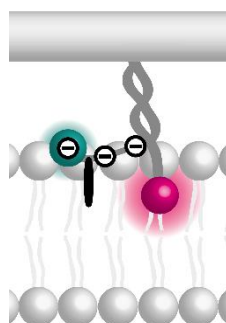


Figure 20. New surface charge sensor design. In this design, the surface charge sensor's membrane-bound state is stabilized due to strong hydrophobic interactions making this sensor sensitive for high membrane surface charges.

The membrane charge sensor in chapter 5.2 could also benefit from further optimization. The two designs introduced in this thesis already suggested that small chemical changes strongly influence the equilibrium between the high-FRET membrane-bound state and the low-FRET membrane-unbound state. Understanding the mechanism behind this helps to further tune the sensor's sensitivity. An interesting inspiration could be the genetically-encoded membrane charge sensor with FRET read-out by Ma *et al.*⁹¹ There, the sensor consisted of a static and a flexible FRET part similar to the system presented here. By strongly anchoring the flexible unit

to the membrane surface, the FRET contrast was drastically increased. A similar strategy could be tested for the membrane surface charge sensor presented here (Figure 20). Introducing a strongly hydrophobic anchor could stabilize the membrane-bound state for low to intermediate surface charges, while strong surface charges induce a release of the sensing unit

For both of the presented membrane sensors, suitable strategies for stabilization against DNase degradation have to be tested to increase the DNA origami lifetime in cellular environment while not compromising its functionality.¹⁴⁷ There are different options available for stabilization, from covalent helix-crosslinking⁴⁸ to non-covalent shielding⁴⁴⁻⁴⁷ to smart structure design.⁴³ Once a suitable strategy is found, the single-molecule biosensors can be applied to cells. At this point, the programmability of DNA nanotechnology could also be used to not only specifically target the cell membrane, but also certain types of cells by addition of *e.g.* receptor recognition units.^{29,51,80} This way, these custom-tailored membrane sensors can unravel information collected at the nanoscale with potentially low invasiveness.

Overall, in this thesis different strategies were suggested how DNA origami can serve as an assembly platform for the development of single-molecule biosensors. The focus was on a strategy to be applied for *in vitro* diagnostic purposes and another strategy for electrical membrane sensing, but the possible combination of different chemical functionalities is almost unlimited. Therefore, it is certain that DNA origami techniques will yield more and also more complex biosensors for single-molecule applications in the near future.

7 Appendix

7.1 Associated publication P1

Optical Nanoantenna for Single Molecule-Based Detection of Zika Virus Nucleic Acids without Molecular Multiplication

by

**Sarah E. Ochmann, Carolin Vietz, Kateryna Trofymchuk,
Guillermo P. Acuna, Birka Lalkens, Philip Tinnefeld**

Reprinted with permission from

Analytical Chemistry, 89 (23), 13000-13007 (2017)

Copyright 2022 American Chemical Society



Optical Nanoantenna for Single Molecule-Based Detection of Zika Virus Nucleic Acids without Molecular Multiplication

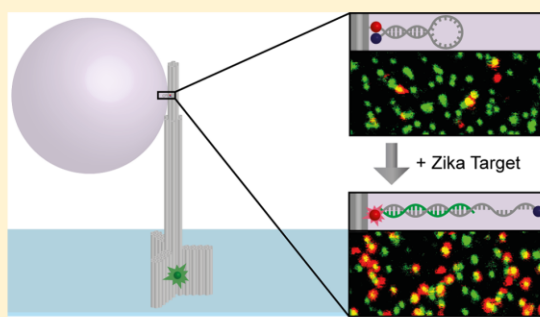
Sarah E. Ochmann,[†] Carolin Vietz,^{†,‡} Kateryna Trofymchuk,[†] Guillermo P. Acuna,^{†,§} Birka Lalkens,[†] and Philip Tinnefeld^{*,†,‡,§}

[†]Institute for Physical and Theoretical Chemistry, and Braunschweig Integrated Centre of Systems Biology (BRICS), and Laboratory for Emerging Nanometrology (LENA), Braunschweig University of Technology, Rebenring 56, 38106 Braunschweig, Germany

[‡]Department of Chemistry and Center for NanoScience, Ludwig-Maximilians-Universitaet Muenchen, Butenandtstrasse 5-13, 81377 Muenchen, Germany

Supporting Information

ABSTRACT: Because of the limited signal-to-background ratio, molecular diagnostics requires molecular amplification of the target molecules or molecular signal amplification after target recognition. For direct molecular detection, we demonstrate a purely physical fluorescence enhancement process which can elevate the fluorescence signal of single fluorescent dyes by several orders of magnitude. To this end, DNA origami-based optical antennas with a height of around 125 nm are used, which utilize metallic nanoparticles to create a hotspot where fluorescence signals are enhanced by plasmonic effects. By equipping the hotspot with a molecular beacon-like structure, we combine the plasmonic signal enhancement with a specific signal generation, leading to an enhanced and therefore easy to detect signal only in the presence of the specific target nucleic acid. Exemplified with Zika virus detection, we show the applicability of this approach by detecting Zika-specific artificial DNA and RNA both in buffer and in heat-inactivated human blood serum. We show the sensitivity against small nucleotide variations of this approach, allowing the discrimination of closely related pathogens. Furthermore, we show how the modularity offered by DNA nanotechnology enables multiplexing by incorporating orthogonal fluorescent labels for the simultaneous detection of different sequences. The achieved signal enhancement will allow technically simplified signal detection, paving the way for single molecule-based point-of-care diagnosis.



Early detection of diseases caused by pathogens is a prerequisite for efficient patient treatment. The key question is how to generate a signal that is strong enough against background to obtain a meaningful diagnosis from disease-specific target molecules that exist, especially in the onset of disease, only in low abundance. Since its market launch in 1996, real-time PCR^{1,2} has revolutionized molecular diagnostics of nucleic acids in clinical laboratories.³ Real-time monitoring of the molecular amplification through a fluorescence readout can give rapid and quantitative results. Despite advances, there are still drawbacks concerning the robustness and reproducibility. PCR is sensitive toward contamination that might cause false-positive or false-negative results and hamper identification and quantification of pathogens. The exponential nature of signal generation can also amplify the influence of small deviations from the standard protocol and batch quality. Well-trained staff, sophisticated equipment and cautious handling are essential to achieve the required quality.⁴ This is only guaranteed in specialized laboratories increasing the waiting time and uncertainty of the patient and at the same time impeding such methods in

developing countries. More direct and robust detection is a grand challenge to improve speed, robust quantification, and multiplexing in molecular assays. Anyhow, the direct detection of low-abundance analytes is hindered by low signal-to-background ratio: The large number of solvent or other molecules in the observation volume as well as unspecific surface binding lead to scattering and background. Consequently, the few fluorescent molecules of interest are indistinguishable from background.⁵ Recent realizations of molecular diagnostics without molecular amplification include microarray technologies,^{6,7} branched DNA^{8–10} or detection with plasmonic nanoparticles.^{11–13} Branched DNA, for example, increases the signal by a cascade of hybridization reactions incorporating many fluorophores in the branched DNA hybrids.

Here, we introduce a nucleic acid detection method that avoids molecular amplification by a direct physical fluorescence

Received: October 5, 2017

Accepted: November 16, 2017

Published: November 16, 2017

amplification mechanism. This amplification mechanism involves DNA origami-based¹⁴ optical antennas that incorporate the assay for fluorescence detection. Recently, fluorescence enhancement of several orders of magnitude was demonstrated using DNA origami optical antennas.¹⁵ A DNA origami scaffold served to place noble metal nanoparticles that create a plasmonic hotspot for fluorescence enhancement. Because of the scaffolding by the DNA origami, the optical antennas have the unique ability that objects such as fluorescent dyes can be precisely placed in the plasmonic hotspot next to a noble metal nanoparticle or in the gap between two nanoparticles.^{16–19}

In this work, we exploit the unique scaffolding properties of DNA origami to place a fluorescence-quenching hairpin (FQH) near a plasmonic nanoparticle that acts as an optical antenna. Previously, it was shown that both effects can be combined modularly.²⁰ On the basis of Zika virus model system that gained publicity after its epidemic spread in South America,²¹ we demonstrate the fluorescence enhancement-based detection of specific DNA sequences. Using synthetic Zika-specific target DNA and RNA, we successfully show its detection in buffer as well as human blood serum, discuss the sensitivity toward single-nucleotide variations, and demonstrate its potential application for multiplexing assays. These results indicate how the modularity of DNA nanotechnology allows inserting different functionalities into a DNA nanolab toward simplified diagnostics of low-abundance molecules in a point-of-care environment.

■ EXPERIMENTAL SECTION

Functionalization of Silver Nanoparticles. Silver nanoparticles with a diameter of 80 nm (BBI Solutions) were functionalized with 25T single-stranded DNA oligonucleotides with a thiol modification at the 5' end (Ella Biotech GmbH) following a protocol included in the [Supporting Information](#). Afterward the silver nanoparticles were diluted in 1xTE containing 12 mM MgCl₂ and 100 mM NaCl to an absorption of 0.1 on an UV–vis spectrometer (Nanodrop 2000, Thermo Scientific).

Serum Preparation. The human blood serum was extracted from whole blood derived from blood donors. The whole blood was clotted after 30 min of incubation at room temperature. It was centrifuged for 10 min at 2 krcf and 4 °C. Then the supernatant was stored at –20 °C until it was used. Before adding it to the sample, the serum was heat inactivated by exposing it for 30 min to 56 °C and enriched with 1 nM target DNA, 12 mM MgCl₂, and 100 mM NaCl.

DNA Origami. The DNA origami pillar used for the experiments was designed in CaDNAo and is based on a p8064 scaffold derived from M13mp18 bacteriophages. For folding 10 nM of the scaffold, staple strands (Eurofins Genomics GmbH, biomers.net GmbH and IBA GmbH, sequences in the [Supporting Information](#)) were added in 10-fold excess in 1xTE containing 14 mM MgCl₂. The mixture was heated and slowly cooled down as shown in the [Supporting Information](#). The origami pillars were purified from the excess staple strands by Amicon filtering (Amicon Ultra-0.5 mL, Ultracel-100 K Membrane, Millipore) and three times washing with 1xTE containing 14 mM MgCl₂. Each time it was centrifuged for 5 min at 10 krcf and 20 °C. Finally, the Amicon filter was flipped and placed in a new tube. By centrifuging it for 5 min at 1 krcf and 20 °C, the DNA origami was extracted.

Sample Preparation. A Lab-Tek chamber (Thermo Fisher Scientific) was coated with bovine serum albumin (BSA)-biotin

(Sigma-Aldrich) and neutravidin (Sigma-Aldrich) to immobilize the DNA origami pillars on the surface in a concentration of about 50 pM. The diluted nanoparticle solution was added to the DNA origami and incubated for 48 h at 4 °C. To remove unbound nanoparticles, the sample was washed three times with 1xTE containing 12 mM MgCl₂ and 100 mM NaCl. Fluorescence scans were taken on a custom-built confocal microscope described below, before the target DNA or RNA (Eurofins Genomics GmbH) was added at a final concentration of 1 nM in 1xTE containing 12 mM MgCl₂ and 100 mM NaCl and incubated for 18 h at 4 °C. For the samples treated with serum, the target DNA was enriched in serum and added to the samples the same way. Finally, fluorescence scans were taken again as well as fluorescence transients, after three times of washing with 1xTE containing 12 mM MgCl₂ and 100 mM NaCl. The nanoparticle-free and/or target-free samples were treated and washed the same way without the addition of metallic nanoparticles and/or the target DNA, respectively.

Preparation of RNA Samples. To exclude RNase contaminations, all solutions were incubated at 37 °C overnight with 0.1% diethyl pyrocarbonate (DEPC, Sigma-Aldrich) and autoclaved at 121 °C for 15 min to eliminate residual DEPC. All plasticware was rinsed with 0.1 M NaOH/0.1 mM EDTA and then with DEPC-treated water. The RNA target (Eurofins Genomics GmbH) was added and imaged in the same way as the DNA target.

Confocal Measurements and Data Analysis. The custom-build confocal microscope was based on an Olympus IX-71. A 80 MHz pulsed laser at 640 nm (LDH-D-640, Picoquant) was used for the red excitation and a 80 MHz pulsed laser at 532 nm (LDH-P-FA530B, Picoquant) was used for the green excitation. With variable neutral density filters, the red laser power was set to 2 μW for scans and 1 μW to take transients of samples with nanoparticles. The green laser power was set to 6 μW for the multiplexing experiments and to 1.5 μW for all other tests with variable neutral density filters. Green and red excitation were altered through an AOTF filter (AOTFnc-VIS, AA optoelectronic). The experiments were performed with circular polarized light by a combination of a linear polarizer and a quarter-wave plate. With a dual-band dichroic beam splitter (Dualband z532/633, AHF) the laser was coupled into the oil-immersion objective (UPlanSApo 60XO/1.35 NA, Olympus). The confocal scans were performed with a piezo stage (P-517.3CL, Physik Instrumente GmbH & Co. KG) which also allows the positioning of a molecule in the laser focus for time-resolved inquiry. A dual-band dichroic beam splitter separated the resulting fluorescence from the excitation light, before it is focused on a 50 μm pinhole (Linos). Red and green emission channels were separated at another dichroic beam splitter (640DCXR, AHF). With two spectral filters for each channel (red, ET 700/75m, AHF and RazorEdge LP 647, Semrock; and green, HC582/75, AHF and RazorEdge LP 532, Semrock) the light was further spectrally purified.

Finally, the fluorescence was detected by single-photon avalanche diodes (τ -SPAD-100, Picoquant) and registered by a time-correlated single-photon counting PC card (SPC-830, Becker & Hickl). For data processing, a custom-made LabVIEW software (National Instruments) was used to select single-step photobleaching transients for further analysis. With the program FluoFit (PicoQuant), fluorescence-lifetime decays were fitted monoexponentially and deconvolved from the instrument response function. To calculate the fluorescence enhancement of the samples with nanoparticles, for each

molecule the resulting counts were divided by the mean value of the counts per molecule for the nanoparticle-free sample. For the fraction of opened hairpins, the fluorescence scans were analyzed. The fraction of opened hairpins was calculated by dividing the number of red-green spots by the sum of green and red-green spots. The data was plotted as histograms and the standard deviation was included. Unpaired *t* tests with *p*-critical values of 0.05 were done as indicated in the figures.

RESULTS AND DISCUSSION

Fluorescence-Quenching Hairpin Opening on an Optical Antenna. To detect Zika-specific DNA with single molecule sensitivity, a fluorescence-quenching hairpin (FQH) was used as shown in Figure 1a with a 12 bp stem and a 12 nt loop, which is based on the principle of molecular beacons.²² The 5' end is modified with an ATTO 647N dye and the 3' end with BlackBerry quencher 650 forming a static dye-quencher pair. Part of the hairpin is complementary to 23 nt of the sequence for Zika's envelope protein (Uniprot: Q91KX7_ZIKV). The FQH's 5' end is extended to incorporate it into a DNA origami pillar during folding of the nanostructures (Figure 1b). The DNA origami pillar has eight biotins bound which are used to immobilize the origami onto a BSA-biotin/neutravidin-coated coverslip as described elsewhere.²³ Only in the presence of Zika-specific target DNA, a fluorescence signal can be detected because the target DNA hybridizes with the hairpin breaking its secondary structure. Consequently, the fluorophore and the quencher are separated from each other and a red fluorescence signal is generated. In the closed form, the red ATTO647N fluorophore is fully quenched and no fluorescence at all is detected after background subtraction.²⁰ The DNA origami is equipped with protruding oligonucleotide strands serving as binding sites for silver nanoparticles (NP) with a diameter of 80 nm which are functionalized with thiol-labeled oligonucleotides complementary to the capturing strands of the DNA pillars (Figure 1b, top view inset); sequences are given in the Supporting Information. For steric reasons, only one NP per origami attaches forming monomer optical antennas (see the Supporting Information Figure S1a for details). When a silver NP is present, a dye placed within this region is exposed to a higher electric field resulting in fluorescence enhancement.^{16,24,25} Additionally, an ATTO 542 dye molecule is incorporated into the base of the DNA origami, indicating its location during the measurements (shown as a green dot in Figure 1b). With this optical antenna design, several experiments were performed. First, the specificity of the FQH opening was tested by taking fluorescence scans before and after the addition of target DNA (Figure 2a) with an alternating 532 and 640 nm excitation for ATTO 542 and ATTO 647N, respectively. In the false-color images, each green spot corresponds to a single DNA origami. Red spots indicate opened FQHs and hence, yellow spots represent colocalization of red and green spots which stand for functional single DNA origamis with an opened FQH. At $t = 0$ only a few red-green colocalized spots are visible which might represent mislabeled FQHs or unspecifically opened FQHs. After the incubation overnight with an excess of 1 nM target DNA to ensure the opening of the hairpin, the amount of red-green colocalized spots increases whereas in the target-free samples no additional hairpin opening is observed. This shows that the FQH is opened specifically, generating a fluorescence signal and indicating the presence of the target. Subsequently, the same

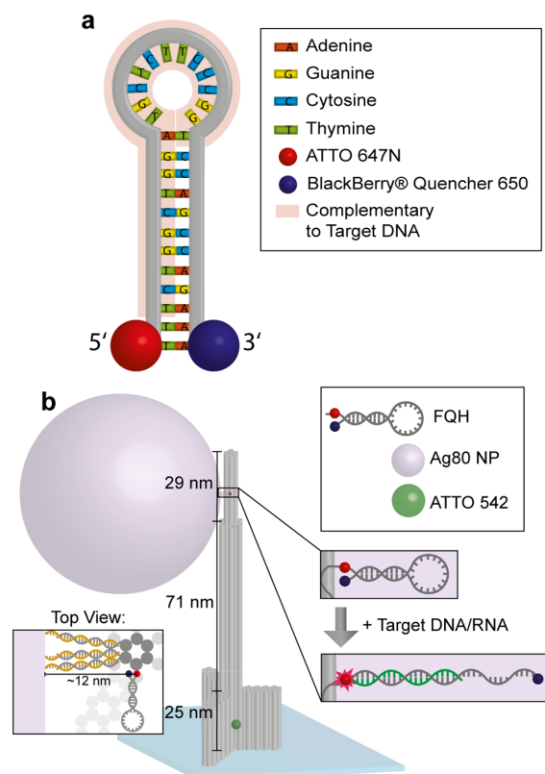


Figure 1. FQH and DNA origami design: (a) DNA-based fluorescence-quenching hairpin (FQH) is used for the detection of Zika-specific DNA. It consists of a 12 bp long stem and a 12 nt long loop and has a complementary region to a sequence encoding for Zika's envelope protein highlighted in red. On its 5' end, the FQH carries an ATTO 647N dye and on its 3' end it carries a BlackBerry quencher 650. (b) DNA origami pillar with a total height of 125 nm is immobilized via biotin modifications on a BSA-biotin/neutravidin surface in a low concentration to ensure single molecule detection. An ATTO 542 dye is incorporated into its bottom part to localize the origami (green dot in sketch). On its upper part, an FQH is bound to the pillar by extending its strand on the 5' end. This allows incorporation of the FQH into the origami pillar during folding of the nanostructures (insets). Upon the addition of specific target DNA/RNA, the FQH is opened resulting in red fluorescence. To enhance the fluorescence arising from the FQH a silver nanoparticle (NP, 80 nm diameter) is attached to the origami as shown in the top view. The thiol-labeled oligonucleotides hybridize with the protruding strands of the DNA pillar.

experiment was performed upon the addition of silver NPs forming optical antennas. After an incubation of 48 h with the NPs, the target DNA was added. The fluorescence scans show the same trend as in the particle-free sample. For quantification, the fraction of opened FQHs' was calculated by dividing the number of red-green colocalized spots by the sum of green and red-green spots (Figure 2b). After the incubation with target DNA, the amount of opened FQHs increases significantly to ~50% compared to samples without target DNA. The difference between the sample with and without NPs is not significant, verifying that there is no effect of the NPs on the FQH opening. Comparing the scans with and without NPs shows a strongly increased red signal in the samples with NPs

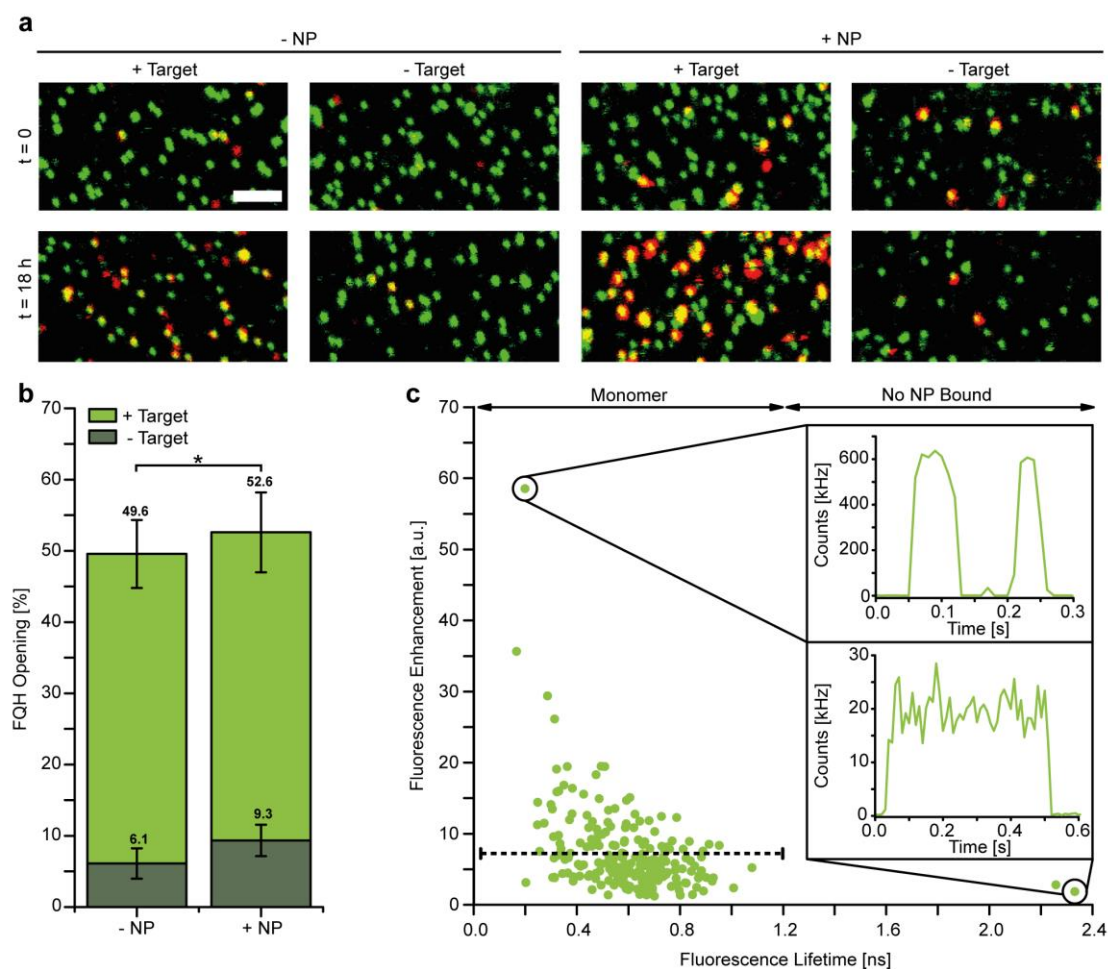


Figure 2. Fluorescence enhancement and opening of FQHS: (a) Fluorescence scans of surface-immobilized optical antennas before and after 18 h of incubation with 1 nM target DNA. These tests were performed with and without the addition of NPs as well as control samples without target DNA. Each green spot corresponds to a single DNA origami on the surface. Red spots indicate an opening of the FQH as no fluorescence is emitted by the red dye in the closed form. Consequently, red-green colocalized spots refer to intact DNA origami with an opened FQH. Scale bar: 2 μm . (b) Fraction of opened FQHS. This was quantified by dividing the number of red-green colocalized spots by the sum of green spots and red-green spots. Number of analyzed molecules with and without target, respectively, $- \text{NP}$, 825/1023; $+ \text{NP}$, 1328/619. An unpaired t test was carried out to check for the similarity of distributions, where * is $p > 0.05$. Error bars show the standard deviation from the mean. (c) Fluorescence enhancement versus fluorescence lifetime scatter plot of opened FQHS on DNA origami optical antennas with NPs. The dashed line illustrates the mean fluorescence enhancement. Insets show fluorescence transients of an optical antenna with a NP (monomer) and without a NP bound.

bound, indicating fluorescence enhancement caused by the NPs. The fluorescence enhancement due to the presence of NPs was calculated by referring to a NP-free sample. Figure 2c shows the corresponding fluorescence-enhancement/fluorescence-lifetime scatter plot. Because of the correlation between fluorescence lifetime and enhancement,²⁶ the molecules with a high enhancement show a short lifetime. The shortened fluorescence lifetime also indicates that most of the DNA origamis have a NP bound.²⁴ Up to 60-fold enhancement of the signal was achieved, although most of the molecules show a lower fluorescence enhancement with an average of 7.3-fold. The heterogeneity is related to the polydispersity of silver nanoparticles, the distribution of binding positions on the metal nanoparticle as well as orientational distribution of the DNA

pillar on the surface. When comparing the transient of the brightest spot to one without a NP bound (Figure 2c insets), it is obvious that the dye emits brighter.²⁷ These experiments proof that DNA-based optical antennas can successfully be combined with a molecular diagnostic assay to gain specific signals on a single molecule basis.

Although we used a sophisticated single-molecule sensitive microscope, signal enhancement might be the basis to facilitate the detection, eliminating the need of technically complex instruments. As the enhanced fluorescence signal originates from an extremely small region in the near-field of the nanoparticle, positive signals might also be distinguished from unavoidable spurious binding of single dye molecules to the

coverslip and unspecific binding in the enhanced region is likewise improbable.

Influences of Single-Nucleotide Variations. To further verify the FQH for a potential diagnostic application, the influence of single-nucleotide variations (SNVs)^{2,5} on the FQH opening was tested. Three alternative target DNAs were used that included one, two, or three mismatches to the FQH (Figure 3a). The mismatched positions were located at the

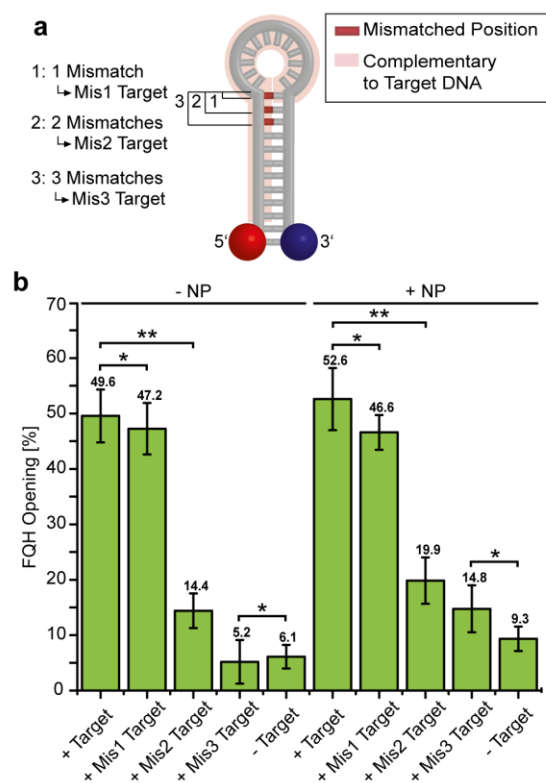


Figure 3. Influence of SNVs on hairpin opening. (a) Schematic representation of mismatched positions of the target DNA complementary to the FQH sequence. Mis1 target has one mismatch located at position 1, Mis2 target two mismatches at position 2, and Mis3 target three mismatches at position 3. (b) Fraction of opened FQHs after 18 h of incubation with 1 nM of respective target DNA and with and without the addition of NPs. The opened fraction was quantified by dividing the number of red-green colocalized spots by the sum of the red-green and green spots resulting from the fluorescence scans. Number of analyzed molecules from left to right: 825, 430, 459, 216, 1023, 1328, 585, 429, 477, 619. An unpaired *t* test was done, where * is $p > 0.05$ and ** $p < 0.05$. Error bars show the standard deviation from the mean.

beginning and downward of the FQH's stem region. The Mis1 target had one mismatch, the Mis2 target had one additional mismatch and the Mis3 target had two additional mismatches to the Mis1 target. As in the experiments before, fluorescence scans were acquired after overnight incubation with 1 nM of the respective target DNA (see Supporting Information Figure S2). These experiments were performed with and without NPs bound to the DNA origami structure. With each extra mismatched position of the target DNA to the FQH the

fraction of opened FQHs decreases (Figure 3b). The difference between the perfect matched target DNA and the Mis1 target DNA is low but already two exchanged bases in the target DNA lead to a significant reduction of the FQH opening, whereas there is no significant difference between the sample with the Mis3 target DNA and the one without the addition of any target DNA. Already two SNVs have a strong effect on the FQH opening and with a third SNV the opened FQH amount cannot be distinguished from the target-free sample anymore. Therefore, this assay is sensitive for the differentiation between closely related pathogens.

FQH Opening in Human Serum. To check the applicability of the FQH-based optical antennas under relevant conditions, we tested the performance in human blood serum as typical specimen for the detection of the Zika virus.²⁹ To emulate this test, we enriched human serum derived from blood donors with synthetic target DNA. After the surface-immobilized DNA origami were equipped with NPs, heat inactivated human serum³⁰ was enriched with 1 nM of target DNA. The serum mixture was incubated with the sample overnight at 4 °C before it was washed and imaged as described above. Figure 4a shows fluorescence scans after the incubation with serum upon the addition of target DNA and as a control without target DNA. The control sample without target DNA indicates both that the stability of the DNA origami is not affected by the treatment with serum and that the serum does not unspecifically open FQHs. Similarly, serum does not affect the successful opening of the FQH by the target as shown in Figure 4a, left panel. The serum has neither an effect on the control sample nor on the sample with target DNA enriched in serum. The quantification of the FQH opening confirms this observation (Figure 4b). The fraction of opened FQHs is even slightly higher when the sample is treated with serum and the number of unspecific opened FQHs is also not increasing. These findings proof the robustness of DNA-based optical antennas to be used under realistic conditions. Next we analyzed the fluorescence enhancement of the opened FQHs induced by the NP. The average fluorescence enhancement was calculated by referencing to the fluorescence intensity of single ATTO 647N molecules (Figure 4c).

We find similar average fluorescence enhancement of 4.9-fold and 7.3-fold for the serum and the serum-free samples. Although the average numbers seem to be different, high standard errors have to be considered as observed elsewhere and discussed above.¹⁶ It is an interesting question whether only the opened form of the FQH is enhanced or whether also the contrast between the opened and the closed form is increased. Recently, we showed that the fluorescence of the closed FQH is quantitatively quenched and that the modular combination of a DNA hairpin assay with fluorescence enhancement can yield synergetic effects.²⁰ Further structural optimization ensuring the binding of two silver NPs to the DNA origami will allow higher fluorescence enhancement.^{16,23}

RNA Detection. In many diagnostic tests like for Zika virus the pathogen's RNA instead of DNA is detected. Hence, we further tested the FQH opening on optical antenna upon hybridization with RNA targets. Analogous to the DNA target used before, the RNA target is complementary to the red-shaded region of the FQH as depicted in Figure 1a. The samples with NPs bound were incubated with the target RNA overnight as described above. After the incubation, the amount of opened FQHs is ~37% (Figure 5) which is slightly lower than for the opening with DNA. As RNA tends to form more

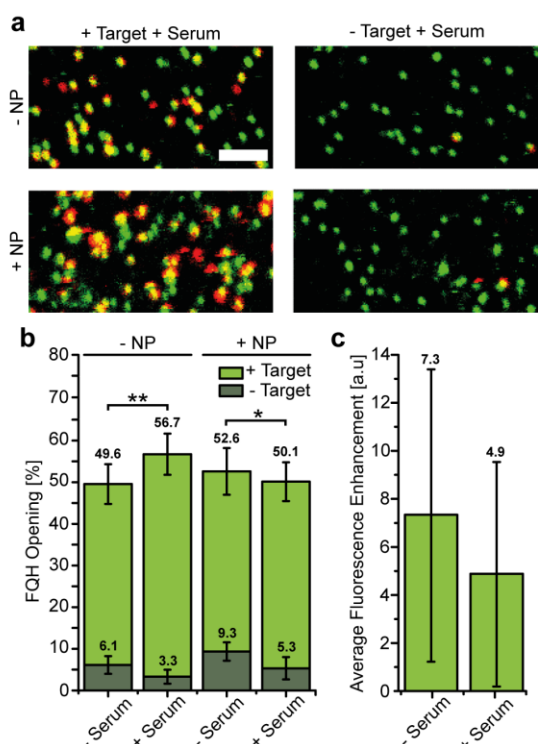


Figure 4. FQH opening and fluorescence enhancement in target-enriched serum. (a) Fluorescence scans after 18 h of incubation with target-enriched serum (1 nM target) and serum without target as a control with and without the addition of NPs, respectively. Each green spot corresponds to a single DNA origami on the surface. Red spots indicate opening of the FQH. Consequently, red-green colocalized spots refer to intact DNA origami with an opened FQH. Scale bar: 2 μm . (b) Fraction of opened FQHs in samples treated with serum and buffer upon addition of 1 nM target DNA, without target as a control and with and without NPs, respectively. Quantification was done by dividing the number of red-green colocalized spots by the sum of red-green and green spots in the fluorescence scans. Number of analyzed molecules from left to right with and without target, respectively: 825/1023, 521/303, 1328/619, 671/492. An unpaired t test was done, where * is $p > 0.05$ and ** $p < 0.05$. Error bars show the standard deviation from the mean. (c) Average fluorescence enhancement of monomer optical antennas with and without the presence of serum. Number of analyzed molecules from left to right: 209, 150. Error bars show the standard deviation from the mean.

secondary and tertiary structures than DNA, this result is not surprising and has the potential to be further optimized. Still, it could be shown that this assay is also compatible for the detection of RNA molecules.

Multiplexing with the Optical Antenna. As the FQH has a pronounced selectivity, we were interested whether this assay is suitable for multiplexed analysis. To this end, a second optical antenna was designed (Figure 6a) which has an FQH complementary to an artificial target DNA with a length of 30 nt which is called FQH II optical antenna in the following (sequences shown in the Supporting Information Table S5). It also carries an ATTO 647N and a BlackBerry quencher 650 at the hairpin as the dye-quencher pair. Since the signal arising from these two FQHs upon successful hybridization with the

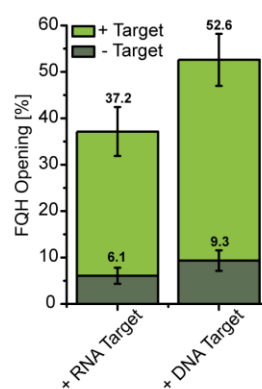


Figure 5. RNA target for FQH opening. Fraction of opened FQHs on optical antennas with NPs after incubation with 1 nM RNA target compared to the incubation with 1 nM DNA target. This was quantified by dividing the number of red-green colocalized spots by the sum of red-green and green spots in the fluorescence scans. Number of analyzed molecules from left to right with and without target, respectively: 1193/611, 1328/619. Error bars show the standard deviation from the mean.

respective target DNA is in both cases based on ATTO 647N in the red spectral range after red excitation, we exploited the modularity of DNA origami and additionally incorporated different fluorescent dyes as barcodes in the base of the origami pillar. The FQH Zika optical antenna, which was used for the experiments described above, is labeled with ATTO 542 giving a green fluorescence signal after green excitation. The FQH II optical antenna has Abberior STAR S20SXP bound. This long Stokes-shift dye is excited in the green spectral range and fluoresces in the red spectral region. Therefore, the optical antennas can be distinguished by the signal arising from green excitation. These two types of optical antennas were immobilized on the same surface. After an incubation with both target DNAs overnight, fluorescence scans were recorded as shown in Figure 6b.

For visualization, blue spots indicate FQH Zika optical antennas, specified by green emission after green excitation, and green spots denote FQH II optical antennas specified by red emission after green excitation. Red spots represent opened FQHs. Therefore, a colocalization with either a blue or a green spot implies an opened FQH on one of the two optical antennas. Hence, a pink spot resulting from a blue-red colocalization is a positive signal of the FQH Zika optical antenna and a yellow spot represents the opened FQH II optical antenna. The false-color representations of fluorescence scans in Figure 6b show successful opening of both FQHs on the same surface. In the Supporting Information, further results confirm that the FQHs are only opened by their specific target DNA, respectively, ensuring orthogonality of the two optical antennas. To demonstrate the signal amplification due to the presence of silver NPs, exemplary fluorescence transients of both opened FQHs are shown in Figure 6c. They are compared to fluorescence transients of particle-free samples implying a fluorescence enhancement of both FQHs. Since the FQH's sequence can principally be chosen at will, this multiplexing assay can be extended to detect even more different target DNAs. Either the fluorophore at the bottom of the DNA origami structure can be exchanged to perform color barcoding as described elsewhere³¹ or the dye-quencher pair. Moreover,

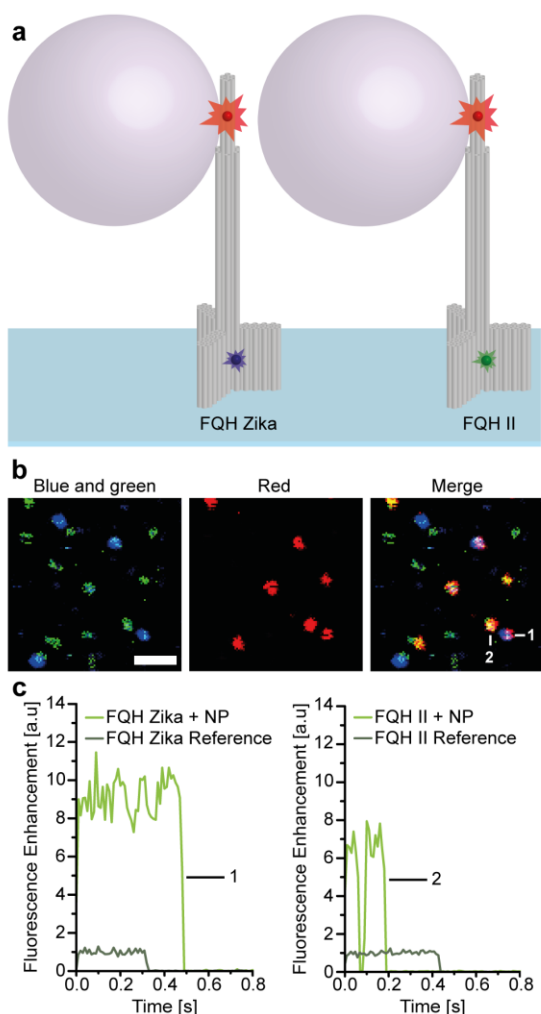


Figure 6. Multiplexing with optical antennas. (a) Sketch of the two different optical antenna designs. The first optical antenna has an FQH for Zika-specific target DNA and an ATTO 542 incorporated as described before. The second optical antenna carries an FQH for an artificial target DNA and three Abberior STAR 520SXP molecules. Both DNA origamis were immobilized on the same surface. (b) Fluorescence scans of optical antennas with NPs after incubation with 1 nM target DNAs specific for both FQHs. Blue spots indicate FQH Zika optical antennas and green spots FQH II optical antennas. Red spots stand for opened FQHs. A blue-red colocalization results in a pink spot in the merged picture and implies an opened FQH Zika on the DNA origami, a red-green colocalization yields a yellow spot which represents an opened FQH II. Scale bar: 1 μm. (c) Fluorescence transients of marked spots in part b for the FQH Zika (1) and the FQH II (2) and reference samples without NPs, respectively.

wavelength-shifting molecular beacons³² or DNA origami beads³³ can be introduced giving even more color combinations.³² Because of the broadband fluorescence enhancement capabilities of silver NPs, even in these cases fluorescence enhancement can be achieved,²³ making this assay a powerful tool for the specific and simultaneous detection of different pathogens.

CONCLUSIONS

In recent years, DNA origami optical antennas were established for fluorescence enhancement of molecules placed in the plasmonic hotspot. Here, we show for the first time that this concept can be successfully combined with a target-specific FQH-based DNA detection. On the basis of the purely physical signal enhancement, a simplified detection of pathogens like Zika virus in a technically less demanding environment might become feasible. Since both DNA and RNA were successfully detected and blood serum does not hamper the detection, a wide variety of diagnostic applications is conceivable. As a single target molecule generates a strong, unambiguous, and specific signal, low concentration targets might be detected without the need of further molecular amplification.

The modular structure of the optical antenna allows the introduction of further functionalities. Here, we exemplified this modularity by synergistically employing a nucleic acid hairpin assay with plasmonic fluorescence enhancement and built-in immobilization capability. Moreover, we introduced a fluorescence barcode in the origami base for multiplexed detection of different targets. Further color barcoding could extend the parallelization. Introduction of additional multiplication processes³⁴ in the optical antenna is an option for further synergistic signal amplification. Optimization of the optical antenna structure for better fluorescence enhancement as well as a more efficient opening of the FQH will increase the signal obtained.

Our work provides a glimpse of the possibilities of DNA nanotechnology for creating a nanolab that can report on the presence of different pathogens with simplified detection devices, enabling sophisticated diagnostics in a point-of-care environment.

ASSOCIATED CONTENT

Supporting Information

The Supporting Information is available free of charge on the ACS Publications website at DOI: 10.1021/acs.analchem.7b04082.

Enhancement-lifetime distribution for monomer optical antennas, intensity comparison of ATTO 647N, fluorescence scans of samples with mismatched target DNA, controls for multiplexing, protocol for NP functionalization, table with staple strands used for DNA origami folding, folding program of the DNA origami, AFM picture of DNA origami pillar, and caDNAno file for the design of the DNA origami pillar (PDF)

AUTHOR INFORMATION

Corresponding Author

*E-mail: philip.tinnefeld@cup.uni-muenchen.de. Phone: +49 89 2180 77549.

ORCID

Carolin Vietz: 0000-0002-8417-4168

Guillermo P. Acuna: 0000-0001-8066-2677

Philip Tinnefeld: 0000-0003-4290-7770

Author Contributions

S.E.O. designed experiments, prepared samples, planned and executed experiments, analyzed and interpreted data, and wrote the manuscript. C.V. and B.L. designed the experiment, interpreted data, and wrote the manuscript. K.T. prepared

samples and analyzed and interpreted data. G.P.A. interpreted data. P.T. designed experiments, interpreted data, wrote the manuscript, and supervised the project.

Notes

The authors declare the following competing financial interest(s): The authors have filed a provisional patent application, EP17159353.6, on the described method of combining nucleic acid hybridization probes with plasmonic enhancement.

ACKNOWLEDGMENTS

We thank Dr. Henk Garritsen, Klinikum Braunschweig, for the blood samples and Johann Bohlen, TU Braunschweig, for AFM images. We are grateful to Bettina Wunsch, Kristina Hübner, and Katharina Kraatz for fruitful discussions. This work was funded by the BMBF (Grants POCEMON, 13N14336 and SIBOF, 03VP03891) and the Deutsche Forschungsgesellschaft (Grants AC 279/2-1 and TI 329/9-1). We further acknowledge support by the German Excellence Initiative via the program Nanosystems Initiative Munich (NIM). C.V. is grateful to the Studienstiftung des deutschen Volkes for a scholarship. K.T. and G.P.A. acknowledge funding of the state ministry for research of lower saxony in the frame of the “Quantum- and Nanometrology” (QUANOMET) strategic research area. Quanomet is part of the LUH-TUBS research alliance.

REFERENCES

- Higuchi, R.; Dollinger, G.; Walsh, P. S.; Griffith, R. *Nat. Biotechnol.* **1992**, *10*, 413–417.
- Higuchi, R.; Fockler, C.; Dollinger, G.; Watson, R. *Nat. Biotechnol.* **1993**, *11*, 1026–1030.
- Kaltenboeck, B.; Wang, C. *Adv. Clin. Chem.* **2005**, *40*, 219–259.
- Holland, N. T.; Smith, M. T.; Eskenazi, B.; Bastaki, M. *Mutat. Res., Rev. Mutat. Res.* **2003**, *543*, 217–234.
- Holzmeister, P.; Acuna, G. P.; Grohmann, D.; Tinnefeld, P. *Chem. Soc. Rev.* **2014**, *43*, 1014–1028.
- Lobenhofer, E. K.; Bushel, P. R.; Afshari, C. A.; Hamadeh, H. K. *Environ. Health Perspect.* **2001**, *109*, 881–891.
- Schena, M.; Shalon, D.; Davis, R. W.; Brown, P. O. *Science* **1995**, *270*, 467–470.
- Collins, M. L.; Irvine, B.; Tyner, D.; Fine, E.; Zayati, C.; Chang, C.; Horn, T.; Ahle, D.; Detmer, J.; Shen, L. P.; Kolberg, J.; Bushnell, S.; Urdea, M. S.; Ho, D. D. *Nucleic Acids Res.* **1997**, *25*, 2979–2984.
- Horn, T.; Chang, C. A.; Urdea, M. S. *Nucleic Acids Res.* **1997**, *25*, 4842–4849.
- Urdea, M. S.; Running, J. A.; Horn, T.; Clyne, J.; Ku, L. L.; Warner, B. D. *Gene* **1987**, *61*, 253–264.
- Csáki, A.; Möller, R.; Fritzsche, W. *Expert Rev. Mol. Diagn.* **2002**, *2*, 187–193.
- Dubertret, B.; Calame, M.; Libchaber, A. J. *Nat. Biotechnol.* **2001**, *19*, 365–370.
- Reichert, J.; Csáki, A.; Köhler, J. M.; Fritzsche, W. *Anal. Chem.* **2000**, *72*, 6025–6029.
- Rothemund, P. W. K. *Nature* **2006**, *440*, 297–302.
- Darvill, D.; Centeno, A.; Xie, F. *Phys. Chem. Chem. Phys.* **2013**, *15*, 15709–15726.
- Acuna, G. P.; Möller, F. M.; Holzmeister, P.; Beater, S.; Lalkens, B.; Tinnefeld, P. *Science* **2012**, *338*, 506–510.
- Kuzyk, A.; Schreiber, R.; Fan, Z.; Pardatscher, G.; Roller, E.-M.; Högele, A.; Simmel, F. C.; Govorov, A. O.; Liedl, T. *Nature* **2012**, *483*, 311–314.
- Schmied, J. J.; Raab, M.; Forthmann, C.; Pibiri, E.; Wunsch, B.; Dammeyer, T.; Tinnefeld, P. *Nat. Protoc.* **2014**, *9*, 1367–1391.
- Thacker, V. V.; Herrmann, L. O.; Sigle, D. O.; Zhang, T.; Liedl, T.; Baumberg, J. J.; Keyser, U. F. *Nat. Commun.* **2014**, *5*, 3448.
- Vietz, C.; Lalkens, B.; Acuna, G. P.; Tinnefeld, P. *Nano Lett.* **2017**, *17*, 6496–6500.
- Ferguson, N. M.; Cucunubá, Z. M.; Dorigatti, I.; Nedjati-Gilani, G. L.; Donnelly, C. A.; Basañez, M.-G.; Nouvellet, P.; Lessler, J. *Science* **2016**, *353*, 353–354.
- Tyagi, S.; Kramer, F. R. *Nat. Biotechnol.* **1996**, *14*, 303–308.
- Vietz, C.; Kaminska, I.; Paz, M. S.; Tinnefeld, P.; Acuna, G. P. *ACS Nano* **2017**, *11*, 4969–4975.
- Acuna, G. P.; Bucher, M.; Stein, I. H.; Steinhauer, C.; Kuzyk, A.; Holzmeister, P.; Schreiber, R.; Moroz, A.; Stefani, F. D.; Liedl, T.; Simmel, F. C.; Tinnefeld, P. *ACS Nano* **2012**, *6*, 3189–3195.
- Novotny, L.; van Hulst, N. F. *Nat. Photonics* **2011**, *5*, 83–90.
- Holzmeister, P.; Pibiri, E.; Schmied, J. J.; Sen, T.; Acuna, G. P.; Tinnefeld, P. *Nat. Commun.* **2014**, *5*, 5356.
- Pellegrotti, J. V.; Acuna, G. P.; Puchkova, A.; Holzmeister, P.; Gietl, A.; Lalkens, B.; Stefani, F. D.; Tinnefeld, P. *Nano Lett.* **2014**, *14*, 2831–2836.
- Maxwell, D. J.; Taylor, J. R.; Nie, S. *J. Am. Chem. Soc.* **2002**, *124*, 9606–9612.
- Frankel, M. B.; Pandya, K.; Gersch, J.; Siddiqui, S.; Schneider, G. *J. Virol. Methods* **2017**, *246*, 117–124.
- Hahn, J.; Wickham, S. F. J.; Shih, W. M.; Perrault, S. D. *ACS Nano* **2014**, *8*, 8765–8775.
- Lin, C.; Jungmann, R.; Leifer, A. M.; Li, C.; Levner, D.; Church, G. M.; Shih, W. M.; Yin, P. *Nat. Chem.* **2012**, *4*, 832–839.
- Tyagi, S.; Marras, S. A.; Kramer, F. R. *Nat. Biotechnol.* **2000**, *18*, 1191–1196.
- Korobchevskaya, K.; Colin-York, H.; Lagerholm, B. C.; Fritzsche, M. *Photonics* **2017**, *4*, 41.
- Wang, D.; Vietz, C.; Schröder, T.; Acuna, G. P.; Lalkens, B.; Tinnefeld, P. *Nano Lett.* **2017**, *17*, 5368–5374.

Supporting Information

An Optical Nanoantenna for Single Molecule-Based Detection of Zika Virus Nucleic Acids without Molecular Multiplication

Sarah E. Ochmann[†], Carolin Vietz[†], Kateryna Trofymchuk[†], Guillermo P. Acuna[†], Birka Lalkens[†] and Philip Tinnefeld^{†,‡,*}

[†]Institute for Physical and Theoretical Chemistry, and Braunschweig Integrated Centre of Systems Biology (BRICS), and Laboratory for Emerging Nanometrology (LENA), Braunschweig University of Technology, Rebenring 56, 38106 Braunschweig, Germany.

[‡]Department of Chemistry and Center for NanoScience, Ludwig-Maximilians-Universitaet Muenchen, Butenandtstr. 5-13, 81377 Muenchen, Germany.

*Email: philip.tinnefeld@cup.uni-muenchen.de; phone: +49 89 2180 77549.

Supplementary Figures.....	S-2
Protocol for the Functionalization of Silver Nanoparticles.....	S-5
Staple Strands for the Folding of DNA Origami Pillars	S-5
Folding Program for the DNA Origami Pillar	S-11
AFM image of the DNA Origami.....	S-12
References	S-13

Supplementary Figures

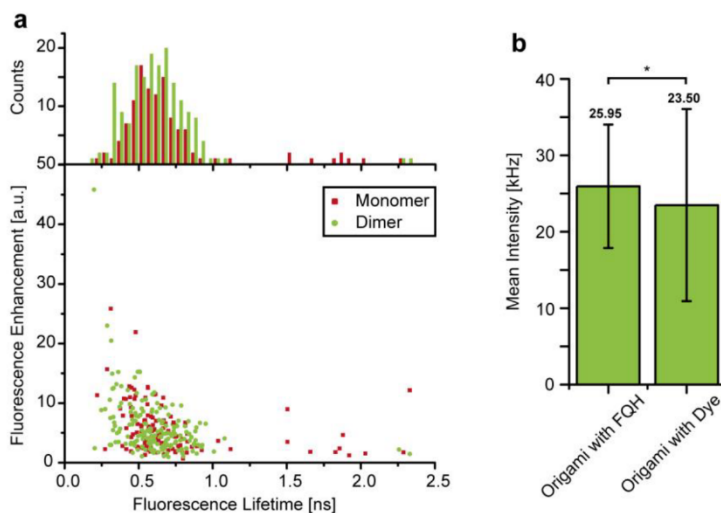


Figure S1: **a:** Comparison of fluorescence-lifetime/fluorescence-enhancement distribution of DNA origami optical nanoantennas with binding sites for one NP (Monomer) and two NPs (Dimer) and histogram of fluorescence lifetime distribution. Red spots result from single molecules of the monomer design and green spots from single molecules of the dimer design. The color code is the same in the histogram. The similarity of the populations resulting from these two designs suggest that even in the dimer design only one NP binds to the DNA origami pillar. Otherwise a clear separation would be visible as shown in other literature [1, 2]. **b:** Mean intensities of ATTO 647N on the FQH bound to the origami and just the dye on the DNA origami. The difference between the mean intensities of both species does not differ significantly indicating a far proximity between the quencher and the dye on the FQH and hence, no FRET quenching of the dye appears. Number of analyzed molecules from left to right: 95, 88. An unpaired t-test was done, where * is $p > 0.05$. Error bars show standard deviations from the mean.

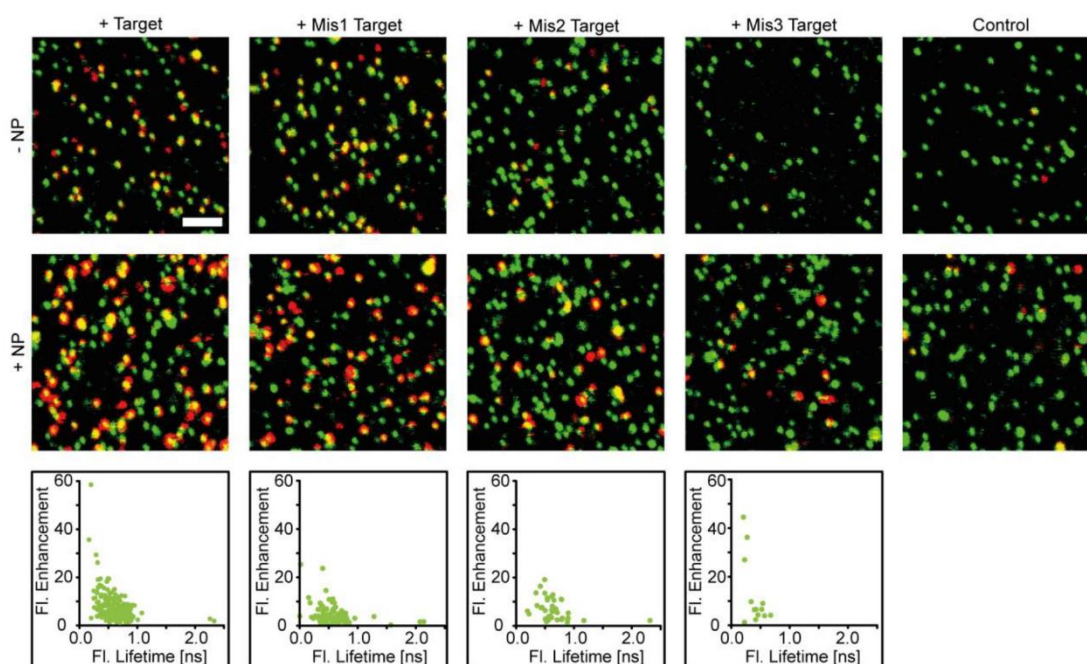


Figure S2: Fluorescence scans of samples incubated for 18 h with mismatched target DNA as shown in figure 4 with and without NPs bound as well as a control sample without the addition of target DNA. Each green spot corresponds to a single DNA origami on the surface. Red spots indicate an opening of the FQH. Consequently, red-green co-localized spots refer to intact DNA origami with an opened FQH. Further, the fluorescence-enhancement/fluorescence-lifetime distribution for each sample with NPs and different target DNA is shown. The distributions look similar for each sample, but with every additional mismatched position the amount of opened FQHs decreases and consequently, the number of molecules shown in the enhancement/lifetime distribution plot as well. Scale bar: 2 μm .

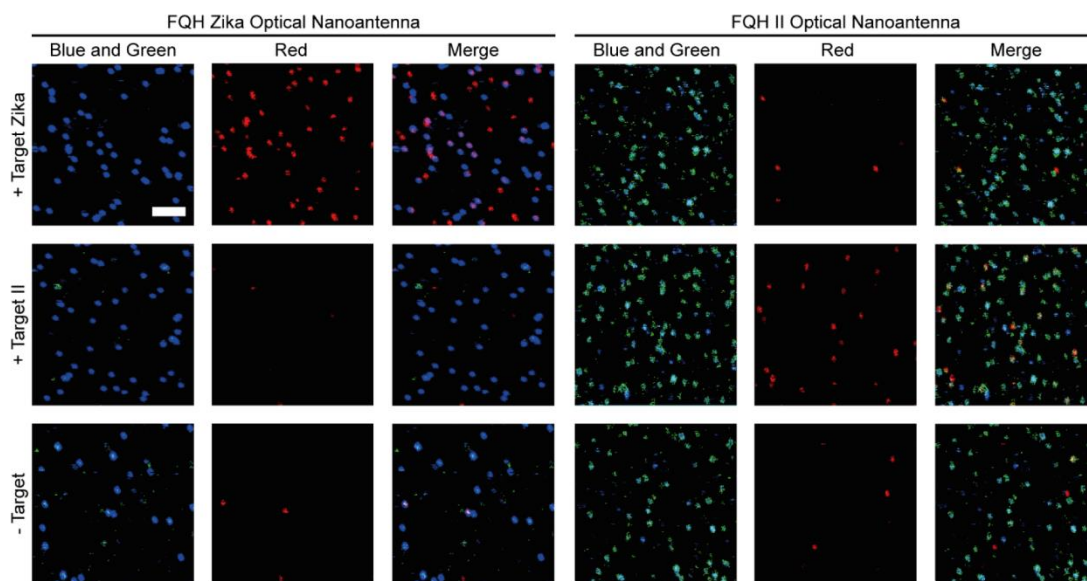


Figure S3: Fluorescence scans of DNA origami optical nanoantennas used for multiplexing tests upon addition of different target DNAs. The FQH Zika optical nanoantenna and the FQH II optical nanoantenna were immobilized onto a surface separately. The target Zika and the target II were added to the samples and incubated for 18 h to test whether the FQH opening is specific to the target DNA. Only upon the addition of the respective target DNA the FQH is opened. Blue spots indicate FQH Zika optical nanoantennas and green spots FQH II optical nanoantennas. Red spots stand for opened FQHs. A blue-red co-localization results in a pink spot in the merged picture and implies an opened FQH Zika on the DNA origami, a red-green co-localization in yellow which is an opened FQH II. Scale bar: 2 μm .

Protocol for the Functionalization of Silver Nanoparticles

The protocol for the functionalization of silver nanoparticles (NP) was modified from Mirkin [3]. The NPs had a diameter of 80 nm (BBI Solution). A volume of 2 mL was heated to 40°C under permanent stirring. 20 µL of 10% Tween20 and 20 µL of a potassium phosphate buffer (4:5 mixture of 1 M monobasic and dibasic potassium phosphate, Sigma Aldrich) were added as well as 10 µL of a 50 nM thiol-modified single stranded DNA solution (5'-thiol-25T-3') and incubated for 1 h at 40°C. Afterwards, 1xPBS buffer containing 3.3 M NaCl was added stepwise over 45 min to the heated and stirred solution, until a final concentration of 750 mM was reached. Then the particles were mixed 1:1 with 1xPBS 10 mM NaCl, 2.11 mM P8709 buffer (Sigma Aldrich), 2.89 mM P8584 buffer (Sigma Aldrich), 0.01 % Tween20 and 1 mM EDTA. For the purification from excess ssDNA, the solution was centrifuged for 15 min at 2.8 kcrf and 20°C. A pellet has formed in which the particles were concentrated. The supernatant was discarded and the washing step repeated for six more times.

Staple Strands for the Folding of DNA Origami Pillars

Table S1: Sequences and length of unmodified staples. These oligonucleotides were purchased from Eurofins Genomics GmbH.

Number	Sequence (5' to 3')	Length [nt]
1	TTAGTTTGAGTGCCCGAGAAATAAAGAAATTGCGTAGAGATA	42
2	TATGACTTTATACATTTTTTTTAAATGGAAACAGTACACCGT	42
3	AATAAACGAACTATGACCCCAACCAAGC	28
4	CTCATCGGGATTGAGTGAGCGAGTAACAACCCGTC	35
5	CCCAGCTACAATGACAGCATTGAGGCAAGTTGAGAAATGAA	42
6	TCATACATTTAATACCGATAGCCCTAAACATCGAACGTAAC	42
7	ACGCGGTCCGTTTTTGGGTAAGTGA	25
8	CTTACGGAACAGTCAGGACGTTGGGAAGAAA	31
9	GGAACCATACAGGCAAGGCAAAATCAAAAAGACGTAGTAGCAT	42
10	CTAAATCGGTCAGAATTAGCAAAATTAAGCAATAAAATAATA	42
11	TTTAGCGATACCAACGCGTTA	21
12	AAGAAAGCTTGATACCGCCACGCATACAGACCAGGCGCTGAC	42
13	CCCGCTAGGGCAACAGCTGGCGAAAGGGGGATGTGCTTATT	42
14	GCCCGAGTACGAGCCGGAAGC	21
15	CATTTGCGAAATGTCATCTGCGAACGAGAGATTCACAATGCC	42
16	TATTTAAATTGCAGGAAGATTG	22
17	AAAGATTACAGAACGGGAGAAGGAAACGTCACCAATGAAACCA	43

18	ACGTAAGAATTCGTTCTTAGAAGAACTCAAACCTATCGGATAA	42
19	GCGAATCAGTGAGGCCACCGAGTAGTAGCAACTGAGAGTTGA	42
20	TCGTGCCGGAGTCAATAGTGAATTTGCAGAT	31
21	TAGCCTCAGAGCATACCCTGT	21
22	AGCAACAAAGTCAGAAATAATATCCAATAATCGGCTCAGGGA	42
23	AGGCTTGCGAGACTCCTCAAGAGAAAAGTATTCGGAAC	38
24	ACCTGACGGGGAAAGCCGGCGAACCAAGTGCTGCGCGTTGC	42
25	CCGTAATCAGTAGCGACAGAATCTAATTATTCATTA AAAAGG	42
26	GAACTGGCTCATTACAACCTTAATCATTCTTGAGATTACTTA	42
27	GAGTTAAAAGGGTAATTGAGCGCTAATATCAGAGGAACTGAACACC	46
28	AGTTTCCAACATTATTACATTATAC	25
29	ACGCGAGAGAAGGCCATGTAATTTAGGCCAGGCTTAATTGAGAATCGC	48
30	ACTAATGCCACTACGAATAAA	21
31	TAGCCAGCTTTCATCCAAAAATAAACGT	28
32	CCTCGTTTACCAGAAACCAAA	21
33	TTAGCCCTGACGAGAAACACCAGAAATTGGGGTGAATTATTTAA	45
34	TGAGTAAAGGATAAGTTTAGCTATATCATAGACCATTAGATA	42
35	ATTTCTGATTATCAGATGATGGCTTTAAAAGACGCTAAAA	42
36	CCAGCCTCCGATCCTCATGCCGGA	24
37	ATGAAGGGTAAAGTTCACGGTGCGGCCATGCCGGTCGCCATG	42
38	TAAGTTGGCATGATTAAGAA	21
39	TAATATCAAAGGCACCGCTTCTGGCACT	28
40	GTCGCAGAAAACTTAAATTTGCC	24
41	GTTAAAGGAAAGACAGCATCTGCCTATTTAAGAGGCAGGAGTTTA	46
42	AAGGCTCCAAAAGGAGCCTTTATATTTTTTACGTGCTACAGTCACCCT	49
43	TAACGACATTTTTACCAGCGCCAAAGAAAGTTACCAGAACCCAAA	45
44	AAGGGATATTCATTACCGTAATCTATAGGCT	31
45	TTCGGTCCCATCGCATAGTTGCGCCGACATGCTTTTCGAGGTG	42
46	AATATCGTTAAGAGAGCAAAGCGGATTGTGAAAAATCAGGTCTTT	45
47	AAATGACGCTAAATGGATTATTTACATTGGCGAATACCTGGA	42
48	ACCGCCACCCTCAGAACCCTACTCTAGGGA	31
49	TTCGGGGTTTCTGCCAGGCCTGTGACGATCC	31
50	AGTACCGCATTCCACAACATGTTTCAGCCTTAAGGTAAAGTAATTC	45
51	CCCGGTTGATAAAGCATGTCAATC	24
52	AGTAGGTATATGCGTTATACA	21
53	CTGGCATTAGGAGAATAAAATGAAGAAACGATTTTTTGAGTA	42
54	CGAACACCAAATAAAATAGCAGCCAAGTTTGCCTTTAGCGTCAGA	45
55	TGCTAAATCGGGGAGCCCCGATTTAGAGCTAGCAGAACATT	42
56	CGCGCTACAGAGTAATAAAAGGGACATTCTGATAGAACTTAG	42
57	AAGACAAATCAGCTGCTCATTCACTGACCA	32

58	TTTTCCAGCATCAGCGGGGCTAAAGAACCTCGTAGCACGCCA	42
59	ACATAAGTAGAAAAATCAAGAAGCAAAGAAGATGTCAT	39
60	CAAATCACCAGAACCCAGAGCCAGATTTTGTACAAATCACAC	42
61	GCTGTAGTTAGAGCTTAATTG	21
62	TTATAAGGGTATGGAATAATTCATCAATATA	31
63	ATAGCGAGAGGCTATCATAACCAAATCCCAAAGAAAATTTTCATCCTCAT	49
64	TTTAGATTCACCAGTCACACGACCGGCGCGTGCTTTCCAGA	42
65	CAAGCCCAATAGGAACCACCCTCACCCGGAA	31
66	AGCTCTTACCGAAGCCCAATA	21
67	CATTTGAGATAACCCACGAAACAATG	26
68	AATACCCCAACATTCATCAAAAATAATTCGCGTCT	35
69	ACGAGCGGCGCGGTCAGGCAAGGCGATTAAGTTGGGTAAAAC	42
70	TAAAACCGTTAAAGAGTCTGTCCATCCAGAAACCACACAATC	42
71	TATTACGAATAATAAACAAATCAGATATGCGT	32
72	GAAGGAGCGGAATTATCATCATATATCATTACATAGCACAA	42
73	CCTCGTCTTTCCACCACCGGAACCGCCTCCCTCA	34
74	AACAAGAGCCTAATGCAGAACGCGC	25
75	AGAAATCGTTAGACTACCTTTTTAAGGCGTTCTGACCTTTTTGCA	45
76	AGTTTATTGTCCATATAACAGTTGATTC	28
77	ATTTGGAAGTTTCATGCCTCAACATGTTTTA	31
78	GAGAACAATATACAAAATCGCGCAGAGGCGATTTCGACAAATCCTTTAAC	49
79	GTCGCGTGCCTTCGAATTGTCAAAG	25
80	GAACCGCCACCCTCCATATCATACC	25
81	CGCGCCGCCACCAGAACAGAGCCATAAAGGTGGAA	35
82	CAAAGCACTAGATAGCTCCATTCAGGCTGCGCAACTGTCTTG	42
83	GAGCCAAGCTTTGAATACCAAGTACGGATTACCTTTTCAA	42
84	GGCGAAGCACCGTAATAACGCCAGGGTTTTCCAGTCATGGG	42
85	TGAAAATCCGGTCAATAACCTAAATTTTAGCCTTT	35
86	TATTGAAAGGAATTGAGGTAG	21
87	GAGCATTTATCCTGAATCAAACGTGACTCCT	31
88	ATCGGTCAGATGATATTCACAAACCAAAGA	31
89	GTAAAACGACGGCCATCACCCAAATCAGCGC	32
90	GGCGCAGACGGTCAATCATCGAGACCTGCTCCATGTGGT	39
91	TTTTTGCGGATGCTCCTAAATGTTTAGATGAATTTTGCAAAGAAGTT	49
92	AAGGCCTGTTTAGTATCATGTTAGCTACCTC	31
93	CGAGGGTACTTTTTTCATGAACGGGGTCATAATGCCGAGCCACCACC	46
94	AGCTTTCAGAGGTGGCGATGGCCAGCGGGAAT	32
95	GGCAACACCAGGGTCTAATGAGTGAGCTCACAACAATAGGGT	42
96	ATCGATGCTGAGAGTCTACAAGGAGAGGGAAACGCCAAAAGGA	42
97	ACCAACAAACCAAATAACAATTTCAATTTGAATTACCGAGG	42

98	GCGAAAATCCCGTAAAAAAGCCGTGGTGCTCATACCGGCGTCCG	45
99	GAATTCGCTCGTCGCTGGGTCTGCAATCCATTGCAACACGG	42
100	CCTGCGCTGGGTGGCGAGAAAGGAAGGAAGGAGCGGGGCCG	42
101	CAAATTATTCATTTCAATTACCTGAGTA	28
102	AATTGTGTCGAAATCCGCGGCACACAACGGAGATTTGTATCA	42
103	TGCGTGTTCCAGGTTGTGTACATCG	24
104	AACCGTGTCATTGCAACGGTAATATATTTTAAATGAAAGGGT	42
105	TGGCTTTTACCGTAGAATGGAAAGCG	27
106	CGTACAGGCCCCCTAACCGTCCCCGGTACCGAGCGTTC	39
107	AAGAAAGCGCTGAACCTCAAATATTCTAAAGGAAAGCGTTCA	42
108	TTCATCGGCATTTTCGGTCATATCAAAA	28
109	CCTAATTTAACAACCCTCAATCAATATCTGATTGCGTAATC	42
110	AAACTCACAGGAACGGTACGCCAGTAAAGGGGGTGAGGAACC	42
111	AATTTCTTAAACCCGCTAATTGTATCGTTGCGGGCGATATA	42
112	GAGAAGGCATCTGCAATGGGATAGGTCAAAC	32
113	CCAATGTTTAAGTACGGTGTCCAAC	25
114	AAATCAGCTCATTTTTTAACCATTTTGTAAAATTCGCATTA	42
115	TTTACCAGTCCCAGCCTGCAGCCACTACGGGCGCACCAGCT	42
116	CTGAATATAGAACCAAATTATTTGCACGTAAAACAACGT	39
117	GTAATTAATTTAGAATCTGGGAAGGGCGATCGGTGCGGCAA	42
118	TAAAGCCTCCAGTACCTCATAGTTAGCG	28
119	AGGGAGCCGCCACGGGAACGGATAGGCGAAAGCATCAGCACTCTG	45
120	TGAGTGTTCCGAAAGCCCTTACCAGCCTAGGCGGTATTA	39
121	TTGGGCGGCTGATTTCCGGCAAAATCCCT	28
122	CCGACTTGTTGCTAAAATTTATTTAGTTCGCGAGAGTCGTCTTCCAGA	49
123	CCATAATGCCAGGCTATCAAGGCCGGAGACATCTA	35
124	TGACCGCGCCTTAATTTACAATATTTTGAATGGCTATCACA	42
125	ACTAAAGAGCAACGTGAAAATCTCCACCCACAACATAAAGGAA	42
126	TTTCCATGGCACCAACCTACGTCATACA	28
127	TTGCGAATAATTTTACAGCGGAGTGAGGTAATAATTTTGGAGG	42
128	ATAAAGTCTTTCCTTATCACT	21
129	AGGACAGATGAACGGTGAACATAAGGAACCGAAGAAT	39
130	CAAGCCGCCCAATAGCAAGTAAACAGCCATATTATTTTGCCATAAC	46
131	AACAACAGGAAGCACGTCCTTGCTGGTAATATCCAGAAACGC	42
132	ACAACGCCTGTAGCATTTACCGTATAGGAAG	31
133	CCGTGTGATAAATAACCTCCGGCTGATG	28
134	AGAATTTTAGAGGAAAACAATATTACCGCCAGCTGCTCATTT	42
135	AGAACTTAGCCTAATTATCCCAAGCCCCCTTATTAGCGTTTGCCA	45
136	CATCGAGATAACGTCAAACATAAAAAGAGCAAAAAGAATT	38
137	TTACCATTAGCAAGGCCTTGAATTAGAGCCAGCCCGACTTGAGC	44

138	GACAATTACGCAGAGGCATTTTCGAG	26
139	AATATTCATTGAATCCATGCTGGATAGCGTCCAAT	35
140	TTAACTCGGAATTAGAGTAAATCAATATATGTGAGTGATTCT	42
141	CGTGTCAAATCACCATCTAGGTAATAGATTT	31
142	TATCAGCAACCGCAAGAATGCCAATGAGCCTGAGGATCTATC	42
143	GGGATATTGACGTAGCAATAGCTAAGATAGC	31
144	TAAGTTTACACTGAGTTTCGT	21
145	ATTGCGTTGCTGTTATCCGCTCACAAATCCAACTCACTTGC GTA	45
146	GCTGGCATAGCCACATTATTC	21
147	CGTACTATGGTAACCACTAGTCTTTAATGCGCGAACTGAATC	42
148	ACGGGCCGATAATCCTGAGAAGTGTTTTATGGAGCTAACCG	42
149	CAAACGGAATAGGAAACCGAGGAATAAGAAATTACAAG	38
150	TCACAGCGTACTCCGTGGTGAAGGGATAGCTAAGAGACGAGG	42
151	TAACATCCAATAAATGCAAAGGTGGCATCAACATTATGAAAG	42
152	CAGCAGCGCCGCTTGTATCAGCTTCACGAAAAA	35
153	TAGCCCGGAATAGGTGAAGGATAAGTGCCGTCGA	35
154	AAATGCGGAAACATCGGTTTTCAGGTTAACGTCAGATTAAC	42
155	ATTTCAACCAAAAATTTCTACTAATAGTTAGTTTCATTTGGGGCGC GAGC	49
156	TGCTGATTGCCGTTGTCATAAACATCGGGCGG	32
157	GGCTAAAACCTCAGAAAAGTTTTGCGGGAGATAGAACC	38
158	GAGTCTGGATTTGTTATAATTACTACATACACCAC	35
159	ATTGTTATCTGAGAAGAAACCAGGCAAAGCGCCATTCGTAGA	42
160	CGGAATAGAAAGGAATGCCTTGCTAAACAACTTTCAAC	38
161	CTAGTCAGTTGGCAAATCAACAGTCTTTAGGTAGATAACAAA	42
162	AGTCGCCTGATACTTGATAACAGAATACGTGGCACAGCTGA	42
163	CACGGCAACAATCCTGATATACTT	24
164	CCTCATACCCCAGCAGGCCTCTTCGCTATTACGCCAGTGCC	42
165	TGAGCAAATTTATACAGGAATAACATCACTTGCCTGAGTCTT	42
166	AATAGAAAAAATAAACGTCTGAGAGGAATATAAGAGCAACACTATGAT	49
167	ATTACGAGATAAATGCCAGCTTTGAGGGGACGACGACAG	39
168	GCTGGTCTGGTCAGGAGCCGGAATCCGCCGTGAACAGTGCCA	42
169	CTTGTAGAACGTCAGCGGCTGATTGCAGAGTTTTTCGACGTT	42
170	ACATAAAGCCCTTACACTGGTCGGGTTAAATTTGT	35
171	TGCCATCCCACGCAGGCAGTTCTCATTGCCGTTTTAAACGA	42
172	GCCAGCAGTTGGGCGCAAATCAGGTTTCTGCCCTGCGTGGT	42
173	TACGGCTGGAGGTGCGCACTCGTCACTGTTTGTCCC GGCAA	42
174	GAGAGATAGACTTTACGGCATCAGA	25
175	AGAGAAAATCCTGTTTGA	18
176	AGACAGCAGAAACGAAAGAGGAAATAAATCGAGGTGACAGTTAAAT	46
177	AATATGCAACTACCATCATAGACCGGAACCGC	32

178	GCGAAACAAAGTGTAACACATGGCCCTCGATTGAACCA	39
179	TTGGTAGAACATTTAATTAAGCAAC	25
180	ACCAGACCGGATTAATTCGAGC	22
181	CTGTATGGGATTACCGTTAGTATCA	25

Table S2: Staple strands labelled with a green dye. ATTO 542-labelled oligonucleotides were purchased from biomers.net GmbH and Abberior STAR 520SXP-labelled oligonucleotides from IBA GmbH.

DNA Pillar Design	Sequence (5' to 3' end)	Instead of
For FQH Zika Optical Nanoantenna	AGACAGCAGAAACGAAAGAGGAAATAAATCGAGGTGACAGTTAAAT(ATTO542)	176
For FQH II Optical Nanoantenna	TTGGTAGAACATTTAATTAAGCAAC(Abberior STAR 520SXP)	179
	CCGTGTGATAAATAACCTCCGGCTGATGT(Abberior STAR 520SXP)	180
	CTGTATGGGATTACCGTTAGTATCA(Abberior STAR 520SXP)	181

Table S3: Staple strands for the attachment of silver NPs to the DNA origami pillar. These oligonucleotides were purchased from Eurofins Genomics GmbH.

Sequence (5' to 3' end)	Length [nt]
TGCATTAATGAGCGGTCCACGCTCACTGCGCCACGTGCCAGC(A) ₂₀	62
AGCGCAGCTCCAACCGTAATCATGGTCACGGGAAACCT(A) ₂₀	58
GCGTCCACTATTCCTGTGTGAAATGCTCACTGCC(A) ₂₀	54
TGGTGGTTGTTCCAGTTTGGAAACA(A) ₂₀	44
GGATGTGGTTTGCCCCAGCAG(A) ₂₀	41
CGCTTCCAGTTAGCTGTTAAAGAACGT(A) ₂₀	49

Table S4: Staple strands modified with biotin for the DNA origami immobilization on a BSA-biotin/neutravidin surface. These oligonucleotides were purchased from Eurofins Genomics GmbH.

Sequence (5' to 3' end)	Length [nt]
Biotin-ATTAGCGGGGTTTTGCTCAGTACCAGGCTGACAACAAGCTG	41
Biotin- TGCCCGTATAAACAGTGTGCCCTTCTGGTAA	30
Biotin-AGAAAACGAGAATGACCATAAATCTACGCCCTCAAATGCTTTA	44
Biotin-ATAACTATATGTAAATGCTTAGGATATAAT	30
Biotin-AGGAATCATTACCGCGTTTTTATAAGTACC	30
Biotin-GATTAGAGAGTACCTTAACTCCAACAGG	28
Biotin-CCTTAAATCAAGATTAGCGGGAGGCTCAAC	30
Biotin-GCATGTAGAAACCAATCCATCCTAGTCCTG	30

Table S5: Sequences of fluorescence-quenching hairpins and respective target DNA/RNA. Oligonucleotides purchased from biomers.net GmbH are indicated with ^a and from Eurofins Genomics GmbH with ^b.

	Sequence
FQH Zika ^a	TGCAGCAAATCGGCCAACGCGCGGGGAGGGCCCTGAGAGAGTT(ATTO647N)TTC TGGCTGGATGCTCTTCCCAGCCAGAAA(BBQ650)
Target DNA FQH Zika ^b	ACCGGGAAGAGCATCCAGCCAGA
Mis1 Target FQH Zika ^b	ACCGGGAAGAGCAACCAGCCAGA
Mis2 Target FQH Zika ^b	ACCGGGAAGAGCAAGCAGCCAGA
Mis3 Target FQH Zika ^b	ACCGGGAAGAGCAAGGAGCCAGA
Target RNA FQH Zika ^b	ACCGGGAAGAGCAUCCAGCCAGA
FQH II ^a	TGCAGCAAATCGGCCAACGCGCGGGGAGGGCCCTGAGAGAGT(ATTO647N)TTGT TGTGTTGTTGGGGGGGGGGGGGGGCAACAACAACAA(BBQ650)
Target DNA FQH II ^b	GTTGTTGTTGTTGTTGGGGGGGGGGGGGGAACAACAACAAC

Folding Program for the DNA Origami Pillar

Table S6: Temperature and retention time for the folding of the DNA origami pillar.

Temperature [°C]	Time [s]	Temperature [°C]	Time [s]
65	120	44	4500
64	180	43	3600
63	180	42	2700
62	180	41	1800
61	180	39	1800
60	900	38	900
59	900	37	480
58	1800	36	480
57	2700	35	480
56	3600	34	480
55	4500	33	480
54	5400	32	480
53	5400	31	480
52	5400	30	480
51	5400	29	120
50	5400	28	120
49	5400	27	120
48	5400	26	120
47	5400	25	120
46	5400	20	∞
45	5400		

AFM image of the DNA Origami

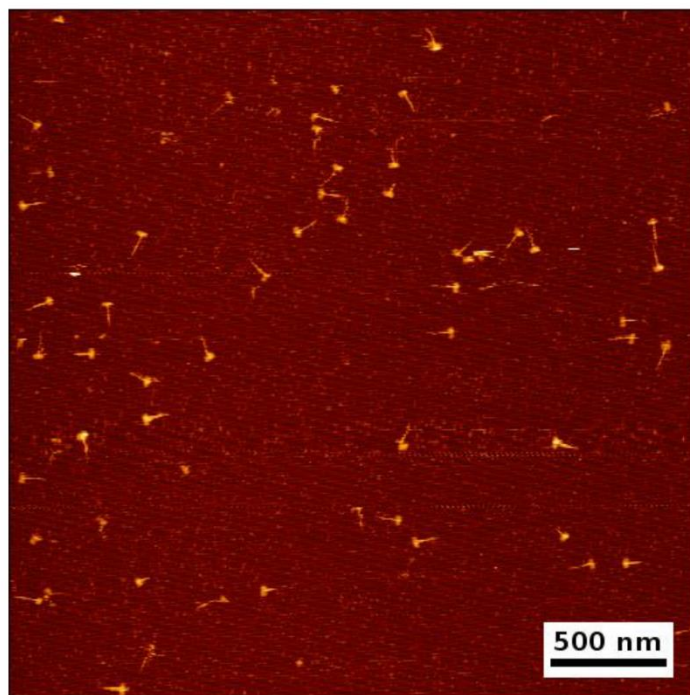


Figure S4: AFM image of the DNA origami pillar.

References

- (1) Acuna, G. P.; Moller, F. M.; Holzmeister, P.; Beater, S.; Lalkens, B.; Tinnefeld, P. *Science* **2012**, *338*, 506–510.
- (2) Vietz, C.; Kaminska, I.; Paz, M. S.; Tinnefeld, P.; Acuna, G. P. *ACS Nano* **2017**, *11*, 4969–4975.
- (3) Mirkin, C.A.; Letsinger, R.L.; Mucic, R.C.; Storhoff, J.J. *Nature* **1996**, *382*, 607–609.

7.2 Associated publication P2

DNA Origami Voltage Sensors for Transmembrane Potentials with Single-Molecule Sensitivity

by

Sarah E. Ochmann, Himanshu Joshi, Ece Büber, Henri G. Franquelim, Pierre Stegemann, Barbara Saccà, Ulrich F. Keyser, Aleksei Aksimentiev, Philip Tinnefeld

Reprinted with permission from

Nano Letters, 21 (20), 8634-8641 (2021)

Copyright 2022 American Chemical Society

DNA Origami Voltage Sensors for Transmembrane Potentials with Single-Molecule Sensitivity

Sarah E. Ochmann, Himanshu Joshi, Ece Büber, Henri G. Franquelim, Pierre Stegemann, Barbara Saccà, Ulrich F. Keyser, Aleksei Aksimentiev, and Philip Tinnefeld*

Cite This: *Nano Lett.* 2021, 21, 8634–8641

Read Online

ACCESS |

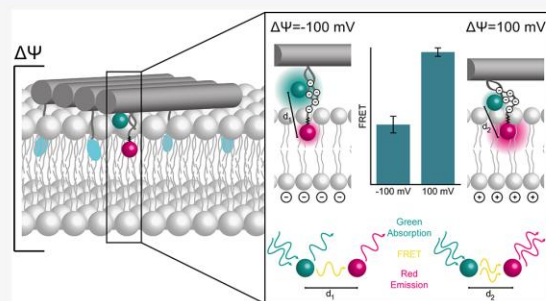
Metrics & More

Article Recommendations

Supporting Information

ABSTRACT: Signal transmission in neurons goes along with changes in the transmembrane potential. To report them, different approaches, including optical voltage-sensing dyes and genetically encoded voltage indicators, have evolved. Here, we present a DNA nanotechnology-based system and demonstrated its functionality on liposomes. Using DNA origami, we incorporated and optimized different properties such as membrane targeting and voltage sensing modularly. As a sensing unit, we used a hydrophobic red dye anchored to the membrane and an anionic green dye at the DNA to connect the nanostructure and the membrane dye anchor. Voltage-induced displacement of the anionic donor unit was read out by fluorescence resonance energy transfer (FRET) changes of single sensors attached to liposomes. A FRET change of $\sim 5\%$ for $\Delta\Psi = 100$ mV was observed. The working mechanism of the sensor was rationalized by molecular dynamics simulations. Our approach holds potential for an application as nongenetically encoded membrane sensors.

KEYWORDS: DNA origami, voltage sensor, single-molecule FRET, transmembrane potential, voltage imaging, molecular dynamic simulations



INTRODUCTION

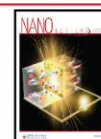
On the cellular level, the electrical transmembrane potential $\Delta\Psi$ is a key parameter in neuroscience. The introduction of fluorescence-based voltage sensors was a milestone toward a broader application and noninvasive visualization in contrast to electrophysiological approaches that are invasive, serial, and time-consuming.¹ Many challenges with respect to signal, contrast, and response time have been addressed with genetically encoded voltage indicators (GEVIs)^{2–4} that offer targetability to cell membranes. For improved contrast and imaging durations, hybrid approaches combining GEVIs with organic fluorophores have been introduced.^{5,6} These approaches, however, require transfected cell lines or transgenic animals.

In contrast, conventional voltage-sensing dyes face the challenge that all functionalities, including targeting membranes and sensing and transducing a signal, have to be encoded in simple, chemically accessible structures. The development of a first generation of sensors yielded low-contrast Stark-effect voltage-sensing dyes and probes that disturbed cellular functions.⁷ A higher contrast was achieved with sensors based on fluorescence energy transfer (FRET), which consisted of one component in the membrane core changing position according to the voltage and a second component on the membrane surface.^{8,9} However, as the

components were not chemically linked, high probe concentrations had to be used, leading to capacitive loading.¹⁰ Therefore, in recent approaches the complexity of sensors has been increased, including bottom-up nanotechnological ideas, to develop quantum-confined semiconductor nanoparticles or quantum dot–fullerene bioconjugates for voltage sensing.^{11–13} Recently, DNA was used as a scaffolding material to combine electron-transfer-based voltage-sensing dyes^{7,14,15} with targeting and intensity referencing for voltage sensing in organelles.¹⁶

In this paper, we used DNA origami to modularly address different challenges of voltage sensor design and demonstrate an alternative voltage-sensing strategy that allows sensing with bright dyes compatible with single-molecule imaging. DNA origami and similar self-assembly techniques offer the potential to meet broad demands such as targeting lipid membranes, incorporating a sensing unit, optionally providing a transduction mechanism with internal referencing, and being biocompatible and minimally invasive.

Received: July 2, 2021
Revised: October 8, 2021
Published: October 18, 2021



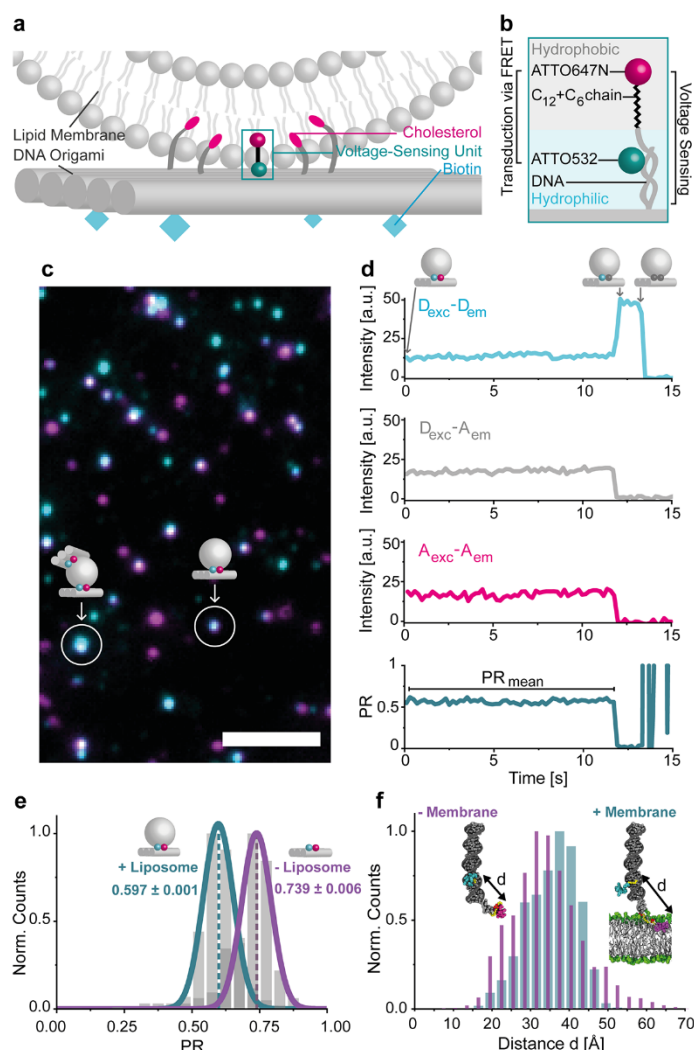


Figure 1. (a) DNA origami sensor of transmembrane potentials. A rectangular DNA origami plate was decorated with cholesterol to bind a liposome and with biotins to attach to the neutravidin-functionalized surface of a microscope's coverslip. The voltage-sensing unit was positioned in the center of the DNA origami. (b) Voltage-sensing unit consisting of dsDNA protruding from the DNA origami plate and carrying an ATTO532 dye and a complementary strand with an ATTO647N dye connected via a C₁₂+C₆ linker (see Figure S2 for the chemical structure). The transduction of the voltage signal to fluorescence was fulfilled by FRET from the donor ATTO532 to the acceptor ATTO647N. (c) Superimposed TIRF image of the donor (blue) and acceptor (pink) fluorescence from the DNA origami sensor. White spots indicate DNA origami plates with both donor and acceptor dyes. The scale bar refers to 5 μm. (d) Single-molecule FRET transient. The fluorescence intensity over time is shown for the donor excitation–donor emission D_{exc}–D_{em} channel (light blue), the donor excitation–acceptor emission D_{exc}–A_{em} channel (gray), and the acceptor excitation–acceptor emission A_{exc}–A_{em} channel (pink). From the D_{exc}–D_{em} and the D_{exc}–A_{em} channels, the proximity ratio (PR) and the PR_{mean} are determined (dark blue). (e) PR distributions for DNA origami constructs with (cyan) and without (purple) the liposome attachment. The error refers to the standard error of the mean. For each sample, N_{molecule} ≥ 100. (f) Histogram of interdyde distances obtained from MD simulations of a dsDNA duplex decorated with the two dyes positioned at the lipid–water interface (cyan) and in an aqueous solution (purple). Simulation times are as follows: –Membrane, 1.35 μs and +Membrane, 1.55 μs.

In the DNA origami method, a long single-stranded DNA molecule (ssDNA, > 7000 nucleotides long) is folded into a desired shape by hybridization with short oligonucleotides, producing billions of identical nanostructures.^{17–19} This bottom-up nanoassembly method offers the ability to place any chemical moiety on the nanostructure like on a molecular breadboard by the integration of modified oligonucleotides.

Using the DNA origami technique, a variety of sensors have been realized,²⁰ from nanopores^{21–23} to drug delivery systems^{24,25} to force sensors.^{26,27} By capturing DNA origami on nanocapillary tips, Hemmig and Fitzgerald et al. demonstrated the feasibility of using a DNA origami construct as a single-molecule voltage sensor.²⁸ Two fluorophores capable of interacting via FRET are placed on a DNA

nanostructure such that, when subject to a voltage bias at the tip of a nanopipet, the FRET efficiency is modulated by the voltage magnitude.

Here, we demonstrate the single-molecule transmembrane voltage read-out from the surface of a lipid membrane. Using a rectangular DNA origami to arrange the different components needed, we created a sensor that optically reads out defined potentials via FRET with a change of $\sim 5\%$ for $\Delta\Psi = 100$ mV. FRET offers an advantageous ratiometric signal read-out and is therefore signal intensity independent. We detected single FRET pairs by spacing out origami structures beyond the diffraction limit and hence provide a pathway for imaging at the nanoscale beyond ensemble averages. When a sensor can be detected at the level of single molecules, minimal invasiveness and optical superresolution can be achieved in combination with single-molecule localization-related imaging schemes.^{29,30} We rationalized the functioning of the sensor through molecular dynamics (MD) simulations of the DNA–lipid membrane assembly. Further, we demonstrate the potential of DNA nanotechnology for voltage sensing by introducing small molecular changes in the sensing unit to shift the sensitivity of the sensor toward a negative $\Delta\Psi$.

RESULTS

The transmembrane voltage sensor was based on a rectangular DNA origami with dimensions of 70×100 nm^{17,31,32} that functions as a platform to program all the functionalities required into a small entity. To bind to liposomes, the nanostructure was equipped with ten cholesterol moieties; to bind to biotinylated PLL-e-PEG passivated surfaces, additional six biotin moieties were incorporated (Figures 1a and S1 and Table S1). Surface binding of the liposomes via the DNA origami facilitated imaging by total internal reflection microscopy (TIRF) while avoiding direct surface interactions of the liposomes.³³ The voltage-sensing unit was placed centrally on the platform protruding from the structure. The hydrophobic and cationic dye ATTO647N connected to DNA by a C₁₂–phosphate–C₆ chain (C₁₂+C₆) was expected to anchor the sensor unit in the lipid membrane (see Figures 1b and S2 for molecular structures). Insertion into the lipid core of the membrane was previously observed for ATTO647N.³⁴ The DNA connection from ATTO647N to the DNA origami platform contained the anionic fluorophore ATTO532. We reasoned that any change of the potential should have opposite effects on the average positions of the cationic ATTO647N dye and the anionic ATTO532 dye on the anionic DNA linker. The opposite forces on the two dyes should translate $\Delta\Psi$ into a change of the FRET that can be read out optically on the level of single molecules.

For imaging, we performed single-molecule FRET (smFRET) experiments³⁵ of the optical potential sensor on a home-built TIRF microscope with green–red alternating laser excitation (ALEX, for details see the SI).^{36,37} We acquired videos to follow the fluorescence over time and verify that single DNA origamis were observed. Figure 1c presents a superimposed TIRF image with donor dyes in blue, acceptor dyes in pink, and an overlay of the two in white. Some of the spots are brighter than others, which is caused by multiple DNA origamis being bound to a single liposome or origami multimers. To eliminate such aggregates in further analysis, we generated intensity-time transients from the videos for each spot with the software iSMS³⁸ and inspected them visually. An exemplary transient is shown in Figure 1d with D_{exc}–D_{em} (light

blue), D_{exc}–A_{em} (gray), and A_{exc}–A_{em} (pink), where the subscript indicates the excitation and emission channels of the donor (D) and acceptor (A), respectively. A correlated intensity increase in D_{exc}–D_{em} upon an intensity decrease in D_{exc}–A_{em} and A_{exc}–A_{em} and the rapid photobleaching in D_{exc}–D_{em} are clear indications that a single DNA origami indeed was observed. From the intensities I_{DD} of the D_{exc}–D_{em} channel and the intensity I_{DA} of the D_{exc}–A_{em} channel, FRET was quantified as the proximity ratio (PR), where

$$\text{PR} = \frac{I_{DA}}{I_{DD} + I_{DA}} \quad (1)$$

The PR_{mean} was calculated over the whole period of the energy transfer (bottom transient in Figure 1d), yielding one data point for each voltage sensor. All single-molecule transients were carefully reviewed, and the ones showing a clear correlation between the three channels mentioned above were picked while transients showing multichromophore behavior were rejected. An exemplary selection of transients is shown in Figures S3 and S4.

We first tested whether an interaction between the voltage sensor and the lipid membrane as intended is detected. To this end, we studied the DNA origamis with and without 100 nm DOPC liposomes by mixing the origami structures with an excess of liposomes and immobilizing the complexes on a surface. After performing smFRET measurements, we obtained PR distributions, as shown in Figure 1e. The liposome-free sample yielded a mean PR of 0.739 ± 0.006 (standard error of the mean, SEM) that was obtained from a Gaussian fitting of the distribution, which decreased to 0.597 ± 0.001 for the liposome-containing sample (Figure 1e). The fact that we obtained narrow homogeneous populations that were clearly shifted with respect to each other indicates quantitative binding of DNA origami voltage sensors to the liposomes. In addition, the decrease of the FRET supports the idea that the hydrophobic ATTO647N is diving into the membrane core so that the average distance of donor and acceptor is substantially increased upon membrane binding.

We further rationalized the idea of the FRET-acceptor anchoring in the membrane by MD simulations of the voltage-sensing unit with and without a lipid membrane present. Figure 1f and Movie S1, provided in the SI, revealed a coiling of ATTO647N with the alkyl chain, resulting in a close proximity of the dyes. This secondary structure was broken in the presence of a lipid membrane (Movie S2) as ATTO647N and the alkyl chain insert to and remain in the hydrophobic core of the membrane. Figure 1f shows the distributions for the interdy distances for both samples that were determined from the MD simulations. The observed shift toward larger distances for the sensor in the presence of a membrane is in good agreement with the experimental results (Figure 1e) and suggests that the lower PR upon liposome addition is a result of the spatial separation of the two dyes. According to Figure S6, the dyes did not show a preferred orientation to each other so that an angular effect on the PR is unlikely. Another interesting observation from the simulations is that the ATTO647N dye remained embedded closest to the membrane and interacted with the phosphate moieties of the lipid head groups (likely because of its positive charge), while the main body of the dye resided inside the hydrophobic core of the membrane.

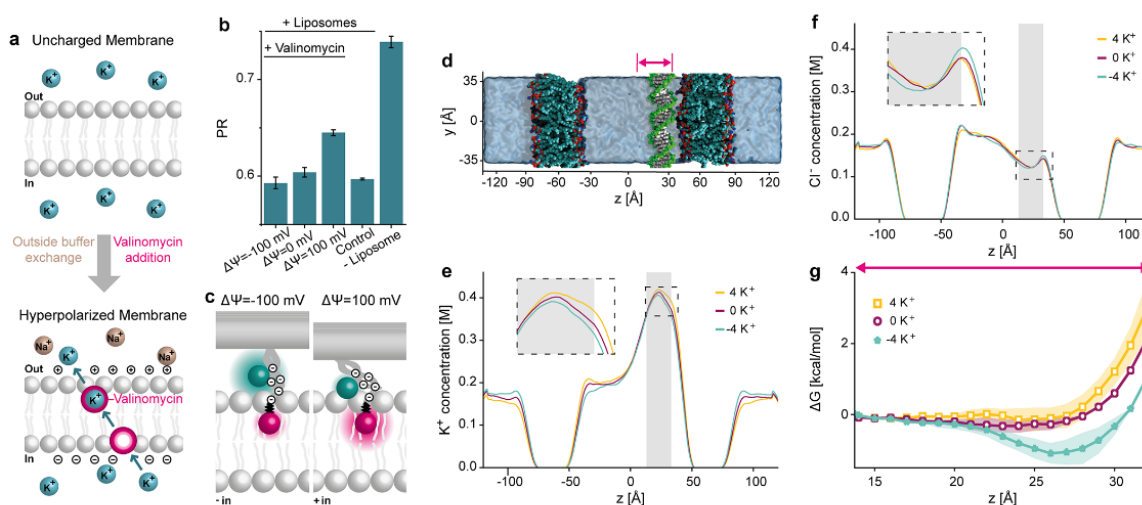


Figure 2. (a) Creation of electrical transmembrane potentials $\Delta\Psi$. By exchanging the outside buffer, a potassium ion gradient across the lipid membrane was built up. Equilibration of the potassium gradient by the ionophore valinomycin converted the chemical potential to an electrical transmembrane potential $\Delta\Psi$. (b) Mean PR and standard errors of the mean derived from Gaussian fits to the distributions (Figures S8 and S9) of the DNA origami–liposome complexes with different $\Delta\Psi$ values in comparison to control samples presented in Figure 1e. For each sample, $N_{\text{molecule}} \geq 100$. (c) Proposed working principle of the voltage-sensing DNA origami. The ATTO647N remains as an anchor in the membrane’s hydrophobic core, whereas the surrounding DNA with its anionic nature is attracted toward the membrane by the K^+ excess inside of the liposome, resulting in a shorter interdye distance and increased FRET. (d) Representative configuration of a simulated double membrane system, where two membrane patches separated two compartments filled with a 150 mM KCl solution. A single dsDNA molecule was placed near one membrane to characterize effective interactions between the DNA and the membrane. A gradient of the K^+ concentration was established by transferring four K^+ ions from one compartment to the other, corresponding to a drop of $\Delta\Psi = \pm 1.3$ V. The local concentrations of (e) K^+ and (f) Cl^- ions along the lipid bilayer are shown for the three ion gradient conditions. The z -axis is defined in panel d. The profiles were averaged over 21 replica windows of the respective REUS MD simulations, each replica simulation being 120 ns long. The shaded region shows the location of the center of DNA in various windows. (g) Free energy ΔG of the 21 base pair dsDNA as a function of its z -coordinate for the three ion gradient conditions. The arrow implies the region shown in panel d.

To test the performance of our voltage-sensing DNA origami, we used ion exchange by the ionophore valinomycin³⁹ to create a well-defined change of $\Delta\Psi$ across the liposome membrane. In a typical experiment, the origami–liposome complexes were imaged, the buffer surrounding was exchanged to introduce a potassium gradient across the lipid membrane, and valinomycin was added before the sample is imaged again (Figure 2a). Valinomycin specifically complexes potassium ions but not sodium ions and shuttles them across the lipid membrane until an equilibrium is reached and a polarized membrane results, following the Nernst equation

$$\Delta\Psi = \frac{RT}{Fz} \ln \left(\frac{c_{\text{in}}^{\text{K}^+}}{c_{\text{out}}^{\text{K}^+}} \right) \quad (2)$$

where R is the gas constant, T is the temperature, F is the Faraday constant, z is the charge number, and $c_{\text{in}}^{\text{K}^+}$ and $c_{\text{out}}^{\text{K}^+}$ are the potassium concentrations inside and outside the liposome, respectively. By adjusting the initial K^+ concentration gradient, we produced a well-defined transmembrane potential (Table S2). Figure S7 confirms the functionality of our assay in bulk experiments using a commercially available voltage-sensing dye.

First, we were interested in three scenarios: a hyperpolarized membrane, a neutral membrane, and a depolarized membrane with respect to the inner leaflet. We chose the hyperpolarization to be $\Delta\Psi = -100$ mV and the depolarization to be $\Delta\Psi = 100$ mV, for which the buffer outside was exchanged

with respect to the desired $\Delta\Psi$ and valinomycin was added before imaging. Single Gaussian distributions were obtained for all the samples, and mean PR values of 0.593 ± 0.006 for $\Delta\Psi = -100$ mV, 0.604 ± 0.005 for $\Delta\Psi = 0$ mV, and 0.645 ± 0.003 for $\Delta\Psi = 100$ mV were determined (Figures 2b and S8). When compared to that of the liposome-free sample, all the PR values are lower, which in combination with the mono-Gaussian nature of the distributions strongly suggests that the liposomes stayed intact throughout the experimental procedure. As the $\Delta\Psi = 0$ mV sample shows an almost identical PR histogram as the control sample before the valinomycin addition, we are confident that all observed changes in the single-molecule fluorescence result from the $\Delta\Psi$ created and are not from interference with the ionophore (Figures 2b and S9). In contrast, there is a notable increase in the PR for the depolarized membrane compared to those for the hyperpolarized and neutral membranes, which implies that the DNA origami-based sensor is able to report transmembrane potentials on the single-molecule level.

The direction of the FRET change suggests that a more positive charge on the inside would attract the anionic donor dye–DNA hybrid toward the membrane so that FRET would increase (see Figure 2c). An alternative mechanism, where the change of the ion concentration outside the membranes modulates the electrostatic force acting on the dye embedded in the lipid membrane, was ruled out through a set of MD simulations that examined the distribution of the electrostatic potential in a double-membrane system (Figure S10 and

S11). It has been previously established that the electric potential of the membrane's interior is approximately 500 mV higher than the electric potential of the surrounding electrolyte.^{40,41} A slight imbalance of ion concentration, i.e., a transfer of just one ion between the compartments of our simulated double-membrane system as shown in Figure S10, produced the expected voltage difference between the electrolyte compartments. However, the gradient of the electrostatic potential across the leaflets of the lipid bilayers remained largely unaffected by the ion concentration gradient as most of the additional potential drop occurs at the interface of the lipid head groups and the electrolyte, which is why we ruled out a movement of the membrane-anchored ATTO647N.

To directly probe the effect of an ion concentration gradient on the interaction between DNA and a lipid membrane, we simulated another double-membrane system (Figure 2d) where one DNA molecule was placed near the surface of one of the membranes parallel to the membrane surface. In addition to the system containing two charge-neutral electrolyte compartments (0 K⁺), two variants of the system were created by moving four K⁺ either to (4 K⁺) or from (−4 K⁺) the compartment containing the DNA, which corresponded to $\Delta\Psi = 0$, $\Delta\Psi = +1.3$, and $\Delta\Psi = -1.3$ V, respectively (Figure S11). Such higher than experimental bias conditions were chosen to increase the effective force on the dsDNA, facilitating convergence of the free-energy calculations (described below). Replica exchange umbrella sampling (REUS) simulations⁴² were performed for each system using 21 sampling windows (in 1 Å increments) for the distance between the centers of mass of the dsDNA and the nearby membrane along the z-axis. The resulting ion gradient produced the expected $\Delta\Psi$ across the compartments (Figure S11). Further, the local concentrations of K⁺ (Figure 2e) and Cl[−] (Figure 2f) ions show a nontrivial behavior. In the profiles for all three samples, it is clearly visible that the K⁺ concentration was higher close to the DNA while the Cl[−] concentration was lower, which is due to the electrostatic attraction and repulsion to the anionic DNA backbone, respectively. In the case of an excess of K⁺ ions inside (4 K⁺), the K⁺ concentration was also higher close to the inner leaflets. Interestingly, the concentration at the respective outer leaflets was lower, indicating a capacitive effect. The opposite behavior was observed for the lack of K⁺ ions inside (−4 K⁺). A complementary effect was observed for the Cl[−] concentration (Figure 2f).

Further analysis of the REUS simulations yields the free energy of the dsDNA as a function of its proximity to the lipid membrane (Figure 2g). In the absence of a K⁺ gradient, the free energy has a shallow minimum near the membrane surface, which is in agreement with our previous calculations.⁴³ Moving the positive charge across the membrane from the compartment housing (−4 K⁺ trace) produced a free-energy minimum near the membrane surface, promoting DNA attraction to the membrane surface. Moving the positive charge into the DNA compartment (4 K⁺ trace) slightly increased the repulsive interaction between DNA and the lipid membrane. These simulation results are in a qualitative agreement with our observation of a FRET increase for depolarized membranes and support the mechanism shown in Figure 2c.

Next, we studied the sensitivity of our voltage sensor in more detail and varied the potentials from $\Delta\Psi = -125$ mV to $\Delta\Psi = 125$ mV in steps of 25 mV. For each sample, the mean

PR before creating $\Delta\Psi$ was approximately the same (Figure S12). We therefore merged all reference data and defined it as the mean of the control sample PR_{before}. This value was subtracted from the PR after $\Delta\Psi$ was built up (Figure S8) as

$$\Delta\text{PR} = \text{PR} - \text{PR}_{\text{before}} \quad (3)$$

to yield the change ΔPR . The respective SEM was derived after Gaussian error propagation (see the SI), and the data are presented in Figure 3. In accordance with the results discussed

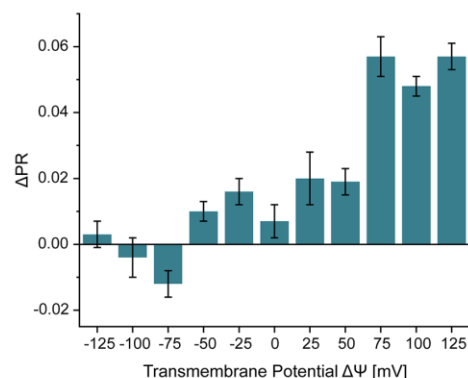


Figure 3. Changes ΔPR of the voltage sensor exposed to liposomes with different electrical transmembrane potentials $\Delta\Psi$. ΔPR was calculated by subtracting the mean PR before the potentials $\Delta\Psi$ were created from the respective PR of the sample, as indicated. The error bars represent the standard error of the mean after Gaussian error propagation. For each sample, $N_{\text{molecule}} = 100$.

above, the PR value only slightly increased up to $\Delta\Psi = 50$ mV and increased strongly in the range from 50 to 100 mV. The voltage sensor is thus able to transduce small changes in $\Delta\Psi$ to single-molecule fluorescence signals. The nonlinear response might indicate that the sensing unit above the membrane did not progressively shift in the changing $\Delta\Psi$ but that more specific conformational changes or displacements of the dyes occurred.

As our proposed mechanism strongly relies on the relative positioning of the donor dye with respect to the acceptor dye, we checked the sensitivity of the system for small changes of the linker. We therefore changed the voltage-sensing unit minimally by shortening the carbon chain from a C₁₂+C₆ to a C₁₂ chain, also eliminating the additional phosphate group (Figure 4a, for details see Figure S2). Interestingly, in the absence of the liposomes the PR was only minimally higher for the shorter linker (PR = 0.754 instead of 0.739). Upon binding to the liposome, however, the PR did only slightly decrease to PR = 0.732 for the shorter linker, indicating that stretching of the hydrophobic linker is mainly responsible for the FRET reduction in case of the C₁₂+C₆ linker (Figures S13 and S14). Varying the transmembrane potential of the liposomes exposed to the DNA origami voltage sensor with the shortened linker had an interesting effect on the measured PR values. Most of the signal change now occurred in the more physiologically relevant range between −100 and 0 mV, whereas only a small PR increase was detected for positive $\Delta\Psi$ (Figures 4b, S14, and S15). The direction of change is compatible with the idea that the FRET reduction is not a linear displacement in the $\Delta\Psi$ but instead is related to a more specific conformational change. As the DNA and the negatively charged dye are pulled

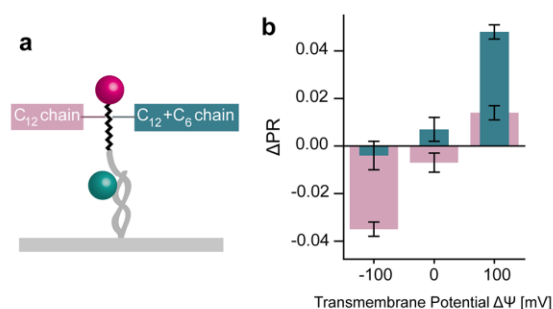


Figure 4. (a) Voltage sensing unit with a C₁₂ chain (pink) and a C₁₂+C₆ chain (blue). (b) ΔPR changes of the sensor with a C₁₂ chain (pink) in the voltage-sensing unit illustrated in panel a exposed to liposomes with ΔΨ = -100, 0, and 100 mV compared to the voltage-sensing unit with a C₁₂+C₆ chain (blue). ΔPR was estimated by subtracting the mean PR before of the potentials were created from the respective PR of the sample, as indicated. The error bars represent the standard error of the mean after Gaussian error propagation. For each sample, $N_{\text{molecule}} \geq 91$ for each sample.

toward the membrane by the shorter linker, a more negative potential is required to displace them from the membrane so that the FRET reduction occurs. To prove that the sensing mechanism is reversible, we performed an experiment in which the potential was destroyed by ion channels in the membrane. The data in Figures S16 and S17 show a recovery of the PR signal.

CONCLUSION

Transmembrane potentials are key parameters to understand cellular functions and interactions, and there is a great need for the development of smart sensing systems. We here present a DNA origami voltage sensor offering a robust platform to include many functionalities, such as surface immobilization and liposome binding. DNA origami applications in live-cell experiments have been established, and DNA origami stabilization strategies^{44–46} such as those against nucleases exist that could be tested for their compatibility with the sensor functionality. The DNA origami nanotech platform could then be extended by further smart functionalities, including specific cell or organelle recognition or for immune system camouflage.^{44,47,48}

We also introduced a new sensing unit that is based on FRET between a hydrophobic dye that preferred a location in the hydrophobic membrane core and a hydrophilic and anionic dye–DNA moiety that reacted with a PR change of ~5% for ΔΨ = 100 mV. The DNA origami voltage sensors were studied by single-molecule spectroscopy on liposomes, and the results were rationalized by MD simulations. While the fundamental working principle is implied by the experimental results, the MD simulations provide evidence that more specific interactions between the membrane and the sensing unit determine the sensitive voltage range that could be tuned by the adaptation of the linker between donor and acceptor. Overall, our data show profound potential for this novel approach for ΔΨ sensors that could similarly be adapted for other sorts of sensors.

ASSOCIATED CONTENT

Supporting Information

The Supporting Information is available free of charge at <https://pubs.acs.org/doi/10.1021/acs.nanolett.1c02584>.

Materials and methods, illustration of the DNA origami design, DNA oligonucleotides used as staple strands, detailed sketch of the voltage-sensor designs, exemplary fluorescence transients, equilibrium MD simulation of dye-conjugated dsDNA in aqueous and membrane-anchored environments, angle distributions, concentration of KCl and NaCl in the buffer inside and outside of the LUVs, valinomycin bulk test, PR distributions, voltage bias, average electrostatic profiles, reversibility experiment for the C₁₂ sensor, and captions to the supplementary movies (PDF)

All-atom MD simulation of dyes on dsDNA (MP4)

All-atom MD simulation of dyes on dsDNA with a lipid membrane (MP4)

mrDNA simulation of the DNA origami (MP4)

AUTHOR INFORMATION

Corresponding Author

Philip Tinnefeld – Department of Chemistry and Center for NanoScience, Ludwig-Maximilians-Universität München, 81377 München, Germany; orcid.org/0000-0003-4290-7770; Email: philip.tinnefeld@cup.uni-muenchen.de

Authors

Sarah E. Ochmann – Department of Chemistry and Center for NanoScience, Ludwig-Maximilians-Universität München, 81377 München, Germany; orcid.org/0000-0002-7553-4600

Himanshu Joshi – Department of Physics and Beckman Institute for Advanced Science and Technology, University of Illinois, Urbana, Illinois 61820, United States; orcid.org/0000-0003-0769-524X

Ece Büber – Department of Chemistry and Center for NanoScience, Ludwig-Maximilians-Universität München, 81377 München, Germany

Henri G. Franquelim – Max Planck Institute of Biochemistry, 82152 Planegg, Germany; orcid.org/0000-0001-6229-4276

Pierre Stegemann – Center of Medical Biotechnology (ZMB) and Center for Nano Integration Duisburg-Essen (CENIDE), University of Duisburg—Essen, 45117 Essen, Germany

Barbara Saccà – Center of Medical Biotechnology (ZMB) and Center for Nano Integration Duisburg-Essen (CENIDE), University of Duisburg—Essen, 45117 Essen, Germany; orcid.org/0000-0003-2708-2272

Ulrich F. Keyser – Cavendish Laboratory, Department of Physics, University of Cambridge, Cambridge CB3 0HE, United Kingdom; orcid.org/0000-0003-3188-5414

Aleksei Aksimentiev – Department of Physics and Beckman Institute for Advanced Science and Technology, University of Illinois, Urbana, Illinois 61820, United States; orcid.org/0000-0002-6042-8442

Complete contact information is available at:

<https://pubs.acs.org/doi/10.1021/acs.nanolett.1c02584>

Funding

Deutsche Forschungsgemeinschaft (DFG) (Grants INST 86/1904-1 FUGG and TI 329/10-1 and Project SFB1032 (ID

201269156)), the National Science Foundation (USA) (DMR-1827346), an XSEDE allocation Grant (MCA05S028), and the Leadership Resource Allocation (MCB20012).

Notes

The authors declare no competing financial interest.

ACKNOWLEDGMENTS

A.A. and H.J. would like to thank Christopher Maffeo for his help in setting up the initial mrDNA simulation.

ABBREVIATIONS

GEVI, Genetically-Encoded Voltage Indicator; FRET, Fluorescence Resonance Energy Transfer; ssDNA, Single-Stranded DNA; MD, Molecular Dynamic; TIRF, Total Internal Reflection Fluorescence; dsDNA, Double-Stranded DNA; smFRET, Single-Molecule FRET; ALEX, Alternating Laser Excitation; PR, Proximity Ratio; SEM, Standard Error of the Mean; REUS, Replica Exchange Umbrella Sampling

REFERENCES

- (1) Sepehri Rad, M.; Choi, Y.; Cohen, L. B.; Baker, B. J.; Zhong, S.; Storace, D. A.; Braubach, O. R. Voltage and Calcium Imaging of Brain Activity. *Biophys. J.* **2017**, *113* (10), 2160–2167.
- (2) Platasa, J.; Pieribone, V. A. Genetically encoded fluorescent voltage indicators: Are we there yet? *Curr. Opin. Neurobiol.* **2018**, *50*, 146–153.
- (3) Adam, Y.; Kim, J. J.; Lou, S.; Zhao, Y.; Xie, M. E.; Brinks, D.; Wu, H.; Mostajo-Radji, M. A.; Kheifets, S.; Parot, V.; Chettih, S.; Williams, K. J.; Gmeiner, B.; Farhi, S. L.; Madisen, L.; Buchanan, E. K.; Kinsella, I.; Zhou, D.; Paninski, L.; Harvey, C. D.; Zeng, H.; Arlotta, P.; Campbell, R. E.; Cohen, A. E. Voltage imaging and optogenetics reveal behaviour-dependent changes in hippocampal dynamics. *Nature* **2019**, *569* (7756), 413–417.
- (4) Ma, Y.; Yamamoto, Y.; Nicovich, P. R.; Goyette, J.; Rossy, J.; Gooding, J. J.; Gaus, K. A FRET sensor enables quantitative measurements of membrane charges in live cells. *Nat. Biotechnol.* **2017**, *35* (4), 363–370.
- (5) Chanda, B.; Blunck, R.; Faria, L. C.; Schweizer, F. E.; Mody, I.; Bezanilla, F. A hybrid approach to measuring electrical activity in genetically specified neurons. *Nat. Neurosci.* **2005**, *8* (11), 1619–1626.
- (6) Abdelfattah, A. S.; Kawashima, T.; Singh, A.; Novak, O.; Liu, H.; Shuai, Y.; Huang, Y.-C.; Campagnola, L.; Seeman, S. C.; Yu, J.; Zheng, J.; Grimm, J. B.; Patel, R.; Friedrich, J.; Mensh, B. D.; Paninski, L.; Macklin, J. J.; Murphy, G. J.; Podgorski, K.; Lin, B.-J.; Chen, T.-W.; Turner, G. C.; Liu, Z.; Koyama, M.; Svoboda, K.; Ahrens, M. B.; Lavis, L. D.; Schreier, E. R. Bright and photostable chemigenetic indicators for extended in vivo voltage imaging. *Science* **2019**, *365* (6454), 699–704.
- (7) Miller, E. W.; Lin, J. Y.; Frady, E. P.; Steinbach, P. A.; Kristan, W. B.; Tsien, R. Y. Optically monitoring voltage in neurons by photo-induced electron transfer through molecular wires. *Proc. Natl. Acad. Sci. U. S. A.* **2012**, *109* (6), 2114–2119.
- (8) González, J. E.; Tsien, R. Y. Voltage sensing by fluorescence resonance energy transfer in single cells. *Biophys. J.* **1995**, *69* (4), 1272–1280.
- (9) González, J. E.; Tsien, R. Y. Improved indicators of cell membrane potential that use fluorescence resonance energy transfer. *Chem. Biol.* **1997**, *4* (4), 269–277.
- (10) Miller, E. W. Small molecule fluorescent voltage indicators for studying membrane potential. *Curr. Opin. Chem. Biol.* **2016**, *33*, 74–80.
- (11) Nag, O. K.; Stewart, M. H.; Deschamps, J. R.; Susumu, K.; Oh, E.; Tsytsarev, V.; Tang, Q.; Efros, A. L.; Vaxenburg, R.; Black, B. J.; Chen, Y.; O’Shaughnessy, T. J.; North, S. H.; Field, L. D.; Dawson, P. E.; Pancrazio, J. J.; Medintz, I. L.; Chen, Y.; Erzurumlu, R. S.; Huston, A. L.; Delehanty, J. B. Quantum Dot-Peptide-Fullerene Bioconjugates for Visualization of in Vitro and in Vivo Cellular Membrane Potential. *ACS Nano* **2017**, *11* (6), 5598–5613.
- (12) Park, K.; Kuo, Y.; Shvachak, V.; Ingarola, A.; Dai, X.; Hsiung, L.; Kim, W.; Zhou, H.; Zou, P.; Levine, A. J.; Li, J.; Weiss, S. Membrane insertion of and membrane potential sensing by semiconductor voltage nanosensors: Feasibility demonstration. *Sci. Adv.* **2018**, *4* (1), No. e1601453.
- (13) Liu, J.; Zhang, R.; Shang, C.; Zhang, Y.; Feng, Y.; Pan, L.; Xu, B.; Hyeon, T.; Bu, W.; Shi, J.; Du, J. Near-Infrared Voltage Nanosensors Enable Real-Time Imaging of Neuronal Activities in Mice and Zebrafish. *J. Am. Chem. Soc.* **2020**, *142* (17), 7858–7867.
- (14) Klymchenko, A. S.; Stoekel, H.; Takeda, K.; Mély, Y. Fluorescent probe based on intramolecular proton transfer for fast ratiometric measurement of cellular transmembrane potential. *J. Phys. Chem. B* **2006**, *110* (27), 13624–13632.
- (15) Nag, O. K.; Jeong, J.-E.; Le, V. S.; Oh, E.; Woo, H. Y.; Delehanty, J. B. Anionic Conjugated Polyelectrolytes for FRET-based Imaging of Cellular Membrane Potential. *Photochem. Photobiol.* **2020**, *96* (4), 834–844.
- (16) Saminathan, A.; Devany, J.; Veetil, A. T.; Suresh, B.; Pillai, K. S.; Schwake, M.; Krishnan, Y. A DNA-based voltmeter for organelles. *Nat. Nanotechnol.* **2021**, *16* (1), 96–103.
- (17) Rothmund, P. W. K. Folding DNA to create nanoscale shapes and patterns. *Nature* **2006**, *440* (7082), 297–302.
- (18) Douglas, S. M.; Dietz, H.; Liedl, T.; Högberg, B.; Graf, F.; Shih, W. M. Self-assembly of DNA into nanoscale three-dimensional shapes. *Nature* **2009**, *459* (7245), 414–418.
- (19) Douglas, S. M.; Marblestone, A. H.; Teerapittayanon, S.; Vazquez, A.; Church, G. M.; Shih, W. M. Rapid prototyping of 3D DNA-origami shapes with caDNAno. *Nucleic Acids Res.* **2009**, *37* (15), 5001–5006.
- (20) Shen, L.; Wang, P.; Ke, Y. DNA Nanotechnology-Based Biosensors and Therapeutics. *Adv. Healthcare Mater.* **2021**, *10* (15), No. 2002205.
- (21) Wei, R.; Martin, T. G.; Rant, U.; Dietz, H. DNA origami gatekeepers for solid-state nanopores. *Angew. Chem., Int. Ed.* **2012**, *51* (20), 4864–4867.
- (22) Hernández-Ainsa, S.; Bell, N. A. W.; Thacker, V. V.; Göpfrich, K.; Misiunas, K.; Fuentes-Perez, M. E.; Moreno-Herrero, F.; Keyser, U. F. DNA origami nanopores for controlling DNA translocation. *ACS Nano* **2013**, *7* (7), 6024–6030.
- (23) Thomsen, R. P.; Malle, M. G.; Okholm, A. H.; Krishnan, S.; Bohr, S. S.-R.; Sørensen, R. S.; Ries, O.; Vogel, S.; Simmel, F. C.; Hatzakis, N. S.; Kjems, J. A large size-selective DNA nanopore with sensing applications. *Nat. Commun.* **2019**, *10* (1), S655.
- (24) Jiang, Q.; Song, C.; Nangreave, J.; Liu, X.; Lin, L.; Qiu, D.; Wang, Z.-G.; Zou, G.; Liang, X.; Yan, H.; Ding, B. DNA origami as a carrier for circumvention of drug resistance. *J. Am. Chem. Soc.* **2012**, *134* (32), 13396–13403.
- (25) Zhang, Q.; Jiang, Q.; Li, N.; Dai, L.; Liu, Q.; Song, L.; Wang, J.; Li, Y.; Tian, J.; Ding, B.; Du, Y. DNA origami as an in vivo drug delivery vehicle for cancer therapy. *ACS Nano* **2014**, *8* (7), 6633–6643.
- (26) Nickels, P. C.; Wünsch, B.; Holzmeister, P.; Bae, W.; Kneer, L. M.; Grohmann, D.; Tinnefeld, P.; Liedl, T. Molecular force spectroscopy with a DNA origami-based nanoscopic force clamp. *Science* **2016**, *354* (6310), 305–307.
- (27) Kramm, K.; Schröder, T.; Gouge, J.; Vera, A. M.; Gupta, K.; Heiss, F. B.; Liedl, T.; Engel, C.; Berger, I.; Vannini, A.; Tinnefeld, P.; Grohmann, D. DNA origami-based single-molecule force spectroscopy elucidates RNA Polymerase III pre-initiation complex stability. *Nat. Commun.* **2020**, *11* (1), 2828.
- (28) Hemmig, E. A.; Fitzgerald, C.; Maffeo, C.; Hecker, L.; Ochmann, S. E.; Aksimentiev, A.; Tinnefeld, P.; Keyser, U. F. Optical Voltage Sensing Using DNA Origami. *Nano Lett.* **2018**, *18* (3), 1962–1971.
- (29) Weiss, S. Fluorescence spectroscopy of single biomolecules. *Science* **1999**, *283* (5408), 1676–1683.

- (30) Tinnefeld, P.; Sauer, M. Branching out of single-molecule fluorescence spectroscopy: challenges for chemistry and influence on biology. *Angew. Chem., Int. Ed.* **2005**, *44* (18), 2642–2671.
- (31) Woo, S.; Rothmund, P. W. K. Programmable molecular recognition based on the geometry of DNA nanostructures. *Nat. Chem.* **2011**, *3* (8), 620–627.
- (32) Schmied, J. J.; Gietl, A.; Holzmeister, P.; Forthmann, C.; Steinhauer, C.; Dammeyer, T.; Tinnefeld, P. Fluorescence and super-resolution standards based on DNA origami. *Nat. Methods* **2012**, *9* (12), 1133–1134.
- (33) Gietl, A.; Holzmeister, P.; Grohmann, D.; Tinnefeld, P. DNA origami as biocompatible surface to match single-molecule and ensemble experiments. *Nucleic Acids Res.* **2012**, *40* (14), No. e110.
- (34) Mobarak, E.; Javanainen, M.; Kulig, W.; Honigmann, A.; Sezgin, E.; Aho, N.; Eggeling, C.; Rog, T.; Vattulainen, I. How to minimize dye-induced perturbations while studying biomembrane structure and dynamics: PEG linkers as a rational alternative. *Biochim. Biophys. Acta, Biomembr.* **2018**, *1860* (11), 2436–2445.
- (35) Ha, T.; Enderle, T.; Ogletree, D. F.; Chemla, D. S.; Selvin, P. R.; Weiss, S. Probing the interaction between two single molecules: Fluorescence resonance energy transfer between a single donor and a single acceptor. *Proc. Natl. Acad. Sci. U. S. A.* **1996**, *93* (13), 6264–6268.
- (36) Kapanidis, A. N.; Lee, N. K.; Laurence, T. A.; Doose, S.; Margeat, E.; Weiss, S. Fluorescence-aided molecule sorting: Analysis of structure and interactions by alternating-laser excitation of single molecules. *Proc. Natl. Acad. Sci. U. S. A.* **2004**, *101* (24), 8936–8941.
- (37) Margeat, E.; Kapanidis, A. N.; Tinnefeld, P.; Wang, Y.; Mukhopadhyay, J.; Ebright, R. H.; Weiss, S. Direct observation of abortive initiation and promoter escape within single immobilized transcription complexes. *Biophys. J.* **2006**, *90* (4), 1419–1431.
- (38) Preus, S.; Noer, S. L.; Hildebrandt, L. L.; Gudnason, D.; Birkedal, V. iSMS: Single-molecule FRET microscopy software. *Nat. Methods* **2015**, *12* (7), 593–594.
- (39) Hope, M. J.; Bally, M. B.; Webb, G.; Cullis, P. R. Production of large unilamellar vesicles by a rapid extrusion procedure. Characterization of size distribution, trapped volume and ability to maintain a membrane potential. *Biochim. Biophys. Acta, Biomembr.* **1985**, *812* (1), 55–65.
- (40) Cheng, J.-X.; Pautot, S.; Weitz, D. A.; Xie, X. S. Ordering of water molecules between phospholipid bilayers visualized by coherent anti-Stokes Raman scattering microscopy. *Proc. Natl. Acad. Sci. U. S. A.* **2003**, *100* (17), 9826–9830.
- (41) Aksimentiev, A.; Schulten, K. Imaging alpha-hemolysin with molecular dynamics: Ionic conductance, osmotic permeability, and the electrostatic potential map. *Biophys. J.* **2005**, *88* (6), 3745–3761.
- (42) Sugita, Y.; Kitao, A.; Okamoto, Y. Multidimensional replica-exchange method for free-energy calculations. *J. Chem. Phys.* **2000**, *113* (15), 6042–6051.
- (43) Morzy, D.; Rubio-Sánchez, R.; Joshi, H.; Aksimentiev, A.; Di Michele, L.; Keyser, U. F. Cations Regulate Membrane Attachment and Functionality of DNA Nanostructures. *J. Am. Chem. Soc.* **2021**, *143* (19), 7358–7367.
- (44) Douglas, S. M.; Bachelet, I.; Church, G. M. A logic-gated nanorobot for targeted transport of molecular payloads. *Science* **2012**, *335* (6070), 831–834.
- (45) Keller, A.; Linko, V. Challenges and Perspectives of DNA Nanostructures in Biomedicine. *Angew. Chem., Int. Ed.* **2020**, *59* (37), 15818–15833.
- (46) Chandrasekaran, A. R. Nuclease resistance of DNA nanostructures. *Nat. Rev. Chem.* **2021**, *5*, 225–239.
- (47) Amir, Y.; Ben-Ishay, E.; Levner, D.; Ittah, S.; Abu-Horowitz, A.; Bachelet, I. Universal computing by DNA origami robots in a living animal. *Nat. Nanotechnol.* **2014**, *9* (5), 353–357.
- (48) Li, S.; Jiang, Q.; Liu, S.; Zhang, Y.; Tian, Y.; Song, C.; Wang, J.; Zou, Y.; Anderson, G. J.; Han, J.-Y.; Chang, Y.; Liu, Y.; Zhang, C.; Chen, L.; Zhou, G.; Nie, G.; Yan, H.; Ding, B.; Zhao, Y. A DNA nanorobot functions as a cancer therapeutic in response to a molecular trigger in vivo. *Nat. Biotechnol.* **2018**, *36* (3), 258–264.

Supporting Information for

DNA Origami Voltage Sensors for Transmembrane Potentials with Single-Molecule Sensitivity

Sarah E. Ochmann[†], Himanshu Joshi[‡], Ece Büber[†], Henri G. Franquelim[§], Pierre Stegemann[⊥], Barbara Saccà[⊥], Ulrich F. Keyser^{||}, Aleksei Aksimentiev[‡], Philip Tinnefeld^{*†}

[†]Department of Chemistry and Center for NanoScience, Ludwig-Maximilians-Universität München, 81377 München, Germany

[‡]Department of Physics and Beckman Institute for Advanced Science and Technology, University of Illinois, Urbana, Illinois 61820, United States

[§]Max Planck Institute of Biochemistry, 82152 Planegg, Germany

[⊥]Centre for Medical Biotechnology (ZMB) and Centre for Nano Integration Duisburg-Essen (CENIDE), University of Duisburg-Essen, Universitätstraße 2, 45117 Essen, Germany

^{||}Cavendish Laboratory, Department of Physics, University of Cambridge, JJ Thomson Avenue, Cambridge, CB3 0HE, United Kingdom

*Corresponding author: Philip Tinnefeld: philip.tinnefeld@cup.uni-muenchen.de

Material and Methods

Experimental part

Chemicals

If not declared differently, all chemicals were purchased from Merck KGaA.

DNA origami folding

A rectangular DNA origami¹ was used which is based on a 7249 nt long scaffold derived from the M13mp18 bacteriophage. It was designed in the software CaDNAo² and carried several modifications as indicated in Figure S1. All staple strand sequences are given in Table S1 together with the name of the company from which it was purchased.

The origami structures were folded in buffer containing 10 mM Tris, 1 mM EDTA and 12.5 mM MgCl₂ by mixing 10 nM of the scaffold with 100 nM of unmodified and 300 nM of modified oligonucleotides. The solution was heated to 70°C for 3 min and then cooled down in 1°C-steps remaining 1 min at each temperature in a thermocycler (primus 25, peqlab). During the folding process, the biotin modified oligonucleotides, the binding site containing an ATTO532 dye and three cholesterol strands on a ssDNA leash were incorporated. By PEG precipitation, the folded structures were purified from excess staple strands where the sample was mixed in a 1:1 ratio with a buffer containing 12% PEG-8000 (w/v), 10 mM Tris, 1 mM EDTA, 500 mM NaCl and 12 mM MgCl₂ at pH 7.5 and centrifuged for 30 min at 16 krcf and 4°C. The supernatant was discarded and the pellet dissolved in the buffer used for folding. This step was repeated 4 times. In order to label the DNA origami with seven more cholesterol and the voltage-sensing unit, it was incubated over night at room temperature with 5x excess of the oligonucleotides named above per binding site, before another PEG precipitation for purification was examined. The samples were stored at 4°C until usage.

Liposome preparation

To produce Large Unilamellar Vesicles (LUVs), lipid films were created. Therefore 1,2-dioleoyl-sn-glycero-3-phosphocholine (DOPC, Avanti Polar Lipids, INC.) was dissolved at a concentration of 25 mg/mL in chloroform and 1 mmol was added to a glass vial, dried under a nitrogen stream and for another 4 h under vacuum in a desiccator. These lipid films were stored at -20°C until further usage. To create LUVs, the lipid films were dissolved in LUV buffer containing 5 mM Tris, 1 mM EDTA, 0.5 mM Trolox and either 150 mM KCl or 149 mM NaCl and 1 mM KCl at pH 7 (potassium or sodium LUV buffer, respectively) resulting in a lipid concentration of 2.5 mM. After seven freeze-and-thaw cycles using liquid nitrogen and a 80°C water bath, the solution was extruded with a LiposoFast Basic extruder (Avestin, INC.) using Nucleopore PC membranes with a pore size of 100 nm (Whatman, Cytiva Ltd.).

Preparation of microscope slides

Nunc Lab-Tek II Chambered Slides (Thermo Fisher Scientific Inc.) were cleaned with 1 M KOH for 4 h at room temperature. After washing with 1xPBS buffer, the slides were passivated over night at 4°C with 0.5 mg/mL PLL(20)-g[3.5]-PEG(2)/PEG(3.4)-biotin(50%) (PLL-PEG-biotin, SuSoS AG) in 1xPBS. After washing with 1xPBS, 0.25 mg/mL NeutrAvidin (Thermo Fisher Scientific Inc.) in 1xPBS was added for 20 min and washed off with 1xPBS and the slides were ready to use.

TIRF microscope

A homebuilt Total Internal Reflection (TIRF) microscope based on an Olympus IX71 inverted microscope was used for the single-molecule Fluorescence Resonance Energy Transfer (smFRET) measurements. The beams of a green laser (Sapphire 532 nm, 100 mW, Coherent) and a red laser (iBeam Smart 640 nm, 150 mW, Toptica Photonics) were altered using an acousto-optical tunable filter (AOTF, PCAOM-VIS, Crystal Technology) at a frequency of 10 Hz. The power of the green laser was set to 30 mW and of the red laser to 80 mW. The light was focused on the sample with an oil-immersion objective (APO N 60XO/ 1.49 NA TIRF, Olympus). The emission light was separated from the excitation light by a dual line beamsplitter and further separated into 2 emission channels with an Optosplit III (Cairn Research) equipped with a dichroic beam splitter (640 DCXR, Chroma Technology). The green emission was spectrally filtered with a bandpass filter (BrightLine HC 582/75, Semrock) and the red emission with a longpass filter (647 nm RazorEdge, Semrock), before being focused on a back-illuminated sCMOS camera (KURO 1200B sCMOS, Princeton Instruments) in a dual-view configuration. The LightField software (Princeton Instruments) was used to acquire videos with a length of each min. 300 frames.

Sample preparation and imaging

To obtain DNA origami-liposome complexes, the DNA origami were incubated with the liposomes with a 100x excess of the liposomes over the origami for 2 h at room temperature in the respective LUV buffer (potassium or sodium). Then the structures were immobilized in Lab-Tek chambers at a concentration of 30 pM via biotin-neutravidin interaction and imaged on the homebuilt TIRF microscope described above. The LUV buffer matching the ion composition inside of the liposome was used. These measurements represent the control samples, before in each of these samples an electrical transmembrane potential $\Delta\Psi$ was built up.

To then create the electrical transmembrane potential $\Delta\Psi$, first the buffer surrounding the origami-liposome complexes was exchanged with respect to the desired potential. To determine the ionic gradient required, the Nernst equation

$$\Delta\Psi = \frac{RT}{Fz} \ln \left(\frac{c_{in}^{K^+}}{c_{out}^{K^+}} \right) \quad (1)$$

with R as the universal gas constant, T as the temperature, F as the Faraday constant, z as the charge number and $c_{in}^{K^+}$ or $c_{out}^{K^+}$ as the K^+ concentration inside or outside of the liposome, respectively, was used. Table S2 shows the concentrations of KCl and NaCl used to create the different electrical potentials tested. Secondly, 37.5 nmol of valinomycin was added which locates into the hydrophobic core of the lipid bilayer, complexes potassium ions and shuttles them through the lipid membrane while the Chloride counter ions remain. Thereby an electrical transmembrane potential $\Delta\Psi$ is built up.³ After an incubation of 10 min with the valinomycin, the samples were imaged again on the homebuilt TIRF microscope. For the reversibility experiment, gramicidin was added at a concentration of 20 nM to the solution and incubated for 10 min, before the sample was imaged. For the liposome-free sample, the DNA origami were immobilized without prior LUV incubation and imaged in buffer containing 10 mM Tris, 1 mM EDTA, 0.5 mM Trolox, 149 mM NaCl and 1 mM KCl at pH 7.

Data analysis

For the data analysis, the software iSMS⁴ running on Matlab was used. The split channels of green and red emission were superimposed and from the videos an intensity-time transient was derived for each single spot. These transients were then carefully revised to separate single DNA origami structures showing FRET from multimers or origami not containing both fluorophores. In the three channels of donor excitation-donor emission $D_{exc}-D_{em}$, donor excitation-acceptor emission $D_{exc}-A_{em}$ and acceptor excitation-acceptor emission $A_{exc}-A_{em}$ it was checked for a correlation typical for single-molecule FRET pairs. If there was a clear correlation between the different channels – e.g. an intensity increase in the $D_{exc}-D_{em}$ channel while a decrease in the $D_{exc}-A_{em}$ channel is observed upon a simultaneous drop in the $A_{exc}-A_{em}$ channel – the transient was picked and the period selected over which the mean *Proximity Ratio* PR was calculated as

$$PR = \frac{I_{DA}}{I_{DD} + I_{DA}} \quad (2)$$

with I_{DA} as the intensity from the $D_{exc}-A_{em}$ channel and I_{DD} as the intensity from the $D_{exc}-D_{em}$ channel. The data derived this way was further plotted against its frequency and a Gauss fit was used to determine the mean PR and its standard error for each sample.

The change ΔPR shown in Figure 3 and 4 was calculated as

$$\Delta PR = PR - PR_{before} \quad (3)$$

with PR as the value determined for the respective sample with the transmembrane potential $\Delta\Psi = x$ mV and PR_{before} as the value derived before the addition of valinomycin. The respective standard error $\sigma_{\Delta PR}$ resulted from a Gaussian error propagation as

$$\sigma_{\Delta PR} = \sqrt{\left(\left|\frac{\partial \Delta PR}{\partial PR}\right| \cdot \sigma_{PR}\right)^2 + \left(\left|\frac{\partial \Delta PR}{\partial PR_{before}}\right| \cdot \sigma_{PR_{before}}\right)^2} \quad (4)$$

Valinomycin bulk test

To proof that valinomycin creates electrical transmembrane potential $\Delta\Psi$ in liposomes that have a potassium gradient between the in- and outside, a bulk assay was performed using the voltage-sensitive fluorophore 3,3'-Dipropylthiadicarbocyanine Iodide (DiSC₃(5), Thermo Fisher Inc.), liposomes and the spectrofluorometer FS5 (Edinburgh Instruments). The DiSC₃(5) dye is cationic and accumulates on hyperpolarized lipid membranes where its fluorescence is reduced due to contact quenching. Hence, the fluorescence intensity depends on the electrical potential of the lipid membrane.

High precision cell cuvettes (Ultra-Micro Cell 105.252-QS, Hellma analytics) were passivated with a 1 mg/mL BSA solution (Sigma Aldrich) in 1xPBS buffer to decrease unspecific binding. 100 μ L of LUVs with a lipid concentration of 200 μ M were added. The buffer inside the liposome for each sample tested contained 5 mM Tris, 1 mM EDTA, 0.5 mM Trolox and 150 mM KCl at pH7. The buffer in which the LUVs were diluted to the respective concentration was either the same or instead of the 150 mM KCl contained 149 mM NaCl and 1 mM KCl. The respective buffer combination for each sample is depicted in Figure S4.

The DiSC₃(5) dye was added to the liposome containing cuvette resulting at a final concentration of 1 μ M and an addition of 1% (v/v) DMSO to the solution. After an incubation of 10 min, the sample was placed in the spectrofluorometer and the acquisition started (λ_{ex} =666 nm, bandwidth_{ex}=1 nm, λ_{em} =691 nm, bandwidth_{em}=5 nm, 1 point/s). Once the fluorescence intensity was stable, valinomycin was added resulting in a final concentration of 500 nM and another 0.25% (v/v) DMSO, so the final DMSO concentration in the cuvette was 1.25% (v/v). Then the effect of valinomycin was followed by tracking of the fluorescence intensity. For the samples testing the influence of the buffer on the fluorescence intensity, instead of the valinomycin solution, only the respective buffer outside of the liposome was added together with the same overall DMSO concentration of 1.25% (v/v).

To first neglect an interference between the DiSC₃(5) and valinomycin, the ionophore was added to the free dye (Figure S4a). After the addition, the fluorescence baseline is lower than before, but no further effect is observed. The intensity drop can be affiliated to unspecific binding of the dye to the pipette tip; the overall dye concentration is slightly reduced and as a consequence, the fluorescence signal, too. This underlines the importance to not mix the following samples by multiple pipetting to reduce the effect.

Next, the effect of adding a solution to the liposome-dye mixture was investigated. Therefore the respective buffer with DMSO was added to liposomes with inside and outside potassium buffer (Figure S4b) and with inside potassium and outside sodium buffer (Figure S4c) liposomes. After the addition, for both samples an equilibration towards a higher intensity is observed which is related to a homogeneous distribution after Brownian motion in the field of view. As for the free dye, the baseline is slightly reduced though due to unspecific dye sticking to the pipette tip. Anyhow, no specific intensity decrease is observed. Next, the effect of valinomycin to the liposome-dye mixture was tested when there is no ion gradient to the outside (Figure S4d) and as previously, no change is observed which means that no polarization at the lipid membrane is induced.

Lastly, as in the single molecule experiments, valinomycin was added to a sample with potassium carrying liposomes in sodium buffer with DiSC₃(5) (Figure S4e). Unlike in the samples before, after the valinomycin addition the intensity baseline is not only lower, but also an equilibration towards a lower intensity is observed. This different behavior clearly proves that a transmembrane potential $\Delta\Psi$ is built up and the cationic voltage-sensing dye is attracted to the hyperpolarized membrane where its accumulation leads to contact quenching and hence, a reduced overall intensity.

Simulation part

General simulation protocols

All MD simulations were performed using program NAMD⁵, a 2 fs integration time step, 2-2-6 multiple time stepping, periodic boundary conditions and particle mesh Ewald (PME) method over a 1 Å resolution grid to calculate the long range electrostatic interaction.⁶ The Nose-Hoover Langevin piston⁷ and Langevin thermostat were used to maintain the constant pressure and temperature in the system. An 8-10-12 Å cutoff scheme was used to calculate van der Waals and short-range electrostatic forces. SETTLE algorithm⁸ was applied to keep water molecules rigid whereas RATTLE algorithm⁹ constrained all other covalent bonds involving hydrogen atoms. CHARMM36 force field parameters described the bonded and non-bonded interactions among the atoms of DNA¹⁰, lipid¹¹, water and ions.¹² Magnesium

ions were modeled as magnesium hexahydrates ($\text{Mg}[\text{H}_2\text{O}]_6^{2+}$).¹³ Corrections to non-bonded interactions potentials were applied to improve description of ion-DNA, ion-ion, and DNA-lipid interactions.¹⁴ CHARMM General Force Field (CGenFF)¹⁵ were used to describe the interaction parameters for the dye molecules. The coordinates of the system were saved at an interval of 20 ps. The visualization, analysis and post-processing of the simulation trajectories were performed using VMD¹⁶ and CPPTRAJ.¹⁷

Initial models of lipid bilayer membrane and dye conjugated DNA

Starting with the caDNAo design of DNA origami plate along with the modified strands for anchoring and voltage sensing (Figure S1 and Table S1), we performed coarse-grained MD simulation using mrDNA resulting in the movie S3.¹⁸ The final configuration of the origami plate at the end of the coarse-grained simulation was converted to an all-atom model. In order to obtain the nanoscale structure and dynamics of the dye molecules conjugated to the DNA fragment, we selected the 22 base-pair long DNA strand containing the dye molecules in experimental design. The topology and parameters file for the ATTO647N and ATTO532 dye molecules covalently conjugated using $\text{C}_{12}+\text{C}_6$ linker molecules to DNA were obtained using the CHARMM General Force Field (CGenFF) webserver.¹⁹ We used a custom psfgen script in VMD to covalently connect the dye molecules to DNA according to the chemical sketch shown in Figure S2. Mg^{2+} -hexahydrates were placed near the DNA to neutralize its electrical charge of the DNA backbone.

We simulated two analogs of the dye conjugated DNA, one in an aqueous environment and another anchored in the lipid bilayer membrane leading to the data shown in Figure S3 and the Movies S1 and S2. To create the system in aqueous environment, the dye conjugated DNA molecule was solvated with TIP3P water molecules²⁰ using the Solvate plugin of VMD.¹⁶ Potassium and chloride ions were added to produce 150 mM concentration of KCl in solution using the Autoionize plugin of VMD. Thus, assembled system measured $8 \times 8 \times 15 \text{ nm}^3$ and contained approximately 80,000 atoms. To create the membrane-anchored DNA system, we placed the dye conjugated DNA molecule in a pre-equilibrated patch of 1,2-dioleoyl-sn-glycero-3-phosphocholine (DOPC) lipid bilayer membrane such that the ATTO647N and C_{12} spacer connecting it to the DNA span in the upper leaflet of the membrane. The lipid patch was generated using the CHARMM-GUI membrane builder²¹ and pre-equilibrated for approximately 200 ns. Finally, we solvated the system with TIP3P water molecules²⁰ and added ions to produce a 150 mM concentration of KCl. Thus, the membrane-anchored system measured $10 \times 10 \times 15 \text{ nm}^3$ and contained approximately 130,000 atoms.

The assembled systems were subjected to energy minimization using the conjugate gradient method to remove the steric clashes between the solute and solvent. Following that, we equilibrated each system for 20 ns while harmonically restraining the phosphorus (P) atoms of DNA using a spring constant of $1 \text{ kcal mol}^{-1} \text{ \AA}^{-2}$. Subsequently, we equilibrated the systems for additional 40 ns while maintaining the hydrogen bonds between the complementary base-pairs of DNA using the extrabond utility of NAMD. Finally, we removed all the restraints (except two P atoms of each DNA strand connecting the DNA to the origami plate) and performed approximately 1 μs long production simulations of systems using a constant number of atoms (N), pressure ($P = 1 \text{ bar}$) and temperature ($T = 300 \text{ K}$), the NPT ensemble. Two sets of simulations were carried for each design to improve sampling of the conformational space.

The simulation results presented in Figure S3b for the system without a membrane unravel a very close and stable state of the two fluorophores in the pink trajectory after $\sim 0.75 \mu\text{s}$. Inspecting Movie S1, melting of the dsDNA can be observed which leads to the dyes touching each other. Direct contact between dyes commonly yields complex photophysics with different intensity levels^{22,23} that is not observed in our experiments. We therefore assign the DNA melting and the direct dye-dye contact to a force field artefact in the simulation which has been previously observed for CHARMM36 force fields as used in our system.²⁴ Therefore, for Figure 1f only data is included before the artefact is observed eliminating the prominent peak around 10 \AA visible in Figure S3c. Also, for both the system with and without a lipid membrane, the first $0.2 \mu\text{s}$ of the simulation are excluded as this is approximately the time the system needs to equilibrate.

Double-membrane systems

To mimic the voltage bias created by a difference in the ionic concentration from inside to outside of a lipid vesicle in our simulations, we created a double membrane system having two identical patches of DOPC lipid bilayer membrane kept at a distance of 9 nm away from each other (distance between the center of the membranes) along the bilayer normal. We solvated the double DOPC membrane system using TIP3P water molecules²⁰ and added ions to produce 150 mM concentration of KCl. Thus, assembled double membrane system measured $11 \times 11 \times 20 \text{ nm}^3$ and contains $218,400$ atoms.

The assembled system was subjected to energy minimization using the conjugate gradient method to remove the steric clashes between the solute and solvent. Following that, we equilibrated the double membrane system for 230 ns using the NPT ensemble. Towards the end of the equilibration, the distance between the center of the mass (CoM) of the individual bilayer along the bilayer normal stabilizes close to 8.8 nm . Averaging the dimensions of the simulation box from the last 20 ns of the NPT equilibration, we next performed simulation of the double membrane system in NVT ensemble. We created two other double membrane system named as 1 K^+ and -1 K^+ , by shuffling one potassium ion from the inside chamber (the bulk water region around the center of the simulation box) to the outside chamber (the bulk water region at both ends of the simulation box) and *vice-versa*. Thus, we generated three double-membrane systems: 0 K^+ system having exactly same number of potassium ions inside and outside, 1 K^+ system having two more potassium ions inside as compared to outside and -1 K^+ system having two fewer potassium ions inside as compared to the outside which is equivalent to a transmembrane potential of $\Delta\Psi = \pm 180 \text{ mV}$ for this system's geometry. Finally, all systems were simulated using NVT ensemble with the exact same box dimension for approximately 300 ns . The data is presented in Figure S7.

Free energy calculations of dsDNA binding to double-membrane systems

Starting from a pre-equilibrated conformation of 21 base pair long dsDNA kept over a $10 \times 7.1 \text{ nm}^2$ patch of DPhPE lipid membrane from our earlier study,²⁵ we created a DNA double membrane system by replicating another copy of the simulation cell along the bilayer normal. The DNA fragment is effectively infinite along its helical axis as both of the strands are connected to themselves across the periodic boundary (along the y -axis). We removed dsDNA and neutralizing counterions (42 potassium ions) from the outer chamber, which left us with the desired system having dsDNA only in the inner chamber of the double membrane and 150 mM concentration of KCl in solution (Figure S7a). Thus, assembled DNA double membrane system was measured $10 \times 7.1 \times 25 \text{ nm}^3$ and contains $181,628$ atoms.

Both, the inner and outer chamber of this double membrane-DNA system are charge neutralized and we refer to this system as 0 K⁺.

Next, we created two other systems, 4 K⁺ and -4 K⁺ by shuffling 4 potassium ions from the outer chamber to the inner chamber and *vice-versa* inducing a potential of $\Delta\Psi=\pm 1.3$ V, a high enough value to observe statistically significant differences in the interactions between the DNA and the membrane without causing membrane electroporation. Thus, we have three systems with the same number of atoms but different potassium ions in inner and outer chambers. In 0 K⁺, both the chambers are electrically charge-neutral, 4 K⁺ system has 8e⁺ charge in inner chamber as compared to the outer chamber and -4 K⁺ system has 8 e⁺ charge in the outer chamber as compared to the inner one due the shuffling of the potassium ions.

Twenty-one copies of each system were created by moving the CoM of dsDNA from 13 to 33 Å along the z-axis, the region shown using an arrow in Figure S7a. Note that Z = 0 corresponds to the center of the simulation cell. Since the CoM of the upper membrane lies at z = 63 Å, the distance of the CoM of dsDNA and upper membrane varies from 50 to 13 Å in respective copies of the simulation system. Replica exchange umbrella sampling simulations²⁶ were performed using the 1 Å sampling window for the distance between the CoM of dsDNA's and the upper membrane along the z-axis. A harmonic potential with the spring constant of 2.5 kcal/mol/ Å² was used to maintain the distance between dsDNA and the membrane in each window along the z-axis using colvars module²⁷ of NAMD. Each replica was run for approximately 120 ns. Weighted histogram analysis method (WHAM)²⁸ was used to subtract the effect of the harmonic potential and obtain the PMF profile. The first 5 ns of the simulation trajectories were excluded from the WHAM analysis.



Figure S1. Illustration of DNA origami design in CaDNAno². The number of helices is shown in orange on the left and the nucleotide position described in the grid starting at position [8] and ending at position [295] (top). The scaffold strand is presented in dark grey, the unmodified staple strands in black, the biotinylated strands in blue carrying the modification on the 5' end, in light pink strands with cholesterol on the 3' end of a ssDNA spacer, in dark pink cholesterol attached via dsDNA on the 5' end and in cyan the voltage-sensing unit on the 5' end. The sequences of the strands and more details can be found in Table S1.

Table S1. DNA oligonucleotides used as staple strands for the DNA origami voltage sensor. The staple strands are listed with the 5' position x[y] with x as the helix number and y as the nucleotide number as described in Figure S1, the DNA sequence from the 5' to the 3' end, further modifications in the comment section and the company purchased from. Nucleotides in bold are not incorporated into the DNA origami, but protrude from the structure. For 12[111], either a or b are incorporated.

5' position	Sequence (5' to 3' end)	Comments	Company
/	TATGAGTGACACGATTGTTAAAA[SpC12][ATTO647N]	Voltage sensor C ₁₂ +C ₆ , binds to 12[111]a strand [ATTO647N]: modification on amino-C6 linker [SpC12]: C ₁₂ spacer	biomers.net GmbH
/	[ATTO647N]AAATAACAATCGTGACTACTATA	Voltage sensor C ₁₂ , binds to 12[111]b strand [ATTO647N]: modification on amino-C ₁₂ linker	biomers.net GmbH
12[111] a	TAACA[ATTO532]ATCGTGACTACTCATATAAATCATATAACCTGTTTAGCTAACCTTTAA	Binding site for voltage sensor C ₁₂ +C ₆ [ATTO532]: modification on amino-C ₆ -dT linker	Eurofins Genomics GmbH
12[111] b	TAAATCATATAACCTGTTTAGCTAACCTTTAATATGAGTGTACACGAT[ATTO532]TGTTA	Binding site for voltage sensor C ₁₂ [ATTO532]: modification on amino-C ₆ -dT linker	Eurofins Genomics GmbH
20[79]	TTCCAGTCGTAATCATGGTCATAAAAGGGGAAAAAAAAAAAAAAAA [Chol]	[Chol]: Cholesterol-TEG modification	Integrated DNA Technologies, Inc.
8[47]	ATCCCCCTATACCACATTCAACTAGAAAAATCAAAAAAAAAAAAAAAAA [Chol]	[Chol]: Cholesterol-TEG modification	Integrated DNA Technologies, Inc.
12[175]	TTTTATTTAAGCAAATCAGATATTTTTGTAAAAAAAAAAAAAAAA [Chol]	[Chol]: Cholesterol-TEG modification	Integrated DNA Technologies, Inc.
/	GTGATGTAGTGGTAGAGGA [Chol]	Cholesterol strand, binds to multiple binding sites depicted below [Chol]: Cholesterol-TEG modification	Integrated DNA Technologies, Inc.
11[96]	TCCTTACCACCTACATCACAAATGGTCAACAGGCAAGGCAAAGAGTAATGTG	Cholesterol binding site	Eurofins Genomics GmbH
14[111]	TCCTTACCACCTACATCACGAGGGTAGGATTCAAAGGGTGAGACATCCAA	Cholesterol binding site	Eurofins Genomics GmbH
6[111]	TCCTTACCACCTACATCACATTACCTTTGAATAAGGCTTGC CCAAATCCGC	Cholesterol binding site	Eurofins Genomics GmbH

5' position	Sequence (5' to 3' end)	Comments	Company
7[128]	TCCTCTACCACCTACATCACAGACGACAAAGAAGTTTTGCC ATAATTCCGAGCTTCAA	Cholesterol binding site	Eurofins Genomics GmbH
8[111]	TCCTCTACCACCTACATCACAAATAGTAAACACTATCATAACC CTCATTGTGA	Cholesterol binding site	Eurofins Genomics GmbH
16[111]	TCCTCTACCACCTACATCACTGTAGCCATTAAAATTCGCATT AAATGCCGGA	Cholesterol binding site	Eurofins Genomics GmbH
9[96]	TCCTCTACCACCTACATCACCGAAAGACTTTGATAAGAGGT CATATTTCCGA	Cholesterol binding site	Eurofins Genomics GmbH
21[64]	GCCCTTCAGAGTCCACTATTAAGGGTGCCGT		Integrated DNA Technologies, Inc.
1[160]	TTAGGATTGGCTGAGACTCCTCAATAACCGAT		Integrated DNA Technologies, Inc.
15[96]	ATATTTTGGCTTTCATCAACATTATCCAGCCA		Integrated DNA Technologies, Inc.
22[271]	CAGAAGATTAGATAATACATTTGTGACAA		Integrated DNA Technologies, Inc.
5[128]	AACACCAAATTTCAACTTTAATCGTTTACC		Integrated DNA Technologies, Inc.
20[47]	TTAATGAACTAGAGGATCCCCGGGGGTAACG		Integrated DNA Technologies, Inc.
18[79]	GATGTGCTTCAGGAAGATCGACAATGTGA		Integrated DNA Technologies, Inc.
12[207]	GTACCGCAATTCTAAGAACGCGAGTATTATT		Integrated DNA Technologies, Inc.
4[271]	AAATCACCTCCAGTAAGCGTCAGTAATAA		Integrated DNA Technologies, Inc.
22[207]	AGCCAGCAATTGAGGAAGTTATCATATTTT		Integrated DNA Technologies, Inc.
8[207]	AAGGAAACATAAAGGTGGCAACATTATCACCG		Integrated DNA Technologies, Inc.
15[128]	TAAATCAAATAAATTCGCGTCTCGGAAACC		Integrated DNA Technologies, Inc.
6[271]	ACCGATTGTCGGCATTTTCGGTCATAATCA		Integrated DNA Technologies, Inc.
0[79]	ACAACCTTCAACAGTTTCAGCGGATGTATCGG		Integrated DNA Technologies, Inc.
11[224]	GCGAACCTCAAGAACGGTATGACAATAA		Integrated DNA Technologies, Inc.
8[239]	AAGTAAGCAGACACCACGGAATAATATTGACG		Integrated DNA Technologies, Inc.
19[96]	CTGTGTGATTGCGTTGCGCTCACTAGAGTTGC		Integrated DNA Technologies, Inc.
15[224]	CCTAAATCAAATCATAGGTCTAACAGTA		Integrated DNA Technologies, Inc.
1[192]	GCGGATAACCTATTATTCTGAAACAGACGATT		Integrated DNA Technologies, Inc.
5[160]	GCAAGCCTCACCAGTAGCCATGGGCTTGA		Integrated DNA Technologies, Inc.
12[239]	CTTATCATTCCCGACTTGGGGAGCCTAATTT		Integrated DNA Technologies, Inc.
2[111]	AAGGCCGCTGATACCGATAGTTGCGACGTTAG		Integrated DNA Technologies, Inc.
19[248]	CGTAAACAGAAATAAAATCCTTTGCCCGAAAGATTAGA		Integrated DNA Technologies, Inc.
0[111]	TAAATGAATTTTCTGTATGGGATTAATTTCTT		Integrated DNA Technologies, Inc.
5[32]	CATCAAGTAAACGAACTAACGAGTTGAGA		Integrated DNA Technologies, Inc.

5' position	Sequence (5' to 3' end)	Comments	Company
20[207]	GCGGAACATCTGAATAATGGAAGGTACAAAAT		Integrated DNA Technologies, Inc.
12[143]	TTCTACTACGGAGCTGAAAAGGTTACCGCGC		Integrated DNA Technologies, Inc.
8[143]	CTTTTGACAGATAAAAACCAAATAAAGACTCC		Integrated DNA Technologies, Inc.
2[143]	ATATTCGGAACCATCGCCACGCAGAGAAGGA		Integrated DNA Technologies, Inc.
21[224]	CTTTAGGGCCTGCAACAGTGCCAATACGTG		Integrated DNA Technologies, Inc.
14[239]	AGTATAAAGTTCAGCTAATGCAGATGCTTTC		Integrated DNA Technologies, Inc.
20[111]	CACATTAATAATTGTTATCCGCTCATGCCGGCC		Integrated DNA Technologies, Inc.
3[128]	AGCGCGATGATAAATTGTGTCGTGACGAGA		Integrated DNA Technologies, Inc.
17[128]	AGGCAAAGGGGAGGGCGATCGCAATTCCA		Integrated DNA Technologies, Inc.
17[160]	AGAAAACAAAGAAGATGATGAAACAGGCTGCG		Integrated DNA Technologies, Inc.
2[207]	TTTCGGAAGTGCCGTCGAGAGGGTGAGTTTCG		Integrated DNA Technologies, Inc.
22[79]	TGGAACAACCGCCTGGCCCTGAGGCCGCT		Integrated DNA Technologies, Inc.
10[47]	CTGTAGCTTGACTATTATAGTCAGTTCATTGA		Integrated DNA Technologies, Inc.
16[207]	ACCTTTTTATTTTAGTTAATTCATAGGGCTT		Integrated DNA Technologies, Inc.
9[224]	AAAGTCACAAAATAAACGCGCAGCTTTTA		Integrated DNA Technologies, Inc.
19[224]	CTACCATAGTTTGAGTAACATTTAAAATAT		Integrated DNA Technologies, Inc.
3[96]	ACACTCATCCATGTTACTTAGCCGAAAGCTGC		Integrated DNA Technologies, Inc.
18[239]	CCTGATTGCAATATATGTGAGTGATCAATAGT		Integrated DNA Technologies, Inc.
10[239]	GCCAGTTAGAGGGTAATTGAGCGCTTAAGAA		Integrated DNA Technologies, Inc.
3[32]	AATACGTTTGAAAGAGGACAGACTGACCTT		Integrated DNA Technologies, Inc.
1[128]	TGACAACCTCGCTGAGGCTGCATTATACCA		Integrated DNA Technologies, Inc.
16[47]	ACAAACGGAAAAGCCCCAAAACACTGGAGCA		Integrated DNA Technologies, Inc.
14[175]	CATGTAATAGAATATAAAGTACCAAGCCGT		Integrated DNA Technologies, Inc.
17[192]	CATTTGAAGGCGAATTATTCATTTTTGTTGG		Integrated DNA Technologies, Inc.
19[56]	TACCGAGCTCGAATTCGGGAAACCTGTCGTGCAGCTGATT		Integrated DNA Technologies, Inc.
23[64]	AAAGCACTAAATCGGAACCTAATCCAGTT		Integrated DNA Technologies, Inc.
16[175]	TATAACTAACAAAGAACGCGAGAACGCCAA		Integrated DNA Technologies, Inc.
7[56]	ATGCAGATACATAACGGGAATCGTCATAATAAAGCAAAG		Integrated DNA Technologies, Inc.
3[224]	TTAAAGCCAGAGCCGCCACCCTCGACAGAA		Integrated DNA Technologies, Inc.

5' position	Sequence (5' to 3' end)	Comments	Company
12[47]	TAAATCGGGATTCCCAATTCTGCGATATAATG		Integrated DNA Technologies, Inc.
3[160]	TTGACAGGCCACCACCAGAGCCGCGATTTGTA		Integrated DNA Technologies, Inc.
14[143]	CAACCGTTTCAAATCACCATCAATTCGAGCCA		Integrated DNA Technologies, Inc.
6[79]	TTATACCACCAAATCAACGTAACGAACGAG		Integrated DNA Technologies, Inc.
4[239]	GCCTCCCTCAGAATGGAAAGCGCAGTAACAGT		Integrated DNA Technologies, Inc.
7[248]	GTTTTATTTGTCACAATCTTACCGAAGCCCTTAATATCA		Integrated DNA Technologies, Inc.
1[32]	AGGCTCCAGAGGCTTTGAGGACACGGGTAA		Integrated DNA Technologies, Inc.
0[207]	TCACCAGTACAACTACAACGCTAGTACCAG		Integrated DNA Technologies, Inc.
4[143]	TCATCGCCAACAAAGTACAACGACGCCAGCA		Integrated DNA Technologies, Inc.
16[271]	CTTAGATTTAAGGCGTTAAATAAAGCCTGT		Integrated DNA Technologies, Inc.
13[96]	TAGGTAAACTATTTTTGAGAGATCAAACGTTA		Integrated DNA Technologies, Inc.
21[192]	TGAAAGGAGCAAATGAAAAATCTAGAGATAGA		Integrated DNA Technologies, Inc.
5[224]	TCAAGTTTCATTAAGGTGAATATAAAAGA		Integrated DNA Technologies, Inc.
8[79]	AATACTGCCAAAAGGAATTACGTGGCTCA		Integrated DNA Technologies, Inc.
11[160]	CCAATAGCTCATCGTAGGAATCATGGCATCAA		Integrated DNA Technologies, Inc.
4[111]	GACCTGCTCTTTGACCCCCAGCGAGGGAGTTA		Integrated DNA Technologies, Inc.
2[175]	TATTAAGAAGCGGGGTTTTGCTCGTAGCAT		Integrated DNA Technologies, Inc.
13[184]	GACAAAAGGTAAAGTAATCGCCATATTTAACAAAACTTTT		Integrated DNA Technologies, Inc.
1[96]	AAACAGCTTTTTGCGGGATCGTCAACACTAAA		Integrated DNA Technologies, Inc.
23[192]	ACCCTTCTGACCTGAAAGCGTAAGACGCTGAG		Integrated DNA Technologies, Inc.
15[32]	TAATCAGCGGATTGACCGTAATCGTAACCG		Integrated DNA Technologies, Inc.
18[175]	CTGAGCAAAAATTAATTACATTTTGGGTTA		Integrated DNA Technologies, Inc.
6[175]	CAGCAAAAGGAAACGTCACCAATGAGCCGC		Integrated DNA Technologies, Inc.
18[47]	CCAGGTTGCCAGTTTGAGGGGACCCGTGGGA		Integrated DNA Technologies, Inc.
6[143]	GATGGTTTGAACGAGTAGTAAATTTACCATTA		Integrated DNA Technologies, Inc.
8[175]	ATACCCAACAGTATGTTAGCAAATTAGAGC		Integrated DNA Technologies, Inc.
17[96]	GCTTCCGATTACGCCAGCTGGCGCTGTTTC		Integrated DNA Technologies, Inc.
12[79]	AAATTAAGTTGACCATTAGATACTTTTGGC		Integrated DNA Technologies, Inc.
8[271]	AATAGCTATCAATAGAAAATTCACATTCA		Integrated DNA Technologies, Inc.

5' position	Sequence (5' to 3' end)	Comments	Company
15[192]	TCAAATATAACCTCCGGCTTAGGTAACAATTT		Integrated DNA Technologies, Inc.
21[96]	AGCAAGCGTAGGGTTGAGTGTTGATGGAGCC		Integrated DNA Technologies, Inc.
20[239]	ATTTTAAAATCAAAATTTTGCACGGATTCCG		Integrated DNA Technologies, Inc.
7[224]	AACGCAAAGATAGCCGAACAAACCTGAAC		Integrated DNA Technologies, Inc.
22[239]	TTAACACCAGCACTAACAATAATCGTTATTA		Integrated DNA Technologies, Inc.
18[111]	TCTTCGCTGCACCGCTTCTGGTGCGCCCTCC		Integrated DNA Technologies, Inc.
17[32]	TGCATCTTTCCAGTCACGACGGCCTGCAG		Integrated DNA Technologies, Inc.
4[175]	CACCAGAAAGGTTGAGGCAGGTCATGAAAG		Integrated DNA Technologies, Inc.
13[120]	AAAGCCGGAGACAGCTAGCTGATAAATTAATTTTGT		Integrated DNA Technologies, Inc.
10[175]	TTAACGTCTAACATAAAAAACAGGTAACGGA		Integrated DNA Technologies, Inc.
21[256]	GCCGTCAAAAAACAGAGGTGAGGCCTATTAGT		Integrated DNA Technologies, Inc.
4[47]	GACCAACTAATGCCACTACGAAGGGGTAGCA		Integrated DNA Technologies, Inc.
6[239]	GAAATTATTGCCTTTAGCGTCAGACCCGGAACC		Integrated DNA Technologies, Inc.
18[271]	CTTTTACAAAATCGTCGTATTAGCGATAG		Integrated DNA Technologies, Inc.
14[79]	GCTATCAGAAATGCAATGCCTGAATTAGCA		Integrated DNA Technologies, Inc.
2[47]	ACGGCTACAAAAGGAGCCTTTAATGTGAGAAT		Integrated DNA Technologies, Inc.
21[128]	GCGAAAAATCCCTTATAAATCAAGCCGGCG		Integrated DNA Technologies, Inc.
22[175]	ACCTTGCTTGGTCAGTTGGCAAAGAGCGGA		Integrated DNA Technologies, Inc.
1[64]	TTTATCAGGACAGCATCGGAACGACACCAACCTAAAACGA		Integrated DNA Technologies, Inc.
17[224]	CATAAATCTTTGAATACCAAGTGTTAGAAC		Integrated DNA Technologies, Inc.
16[143]	GCCATCAAGCTCATTTTTTAACCAAAATCCA		Integrated DNA Technologies, Inc.
4[207]	CCACCCTCTATTCACAAACAAATACCTGCCTA		Integrated DNA Technologies, Inc.
2[79]	CAGCGAAACTTGCTTTTCGAGGTGTTGCTAA		Integrated DNA Technologies, Inc.
19[128]	CACAACAGGTGCCTAATGAGTGCCACAGAG		Integrated DNA Technologies, Inc.
19[192]	ATTATACTAAGAAACCACCAGAAGTCAACAGT		Integrated DNA Technologies, Inc.
16[239]	GAATTTATTTAATGGTTTGAATATTCTTACC		Integrated DNA Technologies, Inc.
22[111]	GCCCAGAGTCCACGCTGGTTTGACGCTAACT		Integrated DNA Technologies, Inc.
6[207]	TCACCGACGCACCGTAATCAGTAGCAGAACCG		Integrated DNA Technologies, Inc.
13[224]	ACAACATGCCAACGCTCAACAGTCTTCTGA		Integrated DNA Technologies, Inc.

5' position	Sequence (5' to 3' end)	Comments	Company
20[175]	ATTATCATTCAATATAAATCTGACAATTAC		Integrated DNA Technologies, Inc.
18[207]	CGCGCAGATTACCTTTTTAATGGGAGAGACT		Integrated DNA Technologies, Inc.
10[207]	ATCCCAATGAGAATTAACCTGAACAGTTACCAG		Integrated DNA Technologies, Inc.
14[207]	AATTGAGAATTCTGTCCAGACGACTAAACCAA		Integrated DNA Technologies, Inc.
13[64]	TATATTTTGTCAATGCTGAGAGTGAAGATTGATAAGC		Integrated DNA Technologies, Inc.
7[160]	TTATTACGAAGAACTGGCATGATTGCGAGAGG		Integrated DNA Technologies, Inc.
23[96]	CCCGATTTAGAGCTTGACGGGGAAAAAGAATA		Integrated DNA Technologies, Inc.
3[192]	GGCCTTGAAGAGCCACCACCCTCAGAAACCAT		Integrated DNA Technologies, Inc.
4[79]	GCGCAGACAAGAGGCAAAGAATCCCTCAG		Integrated DNA Technologies, Inc.
15[160]	ATCGCAAGTATGTAATGCTGATGATAGGAAC		Integrated DNA Technologies, Inc.
5[96]	TCATTAGATGCGATTTAAGAACAGGCATAG		Integrated DNA Technologies, Inc.
18[143]	CAACTGTTGCGCCATTCGCCATTCAAACATCA		Integrated DNA Technologies, Inc.
20[271]	CTCGTATTAGAAATTGCGTAGATACAGTAC		Integrated DNA Technologies, Inc.
1[256]	CAGGAGGTGGGGTCAGTGCCTTGAGTCTCTGAATTTACCG		Integrated DNA Technologies, Inc.
13[160]	GTAATAAGTTAGGCAGAGGCATTTATGATATT		Integrated DNA Technologies, Inc.
1[224]	GTATAGCAAACAGTTAATGCCAATCCTCA		Integrated DNA Technologies, Inc.
5[192]	CGATAGCATTGAGCCATTTGGGAACGTAGAAA		Integrated DNA Technologies, Inc.
7[192]	ATACATACCGAGGAAACGCAATAAGAAGCGCATTAGACGG		Integrated DNA Technologies, Inc.
10[111]	TTGCTCCTTTCAAATATCGCGTTTGAGGGGGT		Integrated DNA Technologies, Inc.
13[256]	GTTTATCAATATGCGTTATACAAACCGACCGTGTGATAAA		Integrated DNA Technologies, Inc.
6[47]	TACGTTAAAGTAATCTTGACAAGAACCGAACT		Integrated DNA Technologies, Inc.
16[79]	GCGAGTAAAAATATTTAAATTGTTACAAAG		Integrated DNA Technologies, Inc.
23[256]	CTTTAATGCGCGAACTGATAGCCCCACCAG		Integrated DNA Technologies, Inc.
23[224]	GCACAGACAATATTTTGAATGGGGTCAGTA		Integrated DNA Technologies, Inc.
10[127]	TAGAGAGTTATTTTCATTTGGGGATAGTAGCATT		Integrated DNA Technologies, Inc.
4[63]	ATAAGGGAACCGGATATTCATTACGTCAGGACGTTGGGAA		Integrated DNA Technologies, Inc.
16[63]	CGGATTCTGACGACAGTATCGCCGCAAGGCGATTAAGTT		Integrated DNA Technologies, Inc.
10[191]	GAAACGATAGAAGGCTTATCCGGTCTCATCGAGAACAAGC		Integrated DNA Technologies, Inc.
16[255]	GAGAAGAGATAACCTTGCTTCTGTTCCGGGAGAAACAATAA		Integrated DNA Technologies, Inc.

5' position	Sequence (5' to 3' end)	Comments	Company
4[255]	AGCCACCACTGTAGCGCTTTCAAGGGAGGGAAGGTAAA		Integrated DNA Technologies, Inc.
10[79]	GATGGCTTATCAAAAAGATTAAGAGCGTCC		Integrated DNA Technologies, Inc.
0[47]	AGAAAGGAACAACCTAAAGGAATTCAAAAAA		Integrated DNA Technologies, Inc.
10[271]	ACGCTAACACCCACAAGAATTGAAAATAGC		Integrated DNA Technologies, Inc.
2[271]	GTTTTAACTTAGTACCGCCACCCAGAGCCA		Integrated DNA Technologies, Inc.
14[271]	TTAGTATCACAATAGATAAGTCCACGAGCA		Integrated DNA Technologies, Inc.
9[160]	AGAGAGAAAAAATGAAAATAGCAAGCAAACCT		Integrated DNA Technologies, Inc.
12[271]	TGTAGAAATCAAGATTAGTTGCTCTTACCA		Integrated DNA Technologies, Inc.
23[160]	TAAAAGGGACATTCTGGCCAACAAAGCATC		Integrated DNA Technologies, Inc.
21[160]	TCAATATCGAACCTCAAATATCAATTCGGAAA		Integrated DNA Technologies, Inc.
19[160]	GCAATTCACATATTCCTGATTATCAAAGTGTA		Integrated DNA Technologies, Inc.
10[143]	CCAACAGGAGCGAACCCAGACCGGAGCCTTAC		Integrated DNA Technologies, Inc.
23[32]	CAAATCAAGTTTTTTGGGGTCGAAACGTGGA		Integrated DNA Technologies, Inc.
22[143]	TCCGCAAATCCTGTTTGATGGTGGACCCTCAA		Integrated DNA Technologies, Inc.
0[175]	TCCACAGACAGCCCTCATAGTTAGCGTAACGA		Integrated DNA Technologies, Inc.
0[143]	TCTAAAGTTTTGTCGCTTTCCAGCCGACAA		Integrated DNA Technologies, Inc.
20[143]	AAGCCTGGTACGAGCCGGAAGCATAGATGATG		Integrated DNA Technologies, Inc.
2[239]	GCCCGTATCCGGAATAGGTGTATCAGCCCAAT		Integrated DNA Technologies, Inc.
7[32]	TTTAGGACAAATGCTTTAAACAATCAGGTC		Integrated DNA Technologies, Inc.
23[128]	AACGTGGCGAGAAAGGAAGGAAACCAGTAA		Integrated DNA Technologies, Inc.
21[32]	TTTTCACTCAAAGGGCGAAAAACCATCACC		Integrated DNA Technologies, Inc.
14[47]	AACAAGAGGGATAAAAAATTTTAGCATAAAGC		Integrated DNA Technologies, Inc.
13[32]	AACGCAAAATCGATGAACGGTACCGGTTGA		Integrated DNA Technologies, Inc.
0[271]	CCACCCTCATTTTCAGGGATAGCAACCGTACT		Integrated DNA Technologies, Inc.
9[256]	GAGAGATAGAGCGTCTTCCAGAGGTTTTGAA		Integrated DNA Technologies, Inc.
11[256]	GCCTTAAACCAATCAATAATCGGCACGCGCCT		Integrated DNA Technologies, Inc.
0[239]	AGGAACCCATGTACCGTAACACTTGATATAA		Integrated DNA Technologies, Inc.
9[32]	TTTACCCCAACATGTTTTAAATTTCCATAT		Integrated DNA Technologies, Inc.
11[32]	AACAGTTTTGTACCAAAAACATTTTATTTTC		Integrated DNA Technologies, Inc.

5' position	Sequence (5' to 3' end)	Comments	Company
22[47]	CTCCAACGCAGTGAGACGGGCAACCAGCTGCA		Integrated DNA Technologies, Inc.
19[32]	GTCGACTTCGGCCAACGCGGGGTTTTTC		Integrated DNA Technologies, Inc.
7[96]	TAAGAGCAAATGTTTAGACTGGATAGGAAGCC		Integrated DNA Technologies, Inc.
11[64]	GATTTAGTCAATAAAGCCTCAGAGAACCCTCA		Integrated DNA Technologies, Inc.
9[64]	CGGATTGCAGAGCTTAATTGCTGAAACGAGTA		Integrated DNA Technologies, Inc.

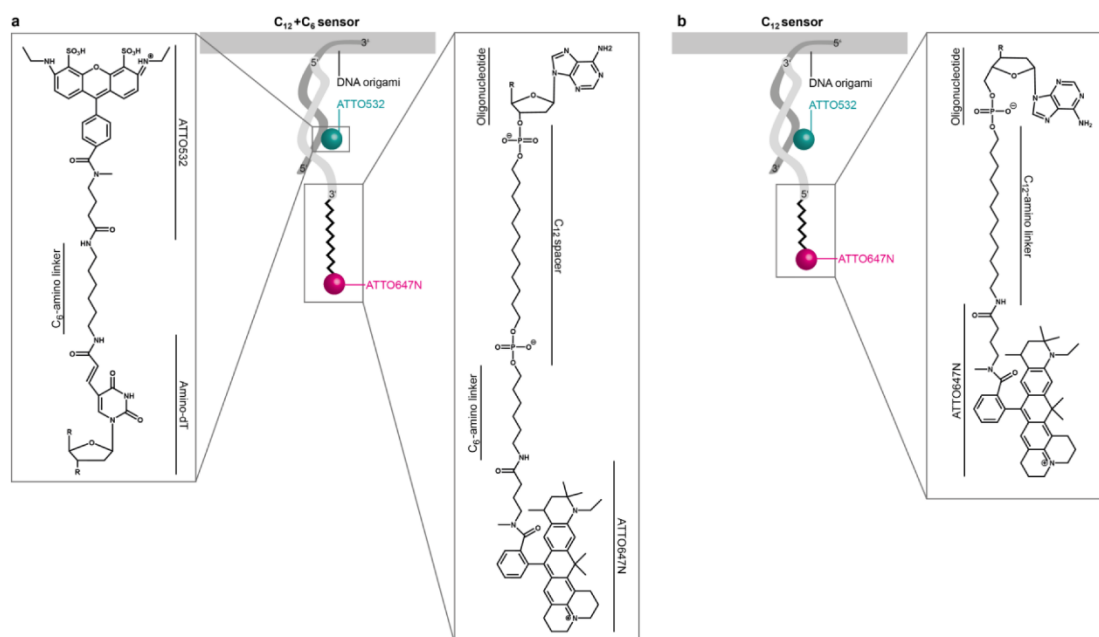


Figure S2. Detailed sketch of the different voltage-sensor designs. (a) For the $C_{12}+C_6$ sensor, a strand from the DNA origami is extended from the 5' end (dark grey) and carries an ATTO532 (cyan, zoom-in left for details). In light grey, the counter strand is shown with the 3' end carrying a carbon chain and an ATTO647N (pink). The right zoom-in shows how the ATTO647N is connected to the DNA's 3' end via a C_{12} spacer and a C_6 -amino linker. (b) For the C_{12} sensor, the strand in the origami is extended on the 3' end (dark grey) and also carries the ATTO532 (cyan) which is connected as shown in the zoom-in in (a). The counter strand carries on the 5' end the carbon chain with the ATTO647N. In the zoom-in, the connection between the 5' end of the DNA and the ATTO647N via a C_{12} -amino linker is shown.

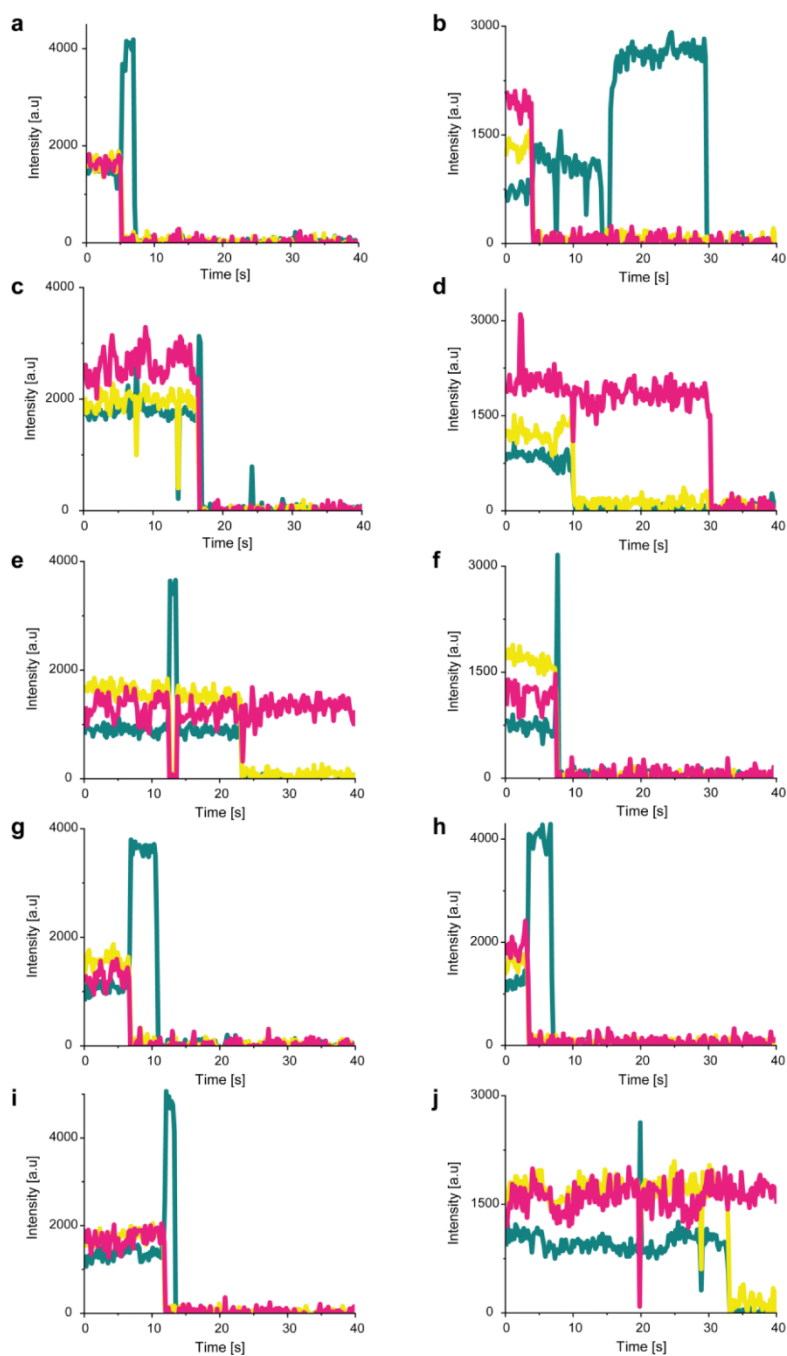


Figure S3. Exemplary fluorescence transients selected in analysis. For (a) to (j), the intensity derived from the donor excitation-donor emission $D_{ex}-D_{em}$ channel is shown in cyan, from the donor excitation-acceptor emission $D_{ex}-A_{em}$ channel in yellow and from the acceptor excitation-acceptor emission $A_{ex}-A_{em}$ channel in pink.

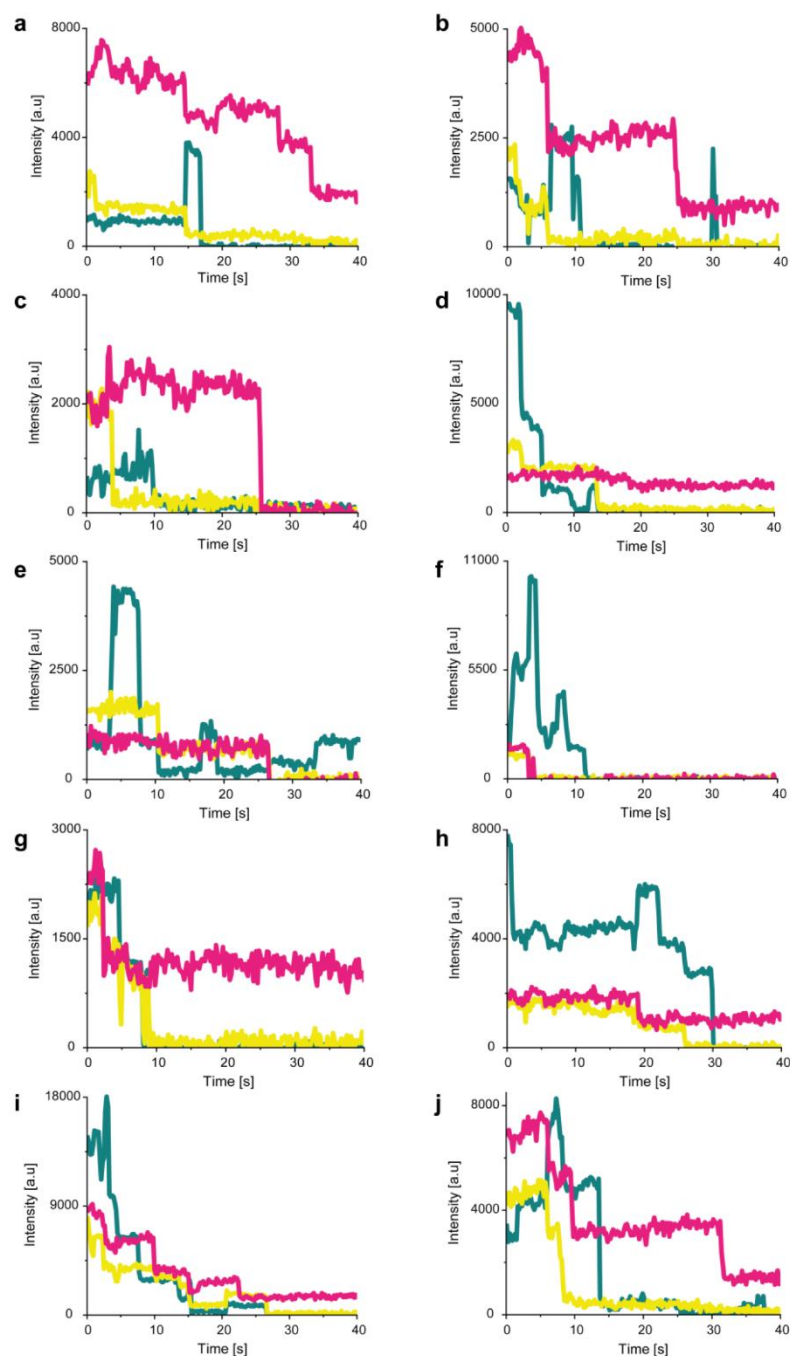


Figure S4. Exemplary fluorescence transients rejected in analysis. For (a) to (j), the intensity derived from the donor excitation-donor emission $D_{ex}-D_{em}$ channel is shown in cyan, from the donor excitation-acceptor emission $D_{ex}-A_{em}$ channel in yellow and from the acceptor excitation-acceptor emission $A_{ex}-A_{em}$ channel in pink.

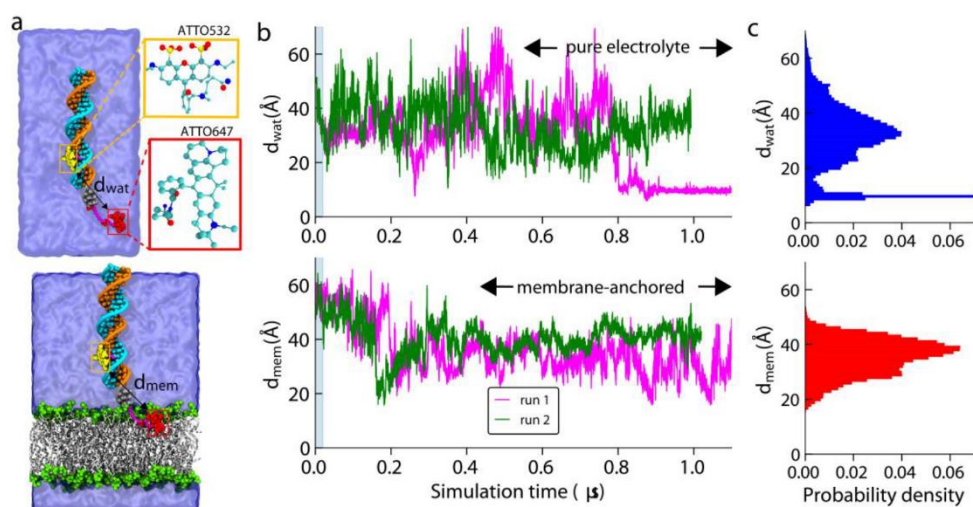


Figure S5. Equilibrium MD simulation of dye conjugated dsDNA in aqueous and membrane anchored environment. (a) A cut-away view of the all-atom models of 22-base pair long dsDNA conjugated to ATTO532 (yellow) and ATTO647N (red) dye molecules, solvated in the aqueous solution (top panel); anchored to lipid bilayer membrane and then solvated (bottom panel). The alkyl carbon chains (C_6 and C_{12}) connecting the dye molecules to the DNA (as shown in the chemical sketch in Figure S2) are shown in magenta. Complementary strands of the DNA are shown in turquoise and orange, the DOPC lipid head groups are shown as green spheres whereas the lipid tails are shown as white lines, water and ions are not shown for the sake of clarity. The enlarged atomic structures of the respective dye molecules are shown in yellow and red boxes. (b) Distance between the center of mass of the ATTO532 and ATTO647N dye molecules as a function of simulation time from two independent simulation runs in a box of water (top panel) and while anchored in lipid bilayer membrane (bottom panel). (c) The histogram of the distance between the dye molecules in water (top) and while anchored in membrane (bottom) excluding the first 200 ns from each simulation run.

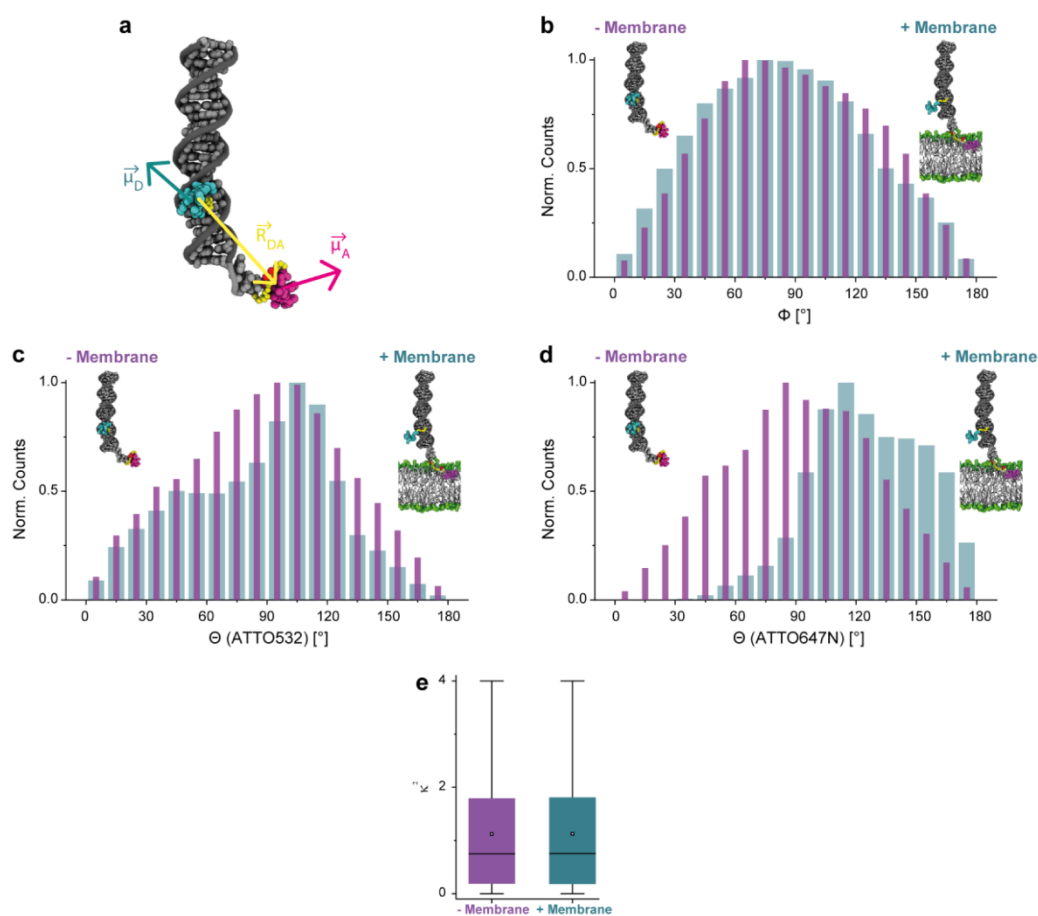


Figure S6. Angle distributions obtained from MD simulations between the donor ATTO532 and the acceptor ATTO647N. (a) $\vec{\mu}_D$ shows the direction of the transition dipole moment of the donor and $\vec{\mu}_A$ of the acceptor. \vec{R}_{DA} is the vector connecting the two dyes' center of mass. (b) Distributions of the angle Φ between $\vec{\mu}_D$ and $\vec{\mu}_A$ for the sample without a membrane (purple) and with a membrane (cyan). (c) Distribution of the angle θ of the donor ATTO532 which refers to the angle between $\vec{\mu}_D$ and \vec{R}_{DA} for the sample without a membrane (purple) and with a membrane (cyan). (d) Distribution of the angle θ of the acceptor ATTO647N which refers to the angle between $\vec{\mu}_A$ and \vec{R}_{DA} for the sample without a membrane (purple) and with a membrane (cyan). (e) Boxplot comparing the κ^2 for the sample without membrane (purple) and with membrane (cyan). The point marks the mean, the line the median, the box shows the percentile of 25% to 75% and the whiskers the minimum and the maximum values. Simulation times: - Membrane 1.35 μ s, + Membrane 1.55 μ s.

Table S2. Concentration of KCl and NaCl in the buffer inside and outside of the LUVs. To build up a certain transmembrane potential $\Delta\Psi$ with respect to the Nernst equation, the buffers used inside and outside of the LUVs were varied. The KCl gradient is responsible for the potential creation whereas NaCl is added to prevent osmotic pressure. The NaCl/KCl concentrations add up to buffers containing 5 mM Tris, 1 mM EDTA and 0.5 mM Trolox at pH 7 as previously described as the LUV buffer.

$\Delta\Psi$ [mV]	C_{inside} [mM]		C_{outside} [mM]	
	KCl	NaCl	KCl	NaCl
-125	150	0	1.1	148.9
-100	150	0	3	147
-75	150	0	8	142
-50	150	0	21	129
-25	150	0	56	94
0	150	0	150	0
0	1	149	1	149
25	1	149	2.7	147.3
50	1	149	7	143
75	1	149	19	131
100	1	149	50	100
125	1	149	134	16

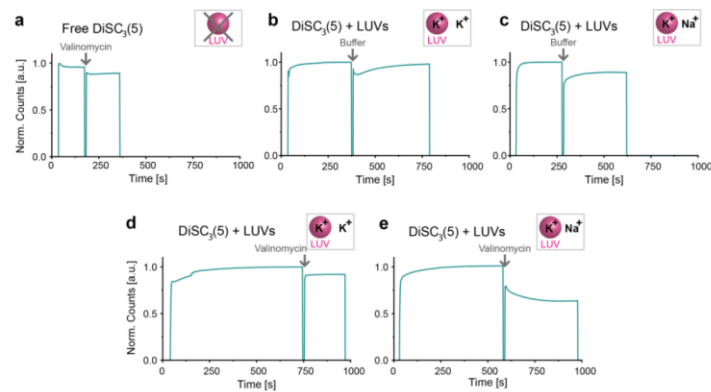


Figure S7. Valinomycin bulk test. On a spectrofluorometer, it was proven that a transmembrane potential $\Delta\Psi$ is built up with the valinomycin assay using the voltage-sensitive dye DiSC₃(5). As a control, the DiSC₃(5) was investigated without LUVs in the cuvette and valinomycin was added to the solution (a). The intensity drop results from the dye sticking to the pipette tip while adding the solution. No further effect is observed. As another control, LUVs with potassium buffer inside and outside of the liposome (b) and inside potassium and outside sodium (c) were used and buffer was added to the samples. The intensity drop due to dye sticking to the pipette is observed as previously. Further, the intensity equilibrates after the buffer addition for both samples which is related to the homogeneous distribution after Brownian motion in the field of view. Next, valinomycin was added to LUVs with inside and outside potassium ions and buffer was injected (d). As for the other controls, an intensity drop due to dye sticking is observed, but no further effect. Only LUVs with inside potassium and outside sodium show a clear drop in intensity (e) which equilibrates after a while following Brownian motion. As more of the DiSC₃(5) is attracted to the charged membrane, contact quenching of the dyes take place and the intensity is reduced. For details see the chapter on “Valinomycin bulk assay” above.

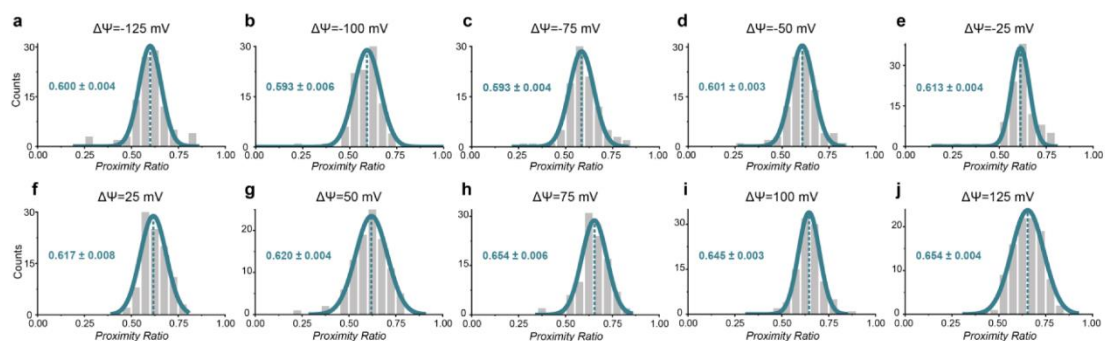


Figure S8. PR distributions for all samples of the $C_{12}+C_6$ sensor with transmembrane potentials $\Delta\Psi$. The samples were imaged after buffer exchange, addition of valinomycin and hence, the creation of a transmembrane potential of (a) $\Delta\Psi=-125$ mV, (b) $\Delta\Psi=-100$ mV, (c) $\Delta\Psi=-75$ mV, (d) $\Delta\Psi=-50$ mV, (e) $\Delta\Psi=-25$ mV, (f) $\Delta\Psi=25$ mV, (g) $\Delta\Psi=50$ mV, (h) $\Delta\Psi=75$ mV, (i) $\Delta\Psi=100$ mV and (j) $\Delta\Psi=125$ mV. The respective mean resulting from the Gauss fit as well as the standard error of the mean is given for each distribution. N_{molecule} : (a)-(j) 100.

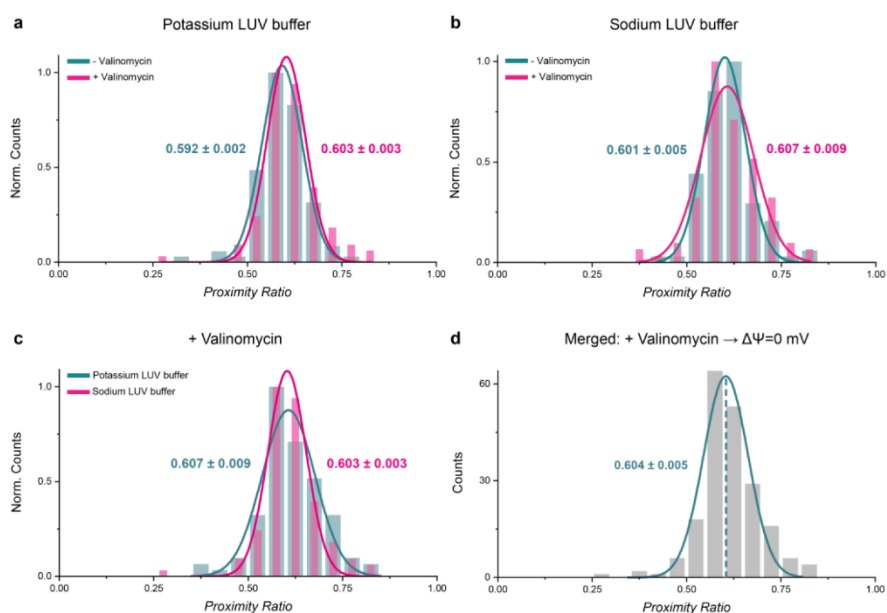


Figure S9. PR distributions of various $C_{12}+C_6$ samples compared. Control for $\Delta\Psi=0$ mV with potassium LUV buffer in cyan with the sample after the addition of valinomycin in pink (a), control for $\Delta\Psi=0$ mV with sodium LUV buffer in cyan with the sample after the addition of valinomycin in pink (b) and both $\Delta\Psi=0$ mV samples in potassium (cyan) and sodium (pink) LUV buffer with their respective mean from Gauss fitting and the standard error of the mean. All derived mean values are very similar which is why on the one hand a buffer effect on the PR value and on the other hand an effect of the valinomycin can be neglected. Therefore, the data for both samples with valinomycin (c) are merged and presented in (d) which in the following is the $\Delta\Psi=0$ mV sample. N_{molecule} : (a)-(c) 100 for each distribution, (d) 200.

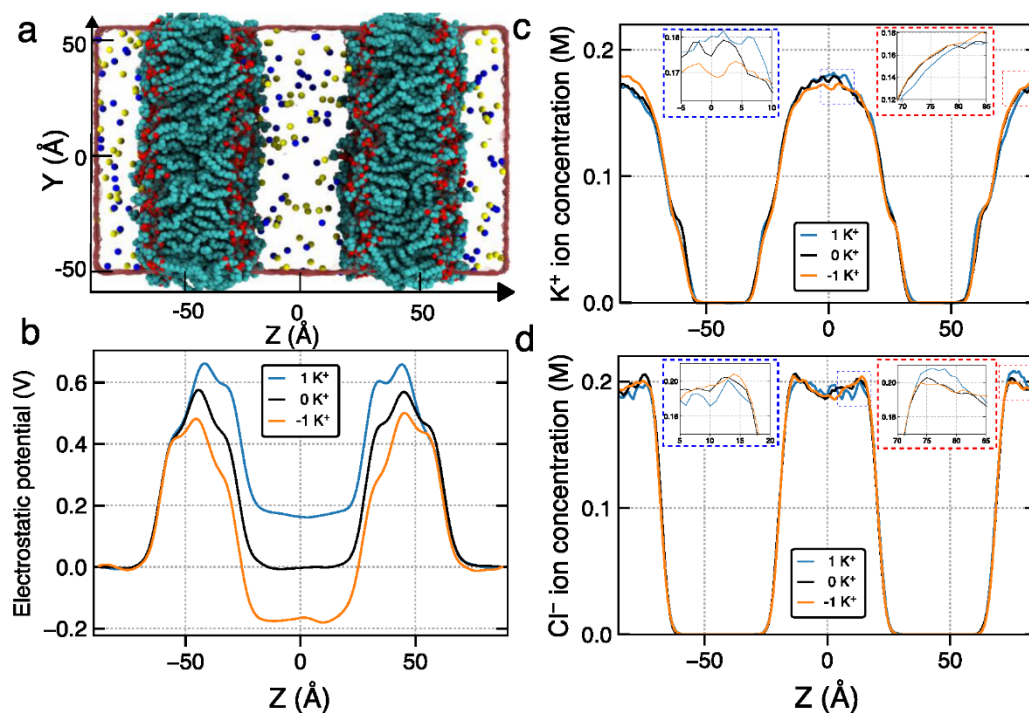


Figure S10. Voltage bias created by shuffling of a single ion in double membrane systems. (a) A representative snapshot of the all-atom model of double DOPC lipid bilayer membrane solvated in 150 mM solution of KCl. Non-hydrogen atoms of the lipid (DOPC) membrane are shown as blue (N), tan (P), red (O), and cyan (C) spheres. The transparent surface illustrates the volume occupied by the water molecules. The potassium and chloride ions are shown in blue and yellow spheres. (b) Average electrostatic potential profile of various systems along the z-axis. Local concentration of (c) potassium and (d) chloride ions along the lipid bilayer normal averaged over last 300 ns of NVT simulation. The images inside the close-in boxes shows the zoomed in region in the plots. The density was obtained by dividing the z-axis in the bins of 1 Å and then Savitzky Golay filter (window length 21 with a polynomial of degree 2) is used for smoothening of the data.

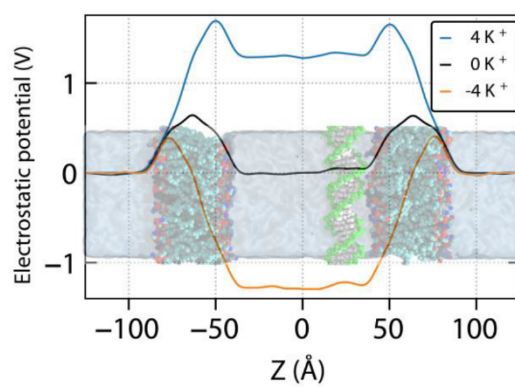


Figure S11. Average electrostatic profile of the 0 K⁺, 4 K⁺ and -4 K⁺ systems along the bilayer normal during the REUS MD simulations.

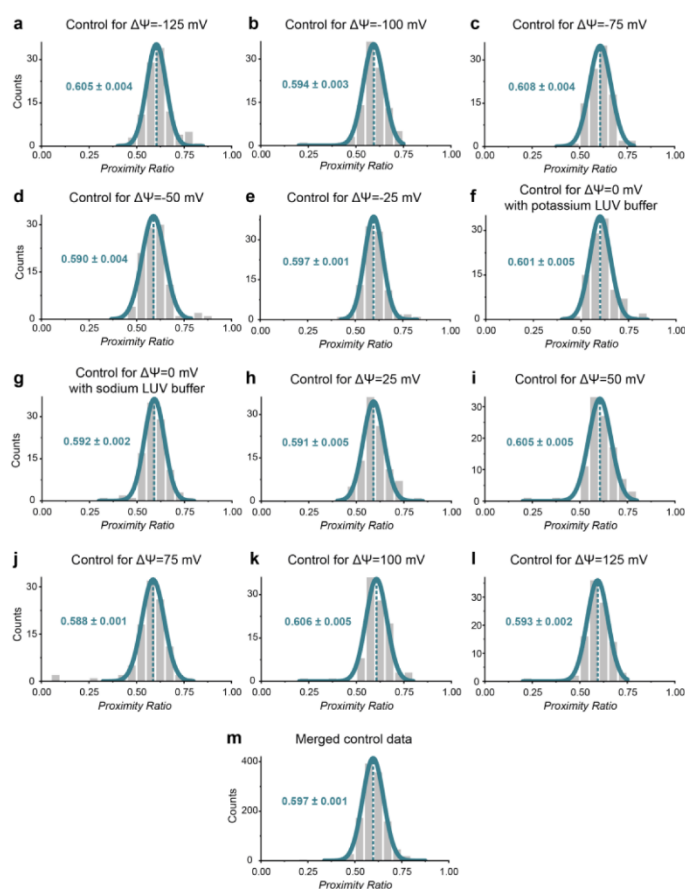


Figure S12. PR distributions for all control samples of the $C_{12}+C_6$ sensor. The samples were imaged before buffer exchange and transmembrane potential creation via valinomycin and the plots show the distributions with their respective mean and standard error of the mean from the Gauss fit. Control sample resulting in (a) $\Delta\Psi=-125$ mV, (b) $\Delta\Psi=-100$ mV, (c) $\Delta\Psi=-75$ mV, (d) $\Delta\Psi=-50$ mV, (e) $\Delta\Psi=-25$ mV, (f) $\Delta\Psi=0$ mV with potassium LUV buffer, (g) $\Delta\Psi=0$ mV with sodium LUV buffer, (h) $\Delta\Psi=25$ mV, (i) $\Delta\Psi=50$ mV, (j) $\Delta\Psi=75$ mV, (k) $\Delta\Psi=100$ mV, (l) $\Delta\Psi=125$ mV. As all of the samples show similar mean values, their data is merged and plotted together in (m) and further referred to as the sample before the valinomycin addition. N_{molecule} : (a)-(l) 100, (m) 1200.

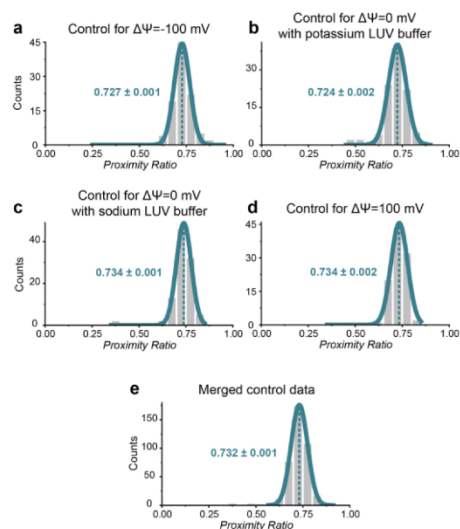


Figure S13. PR distributions for all control samples of the C_{12} sensor. The samples were imaged before buffer exchange and transmembrane potential creation via valinomycin and the plots show the distributions with their respective mean and standard error of the mean from the Gauss fit. Control sample resulting in (a) $\Delta\Psi=-100$ mV, (b) $\Delta\Psi=0$ mV with potassium LUV buffer, (c) $\Delta\Psi=0$ mV with sodium LUV buffer and (d) $\Delta\Psi=125$ mV. As all of the samples show similar mean values, their data is merged and plotted together in (e) and further referred to as the sample before the valinomycin addition. N_{molecule} : (a)-(d) 100, (e) 400.

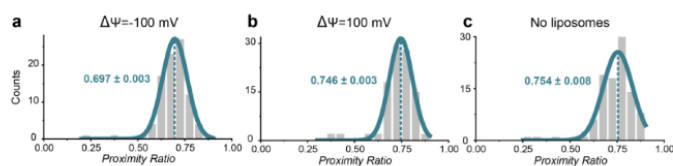


Figure S14. PR distributions for samples of the C_{12} sensor with transmembrane potentials $\Delta\Psi$ and without liposomes. For the creation of transmembrane potentials of (a) $\Delta\Psi = -100$ mV and (b) $\Delta\Psi = 100$ mV, the outside buffer was exchanged and valinomycin was added to create the potentials. (c) PR distribution for sample without liposomes. The respective mean resulting from the Gauss fit as well as the standard error of the mean is given for each distribution. N_{molecule} : (a) 91, (b)-(c) 100.

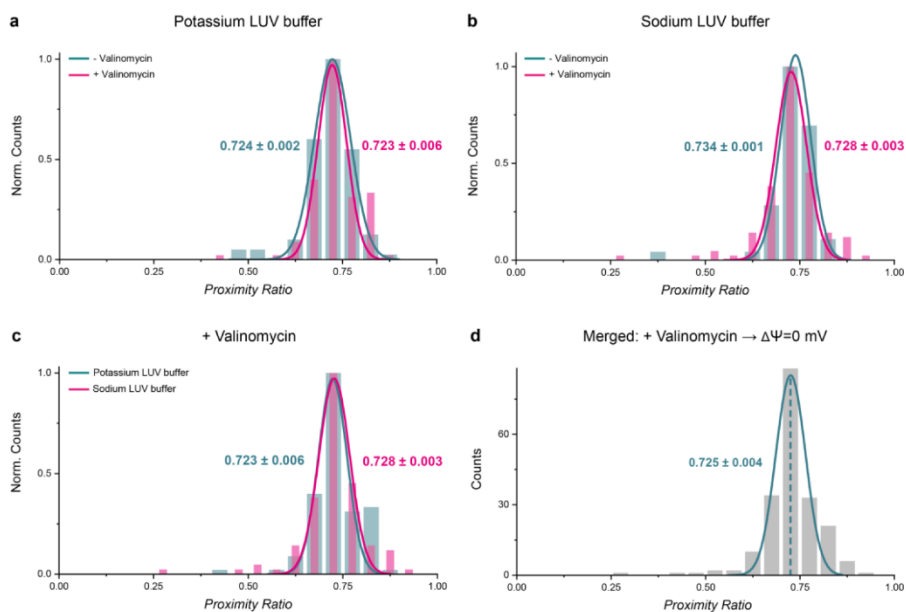


Figure S15. PR distributions of various C_{12} samples compared. Control for $\Delta\Psi=0$ mV with potassium LUV buffer in cyan with the sample after the addition of valinomycin in pink (a), control for $\Delta\Psi=0$ mV with sodium LUV buffer in cyan with the sample after the addition of valinomycin in pink (b) and both $\Delta\Psi=0$ mV samples in potassium (cyan) and sodium (pink) LUV buffer with their respective mean from Gauss fitting and the standard error of the mean. All derived mean values are very similar which is why on the one hand a buffer effect on the PR and on the other hand an effect of the valinomycin can be neglected. Therefore, the data for both samples with valinomycin (c) are merged and presented in (d) which in the following is the $\Delta\Psi=0$ mV sample. N_{molecule} : (a) cyan: 100, pink: 99, (b) each 100, (c) cyan: 99, pink: 100, (d) 199.

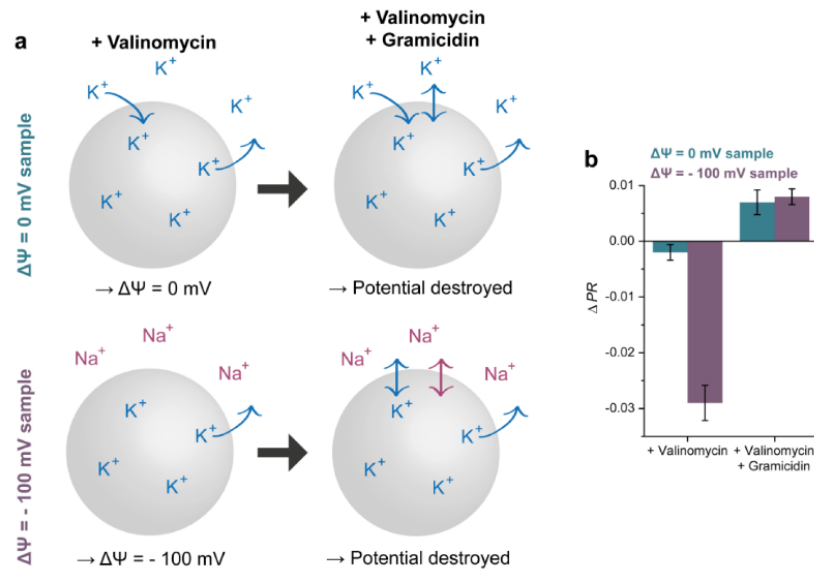


Figure S16. Reversibility experiment for C_{12} voltage sensor. (a) Concept of experiment. For the control sample resulting in $\Delta\Psi=0$ mV, the inside and the outside buffer remains the same, whereas for the in $\Delta\Psi=-100$ mV sample, the outside buffer is changed containing Na^+ according to Table S2. After the addition of valinomycin (monodirectional arrow) which shuffles K^+ ions against a K^+ gradient, the respective potential is built up. After imaging, gramicidin (bidirectional arrow) is added which forms an ion channel in the membrane and enables a bidirectional diffusion of K^+ (blur arrow) and Na^+ (purple arrow) until an equilibrium destroying the $\Delta\Psi$. The sample is imaged again. (b) Change of the energy transfer before and after neutralization by gramicidin. ΔPR represents the proximity ratio subtracted by the value before the addition of the ionophores as presented in Figure S17a. For the $\Delta\Psi=-100$ mV sample, the PR reduces and recovers after the potential is destroyed whereas for the $\Delta\Psi=0$ mV sample, no specific effect is observed.

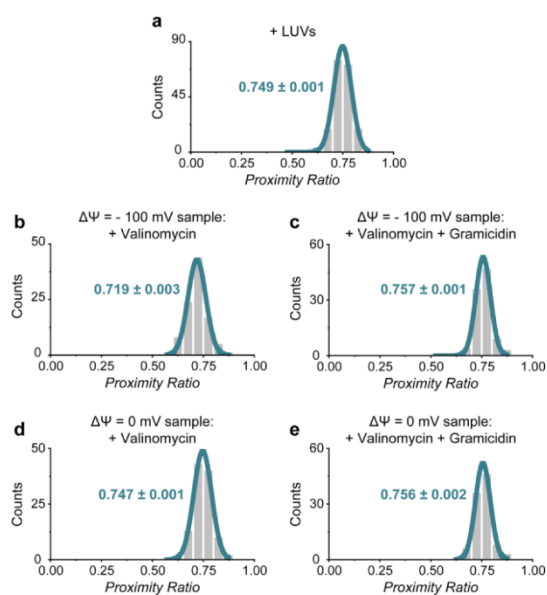
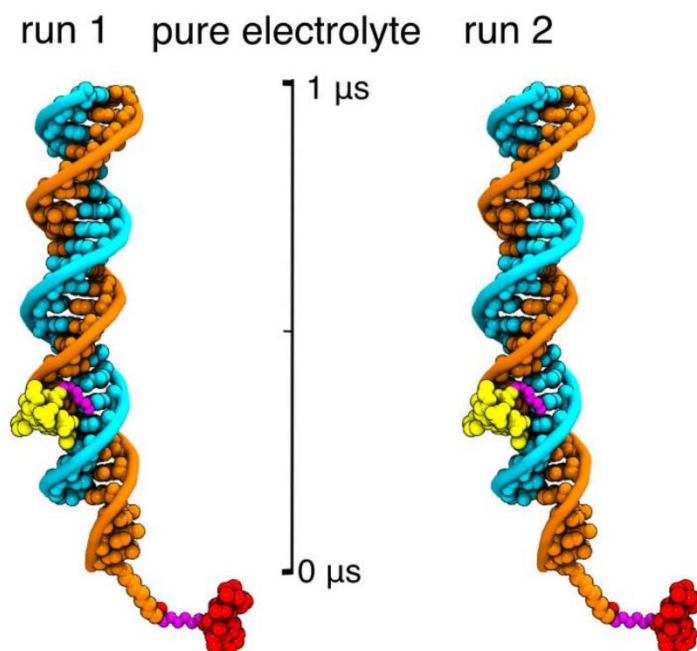
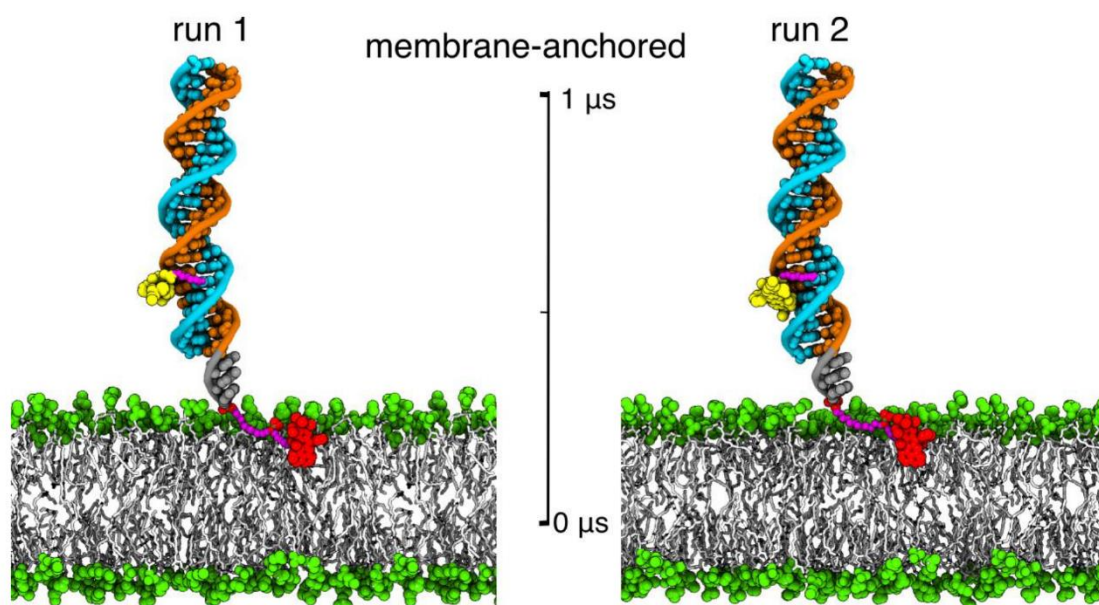


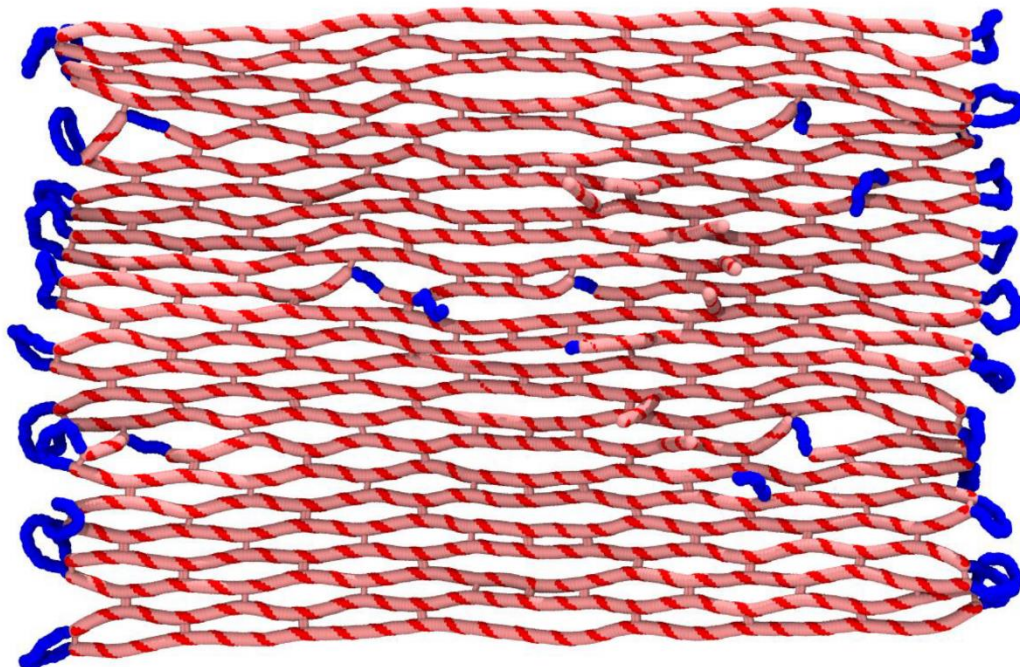
Figure S17. PR distributions of the C_{12} sensor samples for the reversibility experiment. Distribution for (a) sample with liposomes, (b) $\Delta\Psi = -100$ mV sample after valinomycin addition, (c) $\Delta\Psi = -100$ mV sample after valinomycin and gramicidin addition, (d) $\Delta\Psi = 0$ mV sample after valinomycin addition and (e) $\Delta\Psi = 0$ mV sample after valinomycin and gramicidin addition. N_{molecule} : (a) 191, (b) 100, (c) 100, (d) 110, (e) 100.

Captions to Supplementary Movies

Supplementary Movie 1. All-atom molecular dynamics simulation of ATTO532 (yellow) and ATTO647N (red) dye molecules conjugated to dsDNA in purely aqueous solution. The movie illustrates MD trajectories of two independent simulation runs (run 1 and run 2) starting from the same initial configuration. Water and ions are not shown for clarity.



Supplementary Movie 2. All-atom molecular dynamics simulation of ATTO532 (yellow) and ATTO647N (red) dye molecules conjugated to dsDNA anchored in DOPC lipid bilayer membrane. The movie illustrates MD trajectories of two independent simulation runs (run 1 and run 2) starting from the same initial configuration. Water and ions are not shown for clarity.



Supplementary Movie 3. A typical mrDNA¹⁸ simulation of the DNA origami plate designed as a sensor of transmembrane potentials. The coarse-grained simulation starts with the caDNAno design of the origami plate which is first mapped into a 5-bp/bead model followed by a 1-bead/bp model. Finally, the all-atom model of the system was obtained by averaging equilibrated conformations in coarse-grained simulation. At the end, the all-atom model was simulated for couple of nanoseconds in vacuum using the network of elastic restraints.²⁹

References

- (1) Schmied, J. J.; Gietl, A.; Holzmeister, P.; Forthmann, C.; Steinhauer, C.; Dammeyer, T.; Tinnefeld, P. Fluorescence and super-resolution standards based on DNA origami. *Nat Methods* **2012**, *9* (12), 1133–1134. DOI: 10.1038/nmeth.2254.
- (2) Douglas, S. M.; Marblestone, A. H.; Teerapittayanon, S.; Vazquez, A.; Church, G. M.; Shih, W. M. Rapid prototyping of 3D DNA-origami shapes with caDNAo. *Nucleic Acids Res* **2009**, *37* (15), 5001–5006. DOI: 10.1093/nar/gkp436.
- (3) Hope, M. J.; Bally, M. B.; Webb, G.; Cullis, P. R. Production of large unilamellar vesicles by a rapid extrusion procedure. Characterization of size distribution, trapped volume and ability to maintain a membrane potential. *Biochimica et Biophysica Acta (BBA) - Biomembranes* **1985**, *812* (1), 55–65. DOI: 10.1016/0005-2736(85)90521-8.
- (4) Preus, S.; Noer, S. L.; Hildebrandt, L. L.; Gudnason, D.; Birkedal, V. ISMS: Single-molecule FRET microscopy software. *Nat Methods* **2015**, *12* (7), 593–594. DOI: 10.1038/nmeth.3435.
- (5) Phillips, J. C.; Hardy, D. J.; Maia, J. D. C.; Stone, J. E.; Ribeiro, J. V.; Bernardi, R. C.; Buch, R.; Fiorin, G.; Hémin, J.; Jiang, W.; McGreevy, R.; Melo, M. C. R.; Radak, B. K.; Skeel, R. D.; Singharoy, A.; Wang, Y.; Roux, B.; Aksimentiev, A.; Luthey-Schulten, Z.; Kalé, L. V.; Schulten, K.; Chipot, C.; Tajkhorshid, E. Scalable molecular dynamics on CPU and GPU architectures with NAMD. *J Chem Phys* **2020**, *153* (4), 44130. DOI: 10.1063/5.0014475.
- (6) Batcho, P. F.; Case, D. A.; Schlick, T. Optimized particle-mesh Ewald/multiple-time step integration for molecular dynamics simulations. *J Chem Phys* **2001**, *115* (9), 4003–4018. DOI: 10.1063/1.1389854.
- (7) Feller, S. E.; Zhang, Y.; Pastor, R. W.; Brooks, B. R. Constant pressure molecular dynamics simulation: The Langevin piston method. *J Chem Phys* **1995**, *103* (11), 4613–4621. DOI: 10.1063/1.470648.
- (8) Miyamoto, S.; Kollman, P. A. Settle: An analytical version of the SHAKE and RATTLE algorithm for rigid water models. *J. Comput. Chem.* **1992**, *13* (8), 952–962. DOI: 10.1002/jcc.540130805.
- (9) Andersen, H. C. Rattle: A “velocity” version of the shake algorithm for molecular dynamics calculations. *Journal of Computational Physics* **1983**, *52* (1), 24–34. DOI: 10.1016/0021-9991(83)90014-1.
- (10) Hart, K.; Foloppe, N.; Baker, C. M.; Denning, E. J.; Nilsson, L.; Mackerell, A. D. Optimization of the CHARMM additive force field for DNA: Improved treatment of the BI/BII conformational equilibrium. *J Chem Theory Comput* **2012**, *8* (1), 348–362. DOI: 10.1021/ct200723y.
- (11) Klauda, J. B.; Venable, R. M.; Freites, J. A.; O’Connor, J. W.; Tobias, D. J.; Mondragon-Ramirez, C.; Vorobyov, I.; Mackerell, A. D.; Pastor, R. W. Update of the CHARMM all-atom additive force field for lipids: validation on six lipid types. *J Phys Chem B* **2010**, *114* (23), 7830–7843. DOI: 10.1021/jp101759q.
- (12) Beglov, D.; Roux, B. Finite representation of an infinite bulk system: Solvent boundary potential for computer simulations. *J Chem Phys* **1994**, *100* (12), 9050–9063. DOI: 10.1063/1.466711.
- (13) Yoo, J.; Aksimentiev, A. Improved Parametrization of Li⁺, Na⁺, K⁺, and Mg²⁺ Ions for All-Atom Molecular Dynamics Simulations of Nucleic Acid Systems. *J. Phys. Chem. Lett.* **2012**, *3* (1), 45–50. DOI: 10.1021/jz201501a.
- (14) Yoo, J.; Aksimentiev, A. Improved Parameterization of Amine-Carboxylate and Amine-Phosphate Interactions for Molecular Dynamics Simulations Using the CHARMM and AMBER Force Fields. *J Chem Theory Comput* **2016**, *12* (1), 430–443. DOI: 10.1021/acs.jctc.5b00967.
- (15) Vanommeslaeghe, K.; Hatcher, E.; Acharya, C.; Kundu, S.; Zhong, S.; Shim, J.; Darian, E.; Guvench, O.; Lopes, P.; Vorobyov, I.; Mackerell, A. D. CHARMM general force field: A force field for drug-like molecules compatible with the CHARMM all-atom additive biological force fields. *J. Comput. Chem.* **2010**, *31* (4), 671–690. DOI: 10.1002/jcc.21367.

- (16) Humphrey, W.; Dalke, A.; Schulten, K. VMD: Visual molecular dynamics. *Journal of Molecular Graphics* **1996**, *14* (1), 33–38. DOI: 10.1016/0263-7855(96)00018-5.
- (17) Case, D. A.; V. Babin; J.T. Berryman; R.M. Betz; Q. Cai; D.S. Cerutti; T.E. Cheatham, I.; T.A. Darden; R.E. Duke; H. Gohlke; A.W. Goetz; S. Gusarov; N. Homeyer; P. Janowski; J. Kaus; I. Kolossváry; A. Kovalenko; T.S. Lee; S. LeGrand; T. Luchko; R. Luo; B. Madej; K.M. Merz; F. Paesani; D.R. Roe; A. Roitberg; C. Sagui; R. Salomon-Ferrer; G. Seabra; C.L. Simmerling; W. Smith; J. Swails; R.C. Walker; J. Wang; R.M. Wolf; X.Wu; Kollman, P. A. *AMBER* **14**, 2014.
- (18) Maffeo, C.; Aksimentiev, A. MrDNA: a multi-resolution model for predicting the structure and dynamics of DNA systems. *Nucleic Acids Res* **2020**, *48* (9), 5135–5146. DOI: 10.1093/nar/gkaa200.
- (19) Vanommeslaeghe, K.; Mackerell, A. D. Automation of the CHARMM General Force Field (CGenFF) I: bond perception and atom typing. *J Chem Inf Model* **2012**, *52* (12), 3144–3154. DOI: 10.1021/ci300363c.
- (20) Jorgensen, W. L.; Chandrasekhar, J.; Madura, J. D.; Impey, R. W.; Klein, M. L. Comparison of simple potential functions for simulating liquid water. *J Chem Phys* **1983**, *79* (2), 926–935. DOI: 10.1063/1.445869.
- (21) Jo, S.; Kim, T.; Iyer, V. G.; Im, W. CHARMM-GUI: a web-based graphical user interface for CHARMM. *J. Comput. Chem.* **2008**, *29* (11), 1859–1865. DOI: 10.1002/jcc.20945.
- (22) Di Fiori, N.; Meller, A. The Effect of dye-dye interactions on the spatial resolution of single-molecule FRET measurements in nucleic acids. *Biophys J* **2010**, *98* (10), 2265–2272. DOI: 10.1016/j.bpj.2010.02.008.
- (23) Schröder, T.; Scheible, M. B.; Steiner, F.; Vogelsang, J.; Tinnefeld, P. Interchromophoric Interactions Determine the Maximum Brightness Density in DNA Origami Structures. *Nano Lett* **2019**, *19* (2), 1275–1281. DOI: 10.1021/acs.nanolett.8b04845.
- (24) Minhas, V.; Sun, T.; Mirzoev, A.; Korolev, N.; Lyubartsev, A. P.; Nordenskiöld, L. Modeling DNA Flexibility: Comparison of Force Fields from Atomistic to Multiscale Levels. *J Phys Chem B* **2020**, *124* (1), 38–49. DOI: 10.1021/acs.jpcc.9b09106.
- (25) Morzy, D.; Rubio-Sánchez, R.; Joshi, H.; Aksimentiev, A.; Di Michele, L.; Keyser, U. F. Cations Regulate Membrane Attachment and Functionality of DNA Nanostructures. *J Am Chem Soc* **2021**. DOI: 10.1021/jacs.1c00166.
- (26) Sugita, Y.; Kitao, A.; Okamoto, Y. Multidimensional replica-exchange method for free-energy calculations. *J Chem Phys* **2000**, *113* (15), 6042–6051. DOI: 10.1063/1.1308516.
- (27) Fiorin, G.; Klein, M. L.; Hémin, J. Using collective variables to drive molecular dynamics simulations. *Molecular Physics* **2013**, *111* (22-23), 3345–3362. DOI: 10.1080/00268976.2013.813594.
- (28) Kumar, S.; Rosenberg, J. M.; Bouzida, D.; Swendsen, R. H.; Kollman, P. A. THE weighted histogram analysis method for free-energy calculations on biomolecules. I. The method. *J. Comput. Chem.* **1992**, *13* (8), 1011–1021. DOI: 10.1002/jcc.540130812.
- (29) Maffeo, C.; Yoo, J.; Aksimentiev, A. De novo reconstruction of DNA origami structures through atomistic molecular dynamics simulation. *Nucleic Acids Res* **2016**, *44* (7), 3013–3019. DOI: 10.1093/nar/gkw155.

7.3 Associated publication P3

Quantitative Single-Molecule Measurements of Membrane Charges with DNA Origami Sensors

by

Sarah E. Ochmann, Tim Schröder, Clara M. Schulz, Philip Tinnefeld

Reprinted with permission from

Analytical Chemistry, 94, 2633–2640 (2022)

Copyright 2022 American Chemical Society

Quantitative Single-Molecule Measurements of Membrane Charges with DNA Origami Sensors

Sarah E. Ochmann, Tim Schröder, Clara M. Schulz, and Philip Tinnefeld*

Cite This: *Anal. Chem.* 2022, 94, 2633–2640

Read Online

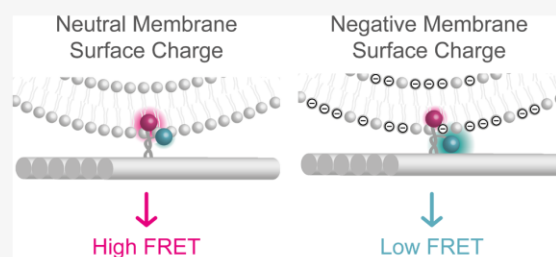
ACCESS |

Metrics & More

Article Recommendations

Supporting Information

ABSTRACT: Charges in lipid head groups generate electrical surface potentials at cell membranes, and changes in their composition are involved in various signaling pathways, such as T-cell activation or apoptosis. Here, we present a DNA origami-based sensor for membrane surface charges with a quantitative fluorescence read-out of single molecules. A DNA origami plate is equipped with modifications for specific membrane targeting, surface immobilization, and an anionic sensing unit consisting of single-stranded DNA and the dye ATTO542. This unit is anchored to a lipid membrane by the dye ATTO647N, and conformational changes of the sensing unit in response to surface charges are read out by fluorescence resonance energy transfer between the two dyes. We test the performance of our sensor with single-molecule fluorescence microscopy by exposing it to differently charged large unilamellar vesicles. We achieve a change in energy transfer of ~10% points between uncharged and highly charged membranes and demonstrate a quantitative relation between the surface charge and the energy transfer. Further, with autocorrelation analyses of confocal data, we unravel the working principle of our sensor that is switching dynamically between a membrane-bound state and an unbound state on the timescale of 1–10 ms. Our study introduces a complementary sensing system for membrane surface charges to previously published genetically encoded sensors. Additionally, the single-molecule read-out enables investigations of lipid membranes on the nanoscale with a high spatial resolution circumventing ensemble averaging.



The plasma membrane represents the barrier between the cell interior to the cell exterior and, hence, comprises various features such as electrical properties. Most prominently discussed is the transmembrane potential built up by different ion concentrations across the membrane, but another very important electrical membrane property is its surface potential, which locally arises at the interface between the membrane and the aqueous solution due to charges in the lipid head groups.^{1–3} Around 10–30% of the lipids in the plasma membrane carry negative charges, most of which are phosphatidylserine (PS).⁴ Lipids of different kinds are not distributed equally between the two leaflets of a lipid bilayer, and negative lipids accumulate at the inside inducing a potential of *ca.* –30 mV.⁵ This asymmetry is highly conserved in eukaryotic cells, supports the negative curvature of the membrane, and stabilizes it.^{6,7} Furthermore, the anionic surface charge offers binding sites for cationic proteins in the cytoplasm.^{8–10} To maintain the asymmetry, there are different adenosine 5'-triphosphate (ATP)-dependent enzymes such as flippases shuffling lipids from the cell exterior to the cell interior and floppases shuffling lipids *vice versa*.¹¹ Nevertheless, under certain circumstances, floppases shuffle PS to the outer leaflet, which is, *e.g.*, involved in T-cell activation.^{12,13} In the so-called immunological synapse, PS is transiently exposed to the exterior and additional lateral heterogeneities¹⁴ lead to a strong

membrane surface potential at the outside. Besides this directional reordering of lipids, there are also ATP-independent scramblases that destroy the asymmetry by mixing the lipids between the two leaflets until an equilibrium is reached.¹¹ This unspecific mixing is relevant in certain cellular processes; for example, it activates scavenger receptors on macrophages for apoptosis or is a mediator for blood clotting.¹⁵

Although the electric surface potential is an extremely relevant feature of the membrane, there are only few charge sensors that enable an easy and noninvasive characterization.¹⁶ Although dye-labeled lipids are used to visualize clustering of charged lipids, the labels do not report on whether the lipids are located in the inner or outer leaflets and the dye labels tend to distort the membrane properties. Clustering does also not report quantitative membrane charge values. A milestone was the development of a sensor based on the K-Ras motif linked

Received: November 23, 2021

Accepted: January 18, 2022

Published: January 28, 2022



to a fluorescent protein¹⁷ and the optimized genetically encoded version R-pre.¹⁸ These cationic proteins show a strong affinity for anionic lipid membranes, and their accumulation at the lipid bilayer is visualized by an increased fluorescence intensity. A PS-specific sensor was developed with the same strategy.¹⁰ However, these assays are concentration- and expression-level-dependent, which makes cell-to-cell comparisons impossible. This limitation was addressed by Ma *et al.* with the development of a genetically encoded sensor with ratiometric read-out.¹⁹ This sensor consists of two components that are both labeled with fluorescent proteins capable of fluorescence resonance energy transfer (FRET). One of the components is permanently linked to the membrane, whereas the other consists of the previously used R-pre, which binds and unbinds to the lipid membrane depending on its surface charge. Thus, the distance and orientation between the two fluorescent proteins change and result in a strong FRET change. Thereby, with a high specificity for the inner leaflet of the membrane, they achieved a read-out independent of the expression level.

As this sensor acts on the inner leaflet of the cell membrane, it is blind to processes taking place at the outer leaflet. In addition, all of the current sensors are genetically encoded, limiting the application to transfected cell lines or transgenic animals. Furthermore, investigations on the nanoscale as achieved, *e.g.*, with single-molecule and superresolution methods are lacking as fluorescent proteins are relatively dim and suffer from fast photobleaching. Thereby, local heterogeneities of the membrane surface charge distribution cannot be visualized. To address these issues, we here present a nongenetically encoded sensor for membrane surface charges at the outer leaflet as a complement to current sensors with the additional feature of an optical single-molecule read-out by employing single-molecule-compatible fluorophores.

As an assembly platform for the sensor, we use a rectangular DNA origami.^{20–22} This nanostructure is based on a 7249 nt long single-stranded DNA (ssDNA), which is folded into the desired shape by hybridization with ~200 oligonucleotides. DNA origamis have been emerging as a platform for the development of biosensors as further chemical moieties are easily introduced using modified staple strands.^{23–27} The DNA origami platform binds to membranes by incorporated cholesterol moieties. Additionally, the sensing unit is attached with FRET read-out. While the FRET acceptor is anchored to the membrane, the negatively charged fluorescent donor is attached to a flexible ssDNA protrusion that reacts to the local electric field by conformational changes. We study this DNA origami surface potential sensing system on large unilamellar vesicles (LUVs) with different lipid compositions by single-molecule fluorescence imaging. We unravel a dynamic working principle of our sensor by confocal correlation analysis, and with this information, we adopt and shift the sensitivity of our sensor. Overall, this work is a complement for investigations on the outer leaflet of membranes and has the potential to provide super-resolved insights into the lateral distribution of charged lipids in the plasma membrane without the need for genetic modifications.

■ EXPERIMENTAL SECTION

DNA Origami. The DNA origami plate^{21,22} is designed in CaDNA²⁸ and based on 7249 nt long ssDNA derived from the M13mp18 bacteriophage functioning as a scaffold. It is folded into the desired shape by short oligonucleotides,

whereby different chemical modifications are inserted (Table S1). The oligonucleotides are purchased from IDT, Eurofins Genomics GmbH, or Biomers GmbH as specified in the Supporting Information (SI). The oligonucleotides are added in a 10× excess over the scaffold in 10 mM Tris, 1 mM ethylenediaminetetraacetic acid (EDTA), 12.5 mM MgCl₂, and 1% dimethyl sulfoxide (DMSO) at pH 7.4 and in a thermocycler, and a temperature ramp with 1 min/1 °C between 70 and 20 °C is driven. The purification of the folded DNA origami structures from the excess is done by poly(ethylene glycol) (PEG) precipitation, where the solution is mixed 1:1 with a buffer containing 10 mM Tris, 1 mM EDTA, 12.5 mM MgCl₂, 500 mM NaCl, and 12% PEG-8000 at pH 7 and centrifuged at 16 000g and 4 °C for 30 min. The DNA origami collects as a pellet, whereas free oligonucleotides are in the supernatant to be discarded. This step is repeated five times. The purified DNA origami is stored at 4 °C until used.

LUV Preparation. The lipids DOPC and DOPG (Avanti Polar Lipids, Inc.) are dissolved in chloroform, and 1 mmol of lipid is added to a glass vial in the desired composition of the two lipids. The chloroform is dried under a nitrogen stream and further for 4 h under vacuum in a desiccator before the lipid films are dissolved in a buffer containing 5 mM Tris, 1 mM EDTA, 150 mM NaCl, and 0.5 mM Trolox at pH 7 and a concentration of 2.5 mM. Seven freeze–thaw cycles are done to prepare unilamellar vesicles that are afterward extruded in a LipoFast Basic extruder (Avestin, Inc.) with a 100 nm Nucleopore PC membrane (Whatman, Cytiva Ltd.) to produce LUVs at the desired size. They are stored at 4 °C until usage.

Surface and Sample Preparation. The samples are imaged in Nunc Lab-Tek II Chambered Slides (Thermo Fisher Scientific, Inc.), which are cleaned with 1 M KOH for 4 h, washed with 1× phosphate-buffered saline (PBS), and passivated with 0.5 mg/mL PLL(20)-g[3.5]-PEG(2)/PEG(3.4)-biotin (50%) (PLL-PEG-biotin, SuSoS AG) in 1× PBS overnight at 4 °C. After washing, 0.25 mg/mL NeutrAvidin (Thermo Fisher Scientific, Inc.) in 1× PBS is added and washed off after 20 min providing binding sites for the biotinylated DNA origami. Meanwhile, the DNA origami is mixed with LUVs in a 100× excess overnight at room temperature. The DNA origami–LUV complexes or the pure DNA origami are bound to the microscopy slides at a concentration of 30–50 pM and imaged in the LUV buffer containing 5 mM Tris, 1 mM EDTA, 150 mM NaCl, and 0.5 mM Trolox at pH 7, where the Trolox suppresses blinking of the dyes.²⁹

Total Internal Reflection Fluorescence (TIRF) Microscope. For the single-molecule FRET (smFRET) measurements, a homebuilt TIRF microscope is used. It is based on an Olympus IX-71 (Olympus Deutschland GmbH) microscope body and has a green laser set to 50 mW (Sapphire 532 nm, 100 mW, Coherent) and a red laser set to 80 mW (iBeam Smart 640 nm, 150 mW, Toptica Photonics). The laser beams are alternated by an acousto-optical tunable filter (AOTF, PCAOM-VIS, Crystal Technology) at a frequency of 10 Hz and focused on the sample with an oil-immersion objective (APO N 60XO/1.49 NA TIRF, Olympus). A dual-line beam splitter separates the excitation from the emission light, before the green and red emissions are further separated by an Optosplit III (Cairn Research) equipped with a dichroic beam splitter (640 DCXR, Chroma Technology), a bandpass filter

for green (BrightLine HC582/75, Semrock), and a long-pass filter for red (647 nm RazorEdge, Semrock). The light is finally focused on a back-illuminated sCMOS camera (KURO 1200B sCMOS, Princeton Instruments) in a dual-view configuration, and the LightField software (Princeton Instruments) is used to acquire videos with 600 frames.

smFRET Analysis. To analyze the data acquired in TIRF measurements, the software iSMS³⁰ is used, where the two split channels are superimposed, and for each spot with green and red fluorescence, an intensity transient is created for the length of the video. The transients are carefully and visually reviewed to exclude DNA origami multimers or aggregates. Only transients showing a clear correlation between the different emission channels discussed in the **Results and Discussion** section typical for single-molecule FRET pairs are picked. The Proximity Ratio (PR) is presented for each frame, and its mean is calculated for the time in which the energy transfer takes place delivering one data point. The data are further analyzed in frequency count plots where a single- or double-Gauss fit is applied to determine the mean PR and its standard error of the mean (SEM) as shown in the **SI**.

Confocal Microscopy. The confocal microscopy setup is based on an Olympus IX-71 (Olympus Deutschland GmbH) inverted microscope. For excitation, a pulsed 532 nm laser (532 nm, LDH-P-FA-530B, PicoQuant GmbH) is used with a repetition rate of 50 MHz and a power of 1.5 μ W in front of the objective. After passing a single-mode fiber (P3-488PM-FC, Thorlabs GmbH), the light is circularly polarized by a linear polarizer (LPVISE100-A, Thorlabs GmbH) and a quarter-wave plate (AQWP05M-600, Thorlabs GmbH). An oil-immersion objective (UPLSAPO100XO, NA 1.40, Olympus Deutschland GmbH) focuses the light onto the sample, which is moved by a piezo stage (P-517.3CD, Physik Instrumente (PI) GmbH & Co. KG) controlled by a piezo controller (E-727.3CDA, Physik Instrumente (PI) GmbH & Co. KG). A dichroic mirror (zt532/640rpc, Chroma) separates the excitation from the emission channel. The light is then focused onto a 50 μ m diameter pinhole (Thorlabs GmbH) and further split into a green channel and a red channel with a dichroic mirror (640 LPXR, Chroma). Afterwards, it is spectrally cleaned by filters (donor detection path: Brightline HC582/75, AHF; RazorEdge LP 532, Semrock; Acceptor detection path: SP 750, ThorLabs; RazorEdge LP 647, Semrock). The photons are detected on avalanche photodiodes (SPCM-AQRH-14-TR, Excelitas) and signals registered by a time-correlated single-photon counting (TCSPC) unit (HydraHarp400, PicoQuant GmbH). For controlling the microscope, a commercial software package is used (SymPho-Time64, Picoquant GmbH).

Correlation Analysis. Shrinking-gate fluorescence correlation spectroscopy (sg-FCS) analysis is performed with home-written Python scripts based on the correlation algorithm proposed by Laurence *et al.*³¹ and published in Schröder *et al.*³² A detailed description can be found in the **Supporting Information**.

RESULTS AND DISCUSSION

The sensors are based on flat, rectangular DNA origami plates with a dimension of 70 \times 100 nm² (Figures 1a and S1)^{20–22} and have to fulfill three functions: outer leaflet membrane targeting, surface charge sensing, and optical signal transduction. For membrane targeting, seven staple strands are equipped with cholesterol moieties.³³ As a charge sensing unit,

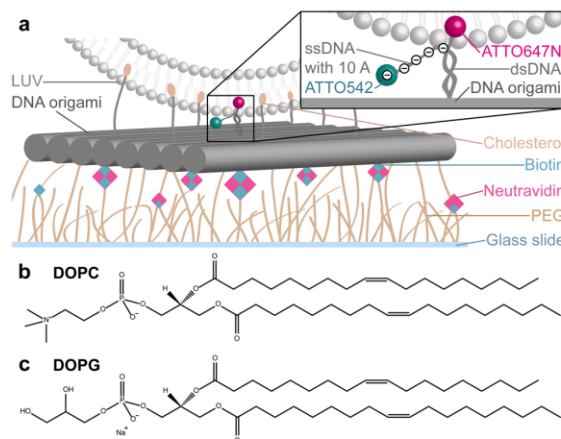


Figure 1. (a) Design of the surface charge-sensing DNA origami. On a rectangular DNA origami nanostructure (gray), cholesterol is placed for liposome binding (beige) to bind to a LUV (light gray) and biotins (blue) for surface immobilization by biotin–neutravidin (rose) interactions on a biotinylated PEG glass slide. Inset: design of the Leash A₂ sensing unit. A dsDNA strand carries an ATTO647N (pink) and on a polyA leash an ATTO542 (cyan). (b) Chemical structures of 1,2-dioleoyl-*sn*-glycero-3-phosphocholine (DOPC) and (c) 1,2-dioleoyl-*sn*-glycero-3-phospho-(1'-*rac*-glycerol) (DOPG).

we use an ssDNA labeled with the strongly negatively charged green fluorophore ATTO542. This flexible ssDNA leash (termed Leash A₂) extends a double-stranded DNA (dsDNA) protruding on the same side of the DNA origami as the cholesterol, and its conformation can respond to a changing electrostatic environment (see Figure 1a for a sketch and Figure S2 for chemical structures).

The surface potential depends on the charge composition of the membrane leaflet and decays with a characteristic Debye length that represents the distance to the membrane surface at which the potential decreased to 1/*e* of its maximum.³⁴ For a 150 mM NaCl solution, *i.e.*, under physiologically relevant conditions, the Debye length is \sim 0.78 nm. This number suggests that the sensing unit has to be in close proximity to the membrane surface. We therefore anchor the anionic sensing unit to the membrane with the hydrophobic red dye ATTO647N.^{35,36} The anchor ATTO647N also acts as a FRET acceptor for the donor ATTO542. The FRET efficiency sensitively and ratiometrically reports on the electrical potential-driven distance of the charged sensing unit consisting of the negatively charged DNA tether and the negatively charged ATTO542.

To demonstrate surface charge sensing on membranes and to study the mechanism of the sensor, we use LUVs with a diameter of 100 nm as a model system. We mix the zwitterionic lipid 1,2-dioleoyl-*sn*-glycero-3-phosphocholine (DOPC) and the anionic 1,2-dioleoyl-*sn*-glycero-3-phospho-(1'-*rac*-glycerol) (DOPG) in defined ratios for LUVs resulting in different surface charges (see Figure 1b,c for chemical structures). The LUVs are immobilized on top of the DNA origami structures that bind on PLL-g-PEG-biotin-passivated coverslips by biotin–neutravidin interaction with six biotin moieties protruding from the other side of the DNA origami structure. This avoids direct membrane–surface interaction and provides a homogeneous environment for the sensor–LUV system.³⁷

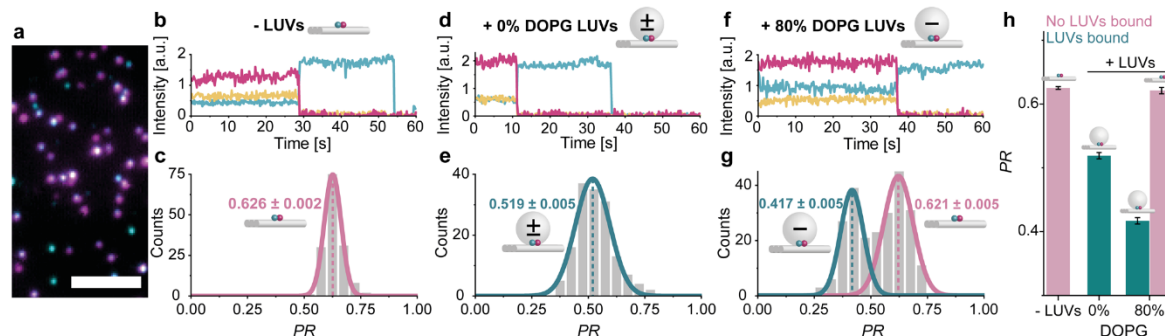


Figure 2. smFRET measurements of the sensor Leash A_2 . (a) Superimposed TIRF image with donor fluorescence in cyan, acceptor in magenta, and both in white. The scale bar refers to $5 \mu\text{m}$. Exemplary intensity transients and proximity ratio (PR) distributions with Gauss fits for the sample without (b, c), with 0% DOPG LUVs (d, e), and with 80% DOPG LUVs (f, g). The donor excitation–donor emission channel in blue, the donor excitation–acceptor emission in yellow, and the acceptor excitation–acceptor emission in pink. The mean value with its standard error of the mean is presented for each peak. $N_{\text{molecules}}$: (c) 150, (e) 150, and (g) 238. (h) Comparison of mean PR for the LUV-unbound populations in rose and LUV-bound in cyan. Error bars refer to the standard error of the mean.

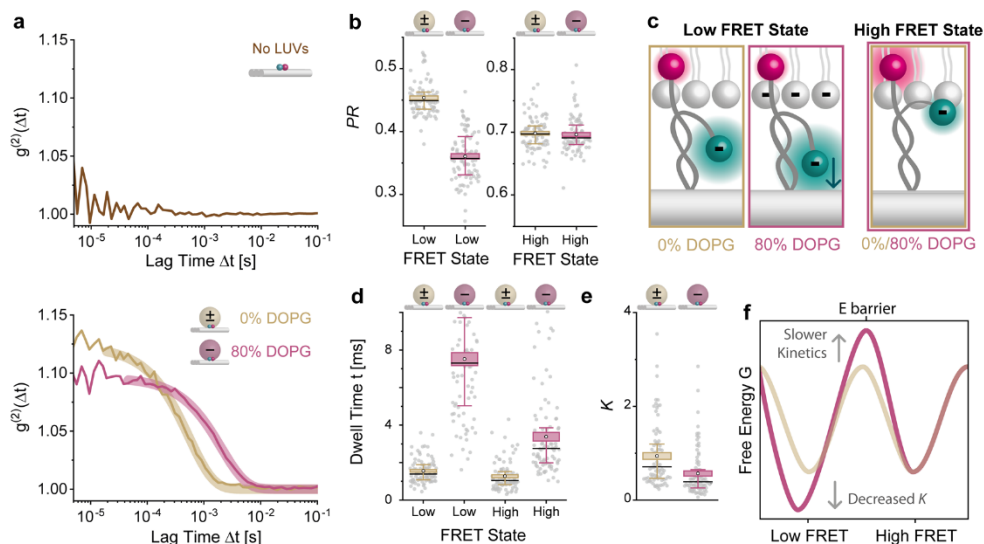


Figure 3. Autocorrelation analysis for Leash A_2 from confocal single-molecule data. (a) Exemplary single-molecule autocorrelation curves of the donor for sensor without LUVs (top) and with 0% (bottom, beige) and 80% (bottom, pink) DOPG LUVs and their monoexponential fits in the respective color. (b) Proximity ratio (PR) for both states of the sensor with 0% (beige) and 80% DOPG LUVs (pink). Black circles show mean, the box shows \pm SEM, the black line shows median, and the whiskers show the percentile of $\pm 2.5\%$. (c) Proposed conformation of the sensor Leash A_2 in both states. (d) Dwell times in the low- and high-FRET states for the sensor with 0% (beige) and 80% DOPG LUVs (pink) and (e) their equilibrium constant K . The boxplots indicate the same as in (b). (f) Energy landscape describing the two states for the sensor with 0% (beige) and 80% DOPG LUVs (pink). $N_{\text{molecules}}$ in (b), (c), and (e): 87 for 0% DOPG, 86 for 80% DOPG.

For single-molecule FRET (smFRET) measurements,³⁸ a homebuilt total internal reflection fluorescence (TIRF) microscope is used with a green-red alternating laser excitation (ALEX)^{39,40} as well as a dual view of the green and red emission channel separately on an sCMOS camera chip (for details, see the [Experimental Section](#)). With an alternation rate of 10 Hz, videos are acquired for 60 s, and by superimposing the two emission channels (Figure 2a), for each molecule, an intensity transient for three different channels is extracted³⁰ as illustrated in Figure 2b. Blue indicates the intensity of the channel with donor excitation and donor emission $I_{D_{\text{ex-D}_{\text{em}}}}$, yellow indicates the intensity of donor excitation and acceptor emission $I_{D_{\text{ex-A}_{\text{em}}}}$, and pink indicates the intensity of

acceptor excitation and acceptor emission $I_{A_{\text{ex-A}_{\text{em}}}}$. In the first ~ 28 s, $I_{D_{\text{ex-D}_{\text{em}}}}$ is relatively low as the donor transfers its energy to the acceptor, which is visible as $I_{D_{\text{ex-A}_{\text{em}}}}$ intensity. The intensity $I_{A_{\text{ex-A}_{\text{em}}}}$ is independent of FRET and indicates photobleaching of the acceptor after ~ 28 s going along with $I_{D_{\text{ex-A}_{\text{em}}}}$ dropping to 0 as no more energy is transferred. Simultaneously, $I_{D_{\text{ex-D}_{\text{em}}}}$ increases until the donor also photobleaches at 54 s. From $I_{D_{\text{ex-D}_{\text{em}}}}$ and $I_{D_{\text{ex-A}_{\text{em}}}}$ before acceptor photobleaching, the energy transfer is quantified as the proximity ratio (PR) with

$$\text{PR} = \frac{I_{D_{\text{ex-A}_{\text{em}}}}}{I_{D_{\text{ex-D}_{\text{em}}}} + I_{D_{\text{ex-A}_{\text{em}}}}} \quad (1)$$

Each molecule showing a typical single-molecule correlation between the three channels discussed above delivers a data point. The resulting histogram for the LUV-free sample (Figure 2c) is fitted with a Gaussian distribution from which a mean PR value of 0.626 ± 0.002 (\pm standard error of the mean, SEM) is obtained. Once exposed to uncharged LUVs composed of 0% DOPG and 100% DOPC, the PR drops to 0.519 ± 0.005 (Figure 2d,e). The shift toward a lower PR indicates a spatial separation of the two dyes and is taken as an indicator for the successful binding of LUVs and the insertion of the ATTO647N to the hydrophobic membrane core.^{35,36}

Next, the sensors are exposed to LUVs with a negative surface charge induced by 80% DOPG. The transient shown in Figure 2f exhibits a further reduced energy transfer compared to neutral LUVs. Analysis of many transients yields a bimodal distribution (Figure 2g) with two distinct peaks: the first with a mean PR of 0.417 ± 0.005 and the second with a mean PR of 0.621 ± 0.005 . For the similar appearance and the reduced binding efficiency due to stronger coulombic repulsion between negatively charged vesicles and negatively charged DNA origamis, we assign the high-FRET distribution to sensors that did not bind a vesicle. Figure 2h compares the PR values discussed above and shows that the high PR population in the 80% DOPG sample is similar to the one obtained for the LUV-free sample. As intended, the PR derived from the LUV-bound fraction of the 80% DOPG sample is reduced by $\Delta\text{PR} = 0.10$ compared to the 0% DOPG sample, indicating that our DNA origami sensor is responsive to the surface charges. Intuitively, a reduction in PR implies a further spatial separation between the membrane-anchored ATTO647N and the ATTO542 on the flexible ssDNA leash. From previous simulations, it is known that in a DOPC membrane, ATTO647N is mainly located in the hydrophobic core of the membrane with its positive charge interacting with the phosphates of the lipid head groups.^{35,36} It is not expected that the lipid composition has a substantial effect on the position of ATTO647N in the membrane as structural differences between the lipids are on the hydrophilic side. Hence, we reason that any change observed results from a movement of the flexible ssDNA-ATTO542 Leash A₂. Following this intuition, the electrostatic repulsion between Leash A₂ and the negatively charged membrane leads to an increased distance of the donor ATTO542 and the acceptor ATTO647N.

At the close to physiological salt conditions employed, the electrostatic potential is decreasing within only a couple of nanometers so that we wonder whether the additional repulsion between the leash and the membrane is sufficient to displace the equilibrium position of the donor dye or whether another mechanism explains the FRET change observed. To obtain a closer look, we record smFRET transients with higher time resolution using a confocal setup equipped with two color channels and time-correlated single-photon counting (for details, see the Experimental Section). The autocorrelation analysis of the donor signal $I_{D_{ex-D_{em}}}$ of the DNA origami sensor Leash A₂ without LUVs reveals a flat autocorrelation (see Figure 3a for exemplary autocorrelation of a single-molecule transient, top panel) indicating the absence of dynamics on the micro- to millisecond timescale.

Interestingly, for both the sample with LUVs composed of 0% and 80% DOPG, the autocorrelation curves show a pronounced monoexponential bunching amplitude in the ca. 1–10 ms range (see exemplary autocorrelation in Figure 3a

bottom), indicating transitions between two distinct intensity states. To study the origin of this fluctuation, we apply recently developed shrinking-gate fluorescence correlation spectroscopy (sg-FCS) that uses the fluorescence lifetime information to select subsets of photons for the analysis.^{32,41} This analysis distinguishes on–off fluctuations, e.g., induced by photo-physical off-states such as triplet states and radical-ion states from FRET dynamics that go along with a change of the fluorescence lifetime τ . Although conventional FCS only yields the characteristic time of a correlation component, sg-FCS also yields the dwell times in the states (in a two-state system) as well as the equilibrium constant and the Proximity Ratios of the two states.^{32,41}

For both membrane compositions, the analysis by sg-FCS reveals two distinct FRET states of our sensor analyzed in terms of the proximity ratio ($\text{PR}_{\text{State } x} = 1 - \frac{\tau_{\text{State } x}}{\tau_0}$, see the SI for details and Figure S5 for τ_0). Interestingly, the high-FRET state has almost identical PRs for both membrane compositions, whereas the low-FRET state exhibits a lower PR in the case of the negatively charged membrane (Figure 3b). We reason that the high-FRET state results from direct interactions of the sensing unit with the membrane. The low-FRET state, on the other hand, represents a state in which the sensing unit is separated from the membrane. For the negatively charged membrane, the average position of this fluctuation is further away from the membrane, yielding a lower PR for the low-FRET state as schematically depicted in Figure 3c. To elucidate whether the structural difference of the low-FRET state is sufficient to explain the average FRET change for the two different membrane compositions, we also extract the dwell times of the high- and low-FRET states (Figure 3d). For the neutral LUV, the dwell times of both states are similar and typically between 1 and 2 ms (beige). In contrast, the dwell time of the low-FRET state for the negatively charged LUVs is substantially longer ($t_{\text{low FRET}} = 0.008 \pm 0.003$ s, standard deviation) but the dwell time of the high-FRET state is somewhat longer ($t_{\text{high FRET}} = 0.0013 \pm 0.0008$ s), indicating an overall higher energy barrier between the states for the 80% DOPG liposomes. Further, the equilibrium constant $K = \frac{t_{\text{high FRET}}}{t_{\text{low FRET}}}$ is shifted so that the low-FRET state is preferred for negatively charged LUVs (Figure 3e).

The FRET efficiency analysis and the kinetic analysis are combined for the schematic energy landscape diagram in Figure 3f. For both membrane compositions, we observe an equilibrium between high- and low-FRET states that we ascribe to a membrane-bound and a membrane-unbound state of the sensing unit. In the case of the negatively charged LUVs, the transitions between the states are slower, which we assign to a higher energy barrier. However, for the 0% DOPG sample, the two states are equally occupied and, thus, their energies are similar; for negatively charged LUVs, the dwell time in the membrane-unbound state is higher, and therefore, this state is energetically lower. Also, the average position of the unbound state is further away from the membrane (states separated further on the reaction coordinate x). In summary, the overall FRET difference between neutral and negatively charged membranes results from a superposition of both a distance change of the low-FRET state and a change of the population of the two states.

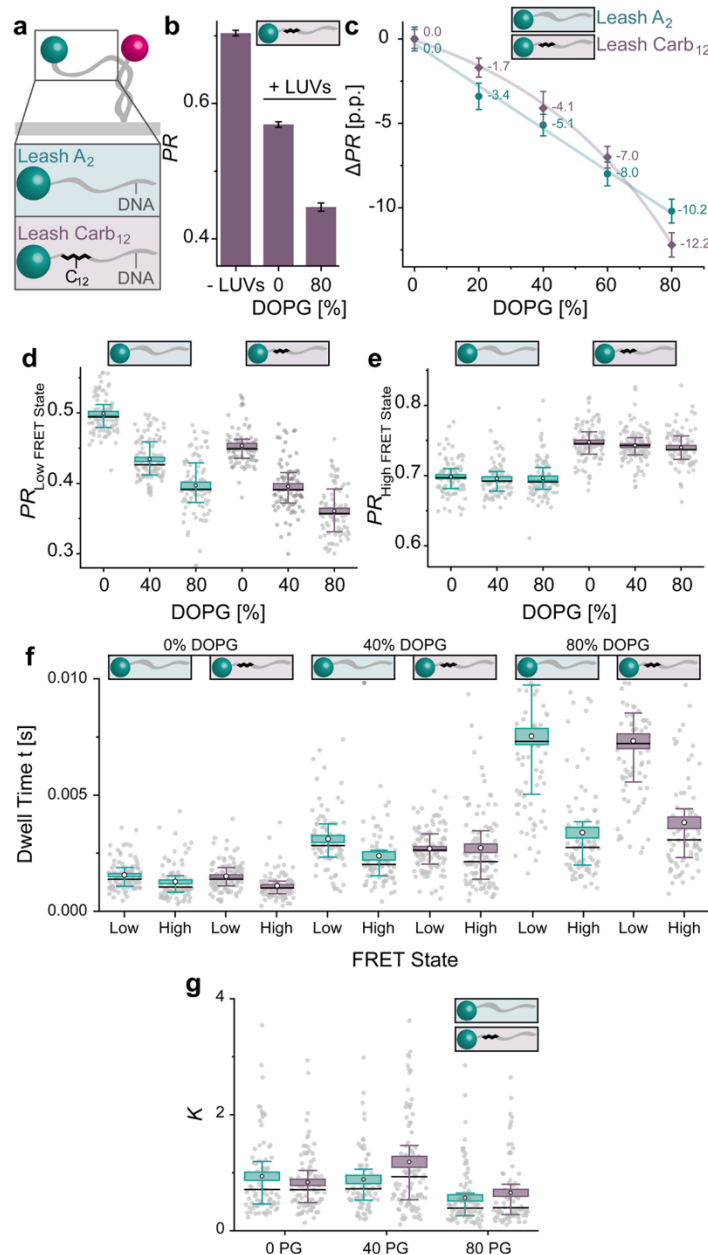


Figure 4. (a) Sketch showing the structure of the two sensing units Leash A₂ and Leash Carb₁₂. (b) Comparison of mean PR derived from TIRF measurements for Leash Carb₁₂. For the + LUV samples, the mean of the LUV-bound population is indicated. Error bars represent SEM. $N_{\text{molecules}}$ for -LUVs and +0 and +80% DOPG LUVs: 150, 156, and 230, respectively. (c) Changes of ΔPR derived from TIRF measurements. Leash A₂ (cyan) and Leash Carb₁₂ (purple) are exposed to LUVs with different DOPG contents. Error bars show the SEM after Gaussian error propagation, and the fit helps guiding the eye. $N_{\text{molecules}}$ for Leash A₂ with 0, 20, 40, 60, and 80% DOPG LUVs: 150, 200, 150, 150, and 238, respectively. $N_{\text{molecules}}$ for Leash Carb₁₂ with 0, 20, 40, 60, and 80% DOPG LUVs: 156, 200, 200, 200, and 230, respectively. (d, e) PR of low-FRET state and high-FRET state derived from confocal sg-FCS analysis for Leash A₂ (cyan) and Leash Carb₁₂ (purple) with different LUVs. (f) Dwell times of each sample in both states and (g) the resulting equilibrium constant K . Black circles show mean, the box shows $\pm\text{SEM}$, the black line shows median, and the whiskers show the percentile of $\pm 25\%$. $N_{\text{molecules}}$ for Leash A₂ with 0, 40, and 80% DOPG: 87, 80, and 86, respectively. $N_{\text{molecules}}$ for Leash Carb₁₂ with 0, 40, and 80% DOPG: 92, 103, and 80, respectively.

Next, we study the sensitivity of the sensing unit for small structural changes. In the original design, termed Leash A₂, the flexible element consists of a polyadenine ssDNA. We

exchange two of the adenines close to the ATTOS42 dye by a 12-carbon alkyl spacer (termed Leash Carb₁₂) as depicted in Figure 4a. For the chemical structure, see Figure S2. The

nonpolar carbon chain could potentially insert into the membrane core, has a reduced charge density in the sensing unit, and thus alters the dynamic behavior. The same experiments as for Leash A₂ are performed, and the resulting PR distributions are shown in Figure S4. The PR obtained for the LUV-free sample is 0.704 ± 0.004 (Figure 4b). Once the sensor is exposed to 0% DOPG LUVs, the PR drops to 0.569 ± 0.004 for the vesicle-bound fraction and further to 0.447 ± 0.006 with 80% DOPG LUVs. This trend indicates a similar behavior to that observed for Leash A₂ with a slightly increased contrast between uncharged and charged membranes.

To characterize the sensors in more detail, both Leash A₂ and Leash Carb₁₂ are exposed to LUVs with different surface charges induced by DOPG contents of 0, 20, 40, 60, and 80%. For a clear comparison of the two designs, the PR change ΔPR in percent points (p.p.) is calculated by

$$\Delta\text{PR} = (\text{PR}_{x\% \text{ DOPG}} - \text{PR}_{0\% \text{ DOPG}}) \times 100 \quad (2)$$

where x is the DOPG fraction. The standard error of the mean is calculated by applying Gaussian error propagation as described in the SI, and the results are shown in Figure 4c (see Figures S3 and S4 for the corresponding PR distributions). Both sensors show a consistent PR decrease with increasing DOPG content, which implies that we are able to quantitatively translate a surface charge into a fluorescent signal. Interestingly, with the introduction of the Carb₁₂ spacer, the sensitivity is lower for a low DOPG content but then becomes steeper in comparison to Leash A₂ (Figure 4c). Our autocorrelation analyses of confocal single-molecule transients recorded for DOPG contents of 0, 40, and 80% reveal similar FRET states for both sensing units with a moderately increased FRET contrast between the high- and low-FRET states for the Carb₁₂ sensing unit (Figure 4d,e). Most strikingly, the transitions between the two FRET states become slower for both sensors with increasing negative membrane charge (see Figure 4f). The different response of the two sensors results from the dwell times reacting slightly differently to the DOPG content. This different reaction is also reflected in the equilibrium constant K that gradually decreases for the Leash A₂ sensor, whereas it has a maximum for the Carb₁₂ sensor at 40% DOPG (Figure 4g). In summary, the FRET dependence on the DOPG content is controlled by a combination of two factors. The FRET efficiency of the low-FRET state decreases, and the equilibrium constant is also overall shifting favoring the low-FRET state for high DOPG content.

CONCLUSIONS

The asymmetric distribution of lipids among the two leaflets call for sensors that can interrogate the properties of both sides independently. In this work, we present a DNA origami-based sensor for negative membrane surface charges with a single-molecule fluorescence read-out. Using DNA nanotech, different functionalities required are combined into small sensors. Targeting of membranes, sensing and read-out are introduced and developed modularly and sequentially. We achieve specific binding of the sensors to the membrane's outer leaflet, sense the electric surface charge, and translate it to an optical signal, which might have the potential to detect physiologically relevant changes. Employing some of the brightest and most photostable dyes, single-molecule FRET can be used for read-out avoiding ensemble averaging and opening the option of superresolution imaging. An application to biological systems could unravel nanoclusters of anionic lipids as well as their

approximate composition. Beyond that, by understanding the working principle of the sensor, we demonstrate how specifically positioned molecular adjustments can tune the sensor. We show simple adaptations of the sensor by modifying the sensing unit with a hydrophobic linker yielding a sensor with a different response function. Further directions could be the incorporation of many sensing units on one DNA origami to create sensing islands with a high signal. Alternatively, the sensor could be stripped off unnecessary parts to create smaller sensors. Overall, a versatile approach for sensing membrane surface charges is presented which is complementary to previously published genetically encoded sensors as it binds to the opposite membrane leaflet.

ASSOCIATED CONTENT

Supporting Information

The Supporting Information is available free of charge at <https://pubs.acs.org/doi/10.1021/acs.analchem.1c05092>.

Details on DNA origami; additional data from measurements on TIRF microscope; detailed information on correlation analysis; and additional data from measurements on confocal microscopy (PDF)

AUTHOR INFORMATION

Corresponding Author

Philip Tinnefeld – Department of Chemistry and Center for NanoScience, Ludwig-Maximilians-Universität München, 81377 München, Germany; orcid.org/0000-0003-4290-7770; Email: philip.tinnefeld@cup.uni-muenchen.de

Authors

Sarah E. Ochmann – Department of Chemistry and Center for NanoScience, Ludwig-Maximilians-Universität München, 81377 München, Germany; orcid.org/0000-0002-7553-4600

Tim Schröder – Department of Chemistry and Center for NanoScience, Ludwig-Maximilians-Universität München, 81377 München, Germany; orcid.org/0000-0002-2474-5395

Clara M. Schulz – Department of Chemistry and Center for NanoScience, Ludwig-Maximilians-Universität München, 81377 München, Germany

Complete contact information is available at: <https://pubs.acs.org/doi/10.1021/acs.analchem.1c05092>

Author Contributions

The manuscript was written through contributions of all authors.

Notes

The authors declare no competing financial interest.

ACKNOWLEDGMENTS

This work was supported by the Deutsche Forschungsgemeinschaft DFG (grants INST 86/1904-1 FUGG, TI 329/10-1, Project-ID: 201269156-SFB1032, excellence cluster e-conversion under Germany's Excellence Strategy—EXC2089/1-390776260). The authors thank Dr. Henri G. Franquelim for providing equipment for the LUV production.

REFERENCES

- (1) Ma, Y.; Poole, K.; Goyette, J.; Gaus, K. *Front. Immunol.* **2017**, *8*, No. 1513.

- (2) Ohki, S. *Phys. Lett. A* **1979**, *75*, 149–152.
- (3) Ben-Tal, N.; Honig, B.; Peitzsch, R. M.; Denisov, G.; McLaughlin, S. *Biophys. J.* **1996**, *71*, S61–S75.
- (4) Vance, J. E.; Steenbergen, R. *Prog. Lipid Res.* **2005**, *44*, 207–234.
- (5) McLaughlin, S. *Annu. Rev. Biophys. Biophys. Chem.* **1989**, *18*, 113–136.
- (6) Manno, S.; Takakuwa, Y.; Mohandas, N. *Proc. Natl. Acad. Sci. U.S.A.* **2002**, *99*, 1943–1948.
- (7) Xu, P.; Baldrige, R. D.; Chi, R. J.; Burd, C. G.; Graham, T. R. *J. Cell Biol.* **2013**, *202*, 875–886.
- (8) McLaughlin, S.; Murray, D. *Nature* **2005**, *438*, 605–611.
- (9) Heo, W. D.; Inoue, T.; Park, W. S.; Kim, M. L.; Park, B. O.; Wandless, T. J.; Meyer, T. *Science* **2006**, *314*, 1458–1461.
- (10) Yeung, T.; Gilbert, G. E.; Shi, J.; Silvius, J.; Kapus, A.; Grinstein, S. *Science* **2008**, *319*, 210–213.
- (11) Fadeel, B.; Xue, D. *Crit. Rev. Biochem. Mol. Biol.* **2009**, *44*, 264–277.
- (12) Elliott, J. I.; Surprenant, A.; Marelli-Berg, F. M.; Cooper, J. C.; Cassady-Cain, R. L.; Wooding, C.; Linton, K.; Alexander, D. R.; Higgins, C. F. *Nat. Cell Biol.* **2005**, *7*, 808–816.
- (13) Rysavy, N. M.; Shimoda, L. M. N.; Dixon, A. M.; Speck, M.; Stokes, A. J.; Turner, H.; Umemoto, E. *Y. Bioarchitecture* **2014**, *4*, 127–137.
- (14) Gagnon, E.; Schubert, D. A.; Gordo, S.; Chu, H. H.; Wucherpfennig, K. W. *J. Exp. Med.* **2012**, *209*, 2423–2439.
- (15) Zwaal, R. F. A.; Comfurius, P.; Bevers, E. M. *CML.S, Cell. Mol. Life Sci.* **2005**, *62*, 971–988.
- (16) Leventis, P. A.; Grinstein, S. *Annu. Rev. Biophys.* **2010**, *39*, 407–427.
- (17) Okeley, N. M.; Gelb, M. H. *J. Biol. Chem.* **2004**, *279*, 21833–21840.
- (18) Yeung, T.; Terebiznik, M.; Yu, L.; Silvius, J.; Abidi, W. M.; Phillips, M.; Levine, T.; Kapus, A.; Grinstein, S. *Science* **2006**, *313*, 347–351.
- (19) Ma, Y.; Yamamoto, Y.; Nicovich, P. R.; Goyette, J.; Rossy, J.; Gooding, J. J.; Gaus, K. *Nat. Biotechnol.* **2017**, *35*, 363–370.
- (20) Rothmund, P. W. K. *Nature* **2006**, *440*, 297–302.
- (21) Woo, S.; Rothmund, P. W. K. *Nat. Chem.* **2011**, *3*, 620–627.
- (22) Schmied, J. J.; Gietl, A.; Holzmeister, P.; Forthmann, C.; Steinhauer, C.; Dammeyer, T.; Tinnefeld, P. *Nat. Methods* **2012**, *9*, 1133–1134.
- (23) Shen, L.; Wang, P.; Ke, Y. *Adv. Healthcare Mater.* **2021**, *10*, No. 2002205.
- (24) Thomsen, R. P.; Malle, M. G.; Okholm, A. H.; Krishnan, S.; Bohr, S. S.-R.; Sørensen, R. S.; Ries, O.; Vogel, S.; Simmel, F. C.; Hatzakis, N. S.; et al. *Nat. Commun.* **2019**, *10*, No. 5655.
- (25) Zhang, Q.; Jiang, Q.; Li, N.; Dai, L.; Liu, Q.; Song, L.; Wang, J.; Li, Y.; Tian, J.; Ding, B.; et al. *ACS Nano* **2014**, *8*, 6633–6643.
- (26) Saminathan, A.; Devany, J.; Veetil, A. T.; Suresh, B.; Pillai, K. S.; Schwake, M.; Krishnan, Y. *Nat. Nanotechnol.* **2021**, *16*, 96–103.
- (27) Wang, W.; Arias, D. S.; Deserno, M.; Ren, X.; Taylor, R. E. *APL Bioeng.* **2020**, *4*, No. 041507.
- (28) Douglas, S. M.; Marblestone, A. H.; Teerapittayanon, S.; Vazquez, A.; Church, G. M.; Shih, W. M. *Nucleic Acids Res.* **2009**, *37*, S001–S006.
- (29) Cordes, T.; Vogelsang, J.; Tinnefeld, P. *J. Am. Chem. Soc.* **2009**, *131*, S018–S019.
- (30) Preus, S.; Noer, S. L.; Hildebrandt, L. L.; Gudnason, D.; Birkedal, V. *Nat. Methods* **2015**, *12*, 593–594.
- (31) Laurence, T. A.; Fore, S.; Huser, T. *Opt. Lett.* **2006**, *31*, 829–831.
- (32) Schröder, T.; Bohlen, J.; Ochmann, S. E.; Schüler, P.; Krause, S.; Tinnefeld, P. Systematic Microtime Gating for Fluorescence Correlation Spectroscopy Yields Equilibrium Constants and Allows Discrimination of Photophysics from Structural Dynamic Processes, in preparation, 2022.
- (33) Czogalla, A.; Petrov, E. P.; Kauert, D. J.; Uzunova, V.; Zhang, Y.; Seidel, R.; Schuille, P. *Faraday Discuss.* **2013**, *161*, 31–43. discussion 113–150.
- (34) Debye, P.; Hückel, E. *Phys. Z.* **1923**, *24*, 185–206.
- (35) Eggeling, C.; Ringemann, C.; Medda, R.; Schwarzmann, G.; Sandhoff, K.; Polyakova, S.; Belov, V. N.; Hein, B.; Middendorff, C.; von Schönle, A.; et al. *Nature* **2009**, *457*, 1159–1162.
- (36) Ochmann, S. E.; Joshi, H.; Büber, E.; Franquelim, H. G.; Stegemann, P.; Saccà, B.; Keyser, U. F.; Aksimentiev, A.; Tinnefeld, P. *Nano Lett.* **2021**, *21*, 8634–8641.
- (37) Gietl, A.; Holzmeister, P.; Grohmann, D.; Tinnefeld, P. *Nucleic Acids Res.* **2012**, *40*, No. e110.
- (38) Ha, T.; Enderle, T.; Ogletree, D. F.; Chemla, D. S.; Selvin, P. R.; Weiss, S. *Proc. Natl. Acad. Sci. U.S.A.* **1996**, *93*, 6264–6268.
- (39) Kapanidis, A. N.; Lee, N. K.; Laurence, T. A.; Doose, S.; Margeat, E.; Weiss, S. *Proc. Natl. Acad. Sci. U.S.A.* **2004**, *101*, 8936–8941.
- (40) Margeat, E.; Kapanidis, A. N.; Tinnefeld, P.; Wang, Y.; Mukhopadhyay, J.; Ebright, R. H.; Weiss, S. *Biophys. J.* **2006**, *90*, 1419–1431.
- (41) Kamińska, I.; Bohlen, J.; Yaadav, R.; Schüler, P.; Raab, M.; Schröder, T.; Zähringer, J.; Zielonka, K.; Krause, S.; Tinnefeld, P. *Adv. Mater.* **2021**, *33*, No. e2101099.

JACS Au
AN OPEN ACCESS JOURNAL OF THE AMERICAN CHEMICAL SOCIETY

Editor-in-Chief
Prof. Christopher W. Jones
Georgia Institute of Technology, USA

Open for Submissions

pubs.acs.org/jacsau ACS Publications
Most Trusted. Most Cited. Most Read.

Supporting Information for

Quantitative Single-Molecule Measurements of Membrane Charges with DNA Origami Sensors

*Sarah E. Ochmann, Tim Schröder, Clara M. Schulz, Philip Tinnefeld**

Department of Chemistry and Center for NanoScience, Ludwig-Maximilians-Universität
München, 81377 München, Germany

* Philip Tinnefeld: philip.tinnefeld@cup.uni-muenchen.de

Content

Details on DNA Origami.....	2
Additional Data from Measurements on TIRF Microscope.....	13
Detailed Information on Correlation Analysis.....	15
Additional Data from Measurements on Confocal Microscope.....	17

Details on DNA Origami

The DNA origami is a rectangular plate with dimensions of 100x70 nm. Different chemical modifications are incorporated as illustrated in Figure S1 with the scaffold in grey, unmodified oligonucleotides in black, biotinylated in cyan, cholesterol-modified in yellow and the surface charge sensor in red.

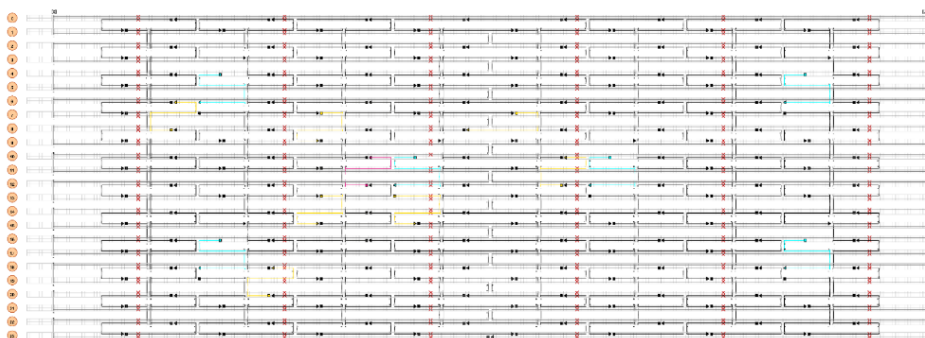


Figure S1. DNA origami design in CaDNAno with the helix number in orange and the nucleotide position on the top starting with [8] and ending at [295]. The scaffold strand is shown in dark grey, unmodified oligonucleotides in black, biotinylated in blue, cholesterol-modified in yellow and the charge sensor in red.

The sequences according to the position marked in Figure S1 are listed in Table S1. Also, the modifications are given as well as the company from which the oligonucleotides are purchased from.

Table S1. Staple strands for the DNA origami. x[y] indicates the 5' position as depicted in Figure S1 with x as the helix number and y as the nucleotide number. Modifications to the DNA oligonucleotides are listed under Comments. Nucleotides in bold are not incorporated into the DNA origami, but protrude from the structure.

5' position	Sequence (5' to 3' end)	Comments	Company
12[111]	[ATTO647N]TAACAATCGTGACTCA TATAAATCATATAACCTGTTTAGCTAAC CTTTAA	ATTO647N anchor, binding site for Leash [ATTO647N]: modification on amino-C6 linker	Eurofins Genomics GmbH
/	TATGAGTGACACGATTGTTAAAAAAA AAA[ATTO542]	Sensor Leash A ₂ , binds to 12[111] [ATTO542]: modification on amino-C6 linker	Biomers GmbH
/	TATGAGTGACACGATTGTTAAAAAAA [SpC12]A[ATTO542]	Sensor Leash Carb ₁₂ , binds to 12[111] [ATTO542]: modification on amino-C6 linker [SpC12]: Carbon ₁₂ spacer	Biomers GmbH
20[79]	TTCCAGTCGTAATCATGGTCATAAAAGGG GAAAAAAAAAAAAAAAAAAAAA [Chol]	[Chol]: Cholesterol-TEG modification	Integrated DNA Technologies, Inc.

S2

5' position	Sequence (5' to 3' end)	Comments	Company
8[47]	ATCCCCCTATACCACATTCAACTAGAAA ATCAAAAAAAAAAAAAAAAAAAAA [Chol]	[Chol]: Cholesterol-TEG modification	Integrated DNA Technologies, Inc.
12[175]	TTTTATTTAAGCAAATCAGATATTTTTGT AAAAAAAAAAAAAAAAAAAA [Chol]	[Chol]: Cholesterol-TEG modification	Integrated DNA Technologies, Inc.
7[160]	TTATTACGAAGAACTGGCATGATTGCGA GAGGAAAAAAAAAAAAAAAA [Chol]	[Chol]: Cholesterol-TEG modification	Integrated DNA Technologies, Inc.
13[96]	TAGGTAAACTATTTTTGAGAGATCAAAC GTTAAAAAAAAAAAA [Chol]	[Chol]: Cholesterol-TEG modification	Integrated DNA Technologies, Inc.
13[120]	AAAGGCCGGAGACAGCTAGCTGATAAA TTAATTTTTGTAAAAAAAA [Chol]	[Chol]: Cholesterol-TEG modification	Integrated DNA Technologies, Inc.
7[96]	TAAGAGCAAATGTTTAGACTGGATAGGA AGCCAAAAAAAAAAAA [Chol]	[Chol]: Cholesterol-TEG modification	Integrated DNA Technologies, Inc.
10[127]	[Bio]TAGAGAGTTATTTTCATTTGGGGAT AGTAGTAGCATT	[Bio]: Biotin modification	
4[63]	[Bio]ATAAGGGAACCGGATATTCATTACG TCAGGACGTTGGGAA	[Bio]: Biotin modification	Eurofins Genomics GmbH
16[63]	[Bio]CGGATTCTGACGACAGTATCGGCCG CAAGGCGATTAAGTT	[Bio]: Biotin modification	Eurofins Genomics GmbH
10[191]	[Bio]GAAACGATAGAAGGCTTATCCGGTC TCATCGAGAACAAGC	[Bio]: Biotin modification	Eurofins Genomics GmbH
16[255]	[Bio]GAGAAGAGATAACCTTGCTTCTGTT CGGGAGAAACAATAA	[Bio]: Biotin modification	Eurofins Genomics GmbH
4[255]	[Bio]AGCCACCACTGTAGCGTTTTCAA GGGAGGGAAGGTAAA	[Bio]: Biotin modification	Eurofins Genomics GmbH
14[47]	AAAAATCCTCTACCACCTACATCAC AAAAAAAAAAAAAAAAAAAAAACAAGA GGGATAAAAAATTTTAGCATAAAGC		Eurofins Genomics GmbH
3[160]	AAAAATCCTCTACCACCTACATCACA AAAAAAAAAAAAAAAAAAAAATTGACAGG CCACCACCAGAGCCGCGATTTGTA		Eurofins Genomics GmbH
21[160]	AAAAATCCTCTACCACCTACATCACA AAAAAAAAAAAAAAAAAAAAATCAATATC GAACCTCAAATATCAATTCCGAAA		Eurofins Genomics GmbH
11[96]	AATGGTCAACAGGCAAGCAAAGAGTA ATGTG		Integrated DNA Technologies, Inc.
14[111]	GAGGGTAGGATTCAAAAGGGTGAGACA TCCAA		Integrated DNA Technologies, Inc.
6[111]	CATTACCTTTGAATAAGGCTTGCCAAA TCCGC		Integrated DNA Technologies, Inc.
7[128]	AGACGACAAAGAAGTTTTGCCATAATTC GAGCTTCAA		Integrated DNA Technologies, Inc.
8[111]	AATAGTAAACACTATCATAACCCTCATT GTGA		Integrated DNA Technologies, Inc.

5' position	Sequence (5' to 3' end)	Comments	Company
16[111]	TGTAGCCATTAAAATTCGCATTAAATGC CGGA		Integrated DNA Technologies, Inc.
9[96]	CGAAAGACTTTGATAAGAGGTCATATTT CGCA		Integrated DNA Technologies, Inc.
21[64]	GCCCTTCAGAGTCCACTATTAAGGGTG CCGT		Integrated DNA Technologies, Inc.
1[160]	TTAGGATTGGCTGAGACTCCTCAATAAC CGAT		Integrated DNA Technologies, Inc.
15[96]	ATATTTTGGCTTTCATCAACATTATCCAG CCA		Integrated DNA Technologies, Inc.
22[271]	CAGAAGATTAGATAATACATTTGTCGAC AA		Integrated DNA Technologies, Inc.
5[128]	AACACCAAATTTCAACTTTAATCGTTTAC C		Integrated DNA Technologies, Inc.
20[47]	TTAATGAACTAGAGGATCCCCGGGGGGT AACG		Integrated DNA Technologies, Inc.
18[79]	GATGTGCTTCAGGAAGATCGACAATGT GA		Integrated DNA Technologies, Inc.
12[207]	GTACCGCAATTCTAAGAACGCGAGTATT ATTT		Integrated DNA Technologies, Inc.
4[271]	AAATCACCTTCCAGTAAGCGTCAGTAAT AA		Integrated DNA Technologies, Inc.
22[207]	AGCCAGCAATTGAGGAAGGTTATCATCA TTTT		Integrated DNA Technologies, Inc.
8[207]	AAGGAAACATAAAGGTGGCAACATTATC ACCG		Integrated DNA Technologies, Inc.
15[128]	TAAATCAAAATAATTCGCGTCTCGGAAA CC		Integrated DNA Technologies, Inc.
6[271]	ACCGATTGTCGGCATTTCGGTCATAATC A		Integrated DNA Technologies, Inc.
0[79]	ACAACCTTCAACAGTTTCAGCGGATGTA TCGG		Integrated DNA Technologies, Inc.
11[224]	GCGAACCTCCAAGAACGGGTATGACAAT AA		Integrated DNA Technologies, Inc.
8[239]	AAGTAAGCAGACACCACGGAATAATATT GACG		Integrated DNA Technologies, Inc.
19[96]	CTGTGTGATTGCGTTGCGCTCACTAGAG TTGC		Integrated DNA Technologies, Inc.
15[224]	CCTAAATCAAAATCATAGGTCTAAACAG TA		Integrated DNA Technologies, Inc.

5' position	Sequence (5' to 3' end)	Comments	Company
1[192]	GCGGATAACCTATTATTCTGAAACAGAC GATT		Integrated DNA Technologies, Inc.
5[160]	GCAAGGCCTCACCAGTAGCCATGGGC TTGA		Integrated DNA Technologies, Inc.
12[239]	CTTATCATTCCCAGCTTGCGGGAGCCTA ATTT		Integrated DNA Technologies, Inc.
2[111]	AAGGCCGCTGATACCGATAGTTGCGACG TTAG		Integrated DNA Technologies, Inc.
19[248]	CGTAAAACAGAAATAAAAATCCTTTGCC CGAAAGATTAGA		Integrated DNA Technologies, Inc.
0[111]	TAAATGAATTTTCTGTATGGGATTAATTT CTT		Integrated DNA Technologies, Inc.
5[32]	CATCAAGTAAAACGAACTAACGAGTTGA GA		Integrated DNA Technologies, Inc.
20[207]	GCGGAACATCTGAATAATGGAAGGTACA AAAT		Integrated DNA Technologies, Inc.
12[143]	TTCTACTACGCGAGCTGAAAAGGTTACC GCGC		Integrated DNA Technologies, Inc.
8[143]	CTTTTGCAGATAAAAACCAAATAAAGA CTCC		Integrated DNA Technologies, Inc.
2[143]	ATATTCGGAACCATCGCCACGCAGAGA AGGA		Integrated DNA Technologies, Inc.
21[224]	CTTTAGGGCCTGCAACAGTGCCAATACG TG		Integrated DNA Technologies, Inc.
14[239]	AGTATAAAGTTCAGCTAATGCAGATGTC TTTC		Integrated DNA Technologies, Inc.
20[111]	CACATTAATAATTGTTATCCGCTCATGCG GGCC		Integrated DNA Technologies, Inc.
3[128]	AGCGCGATGATAAATTGTGTCGTGACGA GA		Integrated DNA Technologies, Inc.
17[128]	AGGCAAAGGGAAGGGCGATCGGCAATT CCA		Integrated DNA Technologies, Inc.
17[160]	AGAAAACAAAGAAGATGATGAAACAGG CTGCG		Integrated DNA Technologies, Inc.
2[207]	TTTCGGAAGTGCCGTCGAGAGGGTGAGT TTCG		Integrated DNA Technologies, Inc.
22[79]	TGGAACAACCGCCTGGCCCTGAGGCCCG CT		Integrated DNA Technologies, Inc.
10[47]	CTGTAGCTTGACTATTATAGTCAGTTCAT TGA		Integrated DNA Technologies, Inc.

5' position	Sequence (5' to 3' end)	Comments	Company
16[207]	ACCTTTTATTTTAGTTAATTTTCATAGGG CTT		Integrated DNA Technologies, Inc.
9[224]	AAAGTCACAAAATAAACAGCCAGCGTTT TA		Integrated DNA Technologies, Inc.
19[224]	CTACCATAGTTTGAGTAACATTTAAAAT AT		Integrated DNA Technologies, Inc.
3[96]	ACACTCATCCATGTTACTTAGCCGAAAAG CTGC		Integrated DNA Technologies, Inc.
18[239]	CCTGATTGCAATATATGTGAGTGATCAA TAGT		Integrated DNA Technologies, Inc.
10[239]	GCCAGTTAGAGGGTAATTGAGCGCTTTA AGAA		Integrated DNA Technologies, Inc.
3[32]	AATACGTTTGAAAGAGGACAGACTGACC TT		Integrated DNA Technologies, Inc.
1[128]	TGACAACCTCGCTGAGGCTTGCATTATAC CA		Integrated DNA Technologies, Inc.
16[47]	ACAAACGGAAAAGCCCCAAAACACTG GAGCA		Integrated DNA Technologies, Inc.
14[175]	CATGTAATAGAATATAAAGTACCAAGCC GT		Integrated DNA Technologies, Inc.
17[192]	CATTTGAAGGCGAATTATTCAATTTTGT TGG		Integrated DNA Technologies, Inc.
19[56]	TACCGAGCTCGAATTCGGGAAACCTGTC GTGCAGCTGATT		Integrated DNA Technologies, Inc.
23[64]	AAAGCACTAAATCGGAACCTAATCCAG TT		Integrated DNA Technologies, Inc.
16[175]	TATAACTAACAAAGAACGCGAGAACGC CAA		Integrated DNA Technologies, Inc.
7[56]	ATGCAGATACATAACGGGAATCGTCATA AATAAAGCAAAG		Integrated DNA Technologies, Inc.
3[224]	TTAAAGCCAGAGCCGCCACCCTCGACAG AA		Integrated DNA Technologies, Inc.
12[47]	TAAATCGGGATTCCAATTCTGCGATAT AATG		Integrated DNA Technologies, Inc.
14[143]	CAACCGTTTCAAATCACCATCAATTCGA GCCA		Integrated DNA Technologies, Inc.
6[79]	TTATACCACCAAATCAACGTAACGAACG AG		Integrated DNA Technologies, Inc.
4[239]	GCCTCCCTCAGAATGGAAAGCGCAGTAA CAGT		Integrated DNA Technologies, Inc.

5' position	Sequence (5' to 3' end)	Comments	Company
7[248]	GTTTATTTTGT CACAATCTTACCGAAGCC CTTTAATATCA		Integrated DNA Technologies, Inc.
1[32]	AGGCTCCAGAGGCTTTGAGGACACGGGT AA		Integrated DNA Technologies, Inc.
0[207]	TCACCAGTACAACTACAACGCCTAGTA CCAG		Integrated DNA Technologies, Inc.
4[143]	TCATCGCCAACAAAGTACAACGGACGCC AGCA		Integrated DNA Technologies, Inc.
16[271]	CTTAGATTTAAGGCGTTAAATAAAGCCT GT		Integrated DNA Technologies, Inc.
21[192]	TGAAAGGAGCAAATGAAAAATCTAGAG ATAGA		Integrated DNA Technologies, Inc.
5[224]	TCAAGTTTCATTAAAGGTGAATATAAAA GA		Integrated DNA Technologies, Inc.
8[79]	AATACTGCCAAAAGGAATTACGTGGCT CA		Integrated DNA Technologies, Inc.
11[160]	CCAATAGCTCATCGTAGGAATCATGGCA TCAA		Integrated DNA Technologies, Inc.
4[111]	GACCTGCTCTTTGACCCCCAGCGAGGGA GTTA		Integrated DNA Technologies, Inc.
2[175]	TATTAAGAAGCGGGGTTTTGCTCGTAGC AT		Integrated DNA Technologies, Inc.
13[184]	GACAAAAGGTAAAGTAATCGCCATATTT AACAAAACTTTT		Integrated DNA Technologies, Inc.
1[96]	AAACAGCTTTTTGCGGGATCGTCAACAC TAAA		Integrated DNA Technologies, Inc.
23[192]	ACCCTTCTGACCTGAAAGCGTAAGACGC TGAG		Integrated DNA Technologies, Inc.
15[32]	TAATCAGCGGATTGACCGTAATCGTAAC CG		Integrated DNA Technologies, Inc.
18[175]	CTGAGCAAAAATTAATTACATTTTGGGT TA		Integrated DNA Technologies, Inc.
6[175]	CAGCAAAAGGAAACGTCACCAATGAGC CGC		Integrated DNA Technologies, Inc.
6[143]	GATGGTTTGAACGAGTAGTAAATTTACC ATTA		Integrated DNA Technologies, Inc.
8[175]	ATACCCAACAGTATGTTAGCAAATTAGA GC		Integrated DNA Technologies, Inc.
17[96]	GCTTTCGATTACGCCAGCTGGCGGCTG TTTC		Integrated DNA Technologies, Inc.

5' position	Sequence (5' to 3' end)	Comments	Company
12[79]	AAATTAAGTTGACCATTAGATACTTTG CG		Integrated DNA Technologies, Inc.
8[271]	AATAGCTATCAATAGAAAATTCAACATT CA		Integrated DNA Technologies, Inc.
15[192]	TCAAATATAACCTCCGGCTTAGGTAACA ATTT		Integrated DNA Technologies, Inc.
21[96]	AGCAAGCGTAGGGTTGAGTGTTGTAGGG AGCC		Integrated DNA Technologies, Inc.
20[239]	ATTTTAAAATCAAATTATTTGCACGGA TTCG		Integrated DNA Technologies, Inc.
7[224]	AACGCAAAGATAGCCGAACAAACCCTG AAC		Integrated DNA Technologies, Inc.
22[239]	TTAACACCAGCACTAACAACTAATCGTT ATTA		Integrated DNA Technologies, Inc.
18[111]	TCTTCGCTGCACCGCTTCTGGTGCGCCT TCC		Integrated DNA Technologies, Inc.
17[32]	TGCATCTTTCCAGTCACGACGGCCTGC AG		Integrated DNA Technologies, Inc.
4[175]	CACCAGAAAGGTTGAGGCAGGTCATGA AAG		Integrated DNA Technologies, Inc.
10[175]	TTAACGTCTAACATAAAAAACAGGTAACG GA		Integrated DNA Technologies, Inc.
21[256]	GCCGTCAAAAAACAGAGGTGAGGCCTAT TAGT		Integrated DNA Technologies, Inc.
4[47]	GACCAACTAATGCCACTACGAAGGGGGT AGCA		Integrated DNA Technologies, Inc.
6[239]	GAAATTATTGCCTTTAGCGTCAGACCGG AACC		Integrated DNA Technologies, Inc.
18[271]	CTTTTACAAAATCGTCGCTATTAGCGAT AG		Integrated DNA Technologies, Inc.
14[79]	GCTATCAGAAATGCAATGCCTGAATTAG CA		Integrated DNA Technologies, Inc.
2[47]	ACGGCTACAAAAGGAGCCTTTAATGTGA GAAT		Integrated DNA Technologies, Inc.
21[128]	GCGAAAAATCCCTTATAAATCAAGCCGG CG		Integrated DNA Technologies, Inc.
22[175]	ACCTTGCTTGGTCAGTTGGCAAAGAGCG GA		Integrated DNA Technologies, Inc.
8[47]	ATCCCCCTATACCACATTCAACTAGAAA AATC		Integrated DNA Technologies, Inc.

5' position	Sequence (5' to 3' end)	Comments	Company
1[64]	TTTATCAGGACAGCATCGGAACGACACC AACCTAAAACGA		Integrated DNA Technologies, Inc.
17[224]	CATAAATCTTTGAATACCAAGTGTTAGA AC		Integrated DNA Technologies, Inc.
16[143]	GCCATCAAGCTCATTTTTTAACCACAAA TCCA		Integrated DNA Technologies, Inc.
4[207]	CCACCCTCTATTCACAAACAAATACCTG CCTA		Integrated DNA Technologies, Inc.
2[79]	CAGCGAAACTTGCTTTCGAGGTGTTGCT AA		Integrated DNA Technologies, Inc.
19[128]	CACAACAGGTGCCTAATGAGTGCCAGC AG		Integrated DNA Technologies, Inc.
19[192]	ATTATACTAAGAAACCACCAGAAGTCAA CAGT		Integrated DNA Technologies, Inc.
16[239]	GAATTTATTTAATGGTTTGAAATATTCTT ACC		Integrated DNA Technologies, Inc.
22[111]	GCCCGAGAGTCCACGCTGGTTTGCAGCT AACT		Integrated DNA Technologies, Inc.
6[207]	TCACCGACGCACCGTAATCAGTAGCAGA ACCG		Integrated DNA Technologies, Inc.
13[224]	ACAACATGCCAACGCTCAACAGTCTTCT GA		Integrated DNA Technologies, Inc.
20[175]	ATTATCATTCAATATAATCCTGACAATTA C		Integrated DNA Technologies, Inc.
18[207]	CGCGCAGATTACCTTTTTTAATGGGAGA GACT		Integrated DNA Technologies, Inc.
10[207]	ATCCCAATGAGAATTAACGAAACAGTTA CCAG		Integrated DNA Technologies, Inc.
14[207]	AATTGAGAATTCTGTCCAGACGACTAAA CCAA		Integrated DNA Technologies, Inc.
13[64]	TATATTTTGTTCATTGCCTGAGAGTGAA GATTGTATAAGC		Integrated DNA Technologies, Inc.
23[96]	CCCGATTTAGAGCTTGACGGGGAAAAAG AATA		Integrated DNA Technologies, Inc.
3[192]	GGCCTTGAAGAGCCACCACCTCAGAAA CCAT		Integrated DNA Technologies, Inc.
4[79]	GCGCAGACAAGAGGCAAAAGAATCCCT CAG		Integrated DNA Technologies, Inc.
15[160]	ATCGCAAGTATGTAAATGCTGATGATAG GAAC		Integrated DNA Technologies, Inc.

5' position	Sequence (5' to 3' end)	Comments	Company
5[96]	TCATTCAGATGCGATTTTAAGAACAGGC ATAG		Integrated DNA Technologies, Inc.
18[143]	CAACTGTTGCGCCATTCGCCATTCAAAC ATCA		Integrated DNA Technologies, Inc.
20[271]	CTCGTATTAGAAATTGCGTAGATACAGT AC		Integrated DNA Technologies, Inc.
1[256]	CAGGAGGTGGGGTCAGTGCCTTGAGTCT CTGAATTTACCG		Integrated DNA Technologies, Inc.
13[160]	GTAATAAGTTAGGCAGAGGCATTTATGA TATT		Integrated DNA Technologies, Inc.
1[224]	GTATAGCAAACAGTTAATGCCCAATCCT CA		Integrated DNA Technologies, Inc.
5[192]	CGATAGCATTGAGCCATTTGGGAACGTA GAAA		Integrated DNA Technologies, Inc.
7[192]	ATACATACCGAGGAAACGCAATAAGAA GCGCATTAGACGG		Integrated DNA Technologies, Inc.
10[111]	TTGCTCCTTTCAAATATCGCGTTTGAGGG GGT		Integrated DNA Technologies, Inc.
13[256]	GTTTATCAATATGCGTTATACAAACCGA CCGTGTGATAAA		Integrated DNA Technologies, Inc.
6[47]	TACGTTAAAGTAATCTTGACAAGAACCG AACT		Integrated DNA Technologies, Inc.
16[79]	GCGAGTAAAAATATTTAAATTGTTACAA AG		Integrated DNA Technologies, Inc.
23[256]	CTTTAATGCGCGAACTGATAGCCCCACC AG		Integrated DNA Technologies, Inc.
23[224]	GCACAGACAATATTTTTGAATGGGGTCA GTA		Integrated DNA Technologies, Inc.
10[79]	GATGGCTTATCAAAAAGATTAAGAGCGT CC		Integrated DNA Technologies, Inc.
0[47]	AGAAAGGAACAACCTAAAGGAATTCAAA AAAA		Integrated DNA Technologies, Inc.
10[271]	ACGCTAACACCCACAAGAATTGAAAATA GC		Integrated DNA Technologies, Inc.
2[271]	GTTTTAACTTAGTACCGCCACCCAGAGC CA		Integrated DNA Technologies, Inc.
14[271]	TTAGTATCACAATAGATAAGTCCACGAG CA		Integrated DNA Technologies, Inc.
9[160]	AGAGAGAAAAAATGAAAATAGCAAGC AAACT		Integrated DNA Technologies, Inc.

5' position	Sequence (5' to 3' end)	Comments	Company
12[271]	TGTAGAAATCAAGATTAGTTGCTCTTAC CA		Integrated DNA Technologies, Inc.
23[160]	TAAAAGGGACATTCTGGCCAACAAAGCA TC		Integrated DNA Technologies, Inc.
19[160]	GCAATTCACATATTCTGATTATCAAAG TGTA		Integrated DNA Technologies, Inc.
10[143]	CCAACAGGAGCGAACCAGACCGGAGCC TTTAC		Integrated DNA Technologies, Inc.
23[32]	CAAATCAAGTTTTTTGGGGTCGAAACGT GGA		Integrated DNA Technologies, Inc.
22[143]	TCGGCAAATCCTGTTTGTATGGTGGACCC TCAA		Integrated DNA Technologies, Inc.
0[175]	TCCACAGACAGCCCTCATAGTTAGCGTA ACGA		Integrated DNA Technologies, Inc.
0[143]	TCTAAAGTTTTGTCTTTCCAGCCGAC AA		Integrated DNA Technologies, Inc.
20[143]	AAGCCTGGTACGAGCCGGAAGCATAGAT GATG		Integrated DNA Technologies, Inc.
2[239]	GCCCGTATCCGGAATAGGTGTATCAGCC CAAT		Integrated DNA Technologies, Inc.
7[32]	TTTAGGACAAATGCTTTAAACAATCAGG TC		Integrated DNA Technologies, Inc.
23[128]	AACGTGGCGAGAAAGGAAGGGAAACCA GTAA		Integrated DNA Technologies, Inc.
21[32]	TTTTCACTCAAAGGGCGAAAAACCATCA CC		Integrated DNA Technologies, Inc.
13[32]	AACGCAAAATCGATGAACGGTACCGGTT GA		Integrated DNA Technologies, Inc.
0[271]	CCACCCTCATTTTCAGGGATAGCAACCG TACT		Integrated DNA Technologies, Inc.
9[256]	GAGAGATAGAGCGTCTTCCAGAGGTTT TGAA		Integrated DNA Technologies, Inc.
11[256]	GCCTTAAACCAATCAATAATCGGCACGC GCCT		Integrated DNA Technologies, Inc.
0[239]	AGGAACCCATGTACCGTAACTTGATA TAA		Integrated DNA Technologies, Inc.
9[32]	TTTACCCCAACATGTTTTAAATTTCCATA T		Integrated DNA Technologies, Inc.
11[32]	AACAGTTTTGTACCAAAAACATTTTATTT C		Integrated DNA Technologies, Inc.

5' position	Sequence (5' to 3' end)	Comments	Company
22[47]	CTCCAACGCAGTGAGACGGGCAACCAGC TGCA		Integrated DNA Technologies, Inc.
19[32]	GTCGACTTCGGCCAACGCGGGGTTTT TC		Integrated DNA Technologies, Inc.
12[111]	TAAATCATATAACCTGTTTAGCTAACCTT TAA		Integrated DNA Technologies, Inc.
11[64]	GATTTAGTCAATAAAGCCTCAGAGAACC CTCA		Integrated DNA Technologies, Inc.
9[64]	CGGATTGCAGAGCTTAATTGCTGAAACG AGTA		Integrated DNA Technologies, Inc.

The chemical structure for both sensors designs Leash A₂ and Leash Carb₁₂ as well as the one for the ATTO647N membrane anchor is shown in Figure S2.

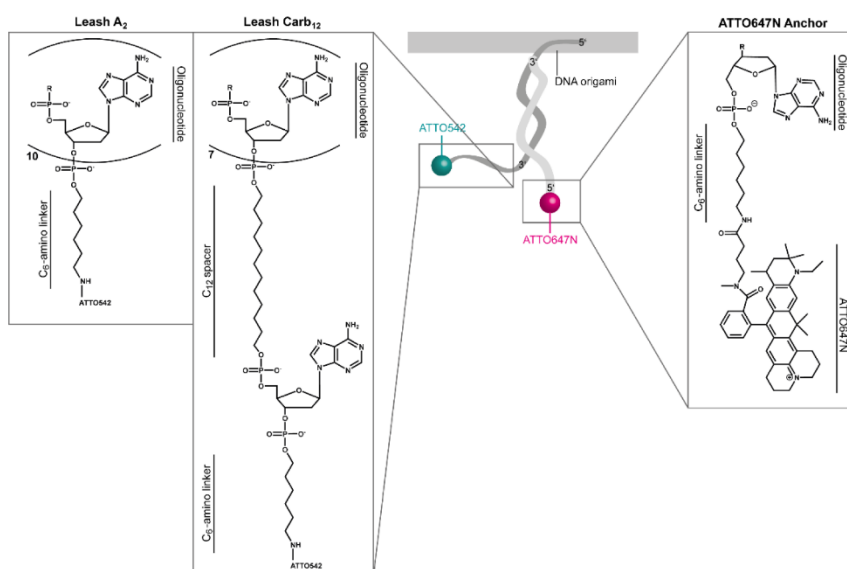


Figure S2. Chemical structures of sensor. The inset in the left shows the chemical structures of the Leash A₂ and the Leash Carb₁₂, whereas the inset on the right presents the chemical structure of the ATTO647N anchor.

Additional Data from Measurements on TIRF Microscope

All smFRET distributions are shown from which the mean PR is determined. Figure S3 presents the data for the Leash A₂ sensor with differently charged LUVs and Figure S4 the one for the Leash Carb₁₂ sensor.

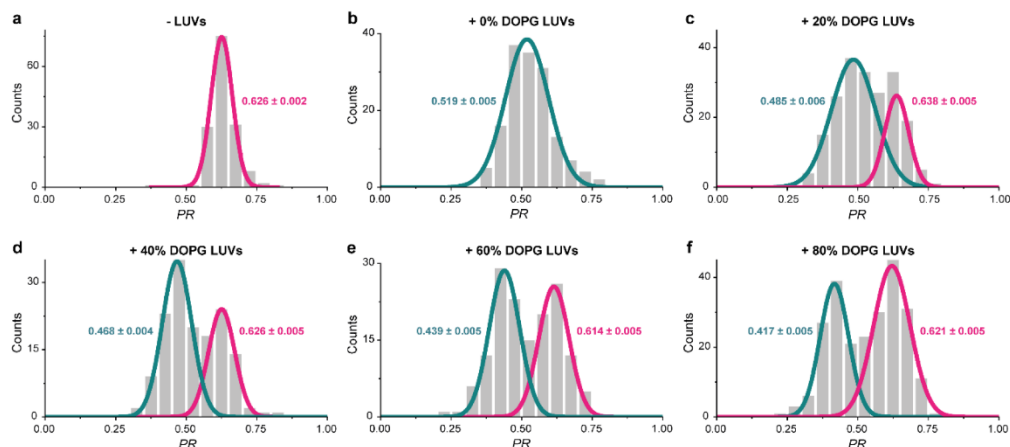


Figure S3. PR distributions of all Leash A₂ samples measured on TIRF microscope. In pink, the Gauss fit for the LUV-unbound sample/population is shown and in cyan the LUV-bound with the resulting mean PR and the standard error of the mean for sample (a) without LUVs, (b) with 0% DOPG LUVs, (c) 20% DOPG LUVs, (d) 40% DOPG LUVs, (e) 60% DOPG LUVs and (f) 80% DOPG LUVs. $N_{\text{molecules}}$ for Leash A₂ with 0%, 20%, 40%, 60% and 80% DOPG LUVs, respectively: 150, 200, 150, 150, 238.

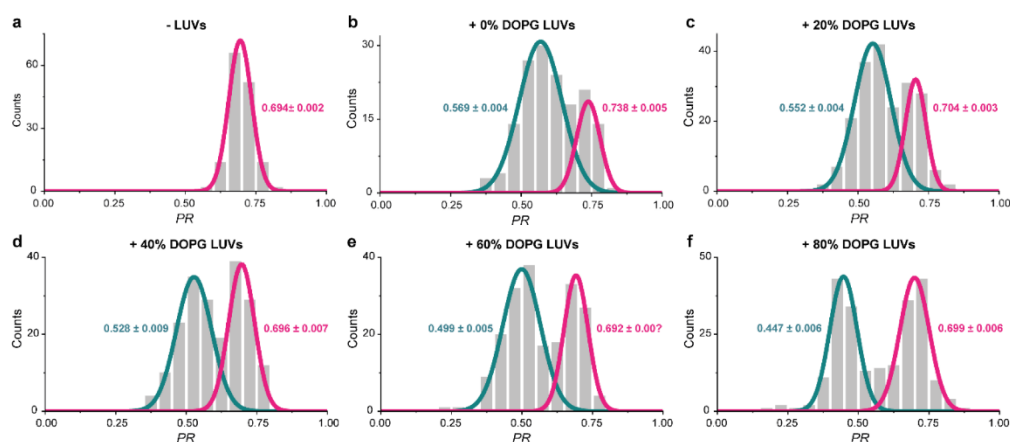


Figure S4. PR distributions of all Leash Carb₁₂ samples measured on TIRF microscope. In pink, the Gauss fit for the LUV-unbound sample/population is shown and in cyan the LUV-bound with the resulting mean PR and the standard error of the mean for sample (a) without LUVs, (b) with 0% DOPG LUVs, (c) 20% DOPG LUVs, (d) 40% DOPG LUVs, (e) 60% DOPG LUVs and (f) 80% DOPG LUVs. $N_{\text{molecules}}$ for Leash Carb₁₂ with 0%, 20%, 40%, 60% and 80% DOPG LUVs, respectively: 156, 200, 200, 200, 230.

For Figure 4, a Gaussian error propagation is performed to determine the standard error of the mean $\sigma_{\Delta PR}$ according to

$$\sigma_{\Delta PR} = \sqrt{\left(\left|\frac{\partial \Delta PR}{\partial PR_{x\% DOFG}}\right| \cdot \sigma_{PR_{x\% DOFG}}\right)^2 + \left(\left|\frac{\partial \Delta PR}{\partial PR_{0\% DOFG}}\right| \cdot \sigma_{PR_{0\% DOFG}}\right)^2} \quad (1)$$

Detailed Information on Correlation Analysis

The following described analysis is published by Schröder *et al.*¹

Shrinking-gate fluorescence correlation spectroscopy (sg-FCS) analysis is performed with home-written python scripts based on the correlation algorithm proposed by Laurence *et al.*² Stochastic switching between two intensity states shows in the $g^{(2)}(\Delta\tau)$ auto correlation as mono-exponential bunching amplitude.

$$g^{(2)}(\Delta\tau) = 1 + A \cdot \exp\left(-\frac{\Delta\tau}{\tau_{CRT}}\right) \quad (2)$$

The correlation decays with a characteristic correlation relaxation time (CRT):

$$\tau_{CRT} = \frac{1}{k_A + k_B} \quad (3)$$

k_A and k_B represent the switching rates between the two intensity states I_A and I_B . Here, I_A represents the bright state and I_B represents the quenched state.

The correlation amplitude A for a two intensity system is given as:³⁻⁵

$$A = K \left(\frac{I_A - I_B}{I_A + K \cdot I_B} \right)^2 \quad (4)$$

Here, K represents the equilibrium constant.

$$K = \frac{k_B}{k_A} \quad (5)$$

Equation (4) holds not a unique solution for K with $I_B \neq 0$. Therefore, we use microtime gating to change the intensity contrast between I_A and I_B with different microtime thresholds t_g . With pulsed excitation the fluorescence intensity decays faster for I_B because in is subject to an additional non-radiative rate $k_{\Delta ET} = k_{ET,high FRET} - k_{ET,low FRET}$ resulting in a shorter fluorescence lifetime and lower quantum yield.

$$I_A(t_g) = \int_{t_g}^{\infty} e^{-(k_r + k_{nr}) \cdot t_g'} dt_g' = \frac{e^{-(k_r + k_{nr}) \cdot t_g}}{k_r + k_{nr}} \quad (6)$$

$$I_B(t_g) = \int_{t_g}^{\infty} e^{-(k_r + k_{nr} + k_{\Delta ET}) \cdot t_g'} dt_g' = \frac{e^{-(k_r + k_{nr} + k_{\Delta ET}) \cdot t_g}}{k_r + k_{nr} + k_{\Delta ET}} \quad (7)$$

Here, k_r and k_{nr} denote the radiative and non-radiative decay rates of the intensity state I_A which includes possible energy transfer to an acceptor dye. Therefore, we can express the microtime dependent $A(t_g)$ as:

$$A(t_g) = K \left(\frac{1 - \frac{k_r + k_{nr}}{k_r + k_{nr} + k_{\Delta ET}} e^{-k_{\Delta ET} \cdot t_g}}{1 + K \cdot \frac{k_r + k_{nr}}{k_r + k_{nr} + k_{\Delta ET}} e^{-k_{\Delta ET} \cdot t_g}} \right)^2 \quad (8)$$

With increasing intensity contrast for larger t , the equation saturates and K can be extracted.

To compensate the laser pulse arrival time, we introduce an offset t_0 which simplifies equation (8) to:

$$A(t_g) = K \left(\frac{1 - e^{-k_{\Delta ET} \cdot (t_g - t_0)}}{1 + K \cdot e^{-k_{\Delta ET} \cdot (t_g - t_0)}} \right)^2 \quad (9)$$

S15

For analysis, sg-FCS is performed from $t_g = 0 \text{ ns}$ to $t_g = 7 - 9 \text{ ns}$ with a 0.1 ns step size. Each microtime gated correlation $g^{(2)}(\Delta\tau, t_g)$ is fitted with the mono-exponential model of equation (2).

$$g^{(2)}(\Delta\tau, t_g) = 1 + A(t_g)e^{-\frac{\Delta\tau}{\tau_{CRT}}} \quad (10)$$

The extracted amplitudes $A(t)$ are fitted with equation (9) yielding K and $k_{\Delta FRET}$. With K and τ_{CRT} the mean dwell times for each state intensity states are calculated.

$$k_A = \frac{1}{t_B} = \frac{1}{\tau_{CRS} \cdot (K+1)} \quad (11)$$

$$k_B = \frac{1}{t_A} = \frac{1}{\tau_{CRS} \cdot (\frac{1}{K}+1)} \quad (12)$$

Fluorescence lifetime fitting

To extract the fluorescence lifetimes of the two FRET states from the photon arrival time histogram $I(t_g)$, we use a reconvolution algorithm. To make the model more robust, we use the equilibrium constant K and the additional non-radiative rate $k_{\Delta ET}$. The fluorescence lifetime decay is fitted by a convolution of the instrument response function I_{IRF} and the sum of two fluorescence lifetime decays

$$I(t_g) = \left(I_{IRF}(t_g) * A \cdot \left(\left(1 - \frac{K}{1+K} \right) \cdot e^{-\frac{1}{\tau_A}(t_g - t_{off})} + \frac{K}{1+K} \cdot e^{-\left(\frac{1}{\tau_A} + k_{\Delta ET}\right)(t_g - t_{off})} \right) \right) + I_{bg} \quad (13)$$

Here, * denotes the convolution operator and t_{off} represents an offset of the decay function that is introduced to compensate an intensity-dependent shift of I_{IRF} . The fit routine iterates over a range of IRF shifts and returns the fit attempt with the best reduced chi-squared test. A scales the model to the histogram heights. $1 - \frac{K}{1+K}$ is the fraction of time the system spent in the intensity state I_A and $\frac{K}{1+K}$ is the fraction of time the system spent in state I_B . I_{bg} denotes the constant offset due to uncorrelated background. With this routine we can extract τ_A which is the fluorescence lifetime of state I_A .

$$\tau_A = \frac{1}{k_r + k_{nr}} \quad (14)$$

With the previous extracted $k_{\Delta ET}$ we can calculate the fluorescence lifetime τ_B of intensity state I_B .

$$\tau_B = \frac{1}{k_r + k_{nr} + k_{\Delta ET}} = \frac{1}{\frac{1}{\tau_A} + k_{\Delta ET}} \quad (15)$$

Additional Data from Measurements on Confocal Microscope

In Figure 3 and 4, the PR is calculated for both states as

$$PR_{State\ x} = 1 - \frac{\tau_{State\ x}}{\tau_0} \quad (16)$$

Therefore $\tau_{State\ x}$ is derived in the analysis for each molecule, whereas τ_0 remains the same. It is determined by an analysis of the fluorescence lifetime in a custom-made LabVIEW software (National Instruments). From the donor excitation-donor emission channel, data is selected after acceptor bleaching and upon an increase in the donor excitation-donor emission channel. The lifetime distribution plot is presented in Figure S5 with the determined mean of $\tau_0=3.3$ ns.

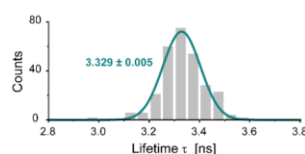


Figure S5. Distribution of the fluorescence lifetime τ_0 of the donor ATTO542 without transferring energy. By Gauss fitting, the mean τ_0 with its standard error of the mean is derived and presented. $N_{\text{molecules}}=282$.

References

- (1) Schröder, T.; Bohlen, J.; Ochmann, S. E.; Schüler, P.; Krause, S.; Tinnefeld, P. Systematic microtime gating for fluorescence correlation spectroscopy yields equilibrium constants and allows discrimination of photophysics from structural dynamic processes. *submitted* **2022**.
- (2) Laurence, T. A.; Fore, S.; Huser, T. Fast, flexible algorithm for calculating photon correlations. *Opt Lett* **2006**, *31* (6), 829–831. DOI: 10.1364/OL.31.000829.
- (3) Zumbusch; Fleury; Brown; Bernard; Orrit. Probing individual two-level systems in a polymer by correlation of single molecule fluorescence. *Phys Rev Lett* **1993**, *70* (23), 3584–3587. DOI: 10.1103/PhysRevLett.70.3584.
- (4) Lamb, D. C.; Schenk, A.; Röcker, C.; Scalfi-Happ, C.; Nienhaus, G. U. Sensitivity Enhancement in Fluorescence Correlation Spectroscopy of Multiple Species Using Time-Gated Detection. *Biophys J* **2000**, *79* (2), 1129–1138. DOI: 10.1016/S0006-3495(00)76366-1.
- (5) Yu, J.; Lammi, R.; Gesquiere, A. J.; Barbara, P. F. Singlet-triplet and triplet-triplet interactions in conjugated polymer single molecules. *J Phys Chem B* **2005**, *109* (20), 10025–10034. DOI: 10.1021/jp0506742.

8 List of Figures

Figure 1. Principle of a biosensor	3
Figure 2. DNA nanotechnology-based biosensors	4
Figure 3. Single-molecule biosensing for <i>in vitro</i> diagnostic applications.....	6
Figure 4. Optical nanoantennas.....	7
Figure 5. Single-molecule <i>in vivo</i> biosensing.....	8
Figure 6. Probes for imaging of the transmembrane potential	10
Figure 7. Ratiometric sensor for membrane surface charges	11
Figure 8. Jablonski diagram.....	12
Figure 9. Concept of FRET	14
Figure 10. Simplified Jablonski diagram illustrating the ROXS mechanism	15
Figure 11. Single-molecule microscopy techniques	16
Figure 12. DNA and DNA nanotechnology.....	18
Figure 13. Plasmonic nanoparticles	19
Figure 14. Electric potentials at lipid bilayers.....	20
Figure 15. Plasmonic nanoantenna enhancing fluorescence for diagnostic purposes	25
Figure 16. Single-molecule transmembrane potential sensor based on DNA origami	28
Figure 17. DNA origami-based surface charge sensor	31
Figure 18. Improved DNA origami nanoantenna for single-molecule imaging on portable microscope....	34
Figure 19. Transmembrane potential sensor designs for improved signal contrast	36
Figure 20. New surface charge sensor design	36

9 Abbreviations

AOTF: Acousto-Optical Tunable Filter

CCD: Charge-Coupled Device

CMOS: Complementary Metal-Oxide-Semiconductor

dsDNA: double-stranded DNA

DOPC: 1,2-dioleoyl-sn-glycero-3-phosphocholine

DOPG: 1,2-dioleoyl-sn-glycero-3-phospho-(1'-rac-glycerol)

EDTA: Ethylenediaminetetraacetic acid

FCS: Fluorescence Correlation Spectroscopy

FRET: Förster Resonance Energy Transfer

GEVI: Genetically-Encoded Voltage Indicators

LOD: Limit of Detection

LSPR: Localized Surface Plasmon Resonance

LUV: Large Unilamellar Vesicle

MD: Molecular Dynamic

PCR: Polymerase Chain Reaction

PET: Photoinduced Electron Transfer

POC: Point-of-Care

ROXS: Reducing and Oxidizing System

TCSPC: Time-Correlated Single Photon Counting

TIRF: Total Internal Reflection Fluorescence

ssDNA: single-stranded DNA

10 References

- (1) Singer, C. Notes on the Early History of Microscopy. *Proceedings of the Royal Society of Medicine* **1914**, *7*, 247–279.
- (2) Renz, M. Fluorescence microscopy-a historical and technical perspective. *Cytometry. Part A: the journal of the International Society for Analytical Cytology* **2013**, *83*, 767–779.
- (3) Moerner; Kador. Optical detection and spectroscopy of single molecules in a solid. *Physical review letters* **1989**, *62*, 2535–2538.
- (4) Orrit; Bernard. Single pentacene molecules detected by fluorescence excitation in a p-terphenyl crystal. *Physical review letters* **1990**, *65*, 2716–2719.
- (5) Dickson, R. M.; Cubitt, A. B.; Tsien, R. Y.; Moerner, W. E. On/off blinking and switching behaviour of single molecules of green fluorescent protein. *Nature* **1997**, *388*, 355–358.
- (6) Patterson, G. H.; Lippincott-Schwartz, J. A photoactivatable GFP for selective photolabeling of proteins and cells. *Science* **2002**, *297*, 1873–1877.
- (7) Abbe, E. Beiträge zur Theorie des Mikroskops und der mikroskopischen Wahrnehmung. *Archiv f. mikrosk. Anatomie* **1873**, *9*, 413–468.
- (8) Hell, S. W.; Wichmann, J. Breaking the diffraction resolution limit by stimulated emission: stimulated-emission-depletion fluorescence microscopy. *Optics letters* **1994**, *19*, 780–782.
- (9) Rust, M. J.; Bates, M.; Zhuang, X. Sub-diffraction-limit imaging by stochastic optical reconstruction microscopy (STORM). *Nat Methods* **2006**, *3*, 793–795.
- (10) Betzig, E.; Patterson, G. H.; Sougrat, R.; Lindwasser, O. W.; Olenych, S.; Bonifacino, J. S.; Davidson, M. W.; Lippincott-Schwartz, J.; Hess, H. F. Imaging intracellular fluorescent proteins at nanometer resolution. *Science* **2006**, *313*, 1642–1645.
- (11) Lavis, L. D.; Raines, R. T. Bright ideas for chemical biology. *ACS Chem. Biol.* **2008**, *3*, 142–155.
- (12) Lavis, L. D.; Raines, R. T. Bright building blocks for chemical biology. *ACS chemical biology* **2014**, *9*, 855–866.
- (13) Vogelsang, J.; Kasper, R.; Steinhauer, C.; Person, B.; Heilemann, M.; Sauer, M.; Tinnefeld, P. A Reducing and Oxidizing System Minimizes Photobleaching and Blinking of Fluorescent Dyes. *Angew. Chem. Int. Ed.* **2008**, *47*, 5465–5469.
- (14) Schermelleh, L.; Heintzmann, R.; Leonhardt, H. A guide to super-resolution fluorescence microscopy. *The Journal of Cell Biology* **2010**, *190*, 165–175.
- (15) Shen, L.; Wang, P.; Ke, Y. DNA Nanotechnology-Based Biosensors and Therapeutics. *Advanced healthcare materials* **2021**, *10*, e2002205.
- (16) Avery, O. T.; MacLeod, C. M.; McCarty, M. STUDIES ON THE CHEMICAL NATURE OF THE SUBSTANCE INDUCING TRANSFORMATION OF PNEUMOCOCCAL TYPES. *The Journal of Experimental Medicine* **1944**, *79*, 137–158.

- (17) WATSON, J. D.; CRICK, F. H. C. Molecular Structure of Nucleic Acids: A Structure for Deoxyribose Nucleic Acid. *Nature* **1953**, *171*, 737–738.
- (18) Seeman, N. C. Nucleic acid junctions and lattices. *Journal of Theoretical Biology* **1982**, *99*, 237–247.
- (19) Seeman, N. C. DNA in a material world. *Nature* **2003**, *421*, 427–431.
- (20) Ong, L. L.; Hanikel, N.; Yaghi, O. K.; Grun, C.; Strauss, M. T.; Bron, P.; Lai-Kee-Him, J.; Schueder, F.; Wang, B.; Wang, P.; *et al.* Programmable self-assembly of three-dimensional nanostructures from 10,000 unique components. *Nature* **2017**, *552*, 72–77.
- (21) Ke, Y.; Ong, L. L.; Shih, W. M.; Yin, P. Three-Dimensional Structures Self-Assembled from DNA Bricks. *Science (New York, N.Y.)* **2012**, *338*, 1177–1183.
- (22) Han, D.; Pal, S.; Yang, Y.; Jiang, S.; Nangreave, J.; Liu, Y.; Yan, H. DNA Gridiron Nanostructures Based on Four-Arm Junctions. *Science (New York, N.Y.)* **2013**, *339*, 1412–1415.
- (23) Rothmund, P. W. K. Folding DNA to create nanoscale shapes and patterns. *Nature* **2006**, *440*, 297–302.
- (24) Douglas, S. M.; Dietz, H.; Liedl, T.; Högberg, B.; Graf, F.; Shih, W. M. Self-assembly of DNA into nanoscale three-dimensional shapes. *Nature* **2009**, *459*, 414–418.
- (25) Integrated DNA Technologies, Inc. Oligo modifications. <https://eu.idtdna.com/pages/products/custom-dna-rna/oligo-modifications> (accessed September 9, 2021).
- (26) biomers.net GmbH. Modifications. <https://www.biomers.net/en/Catalog/Modifications> (accessed September 9, 2021).
- (27) Walter, H.-K.; Bauer, J.; Steinmeyer, J.; Kuzuya, A.; Niemeyer, C. M.; Wagenknecht, H.-A. "DNA Origami Traffic Lights" with a Split Aptamer Sensor for a Bicolor Fluorescence Readout. *Nano letters* **2017**, *17*, 2467–2472.
- (28) Li, Y.; Cu, Y. T. H.; Luo, D. Multiplexed detection of pathogen DNA with DNA-based fluorescence nanobarcodes. *Nat Biotechnol* **2005**, *23*, 885–889.
- (29) Li, S.; Jiang, Q.; Liu, S.; Zhang, Y.; Tian, Y.; Song, C.; Wang, J.; Zou, Y.; Anderson, G. J.; Han, J.-Y.; *et al.* A DNA nanorobot functions as a cancer therapeutic in response to a molecular trigger in vivo. *Nature biotechnology* **2018**, *36*, 258–264.
- (30) Ellington, A. D.; Szostak, J. W. In vitro selection of RNA molecules that bind specific ligands. *Nature* **1990**, *346*, 818–822.
- (31) Tuerk, C.; Gold, L. Systematic evolution of ligands by exponential enrichment: RNA ligands to bacteriophage T4 DNA polymerase. *Science* **1990**, *249*, 505–510.
- (32) Kuzuya, A.; Sakai, Y.; Yamazaki, T.; Xu, Y.; Komiyama, M. Nanomechanical DNA origami 'single-molecule beacons' directly imaged by atomic force microscopy. *Nature communications* **2011**, *2*, 449.

- (33) Funke, J. J.; Dietz, H. Placing molecules with Bohr radius resolution using DNA origami. *Nature Nanotech* **2016**, *11*, 47–52.
- (34) Capaldi, S.; Getts, R. C.; Jayasena, S. D. Signal amplification through nucleotide extension and excision on a dendritic DNA platform. *Nucleic acids research* **2000**, *28*, E21.
- (35) Li, Y.; Tseng, Y. D.; Kwon, S. Y.; d'Espaux, L.; Bunch, J. S.; McEuen, P. L.; Luo, D. Controlled assembly of dendrimer-like DNA. *Nature materials* **2004**, *3*, 38–42.
- (36) Zhao, Y.; Hu, S.; Wang, H.; Yu, K.; Guan, Y.; Liu, X.; Li, N.; Liu, F. DNA Dendrimer-Streptavidin Nanocomplex: an Efficient Signal Amplifier for Construction of Biosensing Platforms. *Anal. Chem.* **2017**, *89*, 6907–6914.
- (37) Omabegho, T.; Sha, R.; Seeman, N. C. A bipedal DNA Brownian motor with coordinated legs. *Science* **2009**, *324*, 67–71.
- (38) Jung, C.; Allen, P. B.; Ellington, A. D. A stochastic DNA walker that traverses a microparticle surface. *Nature Nanotech* **2016**, *11*, 157–163.
- (39) Chen, J.; Luo, Z.; Sun, C.; Huang, Z.; Zhou, C.; Yin, S.; Duan, Y.; Li, Y. Research progress of DNA walker and its recent applications in biosensor. *TrAC Trends in Analytical Chemistry* **2019**, *120*, 115626.
- (40) Wang, D.; Vietz, C.; Schröder, T.; Acuna, G.; Lalkens, B.; Tinnefeld, P. A DNA Walker as a Fluorescence Signal Amplifier. *Nano letters* **2017**, *17*, 5368–5374.
- (41) Zheng, J.; Ji, X.; Du, M.; Tian, S.; He, Z. Rational construction of a DNA nanomachine for HIV nucleic acid ultrasensitive sensing. *Nanoscale* **2018**, *10*, 17206–17211.
- (42) Acuna, G. P.; Möller, F. M.; Holzmeister, P.; Beater, S.; Lalkens, B.; Tinnefeld, P. Fluorescence enhancement at docking sites of DNA-directed self-assembled nanoantennas. *Science (New York, N.Y.)* **2012**, *338*, 506–510.
- (43) Ramakrishnan, S.; Ijäs, H.; Linko, V.; Keller, A. Structural stability of DNA origami nanostructures under application-specific conditions. *Computational and structural biotechnology journal* **2018**, *16*, 342–349.
- (44) Auvinen, H.; Zhang, H.; Nonappa; Kopilow, A.; Niemelä, E. H.; Nummelin, S.; Correia, A.; Santos, H. A.; Linko, V.; Kostianen, M. A. Protein Coating of DNA Nanostructures for Enhanced Stability and Immunocompatibility. *Advanced healthcare materials* **2017**, *6*.
- (45) Ahmadi, Y.; Llano, E. de; Barišić, I. (Poly)cation-induced protection of conventional and wireframe DNA origami nanostructures. *Nanoscale* **2018**, *10*, 7494–7504.
- (46) Perrault, S. D.; Shih, W. M. Virus-inspired membrane encapsulation of DNA nanostructures to achieve in vivo stability. *ACS nano* **2014**, *8*, 5132–5140.
- (47) Mikkilä, J.; Eskelinen, A.-P.; Niemelä, E. H.; Linko, V.; Frilander, M. J.; Törmä, P.; Kostianen, M. A. Virus-encapsulated DNA origami nanostructures for cellular delivery. *Nano letters* **2014**, *14*, 2196–2200.

- (48) Rajendran, A.; Endo, M.; Katsuda, Y.; Hidaka, K.; Sugiyama, H. Photo-cross-linking-assisted thermal stability of DNA origami structures and its application for higher-temperature self-assembly. *Journal of the American Chemical Society* **2011**, *133*, 14488–14491.
- (49) Gerling, T.; Kube, M.; Kick, B.; Dietz, H. Sequence-programmable covalent bonding of designed DNA assemblies. *Science advances* **2018**, *4*, eaau1157.
- (50) Ramakrishnan, S.; Shen, B.; Kostianen, M. A.; Grundmeier, G.; Keller, A.; Linko, V. Real-Time Observation of Superstructure-Dependent DNA Origami Digestion by DNase I Using High-Speed Atomic Force Microscopy. *ChemBioChem* **2019**, *20*, 2818–2823.
- (51) Douglas, S. M.; Bachelet, I.; Church, G. M. A logic-gated nanorobot for targeted transport of molecular payloads. *Science (New York, N.Y.)* **2012**, *335*, 831–834.
- (52) Liu, L.; Rong, Q.; Ke, G.; Zhang, M.; Li, J.; Li, Y.; Liu, Y.; Chen, M.; Zhang, X.-B. Efficient and Reliable MicroRNA Imaging in Living Cells via a FRET-Based Localized Hairpin-DNA Cascade Amplifier. *Anal. Chem.* **2019**, *91*, 3675–3680.
- (53) Zijlstra, P.; Paulo, P. M. R.; Orrit, M. Optical detection of single non-absorbing molecules using the surface plasmon resonance of a gold nanorod. *Nature Nanotech* **2012**, *7*, 379–382.
- (54) Baaske, M. D.; Foreman, M. R.; Vollmer, F. Single-molecule nucleic acid interactions monitored on a label-free microcavity biosensor platform. *Nature Nanotech* **2014**, *9*, 933–939.
- (55) Rissin, D. M.; Kan, C. W.; Campbell, T. G.; Howes, S. C.; Fournier, D. R.; Song, L.; Piech, T.; Patel, P. P.; Chang, L.; Rivnak, A. J.; *et al.* Single-molecule enzyme-linked immunosorbent assay detects serum proteins at subfemtomolar concentrations. *Nat Biotechnol* **2010**, *28*, 595–599.
- (56) Novotny, L.; van Hulst, N. Antennas for light. *Nature Photon* **2011**, *5*, 83–90.
- (57) Kinkhabwala, A.; Yu, Z.; Fan, S.; Avlasevich, Y.; Müllen, K.; Moerner, W. E. Large single-molecule fluorescence enhancements produced by a bowtie nanoantenna. *Nature Photon* **2009**, *3*, 654–657.
- (58) Vietz, C.; Lalkens, B.; Acuna, G. P.; Tinnefeld, P. Synergistic Combination of Unquenching and Plasmonic Fluorescence Enhancement in Fluorogenic Nucleic Acid Hybridization Probes. *Nano letters* **2017**, *17*, 6496–6500.
- (59) Balzarotti, F.; Stefani, F. D. Plasmonics meets far-field optical nanoscopy. *ACS nano* **2012**, *6*, 4580–4584.
- (60) Schuller, J. A.; Barnard, E. S.; Cai, W.; Jun, Y. C.; White, J. S.; Brongersma, M. L. Plasmonics for extreme light concentration and manipulation. *Nature materials* **2010**, *9*, 193–204.
- (61) Puchkova, A.; Vietz, C.; Pibiri, E.; Wünsch, B.; Sanz Paz, M.; Acuna, G. P.; Tinnefeld, P. DNA Origami Nanoantennas with over 5000-fold Fluorescence Enhancement and Single-Molecule Detection at 25 μ M. *Nano letters* **2015**, *15*, 8354–8359.
- (62) Vietz, C.; Kaminska, I.; Sanz Paz, M.; Tinnefeld, P.; Acuna, G. P. Broadband Fluorescence Enhancement with Self-Assembled Silver Nanoparticle Optical Antennas. *ACS nano* **2017**, *11*, 4969–4975.

- (63) Sako, Y.; Minoghchi, S.; Yanagida, T. Single-molecule imaging of EGFR signalling on the surface of living cells. *Nature cell biology* **2000**, *2*, 168–172.
- (64) Hou, W.; Ma, D.; He, X.; Han, W.; Ma, J.; Wang, H.; Xu, C.; Xie, R.; Fan, Q.; Ye, F.; *et al.* Subnanometer-Precision Measurements of Transmembrane Motions of Biomolecules in Plasma Membranes Using Quenchers in Extracellular Environment. *Nano letters* **2021**, *21*, 485–491.
- (65) Sustarsic, M.; Kapanidis, A. N. Taking the ruler to the jungle: single-molecule FRET for understanding biomolecular structure and dynamics in live cells. *Current Opinion in Structural Biology* **2015**, *34*, 52–59.
- (66) Lerner, E.; Cordes, T.; Ingargiola, A.; Alhadid, Y.; Chung, S.; Michalet, X.; Weiss, S. Toward dynamic structural biology: Two decades of single-molecule Förster resonance energy transfer. *Science* **2018**, *359*, eaan1133.
- (67) Sakon, J. J.; Wenginger, K. R. Detecting the conformation of individual proteins in live cells. *Nat Methods* **2010**, *7*, 203–205.
- (68) Sackmann, E.; Merkel, R. *Lehrbuch der Biophysik*, 2. Nachdr; Lehrbuch Physik; Wiley-VCH: Weinheim, 2012.
- (69) Neher, E.; Sakmann, B. Single-channel currents recorded from membrane of denervated frog muscle fibres. *Nature* **1976**, *260*, 799–802.
- (70) Sepehri Rad, M.; Choi, Y.; Cohen, L. B.; Baker, B. J.; Zhong, S.; Storace, D. A.; Braubach, O. R. Voltage and Calcium Imaging of Brain Activity. *Biophysical journal* **2017**, *113*, 2160–2167.
- (71) Platasa, J.; Pieribone, V. A. Genetically encoded fluorescent voltage indicators: Are we there yet? *Current opinion in neurobiology* **2018**, *50*, 146–153.
- (72) Adam, Y.; Kim, J. J.; Lou, S.; Zhao, Y.; Xie, M. E.; Brinks, D.; Wu, H.; Mostajo-Radji, M. A.; Kheifets, S.; Parot, V.; *et al.* Voltage imaging and optogenetics reveal behaviour-dependent changes in hippocampal dynamics. *Nature* **2019**, *569*, 413–417.
- (73) Chanda, B.; Blunck, R.; Faria, L. C.; Schweizer, F. E.; Mody, I.; Bezanilla, F. A hybrid approach to measuring electrical activity in genetically specified neurons. *Nature neuroscience* **2005**, *8*, 1619–1626.
- (74) Abdelfattah, A. S.; Kawashima, T.; Singh, A.; Novak, O.; Liu, H.; Shuai, Y.; Huang, Y.-C.; Campagnola, L.; Seeman, S. C.; Yu, J.; *et al.* Bright and photostable chemigenetic indicators for extended in vivo voltage imaging. *Science (New York, N. Y.)* **2019**, *365*, 699–704.
- (75) Miller, E. W.; Lin, J. Y.; Frady, E. P.; Steinbach, P. A.; Kristan, W. B., JR; Tsien, R. Y. Optically monitoring voltage in neurons by photo-induced electron transfer through molecular wires. *Proceedings of the National Academy of Sciences of the United States of America* **2012**, *109*, 2114–2119.
- (76) Peterka, D. S.; Takahashi, H.; Yuste, R. Imaging voltage in neurons. *Neuron* **2011**, *69*, 9–21.
- (77) González, J. E.; Tsien, R. Y. Voltage sensing by fluorescence resonance energy transfer in single cells. *Biophysical journal* **1995**, *69*, 1272–1280.

- (78) González, J. E.; Tsien, R. Y. Improved indicators of cell membrane potential that use fluorescence resonance energy transfer. *Chemistry & Biology* **1997**, *4*, 269–277.
- (79) Miller, E. W. Small molecule fluorescent voltage indicators for studying membrane potential. *Current opinion in chemical biology* **2016**, *33*, 74–80.
- (80) Saminathan, A.; Devany, J.; Veetil, A. T.; Suresh, B.; Pillai, K. S.; Schwake, M.; Krishnan, Y. A DNA-based voltmeter for organelles. *Nature nanotechnology* **2021**, *16*, 96–103.
- (81) Bar-Elli, O.; Steinitz, D.; Yang, G.; Tenne, R.; Ludwig, A.; Kuo, Y.; Triller, A.; Weiss, S.; Oron, D. Rapid Voltage Sensing with Single Nanorods via the Quantum Confined Stark Effect. *ACS photonics* **2018**, *5*, 2860–2867.
- (82) Park, K.; Kuo, Y.; Shvadchak, V.; Ingargiola, A.; Dai, X.; Hsiung, L.; Kim, W.; Zhou, H.; Zou, P.; Levine, A. J.; *et al.* Membrane insertion of-and membrane potential sensing by-semiconductor voltage nanosensors: Feasibility demonstration. *Science advances* **2018**, *4*, e1601453.
- (83) Vance, J. E.; Steenbergen, R. Metabolism and functions of phosphatidylserine. *Progress in lipid research* **2005**, *44*, 207–234.
- (84) Ma, Y.; Poole, K.; Goyette, J.; Gaus, K. Introducing Membrane Charge and Membrane Potential to T Cell Signaling. *Frontiers in immunology* **2017**, *8*, 1513.
- (85) McLaughlin, S. The Electrostatic Properties of Membranes. *Annu. Rev. Biophys. Biophys. Chem.* **1989**, *18*, 113–136.
- (86) Manno, S.; Takakuwa, Y.; Mohandas, N. Identification of a functional role for lipid asymmetry in biological membranes: Phosphatidylserine-skeletal protein interactions modulate membrane stability. *PNAS* **2002**, *99*, 1943–1948.
- (87) Xu, P.; Baldridge, R. D.; Chi, R. J.; Burd, C. G.; Graham, T. R. Phosphatidylserine flipping enhances membrane curvature and negative charge required for vesicular transport. *The Journal of Cell Biology* **2013**, *202*, 875–886.
- (88) Zwaal, R. F. A.; Comfurius, P.; Bevers, E. M. Surface exposure of phosphatidylserine in pathological cells. *Cellular and molecular life sciences : CMLS* **2005**, *62*, 971–988.
- (89) Elliott, J. I.; Surprenant, A.; Marelli-Berg, F. M.; Cooper, J. C.; Cassady-Cain, R. L.; Wooding, C.; Linton, K.; Alexander, D. R.; Higgins, C. F. Membrane phosphatidylserine distribution as a non-apoptotic signalling mechanism in lymphocytes. *Nature cell biology* **2005**, *7*, 808–816.
- (90) Rysavy, N. M.; Shimoda, L. M. N.; Dixon, A. M.; Speck, M.; Stokes, A. J.; Turner, H.; Umemoto, E. Y. Beyond apoptosis: the mechanism and function of phosphatidylserine asymmetry in the membrane of activating mast cells. *Bioarchitecture* **2014**, *4*, 127–137.
- (91) Ma, Y.; Yamamoto, Y.; Nicovich, P. R.; Goyette, J.; Rossy, J.; Gooding, J. J.; Gaus, K. A FRET sensor enables quantitative measurements of membrane charges in live cells. *Nature biotechnology* **2017**, *35*, 363–370.
- (92) Leventis, P. A.; Grinstein, S. The distribution and function of phosphatidylserine in cellular membranes. *Annual review of biophysics* **2010**, *39*, 407–427.

- (93) Okeley, N. M.; Gelb, M. H. A designed probe for acidic phospholipids reveals the unique enriched anionic character of the cytosolic face of the mammalian plasma membrane. *The Journal of biological chemistry* **2004**, *279*, 21833–21840.
- (94) Yeung, T.; Gilbert, G. E.; Shi, J.; Silvius, J.; Kapus, A.; Grinstein, S. Membrane phosphatidylserine regulates surface charge and protein localization. *Science (New York, N.Y.)* **2008**, *319*, 210–213.
- (95) Yeung, T.; Terebiznik, M.; Yu, L.; Silvius, J.; Abidi, W. M.; Philips, M.; Levine, T.; Kapus, A.; Grinstein, S. Receptor activation alters inner surface potential during phagocytosis. *Science (New York, N.Y.)* **2006**, *313*, 347–351.
- (96) Jabłoński, A. General Theory of Pressure Broadening of Spectral Lines. *Phys. Rev.* **1945**, *68*, 78–93.
- (97) Franck, J.; Dymond, E. G. Elementary processes of photochemical reactions. *Trans. Faraday Soc.* **1926**, *21*, 536.
- (98) Condon, E. A Theory of Intensity Distribution in Band Systems. *Phys. Rev.* **1926**, *28*, 1182–1201.
- (99) Condon, E. U. Wave Mechanics and the Normal State of the Hydrogen Molecule. *PNAS* **1927**, *13*, 466–470.
- (100) Born, M.; Oppenheimer, R. Zur Quantentheorie der Molekeln. *Ann. Phys.* **1927**, *389*, 457–484.
- (101) Kasha, M. Characterization of electronic transitions in complex molecules. *Discuss. Faraday Soc.* **1950**, *9*, 14.
- (102) Stokes, G. G. On the Change of Refrangibility of Light. *Phil. Trans. R. Soc.* **1852**, *142*, 463–562.
- (103) Dexter, D. L. A Theory of Sensitized Luminescence in Solids. *The Journal of chemical physics* **1953**, *21*, 836–850.
- (104) Förster, T. Zwischenmolekulare Energiewanderung und Fluoreszenz. *Ann. Phys.* **1948**, *437*, 55–75.
- (105) Hellenkamp, B.; Schmid, S.; Doroshenko, O.; Opanasyuk, O.; Kühnemuth, R.; Rezaei Adariani, S.; Ambrose, B.; Aznauryan, M.; Barth, A.; Birkedal, V.; *et al.* Precision and accuracy of single-molecule FRET measurements—a multi-laboratory benchmark study. *Nature methods* **2018**, *15*, 669–676.
- (106) Roy, R.; Hohng, S.; Ha, T. A practical guide to single-molecule FRET. *Nature methods* **2008**, *5*, 507–516.
- (107) Hübner, C. G.; Renn, A.; Renge, I.; Wild, U. P. Direct observation of the triplet lifetime quenching of single dye molecules by molecular oxygen. *The Journal of chemical physics* **2001**, *115*, 9619–9622.

- (108) Widengren, J.; Rigler, R. Mechanisms of photobleaching investigated by fluorescence correlation spectroscopy. *Bioimaging* **1996**, *4*, 149–157.
- (109) Aitken, C. E.; Marshall, R. A.; Puglisi, J. D. An Oxygen Scavenging System for Improvement of Dye Stability in Single-Molecule Fluorescence Experiments. *Biophysical Journal* **2008**, *94*, 1826–1835.
- (110) Rasnik, I.; McKinney, S. A.; Ha, T. Nonblinking and long-lasting single-molecule fluorescence imaging. *Nat Methods* **2006**, *3*, 891–893.
- (111) Tinnefeld, P.; Sauer, M. Branching out of single-molecule fluorescence spectroscopy: challenges for chemistry and influence on biology. *Angew. Chem. Int. Ed.* **2005**, *44*, 2642–2671.
- (112) Weiss, S. Fluorescence spectroscopy of single biomolecules. *Science (New York, N.Y.)* **1999**, *283*, 1676–1683.
- (113) Moerner, W. E.; Orrit, M. Illuminating single molecules in condensed matter. *Science* **1999**, *283*, 1670–1676.
- (114) Holzmeister, P.; Acuna, G. P.; Grohmann, D.; Tinnefeld, P. Breaking the concentration limit of optical single-molecule detection. *Chemical Society reviews* **2014**, *43*, 1014–1028.
- (115) Lakowicz, J. R. *Principles of Fluorescence Spectroscopy*, Second Edition; Springer: Boston, MA, 1999.
- (116) Andor. iXon EMCCD Cameras for Microscopy and Life Science. <https://andor.oxinst.com/products/ixon-emccd-cameras-for-life-science> (accessed August 31, 2021).
- (117) Princeton Instruments. KURO Back-Illuminated Scientific CMOS Camera. <https://www.princetoninstruments.com/products/kuro-family/kuro> (accessed August 31, 2021).
- (118) Rigler, R.; Mets; Widengren, J.; Kask, P. Fluorescence correlation spectroscopy with high count rate and low background: analysis of translational diffusion. *Eur Biophys J* **1993**, *22*.
- (119) Kallenbach, N. R.; Ma, R.-I.; Seeman, N. C. An immobile nucleic acid junction constructed from oligonucleotides. *Nature* **1983**, *305*, 829–831.
- (120) Chen, J.; Seeman, N. C. Synthesis from DNA of a molecule with the connectivity of a cube. *Nature* **1991**, *350*, 631–633.
- (121) Jiang, Q.; Song, C.; Nangreave, J.; Liu, X.; Lin, L.; Qiu, D.; Wang, Z.-G.; Zou, G.; Liang, X.; Yan, H.; *et al.* DNA origami as a carrier for circumvention of drug resistance. *Journal of the American Chemical Society* **2012**, *134*, 13396–13403.
- (122) Zhang, Q.; Jiang, Q.; Li, N.; Dai, L.; Liu, Q.; Song, L.; Wang, J.; Li, Y.; Tian, J.; Ding, B.; *et al.* DNA origami as an in vivo drug delivery vehicle for cancer therapy. *ACS nano* **2014**, *8*, 6633–6643.
- (123) Amir, Y.; Ben-Ishay, E.; Levner, D.; Ittah, S.; Abu-Horowitz, A.; Bachelet, I. Universal computing by DNA origami robots in a living animal. *Nature nanotechnology* **2014**, *9*, 353–357.

- (124) Jain, P. K.; El-Sayed, M. A. Plasmonic coupling in noble metal nanostructures. *Chemical Physics Letters* **2010**, *487*, 153–164.
- (125) Harrison, R. K.; Ben-Yakar, A. Role of near-field enhancement in plasmonic laser nanoablation using gold nanorods on a silicon substrate. *Optics express* **2010**, *18*, 22556–22571.
- (126) Yuan, H.; Khatua, S.; Zijlstra, P.; Yorulmaz, M.; Orrit, M. Thousand-fold enhancement of single-molecule fluorescence near a single gold nanorod. *Angewandte Chemie (International ed. in English)* **2013**, *52*, 1217–1221.
- (127) Fu, Y.; Lakowicz, J. R. Modification of single molecule fluorescence near metallic nanostructures. *Laser & photonics reviews* **2009**, *3*, 221–232.
- (128) Taylor, A. B.; Zijlstra, P. Single-Molecule Plasmon Sensing: Current Status and Future Prospects. *ACS Sens.* **2017**, *2*, 1103–1122.
- (129) Mirkin, C. A.; Letsinger, R. L.; Mucic, R. C.; Storhoff, J. J. A DNA-based method for rationally assembling nanoparticles into macroscopic materials. *Nature* **1996**, *382*, 607–609.
- (130) Ohki, S. Membrane potential, surface potential and ionic permeability. *Physics Letters A* **1979**, *75*, 149–152.
- (131) Alberts, B.; Johnson, A.; Lewis, J.; Morgan, D.; Raff, M.; Roberts, K.; Walter, P. *Molekularbiologie der Zelle*, 6. Auflage; Wiley-VCH: Weinheim, 2017.
- (132) Gouy, M. Sur la constitution de la charge électrique à la surface d'un électrolyte. *J. Phys. Theor. Appl.* **1910**, *9*, 457–468.
- (133) Chapman, D. L. A contribution to the theory of electrocapillarity. *The London, Edinburgh, and Dublin Philosophical Magazine and Journal of Science* **1913**, *25*, 475–481.
- (134) Debye, P.; Hückel, E. Zur Theorie der Elektrolyte. I. Gefrierpunktserniedrigung und verwandte Erscheinungen. *Physikalische Zeitschrift* **1923**, *24* (9), 185–206.
- (135) Otto Stern. ZUR THEORIE DER ELEKTROLYTISCHEN DOPPELSCHICHT. *Zeitschrift für Elektrochemie und angewandte physikalische Chemie* **1924**, *30*, 508–516.
- (136) McLaughlin, S.; Murray, D. Plasma membrane phosphoinositide organization by protein electrostatics. *Nature* **2005**, *438*, 605–611.
- (137) Heo, W. D.; Inoue, T.; Park, W. S.; Kim, M. L.; Park, B. O.; Wandless, T. J.; Meyer, T. PI(3,4,5)P₃ and PI(4,5)P₂ lipids target proteins with polybasic clusters to the plasma membrane. *Science (New York, N.Y.)* **2006**, *314*, 1458–1461.
- (138) Wang, L. Measurements and implications of the membrane dipole potential. *Annual review of biochemistry* **2012**, *81*, 615–635.
- (139) Liberman, E. A.; Topaly, V. P. Pronitsaemost' bimolekuliarnykh fosfolipidnykh membran dlia zhirorastvorimykh ionov. *Biofizika* **1969**, *14*, 452–461.

- (140) Woo, S.; Rothmund, P. W. K. Programmable molecular recognition based on the geometry of DNA nanostructures. *Nature chemistry* **2011**, *3*, 620–627.
- (141) Schmied, J. J.; Gietl, A.; Holzmeister, P.; Forthmann, C.; Steinhauer, C.; Dammeyer, T.; Tinnefeld, P. Fluorescence and super-resolution standards based on DNA origami. *Nature methods* **2012**, *9*, 1133–1134.
- (142) Hope, M. J.; Bally, M. B.; Webb, G.; Cullis, P. R. Production of large unilamellar vesicles by a rapid extrusion procedure. Characterization of size distribution, trapped volume and ability to maintain a membrane potential. *Biochimica et Biophysica Acta (BBA) - Biomembranes* **1985**, *812*, 55–65.
- (143) Ochmann, S. E.; Vietz, C.; Trofymchuk, K.; Acuna, G. P.; Lalkens, B.; Tinnefeld, P. Optical Nanoantenna for Single Molecule-Based Detection of Zika Virus Nucleic Acids without Molecular Multiplication. *Analytical chemistry* **2017**, *89*, 13000–13007.
- (144) Ochmann, S. E.; Joshi, H.; Büber, E.; Franquelim, H. G.; Stegemann, P.; Saccà, B.; Keyser, U. F.; Aksimentiev, A.; Tinnefeld, P. DNA Origami Voltage Sensors for Transmembrane Potentials with Single-Molecule Sensitivity. *Nano letters* **2021**, *21*, 8634–8641.
- (145) Ochmann, S. E.; Schröder, T.; Schulz, C. M.; Tinnefeld, P. Quantitative Single-Molecule Measurements of Membrane Charges with DNA Origami Sensors. *Analytical Chemistry* **2022**, *94*, 2633–2640.
- (146) Schröder, T.; Bohlen, J.; Ochmann, S. E.; Schüler, P.; Krause, S.; Tinnefeld, P. Systematic microtime gating for fluorescence correlation spectroscopy yields equilibrium constants and allows discrimination of photophysics from structural dynamic processes. *In preparation* **2022**.
- (147) Keller, A.; Linko, V. Challenges and Perspectives of DNA Nanostructures in Biomedicine. *Angewandte Chemie (International ed. in English)* **2020**, *59*, 15818–15833.
- (148) Chandrasekaran, A. R. Nuclease resistance of DNA nanostructures. *Nature reviews. Chemistry* **2021**, 225–239.
- (149) Trofymchuk, K.; Glembockyte, V.; Grabenhorst, L.; Steiner, F.; Vietz, C.; Close, C.; Pfeiffer, M.; Richter, L.; Schütte, M. L.; Selbach, F.; *et al.* Addressable nanoantennas with cleared hotspots for single-molecule detection on a portable smartphone microscope. *Nature communications* **2021**, *12*, 950.
- (150) Vietz, C.; Schütte, M. L.; Wei, Q.; Richter, L.; Lalkens, B.; Ozcan, A.; Tinnefeld, P.; Acuna, G. P. Benchmarking Smartphone Fluorescence-Based Microscopy with DNA Origami Nanobeads: Reducing the Gap toward Single-Molecule Sensitivity. *ACS Omega* **2019**, *4*, 637–642.
- (151) Pfeiffer, M.; Trofymchuk, K.; Ranallo, S.; Ricci, F.; Steiner, F.; Cole, F.; Glembockyte, V.; Tinnefeld, P. Single antibody detection in a DNA origami nanoantenna. *iScience* **2021**, *24*, 103072.
- (152) Mobarak, E.; Javanainen, M.; Kulig, W.; Honigmann, A.; Sezgin, E.; Aho, N.; Eggeling, C.; Rog, T.; Vattulainen, I. How to minimize dye-induced perturbations while studying biomembrane structure and dynamics: PEG linkers as a rational alternative. *Biochimica et biophysica acta. Biomembranes* **2018**, *1860*, 2436–2445.

(153) Lukinavičius, G.; Umezawa, K.; Olivier, N.; Honigmann, A.; Yang, G.; Plass, T.; Mueller, V.; Reymond, L.; Corrêa, I. R.; Luo, Z.-G.; *et al.* A near-infrared fluorophore for live-cell super-resolution microscopy of cellular proteins. *Nature chemistry* **2013**, *5*, 132–139.

(154) Grimm, J. B.; Muthusamy, A. K.; Liang, Y.; Brown, T. A.; Lemon, W. C.; Patel, R.; Lu, R.; Macklin, J. J.; Keller, P. J.; Ji, N.; *et al.* A general method to fine-tune fluorophores for live-cell and in vivo imaging. *Nature methods* **2017**, *14*, 987–994.

11 Acknowledgements

An dieser Stelle möchte ich einer Reihe von Menschen danken, die zum Gelingen dieser Arbeit beigetragen haben.

Zuallererst danke ich meinem Doktorvater Philip Tinnefeld für die Chance, meine Arbeit in seiner Gruppe anfertigen zu dürfen, für die vielen Diskussionen, die Förderung und Forderung, die mich immer wieder motiviert und inspiriert haben. Auch danke ich ihm für das Vertrauen, was er mir stets geschenkt hat, für die vielen Möglichkeiten auf Konferenzen fahren und mich anderweitig weiterbilden zu können sowie für den freundschaftlichen Umgang. Es war eine tolle Doktorandenzeit.

Prof. Don Lamb danke ich für die Übernahme des Zweitgutachtens, sowie für die spannenden AK Seminare. Ebenso gilt mein Dank den anderen Kommissionsmitgliedern Prof. Dr. Ralf Jungmann, Prof. Dr. Joost Wintterlin, Prof. Dr. Achim Hartschuh und Prof. Dr. Oliver Trapp.

Darüber hinaus danke ich den Kollaborationspartnern, die richtungsgebend für meine Projekte waren und dabei besonders Prof. Dr. Ulrich Keyser, der mich sehr freundlich in seinem Labor willkommen geheißen hat und bei dem ich vieles Wertvolles lernen konnte.

Endloser Dank gilt außerdem meinen lieben Arbeitskollegen, ohne die so Vieles nicht möglich gewesen wäre. Die wunderbare Arbeitsatmosphäre, die stetige Hilfsbereitschaft, die guten Diskussionen und das leckere Bier möchte ich nicht missen. Besonders die Freundschaften, die ich unter meinen Kollegen geknüpft habe, haben mich durch die Achterbahnfahrten des Laboralltags getragen.

Zunächst möchte ich mich im Speziellen bei Bettina, Kathi und Kristina bedanken, mit den ich mir das Büro in Braunschweig geteilt habe, und bei Andrés, Kateryna, Kristina, Fiona, FloSel und Martina, die meine Bürogefährten in München waren. Es war toll, in guten Momenten die Freude zu teilen und in schlechten Momenten ermutigt zu werden.

Dann danke ich Birka für die Betreuung in Braunschweig zum Start meiner Zeit und Carolin für die anfängliche Einarbeitung und die gemeinsame Zusammenarbeit am Nanoantennenthema.

Ich danke allen Studenten, die mich bei meiner Arbeit unterstützt haben – insbesondere Clara. Sie hat nicht nur das Projekt vorangetrieben, sondern war mir eine wunderbare Teamkollegin.

Weiter möchte ich allen danken, die mir geholfen haben, das Weitfeld-Mikroskop aufzubauen und instand zu halten, sowie Kateryna, Kristina und Tim für die Bereitstellung der konfokalen Mikroskope und Angelika, ohne die die Labore niemals laufen würden, und für ihr offenes Ohr.

Tim möchte ich außerdem für die Zusammenarbeit am Surface-Charge-Sensing-Projekt danken, dass er mit viel Mühe immer wieder seine Software angepasst hat und seinen wertvollen Input. Auch generell danke ich ihm für seine Hilfsbereitschaft und die Diskussionen zwischendurch, die manchmal beiläufig wirkten, aber mich in meinem Projekt häufiger weitergebracht haben.

Florian gilt mein Dank für die Geduld und Hilfe, die er immer wieder für mich und meine IT-Probleme aufgebracht hat und Dr. Moritz Ehrl, Frau Steger und Frau Talk für die Erleichterung aller administrativer Arbeiten.

Außerdem möchte ich den Korrekturlesern Carsten, Kateryna und Stefan für ihre Zeit und Mühe danken. Die Kommentare und Anregungen waren unglaublich hilfreich.

Der Laborumzug von Braunschweig nach München war aufregend und hat uns alle zusammengeschweißt. Daher danke an Andrés, Carsten, FloSel, Ija, Johann, Kateryna, Kristina,

Mario, Philip und Tim für diese unfassbare Zeit. Ich möchte sie nicht missen. Und danke an alle aus dem Haus E, die uns so herzlich aufgenommen haben und das eine oder andere Bier mit uns geteilt haben.

Auch das CeNS und insbesondere Susanne haben es am Anfang in München einfach gemacht, sich zu vernetzen und über die Zeit hinweg an vielen wissenschaftlichen und informellen Veranstaltungen spannende Einblicke zu bekommen. Ebenso Teil des SFB1032 zu sein, hat mich und mein Projekt sehr bereichert.

Zuletzt möchte ich meinen Freunden danken, die mich direkt oder auch indirekt während der Promotionszeit unterstützten und immer ein offenes Ohr hatten – ganz besonders Robert. Meiner Familie danke ich, dass sie immer an mich geglaubt und mich mit allen Möglichkeiten unterstützt hat über die letzten über 30 Jahre hinweg. <3